On the 3D-Structures of Meprin α and β, and the Role of Oligomerization for Stability and Activity of Meprin α

Dissertation

zur Erlangung des

Doktorgrades der Naturwissenschaften (Dr. rer. nat.)

der

Naturwissenschaftlichen Fakultät I – Biowissenschaften –

der Martin-Luther-Universität

Halle-Wittenberg,

vorgelegt

von Claudia Fritz geb. Spahn

geb. am 21.08.1991 in Borna

Gutachter:

1. Prof. Dr. Markus Pietzsch
2. Prof. Dr. Stephan Schilling
3. Prof. Dr. Walter Stöcker

Halle (Saale), 06.09.2021

Table of Contents

List of figures

List of tables

Abbreviations

Abz	2-Aminobenzoyl
ADAM	A desintegrin and metalloproteinase
AEBSF	4-(2-Aminoethyl)benzenesulfonyl fluoride
Amp	Ampicillin
AP	Alkaline phosphatase
APP	Amyloid precursor protein
APS	Ammonium persulfate
BACE-1	Beta-site amyloid precursor protein-cleaving enzyme 1
BCA	Bicinchoninic acid
BCIP	5-bromo-4-chloro-3-indoyl phosphate
BiP	Immunoglobulin binding chaperone protein
BSA	Bovine serum albumin
bsd	Blasticidine
$CaCl_2$	Calcium chloride
CD-spectroscopy	Circular dichroism spectroscopy
CD	Crohn's disease
Cryo-EM	Cryo-electron microscopy
CUB	Complement subcomponents C1r/C1s, embryonic sea urchin protein Uegf, BMP-1
DHAP	2,5-dihydroxyacetophenone
DHB	2,5-dihydroxybenzoic acid
DRI	Differential refractive index
DI water	Deionized water
DMSO	Dimethyl sulfoxide
Dnp	2,4-dinitrophenyl

dNTP	Desoxy-nucleoside triphosphate
EBA	Expanded bed adsorption
ECM	Extracellular matrix
EDTA	Ethylenediaminetetraacetic acid
EGF	Epidermal growth factor
EGF/TLR4	Epidermal growth factor/toll-like receptor 4
ER	Endoplasmic reticulum
FSC	Fourier shell correlation
FBS	Fetal bovine serum
GOI	Gene of interest
HCC	Hepatocellular carcinoma
HEK	Human embryonic kidney cells
HIC	Hydrophobic interaction
HRP	Horseradish peroxidase
IBD	Inflammatory bowel disease
IGF	Insulin like growth factor
IL	Interleukin
IMAC	Immobilized metal in affinity chromatography
IPAH	Idiopathic pulmonary arterial hypertension
LB	Lysogeny broth
LPS	Lipopolysaccharide
MALDI-TOF	Matrix-assisted laser desorption/ionization time-of-flight mass spectrometry
MAM	Meprin A5 protein tyrosine phosphatase µ
MMP	Matrix metalloproteinases
MT	Metallothionein

MALS	Multi-angle light scattering
MW	Molecular weight
NaCl	Sodium chloride
NBT	Nitrotetrazolium blue chloride
NEB	New England Biolabs
NF449	4,4′,4″,4‴-[Carbonyl-bis[imino-5,1,3-benzenetriyl bis-(carbonyl-imino)]]tetrakis(benzene-1,3-disulfonic acid
NNGH	N-isobutyl-N-(4-methoxyphenylsulfonyl)-glycyl hydroxamic acid
OD/OD_{600}	Optical density at 600 nm
PAA	Polyacrylamide
PABA-	Peptide (N-benzoyl-tyrosyl-*p*-amino-benzoic acid)
PCR	Polymerase chain reaction
PICS	Proteomic identification of protease cleavage site specificity
PPNDS	Pyridoxal-5′-phosphate-6-(2′-naphthylazo-6′-nitro-4′,8′-disulfonate) tetrasodium
RFU	Relative fluorescent units
RMSD	Root mean square deviation
RT	Room temperature
S2 cells	Schneider's *Drosophila* S2 cells
SDS-PAGE	Sodium dodecyl sulfate-polyacrylamide gel electrophoresis
SEC	Size exclusion chromatography
TAE	TRIS-Acetat/EDTA
TAILS	Terminal amine isotopic labeling of substrates
TEMED	Tetramethylethylenediamine
TEV	Tobacco etch virus
TGFα	Transforming growth factor α

TIMP	Tissue inhibitors of metalloproteases
TNF	Tumor necrosis factor
TRAF	Tumor-necrosis-factor-receptor-associated factor
TEM	Transmission electron microscopy
TRIS	Tris(hydroxymethyl)aminomethane
UV	Ultraviolet
YNB	Yeast nitrogen base

1. Introduction

About 2% of the human genome encodes for proteolytic enzymes and their inhibitors (Puente et al. 2005), accordingly more than 600 individual proteases are characterized and available in the MEROPS database (Rawlings et al. 2014). So, it is not surprising that proteases own multiple biological functions (Ramachandran et al. 2016), such as regulating fate, localization and activity of many proteins. Proteases possess a great variety in structure and size, ranging from 20 kDa to 6 MDa. Some consist of several domains with multiple post translational modifications. In general, proteases are highly regulated and are key players in health and viability of cells. They are involved in many diseases, e.g. Alzheimer's disease, inflammatory diseases or cancer. Consequently, protease inhibitors are useful for medical and industrial application (Bond 2019).

Proteases have been classified in clans, like serine-, aspartic-, glutamic-, threonine-, cysteine- and metalloproteases (Rawlings et al. 2014). Metalloproteases represent the largest group of proteolytic enzymes, and it is known that the murine and the human genome encode for about 200 metalloproteinases (Sterchi et al. 2008). They are involved in cell proliferation, differentiation and remodelling of the extracellular matrix, vascularization as well as cell migration (Chang and Werb 2001). As a consequence, metalloproteases are extrinsic regulators during malignant transformation and normal development (Vu and Werb 2000). These enzymes act pericellularly and extracellularly, since they occur plasma membrane-bound or secreted.

Most metalloproteases belong to the superfamily of metzincins (Stöcker et al. 1995), which are characterized by the conserved zinc-binding motif HExxHxxGxxH/D (x can be any amino acid) within the active site cleft and the 1,4-β-type Met-turn close to the active site (Bode et al. 1992; Stöcker et al. 1993; Stöcker et al. 1995; Gomis-Rüth 2003, 2009). Beside MMPs (matrix metalloproteinases) and ADAMs (a desintegrin and metalloproteinase), also astacins are assigned to the metzincin superfamily. The astacins are named after the proteinase Astacin identified in the crayfish *Astacus astacus* (Titani et al. 1987; Dumermuth et al. 1991; Bode et al. 1992; Stöcker and Zwilling 1995). Several hundred astacins have been identified and are found throughout the animal kingdom (Sterchi et al. 2008). The 3D-structure of the Astacin protease has been elucidated in 1992 by X-ray crystallography (Bode et al. 1992). As described for metzincins, the conserved zinc-binding motif and the Met-turn, close to the active site, have been observed. The active site cleft divides the Astacin protease in an upper and a lower subdomain (in 'standard orientation' according to Gomis-Rüth et al. 2012). Whereas the upper subdomain is characterized by two disulfide bridges between C^{42}-C^{198} and C^{64}-C^{84} and shows a four-stranded antiparallel *β*-sheet as well as three α-helices, the lower subdomain has little secondary structure elements (figure 1).

The first part of the described consensus sequence (HExxHxxGxxH/D) is harbored within an α-helix, which ends with a Glycine allowing for a sharp turn to enter the lower protease subdomain ('standard orientation', figure 1). Within the lower subdomain the third Histidine residue and an adjacent Glutamate are located, which has been described to be specific for astacins (Titani et al. 1987; Bode et al. 1992; Stöcker et al. 1993; Arolas et al. 2012). In addition to a catalytic water molecule, Y^{149} serves as a fifth zinc-binding ligand, as long as no substrate or inhibitor is bound, which results in penta-coordinated zinc ion within the active cleft of Astacin (Bode et al. 1992; Stöcker et al. 1993) (figure 1).
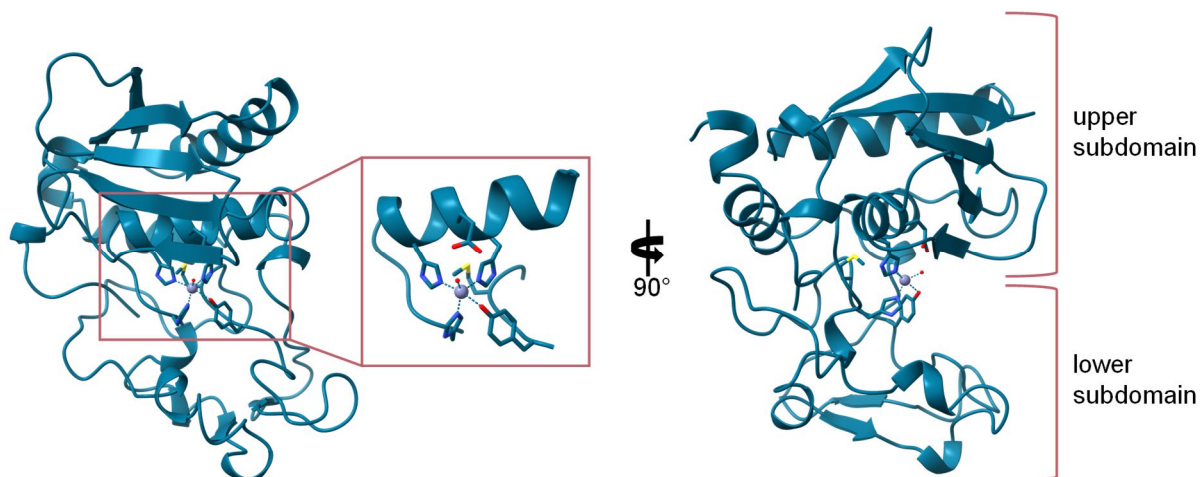
Figure 1: Structure of mature Astacin protease PDB 1AST (Bode et al. 1992), showing the conserved zinc-binding motif with three Histidine residues and one Tyrosine complexing the catalytic zinc. Side view of Astacin, representing 'pac-man' shape of the active site cleft.

The Astacin proteinase is expressed as zymogen, owing a prodomain, which is cleaved off for activation (Yiallouros et al. 2002) and a catalytic domain (Bode et al. 1992) (figure 1). Six astacin family genes have been discovered, including two Meprins, three BMP-1/tolloid-like and one Ovastacin (Sterchi et al. 2008). Most of the astacins are expressed as zymogens and are multidomain proteases with additional domains C-terminally to the protease domain (Bond and Beynon 1995). Based on the C-terminal domains, the astacins can be divided into three major groups: BMP-1/tolloid proteinases, hatching enzymes and Meprin proteinases.

BMP-1/tolloid-like proteinases are involved in dorsal-ventral patterning (Sterchi et al. 2008). Furthermore, human BMP-1 was shown to act as procollagenase involved in the formation of the extracellular matrix (ECM) (Hopkins et al. 2007). The BMP-1/tolloid-like proteinases are additionally important for the activation of growth factors, such as TGF-β1, BMP-2/-4, IGFs (Vadon-Le Goff et al. 2015). This group of actacins is further characterized by the C-terminal EGF-like (epidermal growth factor-like) and CUB domains (complement subcomponents C1r/C1s, embryonic sea urchin protein Uegf, BMP-1). These domains are non-catalytic (Bond and Beynon 1995) and most likely responsible for protein-protein interaction and mediation of intercellular signaling (Gaboriaud et al. 2011; Wouters et al. 2005).

The group of the 'so called' hatching enzymes is involved in the hatching process of embryos and in skeleton formation (Bond and Beynon 1995). These enzymes often contain C-terminal Cysteine rich and CUB domains (Sterchi et al. 2008). Examples are mammalian Ovastacin (Burkart et al. 2012), crayfish embryonic Astacin (Geier and Zwilling 1998) and fish Alveolin (Shibata et al. 2000).

Finally, the group of Meprin metalloproteinases belongs to astacins as well. They have been first discovered in the early 1980s in mouse and rat kidney (Beynon et al. 1981; Barnes et al. 1989) and are of major interest within the present study. Due to their involvement in various disorders, the development of inhibitors is crucial. Hence, the structures of Meprin α und Meprin β in complex with their specific inhibitors are a helpful tool for rational drug design and optimization. Consequently, the structural elucidation of both Meprins with a small molecule inhibitor bound to the active site is one goal of the present work. In general, for Meprin α no structural data is available so far.

1.1 Meprin α and β – Structure and Cellular Localization

Meprins are multidomain proteases belonging to the astacin family of metalloproteases. They are composed of two evolutionary related subunits, α and β, which are encoded on human chromosome 6 (α unit) and 18 (β unit) and separately expressed (Bond et al. 2005). Meprin α and Meprin β are expressed as zymogens, activation requires Trypsin-like proteinases for proteolytic removal of the N-terminal propeptide (Sterchi et al. 2008). Several Serineproteases have been identified as Meprin activators, e.g. Kallikrein-related peptides (Ohler et al. 2010), Plasmin (Rösmann et al. 2002) and Trypsin (Becker et al. 2003). The domain structure from N- to C-terminus consists of the propeptide, the protease domain, the MAM domain (Meprin A5 protein tyrosine phosphatase μ), the TRAF domain (tumor-necrosis-factor-receptor-associated factor), the EGF-like domain (epidermal growth factor like), the transmembrane domain and the cytosolic tail (figure 2) (Arolas et al. 2012; Broder and Becker-Pauly 2013). The major structural difference between the two proteases is the 'inserted domain' in Meprin α, a furin cleavage site. The cleavage finally leads to the release of Meprin α into the extracellular space, whereas Meprin β is anchored at the membrane, forming a homodimer linked by a disulfide bridge within the MAM domain (Broder and Becker-Pauly 2013). During the translation at the ER (endoplasmatic reticulum) the transmembrane domain anchors both Meprins to the membrane. The Meprin monomers are covalently linked after translation in the ER. Thereby, homo- and heterocomplexes of Meprin α and Meprin β are formed, which are later situated at the membrane or released in the extracellular space (figure 2) (Bond and Beynon 1995; Peters et al. 2019). After disulfide linkage in the ER, the dimers are transported to the Golgi. Here, Meprin α is cleaved by furin, which leads to loss of its membrane anchor (Peters et al. 2019).

Upon shedding of Meprin α by furin cleavage and further transport to the extracellular space, oligomers in the MDa range are built by non-covalent interactions of Meprin α dimers, which are also linked by a disulfide bridge within the MAM domain (Marchand et al. 1996; Ishmael et al. 2001). Accordingly, Meprin α could represent the largest secreted protease known. Also Meprin β can be shed from the membrane by ADAM 10 and ADAM 17 (Hahn et al. 2003; Jefferson et al. 2013). Interestingly, ADAM 10, 17 and 9 are also substrates of Meprin β (Wichert et al. 2019). However, in contrast to Meprin α, Meprin β does not oligomerize after shedding from the plasma membrane.
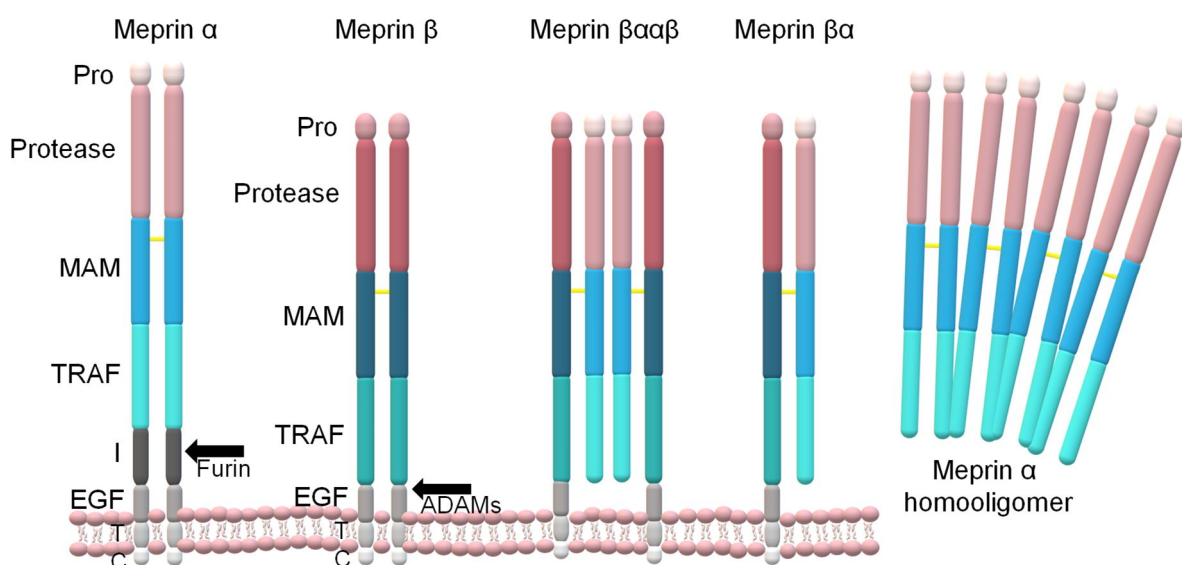
Figure 2: Schematic structure of multidomain Meprins, modified according to Broder and Becker-Pauly (2013). *Meprins are expressed as zymogens, requiring activation by Trypsin-like proteases. The enzymes consist of the propeptide (Pro), the protease domain, MAM domain (Meprin A5 protein tyrosine phosphatase µ), TRAF domain (tumor-necrosis-factor-receptor-associated factor), EGF-like domain (EGF: epidermal growth factor like), transmembrane domain (T) and the cytosolic tail (C). Meprin α and Meprin β are linked by a disulfide bridge within the MAM domain to form dimers. Only Meprin α contains the 'inserted' domain (I), which enables the cleavage of Meprin α within the secretory pathway. Upon cleavage and secretion of Meprin α, homoligomers up to MDa range are built by non-covalent interactions. Recently, human heterocomplexes of Meprin α and Meprin β (tetramers: Meprin βααβ and dimers: Meprin βα) were reported (Peters et al. 2019).*

The non-catalytic domains, MAM and TRAF, might be involved in protein-protein interaction and mediation of intercellular signaling (Gaboriaud et al. 2011; Wouters et al. 2005). Furthermore, it has been stated that the MAM domain is necessary for the correct folding and transport through the secretory pathway and the TRAF domain might be also responsible for correct folding of the zymogen (Tsukuba and Bond 1998). In case of Meprin α, different reasons for the oligomerization have been discussed (at least for recombinant mouse and rat Meprin α), among those intermolecular disulfide bonds in the MAM domain (Ishmael et al. 2001; Marchand et al. 1996) or glycosylations within the MAM domain, which might be involved in oligomerization (Ishmael et al. 2006).

Consequently, especially the MAM domain was supposed to be involved in protein-protein interaction (Beckmann and Bork 1993) and in the formation of oligomeric Meprin α (Bertenshaw et al. 2003; Ishmael et al. 2001). However, no structural basis for the oligomerization of soluble Meprin α could be identified so far.

The catalytic domains of Meprin α, Meprin β and Astacin share 39% sequence identity. The 3D-Structures of Meprin β and Astacin have been elucidated by X-ray crystallography (Arolas et al. 2012; Bode et al. 1992). The architecture of the catalytic domains is very similar and characterized by the conserved zinc-binding motif and the Met-turn, as described above. Because, the protease domain has a 'pac-man' shape with a deep and narrow active cleft (Arolas et al. 2012), the substrates bind in an elongated manner (Sterchi et al. 2008). Whereas Meprin α prefers neutral aliphatic (A, V), aromatic (Y, W) and negatively charged amino acids (D, E), Meprin β shows a striking preference for negatively charged amino acids in P1' [1] (Bertenshaw et al. 2002; Villa et al. 2003; Sterchi et al. 2008). Additionally, a preference for Proline in P2' was observed as well. Interestingly, substrates with negatively charged amino acids in P1' often do not contain a Proline residue in P2' and vice versa (Becker-Pauly et al. 2011). Probably, this is caused by the difference of the amino acids shaping the S1, S1' and S2' subpockets within the active site clefts of both Meprins. In Meprin β three Arginine residues are located within the subpockets (S1: R^{184}, S1': R^{238}, S2': R^{146}). In Meprin α two Tyrosine residues and one Arginine are located there (S1: Y^{187}, S1': R^{242}, S2': Y^{149}). Consequently, a broader substrate specificity for Meprin α than for Meprin β was observed by PICS analysis (proteomic identification of protease cleavage site specificity), as depicted in figure 3 (Becker-Pauly et al. 2011).
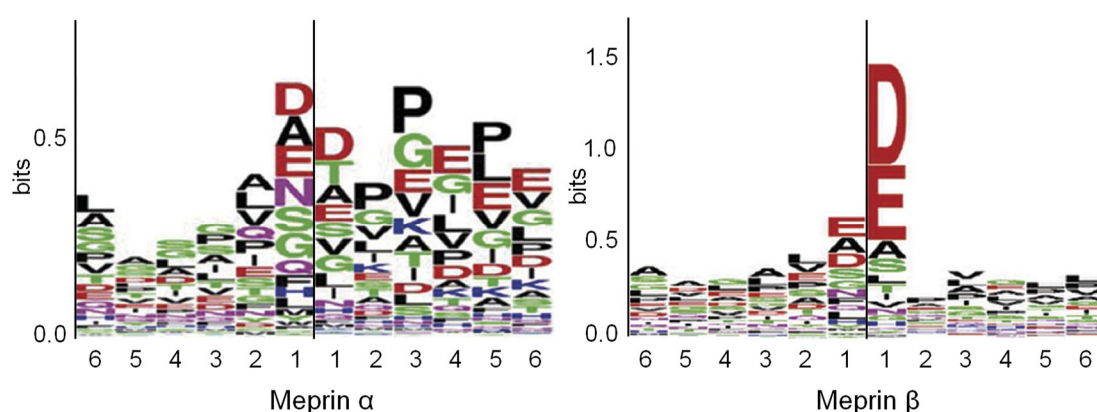
Figure 3: Cleavage sites of Meprins profiled by PICS analysis. *Tryptic peptide library obtained from lysate of cultures human embryonic kidney cells (HEK 293) (Becker-Pauly et al. 2011).*

---

[1] nomenclature by Schechter and Berger (1968).

However, by analyzing the cleavage specifities using TAILS (terminal amine isotopic labeling of substrates), by which cleavage sites in native proteins can be identified, also a striking preference for negatively charged amino acids in P1' was observed for Meprin α, as for Meprin β in PICS and TAILS analysis (Becker-Pauly et al. 2011).

Several protein substrates of Meprins have been identified, among those Procollagen I and III, Collagen IV, Fibronectin and Interleukin 18. Cleavage of these substrates links Meprins to inflammation (Banerjee and Bond 2008; Herzog et al. 2009), extracellular matrix assembly and fibrosis (Broder and Becker-Pauly 2013; Broder et al. 2013) as well as in regulation of cancer progression (Minder et al. 2012; Peters and Becker-Pauly 2019).

1.2 Meprins – Function in Health and Disease

The turnover of ECM proteins associates Meprins to several disorders. Meprin α and Meprin β knockout mice (Norman et al. 2003; Crisman et al. 2004; Sun et al. 2009), show diminished collagen deposition in skin, which leads to 50% reduction of tensile strength compared to wild type mice (Prox et al. 2015; Broder et al. 2013). Accordingly, Meprins are also expressed in human epidermis. Meprin α is expressed in stratum basale, contributing to keratinocyte differentiation and cell migration by processing of Collagen IV, Fibronectin, Laminin and Nidogen-1 (Walker et al. 1998; Köhler et al. 2000; Bertenshaw et al. 2001; Kruse et al. 2004; Jefferson et al. 2013). This allows cells to detach and migrate from basement membrane to upper layers of the epidermis (Broder and Becker-Pauly 2013). Meprin β is expressed in stratum granulosum, where it induces terminal differentiation and therefore might be involved in cornification, but also in desquamation, by cleavage of adhesion molecules such as E-cadherin and Desmogleins (Jefferson et al. 2013; Broder and Becker-Pauly 2013). Decreased Meprin levels lead to reduced Collagen deposition and impaired connective tissue, contributing to immune cell infiltration across the basement membrane during inflammatory processes (Arnold et al. 2017), as it was also shown for MMPs and Elastase (Monaco et al. 2006; Delclaux et al. 1996). Upregulated expression of Meprins is associated with fibrosis (Prox et al. 2015). Furthermore, increased Meprin levels have been observed in keloids and fibrotic skin tumors. Both diseases are associated to excessive accumulation of ECM (Kronenberg et al. 2010). Additionally, it was reported, that both proteases have been shown to be involved in the maturation of Procollagen I and III (Kronenberg et al. 2010; Broder et al. 2013), which initiates the collagen fibril assembly. Especially, Meprin β was shown to be upregulated in lung of transgenic mice suffering from idiopathic pulmonary arterial hypertension (IPAH) (Biasin et al. 2014). This inflammatory process within the lung correlates with excessive deposition of ECM around lung arteries (Ahmed and Palevsky 2014).

Besides involvement of Meprin β in IPAH, Meprins are also related to other chronic inflammatory diseases, among those inflammatory bowel disease (IBD), which is characterized by infiltration of diffuse leucocytes into the intestinal mucosa and a downregulation of the mucosal immune system (Neuman 2007). Meprin α mRNA levels in the epithelium have been shown to be downregulated during intestinal inflammation. Also Meprin β levels are decreased in ileal mucosa of patients with Crohn's disease (CD) (Broder and Becker-Pauly 2013).

Furthermore, Meprins impair the invasion of epithelial cells by adherent-invasive *Escherichia coli*, which is often observed in ileal lesions of CD patients (Vazeille et al. 2011). On the other hand, the processing of pro-inflammatory IL-18 by Meprin β is associated with IBD (Banerjee and Bond 2008). Meprin α was also shown to induce inflammation by release of TGFα (transforming growth factor α) from the cell surface, which activates the EGF/TLR4 signalling cascade (epidermal growth factor/toll-like receptor 4), leading to increased secretion of IL-8, a neutrophil chemoattractant related to cystic fibrosis (Broder and Becker-Pauly 2013).

Meprins are also potentially involved in nephritis and urinary tract infections. About 5% of the total brush-border membrane proteins in kidney of mice and rat are Meprins. Increased as well as decreased expression levels have been associated with kidney diseases (Craig et al. 1987). Whereas Meprin α is secreted into the lumen of the proximal tubule, Meprin β and Meprin α/Meprin β heterooligomers are tethered to the apical membrane (Kaushal et al. 2013). Here, they process peptides and proteins, which were filtered from the plasma or secreted by tubular epithelial cells, for reabsorption (Sterchi et al. 2008). It was shown that mice expressing low levels of Meprin develop less severe kidney damage after IR (ischeamia/reperfusion)-induced nephrotoxicity, than those expressing high levels of Meprin (Trachtman et al. 1995). Also, after Cisplatin-induced nephrotoxicity mice expressing low Meprin levels show lower degree of tubular necrosis. Pretreatment of these mice with protease inhibitor led to decreased serum Creatinine, blood Urea Nitrogen and excretion of Kidney Injury Molecule-1. Thus, Meprin inhibition may leads to a protection from Cisplatin-induced nephrotoxicity (Herzog et al. 2007). Meprins seem to undergo a redistribution form apical brush-border membrane to basolateral tubular basement membrane upon IR-injury and Cisplatin-induced acute kidney injury in rodents. Hence, they are in contact with novel substrates, which leads to degradation of basement membrane components, leucocyte infiltration and inflammation of the kidney (Carmago et al. 2002; Norman et al. 2003; Kaushal et al. 2013). Additionally, studies with Meprin α and Meprin β knockout mice suggested a contribution of Meprins to LPS (lipopolysaccharide)-induced renal damage, since the absence of Meprins protected against LPS-induced injury. It could be also shown that Meprins contribute to infiltration of leucocytes and edema in bladder inflammation (Yura et al. 2009).

Furthermore, it was observed that Meprin α urinary protein levels of women suffering from urinary tract infection are higher than in healthy women, which indicated an involvement of Meprin α in urinary tract infections as well (Bond et al. 2005).

An involvement of Meprin β was also suggested for neurodegeneration in Alzheimer's Disease, which is characterized by cerebral deposition of β-amyloid (Aβ) peptides. Aβ peptides are generated by consecutive cleavage of the amyloid precursor protein (APP), by a *β*-secretase followed by γ-secretase (Querfurth and LaFerla 2010).

In addition to the aspartic protease BACE-1 (beta-site amyloid precursor protein-cleaving enzyme 1), Meprin β acts as an alternative *β*-secretase within the amyloidogenic pathway, generating Aβ peptides (Schönherr et al. 2016; Becker-Pauly and Pietrzik 2016; Armbrust et al. 2019; Schlenzig et al. 2018). However, Meprin β exerts also alternative cleavage of APP, releasing 11 and 20 kDa fragments, which are assumed to be physiological cleavage products (Becker-Pauly and Pietrzik 2016). Furthermore, Meprin β cleaves the *α*-secretase ADAM 10 (Jefferson et al. 2013). ADAM 10 sheds APP within the Aβ-domain in the non-amyloidogenic pathway (Manzine et al. 2019). Additionally, ADAM 10 is also able to shed Meprin β from the cell surface (Herzog et al. 2014) and therefore abolishing *β*-secretase activity. Hence, ADAM 10 activity is regarded as being neuroprotective.

Finally, both Meprins were detected in several tumors and metastases, such as colorectal and pancreatic cancer, hepatocellular and renal cell carcinoma. Meprin α dysregulation influences intestinal proliferation and differentiation, which can be associated with colon cancer (Peters and Becker-Pauly 2019). Hence, Meprin α was identified in the colon carcinoma cell line Caco-2 and in colorectal cancer, where the protease is related to increased migration of colon cancer cells and angiogenesis (Lottaz et al. 1999). An overexpression of Meprin α in human hepatocellular carcinoma (HCC) was observed and linked to poor prognosis, while the expression of Meprin β was not affected. However, Meprin α has been described as target of Reptin, which is an oncogenic protein in HCC, that seems to regulate the Meprin α expression. By silencing the Meprin α expression in human hepatocellular carcinoma cell lines, the cell migration and invasion could be decreased, which suggests Meprin α as a target in HCC (Breig et al. 2017). The contribution of Meprin α to HCC cell proliferation, migration and invasion has been proven by another research group (OuYang et al. 2016). An expression of Meprin β in pancreatic neuroendocrine tumors and associated liver metastases has been described. A role of Meprin β for promoting cancer cell migration and invasion was suggested, which might be related to the capability of Meprin β to cleavage of cell adhesion molecules, such as E-cadherin and CD99 (Peters and Becker-Pauly 2019). CD99 has been shown to be essential for transendothelial migration of leukocytes, which is crucial for inflammation and metastasis. It was shown that Meprin β induces cell migration of Lewis lung carcinoma cells *in vitro*.

Additionally, Meprin β knockout mice show significantly increased CD99 levels in the lung (Bedau et al. 2017).

Summarizing, the substrate spectrum and the localization of Meprins contribute to their physiological and pathophysiological role. Under physiological conditions, Meprins are limited to certain tissues and apical epithelial sites, in case of mislocalization they can turn to harmful proteases contributing to degradation of the ECM, activation of pro-inflammatory Cytokines and cell detachment (Peters and Becker-Pauly 2019).

Consequently, Meprins represent targets for drug development to treat inflammatory, fibrotic and neurodegernative disorders as well as certain types of cancer.

1.3 Meprins – Drug Targets and Development of Specific Inhibitors

The activity of Meprins is regulated by expression and protease inhibitors. Endogenous inhibitors are TIMPs (tissue inhibitors of metalloproteases) (Broder and Becker-Pauly 2013), Fetuin-B (Karmilin et al. 2019), Cystatin-A (only a Meprin α inhibitor) and Nephrosin (Hedrich et al. 2010). Until recently, the most potent inhibitor for both proteases was the naturally occurring hydroxamate Actinonin with a K_i-value for Meprin α of 20±2.3 nM and for Meprin β of 2000±230 nM (Kruse et al. 2004). Moreover, Kruse et al. identified the naturally occurring N-isobutyl-N-(4-methoxyphenylsulfonyl)-glycyl hydroxamic acid (NNGH) as a potential Meprin inhibitor, with a K_i-value for Meprin α of 400±37 nM and for Meprin β of 7400±760 nM. By screening a library of pharmaceutical compounds Madoux et al. identifed two compounds (NF449, K_i=22±10 nM; PPNDS, K_i=8±2 nM) that are partially selective inhibitors of Meprin β (Madoux et al. 2014). Meprins have been also shown to be inhibited by certain MMP inhibitors and TACE (tumor necrosis factor-α-converting enzyme) inhibitors (Sterchi et al. 2008). The application of such compounds might lead to unwanted side effects. As a consequence, a need for selective inhibitors of Meprin α and Meprin β exists. Inhibitors available for MMPs were based on a sulfonamide scaffold and enabling the complexation of zinc in the active site of metzincins by a hydroxamic acid (such as NNGH). Such sulfonaminde scaffolds served as an initial starting point to generate selective Meprin β inhibitors (Ramsbeck et al. 2017). These have been improved and the sulfonamide scaffold was replaced by a tertiary amine scaffold connecting the zinc-complexing hydroxamic acid with moieties that target the subpockets within the active site (Ramsbeck et al. 2018). High selectivity between Meprin β and Meprin α was achieved with a tertiary amine inhibitor with two benzoic acid moieties in *meta*-position (figure 4, inhibitor MWT-S-270) leading to an IC_{50} for Meprin β of 49±11 nM, and for Meprin α of 16050±212 nM. It was assumed that the benzoic acid moieties are targeting the R[184] and R[238] of the subpockets S1 and S1' of Meprin β. In Meprin α the corresponding position at S1 is occupied by Tyrosine residues, which might further lead to repulsive interactions of this inhibitor (Ramsbeck et al. 2018).

As a consequence and to target the subpockets of Meprin α, inhibitors based on the hydroxamic acid linked by a tertiary amine scaffold to hydrogen acceptors were developed (Tan et al. 2018). By an exchange of the benzoic acid moieties to benzodioxolane moieties and the introduction of an additional methylene spacer between the hydroxamic acid and the tertiary amine, a selective inhibitor for Meprin α was designed with an IC_{50} for Meprin α of 160±1 nM and for Meprin β of 2950±350 nM (figure 4, compound MWT-S-698) (Tan et al. 2018).

A   B

Meprin β inhibitor – MWT-S-270
IC_{50} Meprin β   49±11 nM
IC_{50} Meprin α 16050±212 nM

Meprin α inhibitor – MWT-S-698
IC_{50} Meprin α   160±1 nM
IC_{50} Meprin β 2950±350 nM
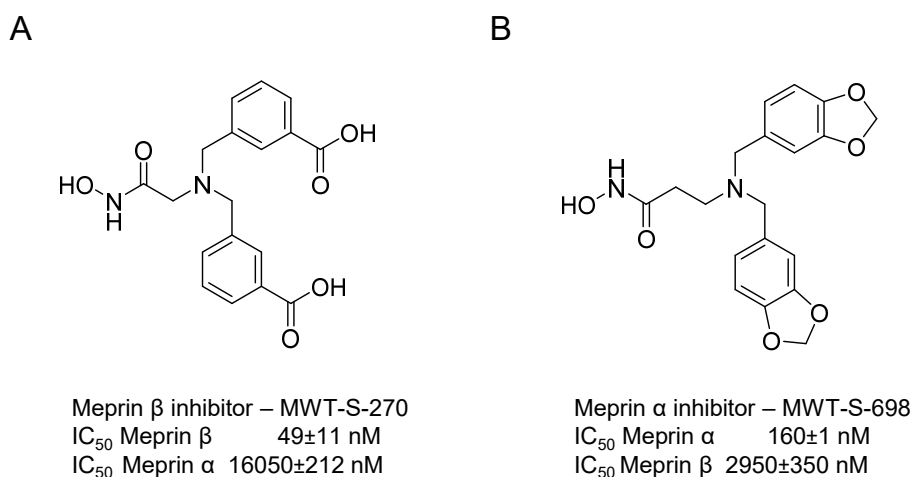
Figure 4: Structures of synthetic inhibitors of Meprin β and Meprin α. A) A tertiary amine scaffold connects the zinc-binding hydroxamic acid with the meta-positioned benzoic acid moieties, IC_{50} Meprin β 49±11 nM, IC_{50} Meprin α 16050±350 nM. B) Loss of charge results in a change of specificity. Consequently, the exchange of benzoic acid by benzodioxolane reverses specificity. IC_{50} Meprin α 160±1 nM, IC_{50} Meprin β 2950±350 nM.

For verification of the binding modes of the described selective inhibitors and for further drug design, the structural elucidation of Meprin α and Meprin β in complex with their specific inhibitors would be a helpful tool, since no structural data of Meprin-inhibitor-complexes have been reported to date.

1.4 Motivation and Aim

Meprin α and Meprin β are multidomain proteases assigned to the astacin family of metalloproteases. The major structural difference between the two proteases is an 'inserted domain' in Meprin α, which leads to its release into the extracellular space, whereas Meprin β is situated at the membrane (Broder and Becker-Pauly 2013). Upon shedding of Meprin α from the membrane, oligomers in the MDa range are built by non-covalent interactions of Meprin α dimers (Ishmael et al. 2001). According to their substrate preferences, which include neutral aliphatic (A, V), aromatic (Y, W) and negatively charged side chains (D, E) for Meprin α and negatively charged amino acids for Meprin β (Sterchi et al. 2008; Becker-Pauly et al. 2011), different substrates of Meprins have been identified, among those Procollagen I and III, Fibronectin, Nidogen-1, E-cadherin and different Interleukin species (Jefferson et al. 2013). Hence, Meprins are important players in fibrosis and keloids, but also in nephritis and neurodegeneration (Broder and Becker-Pauly 2013; Prox et al. 2015). Consequently, they are within focus of current drug discovery (Ramsbeck et al. 2018; Tan et al. 2018). The rational inhibitor design and optimization could significantly improve by knowledge of the binding modes of the inhibitors in the active site of Meprin α and Meprin β.

Accordingly, the first aim of the present work is the characterization of Meprin α and Meprin β, including the structural elucidation of both proteases in complex with their specific inhibitors, MWT-S-698 and MWT-S-270 by X-ray crystallography. A crystal structure of mature Meprin β is published already (Arolas et al. 2012). However, in the active site a cadmium ion is present instead of zinc. Additionally, a co-crystallization with an inhibitor was not performed before. In case of Meprin α, no structural data is available so far. The oligomerization propensity of Meprin α could hamper the crystallization process.

An alternative approach might represent cryo-electron microscopy (cryo-EM) single particle analysis, which was established for structural elucidation of proteins of high molecular mass (Zanotti 2016). In addition, it is anticipated to elucidate the structural basis of Meprin α oligomerization. Further aims were to analyze the impact this oligomerization on the stability and activity of Meprin α as well as to address the question, wheter these oligomers exist *in vivo*.

2 Materials and Methods

2.1 Materials

2.1.1 Chemicals

If not stated otherwise, the utilized chemicals were bought from Sigma Aldrich or Roth and used in analytical grade. SDS was supplied by Serva, Agarose was bought from Peqlab, Coomassie Brilliant Blue G-250 was supplied by BioRad. Zeocin was purchased from Thermo Fisher Scientific and EDTA was obtained from Promega. The inhibitors MWT-S-270 and MWT-S-698 were synthesized at Fraunhofer IZI-MWT.

2.1.2 Enzymes and Antibodies

All restriction enzymes and appropriate buffers have been bought from NEB. Immobilized Trypsin on magnetic beads was purchased from Takara Bio Europe. Polymerases, Ligases and appropriate buffers were supplied by Promega. The applied antibodies are listed in table 1.

Table 1: Antibodies applied for Western blot analysis.

Antibody	Supplier
Goat anti-Meprin α	R&D System
Goat anti-Meprin β	R&D System
Donkey anti-goat, HRP conjugate	R&D System
Donkey anti-goat, AP conjugate	Abcam
Mouse anti-penta His	Qiagen
Goat anti-mouse, HRP conjugate	Santa Cruz
Goat anti-mouse, AP conjugate	Abcam
Mouse anti-STREP-Tag II, HRP conjugate	IBA Lifescience

For the analysis of substrate cleavage by different Meprin α variants (described in chapter 2.2.7, p. 34) Tropoelastin, Fibronectin and Elastin were used. Recombinant Tropoelastin (61 kDa) was provided by Mathias Mende (laboratory of Prof. Pietzsch, Martin-Luther-University Halle-Wittenberg). Fibronectin (260 kDa), purified from human plasma, was bought from Abcam (ab80021). Elastin was isolated from bovine nuchal ligament and provided by Tobias Hedtke (laboratory of Dr. Schmelzer, Fraunhofer IMWS) (Schmelzer et al. 2012).

2.1.3 DNA and Protein Standards

6x loading dye for DNA samples was bought from Peqlab. All DNA and protein standards were supplied by Thermo Scientific/Invitrogen and are listed below.

- DNA standards: Gene Ruler 100 bp DNA ladder, Gene Ruler 1 kp DNA ladder, Gene Ruler 1 kp Plus DNA ladder

- Protein standards: PageRuler™ Plus Prestained Protein ladder, PageRuler™ Unstained Broad Range Protein ladder, HiMark™ Prestained Protein Standard

2.1.4 Oligonucleotides and Plasmids

The applied oligonucleotides and plasmids are listed in table 14 and table 15 in the appendix (pp. 122).

2.1.5 Bacteria and Yeast Strains

For molecular genetic applications the *E.coli* DH5α strain was used, for heterologous expression of Meprin β the wild type yeast strain *Komagataella phaffii* (*Pichia pastoris*) was applied. The genotypes are listed below.

- *E.coli* DH5α: F⁻ Φ80*lac*ZΔM15 Δ(*lac*ZYA-*arg*F) U169 *rec*A1 *end*A1 *hsd*R17 (r$_K^-$, m$_K^+$) *pho*A *sup*E44 λ⁻ *thi*-1 *gyr*A96 *rel*A1
- *Pichia pastoris* – X33: wild type

2.1.6 Insect and Mammalian Cell Lines

The insect cell line Schneider-2 *Drosophila* cells (S2 cells, Thermo Fisher Scientific) was applied for heterologous expression of Meprin α wild type and Meprin α mutants. The Caco-2 cell line (ACC 169) was cultured to investigate the endogenous Meprin α expression and its oligomerization state.

2.2 Methods

2.2.1 Molecular Cloning Methods

2.2.1.1 PCR Methods

The polymerase chain reaction (PCR) was applied for amplification of DNA in order to introduce restriction sites for molecular cloning and to insert mutations as well as to screen for transformed *E.coli* clones. The PCR cycler iCycler iQ™ (BioRad) was used. The described PCR protocols were applied for plasmid construction and used for the heterologous expression of Meprin α and Meprin β.

Standard PCR: The pipetting scheme of a usual PCR is shown on the next page in table 2.

Table 2: Pipetting scheme of a standard PCR.

Substance	Volume [µl]
10x reaction buffer	5
dNTP's (2 mM each)	1
20 µM forward primer	2.5
20 µM reverse primer	2.5
Pfu-polymerase	0.5
Template DNA	1
DI water	37.5

The following temperature protocol was applied (table 3).

*Table 3: Temperature protocol of standard PCR. *depending on the annealing temperature of the primer pair, **depending on the template length.*

Step	Cycles	Temperature [°C]	Time
Hot-Start	1	95	2 min
Denaturing		95	30 s
Annealing	30	*	30 s
Elongation		72	**
Final elongation	1	72	10 min
Hold	1	4	∞

Colony PCR: In order to identify positive *E. coli* clones after transformation, a colony PCR was performed. The *E. coli* colony (serves as a template for PCR) was picked form the agar plate and transferred in a vial with 10 µl DI water. As a positive control the cloned vector with the gene of interest (GOI) was used, DI water served as negative control. The pipetting scheme is shown in table 4.

Table 4: Pipetting scheme of a colony PCR.

Substance	Volume [µl]
DI water with clone	10
5x Green GoTaq® reaction buffer	3
dNTP's (2 mM each)	0.3
20 µM forward primer	0.5
20 µM reverse primer	0.5
GoTaq®-polymerase	0.075
DI water	0.625

The applied temperature protocol for the colony PCR is similar to the protocol in table 3, except the Hot-Start and the final elongation, which were done for 5 min.

Site-Directed Mutagenesis: The site-directed mutagenesis PCR was used to insert mutations in one or two adjacent base pairs. This method was applied for generation of Meprin α mutants. The primers are complementary to each other, enabling the mutation of each DNA strand.

The template DNA must be isolated form a *dam*[+] *E.coli* strain. After the purification of the PCR product (described in the following chapter 2.2.1.2, pp. 15), the DNA was digested with the restriction enzyme *Dpn1* to digest the dam-methylated mother DNA without mutation. The pipetting scheme is the same as applied for the standard PCR (table 2), the temperature protocol is shown in table 5.

Table 5: Temperature protocol of a site-directed mutagenesis PCR. *depending on the length of the vector to be amplified.*

Step	Cycles	Temperature [°C]	Time
Hot-Start	1	95	5 min
Denaturing		95	30 s
Annealing	20	60	30 s
Elongation		72	*
Final elongation	1	72	5 min
Hold	1	4	∞

2.2.1.2   DNA Cloning and Purification Procedures

Agarose Gel Electrophoresis (Aaij and Borst 1972): For separation of DNA, agarose gel electrophoresis was applied. Agarose gels (0.8% (w/v)) were prepared by dissolving 0.4 g agarose in 50 ml TAE buffer (2 M TRIS, 1 M glacial acetic acid. 50 mM EDTA). Ethidium bromide (4% (v/v)) was added to the solubilized agarose gel to visualize the DNA under UV light. The samples were mixed 1:6 with 6x loading dye and the DNA was separated at 120 V for 20 min. Afterwards, the gel was observed using the BioDoc-IT® Imager (UVP) under UV light.

Purification of DNA: For purification of DNA fragments after restriction digest, the samples were separated in an agarose gel and the desired bands were cut out and further purified using the Wizard® SV Gel and PCR Clean-Up System kit (Promega), according the manufacturers manual. The DNA binds to the silica membrane in presence of high salt concentration, whereas impurities like enzymes pass the membrane. This purification method is also suitable to clean up DNA solutions, e.g. PCR products. At the end, the DNA was eluted from the column using 50 µl of preheated (65°C) DI water.

Determination of DNA Concentration: The concentration of purified DNA fragments or plasmids was measured with the NanoDrop™ 2000 spectrophotometer (Thermo Fisher Scientific) at 260 nm. For the calculation of the concentration the extinction coefficient of double stranded DNA of 50 (ng/ml)$^{-1}$cm^{-1} was applied (V1.0 User Manual, Thermo Fisher Scientific). Additionally, the absorption ratio at 260 and 280 nm (absorption maxima of proteins) was used used to determine the purity of the DNA. Values between 1.8 and 2.0 indicate pure DNA.

Restriction Digest of DNA: DNA purification was frequently performed by restriction digest, either to cleave introduced restriction sites as a preparation for ligation into a certain vector, or for checking if the complete insert was ligated. Usually, a 50 µl reaction with 10 units of a certain restriction enzyme and an appropriate restriction buffer (10x restriction buffer diluted to 1x) was incubated in a Thermomixer compact (Eppendorf) at 37°C for 1h, depending on the enzyme's optimal temperature. For analytical purposes, a 20 µl reaction was applied. In order to linearize the plasmid before transformation of *Pichia pastoris*, a 100 µl reaction including 1x CutSmart buffer, 20 µg of plasmid DNA and 40 units of *Pme1* were incubated at 37°C for 4 h. Afterwards the DNA was purified as described above.

Ligation of DNA: The ligation of DNA fragments (digested PCR-product and vector) was executed in a 20 µl reaction in a mass ratio of 3:1 of vector and insert. Additionally, 2 µl of 10x ligation buffer and 1 U of T4 DNA Ligase were added, the solution was filled up with DI water and incubated at 4°C overnight. Afterwards, the ligation reaction was transformed in *E. coli* DH5α (described in chapter 2.2.2.1, p. 17).

Plasmid Isolation: In order to isolate pure plasmid DNA from *E. coli* DH5α for sequencing, transformation or as PCR template, the GeneJET Plasmid Miniprep kit (Thermo Fisher Scientific) was used. To isolate a large amount of endotoxin-free DNA for transformation of *Pichia pastoris* or Schneider's *Drosophila* S2 cells, the GenJET Endo-Free Plasmid Maxiprep kit (Thermo Fisher Scientific) was applied. The procedures were performed as described in the manufacturer's manual. The DNA binds to the silica membrane in presence of high salt concentration, whereas impurities such as enzymes pass the membrane. Finally, the DNA was eluted from the column using preheated (65°C) DI water.

DNA Sequencing (Sanger et al. 1977): The sequencing reactions were sent to Eurofins Genomics, where the chain-terminating reaction by Sanger et al. was applied for sequencing. Therefore, 15 µl of 70 ng/µl DNA solution in DI water were prepared, optionally 2 µl of 10 µM primer were added to the reaction. The sequencing results were evaluated using the software SeqMan Pro (DNASTAR).

2.2.2 Microbiological and Cell Biological Methods

2.2.2.1 Growth and Manipulation of *E. coli* DH5α

The *E.coli* strain DH5α was applied for amplification and storage of plasmids harboring the appropriate gene of interest, either encoding Meprin α or Meprin β.

Cultivation: For the cultivation of *E. coli* DH5α, either LB medium (10 g/l tryptone, 5 g/l yeast extract, 5 g/l NaCl) or LB agar (10 g/l tryptone, 5 g/l yeast extract, 5 g/l NaCl, 3.75 g/l agar agar) were used. For growing under selective pressure, either Zeocin at a final concentration of 100 µg/ml or Ampicilin at a final concentration of 25 µg/ml were applied.

Production of Chemically Competent Cells: For transfer of plasmids into *E. coli* DH5α, chemically competent cells needed to be prepared, therefore the CaCl$_2$-method was utilized (Mandel and Higa 1970). The *E. coli* DH5α strain was cultured at 37°C over night (KS 15 and TH 15, Edmund Bühler), then 500 µl of the preculture were added to 50 ml of LB medium and grown at 37°C (Multitron Standard or Unitron Plus AJ252, Infors HT) until an optical density (OD$_{600}$) of 0.3 was reached. The optical density (absorption at 260 nm) was determined using a SmartSpec^{TM} 3000 spectrophotometer (BioRad). Then, the cells were cooled down on ice for about 10 min and separated by centrifugation at 4000 xg at 4°C for 10 min (Allegra-X22, Beckmann Coulter). The pellet was resuspended in ice cold 0.1 M CaCl$_2$. Finally, 2 ml of 50% (w/v) glycerol were added to the cell suspension, the cells were aliquoted and stored at -80°C.

Transformation: For transfer of the plasmid into the competent cells (Sambrook et al. 1989), the *E.coli* cells (100 µl) were thawed on ice. Then, 100 ng of ligated vector or plasmid were added to the cell suspension and incubated for 30 min. Subsequently, a heat shock was performed at 42°C for 45 s, followed by cooling on ice for 2 min. This cell suspension was combined with 500 µl LB medium and incubated at 37°C for 1 h. Afterwards, the cells were spread on selective agar, containing the appropriate antibiotics, and incubated at 37°C over night (Function line B6, Heraeus).

Glycerol Stocks: For storage of genetically modified strains, glycerol stocks of the *E.coli* strains, bearing the appropriate plasmid, were prepared by mixing 600 µl of an overnight culture with 400 µl of 50% (w/v) glycerol. The stocks are stored at -80°C.

2.2.2.2   Growth and Manipulation of *Pichia pastoris* – Yeast

The yeast strain *P. pastoris* X33 was used for the heterologous expression of Meprin β.

Cultivation and Determination of Optical Density (OD): For the cultivation of *P. pastoris* different media were applied, depending on the purpose of growth. The recipes for the appropriate media are listed in the manual '*Pichia* Expression Kit' (Invitrogen^{TM} life technologies, version MAN0000012). BMGY medium was used for test expressions or precultures. In order to induce the protein expression BMMY medium was applied. Agar plates with YPDS were prepared to store cells at 4°C. For transformation, YPDS and YPD media were used. Zeocin was added to the appropriate growth media at a concentration of 100, 200 or 500 µg/ml for growing under selective pressure. The OD of cultured yeast was determined by measurement of the absorbance at 600 nm (SmartSpec^{TM} 3000 spectrophotometer, BioRad).

Transformation (Becker and Guarente 1991): For stable integration of the expression plasmid containing the GOI into the genome of *P. pastoris*, an electroporation was performed as described in the manual '*Pichia* Expression Kit'.

Briefly, electrocompetent cells were prepared by growing an overnight culture at 30°C in 5 ml of YPD. Then, 500 ml of YPD were inoculated and grown at 30°C (Multitron Standard or Unitron Plus AJ252, Infors HT). After reaching an optical density of 1.0-1.3, the cells were harvested (1500 xg at 4°C for 5 min, Allegra-X22, Beckmann Coulter). The pellet was resuspended in 500 ml ice cold, sterile DI water. After a second centrifugation, the cells were resuspended in 250 ml ice cold DI water and centrifuged again. In the next step, they were resuspended in 20 ml of 1 M sorbitol and centrifuged. Finally, the pellet was resuspended in 1 ml sorbitol and 80 µl of electrocompetent cell suspension was used for transformation. The cells were mixed with 7-8 µg of linearized DNA (linearization of vector described in chapter 2.2.1.2, p. 16) and transferred into the cuvette (2 mm), that was cooled on ice before. The cells were pulsed using the Gene Pulser Xcell™ Electroporation System device (BioRad) at 2000 V for 5 ms. Precooled 1 M Sorbitol was added immediately after the pulse to the cells, the solution was incubated in a 15 ml falcon at 30°C for 2 h without shaking. Then, 1 ml YPD was added and the cells were further incubated at 30°C and 120 rpm (Unitron Plus AJ252, Infors HT) for 4 h. Finally, the *P. pastoris* cells were spread on YPDS agar plates containing 100, 200 and 500 µg/ml Zeocin and incubated at 30°C for about two days (Function line B6, Heraeus). The grown colonies were transferred to a master plate containing Zeocin and a test expression was performed.

Selection of Positive Clones/Test Expression: For the selection of clones which express the protein of interest, 2 ml of BMGY (15 ml culture tubes, Roth) were inoculated with a colony from the master plate and grown at 30°C and 200 rpm for 24 h (Multitron Standard, Infors HT). For induction of the expression by methanol, the medium was exchanged by centrifugation (2000xg, 10 min, Avanti J30I, Beckmann Coulter) and resuspension of the yeast cells in 2 ml BMMY medium. The resulting culture was grown under shaking (200 rpm) at 30°C for 24 h. To maintain the methanol concentration (0.5% (v/v)), 10 µl of methanol were added to the cell suspension for the next two days. On day five, the supernatant was harvested by centrifugation at 2000xg for 10 min and analyzed by determination of the enzymatic activity (chapter 2.2.4.1, pp. 26) and Western blot analysis (chapter 2.2.3.5, pp. 25).

Glycerol Stocks: For preparation of cryo-stocks of clones highly expressing the protein of interest, the appropriate colony was grown on YPDS agar plates containing the appropriate concentration of selection agent at 30°C for two days. A single colony was transferred to 10 ml YPD medium (supplemented with Zeocin) and grown at 30°C overnight. Finally, the suspension was centrifuged (2000xg, 10 min), resuspended in YPD medium containing 15% (v/v) glycerol and stored at -80°C.

2.2.2.3   Schneider's *Drosophila* S2 – insect cell line

For recombinant expression of different Meprin α variants, the Schneider-2 *Drosophila* cells (S2 cells) cell line was applied.

Cultivation of S2 Cells and Cell Counting: For cultivation of the S2 cells, Schneider's Drosophila Medium (Biowest) supplemented with 10% (v/v) fetal bovine serum (FBS) (Gibco™ Fetal Bovine Serum, Thermo Fisher Scientific) was applied. The cells were thawed and cultivated as described in the manual 'Drosophila Expression System' by Invitrogen™ life technologies (version G 092801 25-0191). Briefly, for initiation of a culture, a vial, containing about $1*10^7$ cells, was thawed in a 37°C water bath (Grant Instruments™ Fisher Scientific). 1 ml of thawed cells was added to 4 ml of Schneider's Drosophila Medium containing 10% FBS, centrifuged at 300xg for 2 min (Allegra X30R, Beckmann Coulter), resuspended in 5 ml Schneider's Drosophila Medium with 10% (v/v) FBS and transferred to a 25 cm^2 flask (Sarstedt). The culture was kept at $2\text{-}4*10^6$ cells/ml and 28°C (incubator: Function line B6, Heraeus) either in 25, 75 or 175 cm^2 flasks as adherent culture, or as suspension culture in 50, 125, 500, 1 l shaking flasks (Corning) at 80 rpm (Multitron Standard, Infors HT). For splitting of S2 cells (twice a week), the cells were centrifuged at 300xg for 2 min and resuspended in 2-10 ml Schneider's Drosophila Medium containing 10% (v/v) FBS. For cell counting, 100 µl of this cell suspension was diluted 1:10 in medium, then 100 µl of the dilution was added to 9900 µl Casy®-Ton buffer (OLS OMNI Life Science). The determination of the cell count was done using an automated cell counter (Casy®, Schärfe System). Cell dimensions of 7 µm to 11 µm were applied.

Transfection of S2 Cells: The transfection of S2 cells was performed essentially as described in the manual 'Drosophila Expression System' (Invitrogen™ life technologies, version G 092801 25-0191). The calcium phosphate method (Kingston et al. 2003) was applied. Briefly, 3 ml of $1*10^6$ cells/ml were seeded in a 6-well plate one day pre-transfection (Nunc™, Thermo Fisher Scientific). The next day, solution A was prepared by mixing 36 µl of 2 M CaCl$_2$ with 19 µg of plasmid containing the GOI and 1 µg of selection vector pCoBlast. The solution was filled up to 300 µl by addition of sterile DI water. For solution B, 300 µl of 2x HEPES buffered saline (50 mM HEPES pH 7.1 containing 1.5 mM Na^{2}HPO^4, 280 mM NaCl) was prepared. Then, solution A was added dropwise to solution B under continuous mixing and the combined solutions were incubated at room temperature for 30-40 min. Afterwards, the mix was added dropwise to the cells and incubated at 28°C for 24 h. Then, the cells were washed twice using medium, replaced into the same well of the plate and incubated at 28°C for another two days. For generation of a stable cell line, the cells were centrifuged and resuspended in Schneider's Drosophila Medium supplemented with 50 µg/ml selection agent (blasticidine S hydrochloride) and 10% (v/v) FBS.

For about two to three weeks, the cells were cultured under selective pressure and always replaced into the same well of the plate. Afterwards, a test expression with the generated S2 cell clones was executed and the selective pressure was reduced to a maintenance dose of 25 µg/ml blasticidine S.

Selection of Positive Clones/Test Expression: A test expression was performed in order to investigate the generated S2 cell clones regarding heterologous expression of Meprin α. For this purpose, $3*10^6$ cells/ml were seeded in a 6-well plate in Schneider's Drosophila Medium without FBS and blasticidine S hydrochloride. The heterologous protein expression was induced by addition of 1 mM copper sulfate. After 48 h of incubation at 28°C, the cells were separated by centrifugation (300xg, 2min) and the supernatant was harvested and analyzed by SDS-PAGE followed by Western blot analysis (chapter 2.2.3.5, pp.24).

Cryostocks: The preparation of cryostocks was performed as described in the manual 'Drosophila Expression System' (Invitrogen™ life technologies, version G 092801 25-0191). Briefly, $1*10^7$ cells were resuspended in freezing solution (450 µl fresh Schneider's Drosophila Medium containing 10% (v/v) FBS, 450 µl conditioned media, 100 µl DMSO). The cell suspension was transferred into a cryo-vial (NUNC™ 1.8 ml, Thermo Fischer Scientific) and kept at -80°C in a control rate freezer (Mr. Frosty™, Thermo Fischer Scientific) overnight. Finally, the frozen cell suspensions were stored in liquid nitrogen.

2.2.2.4   Caco-2 – Mammalian Cell Line

In order to analyze the endogenous Meprin α expression and its oligomerization state, Caco-2 cells were cultured in MEM medium (Gibco™ MEM, Thermo Fisher Scientific) supplemented with 10% (v/v) FBS (Gibco™ Fetal Bovine Serum, Thermo Fisher Scientific) and 1x non-essential amino acids (Gibco™ MEM Non-Essential Amino Acids Solution 100x, Thermo Fisher Scientific) for 38 days. The medium was exchanged twice a week, and samples of the supernatants were frozen in liquid nitrogen and stored at -20°C until analyzed by Western blot (chapter 2.2.3.5, pp. 25).

2.2.3   Protein Biochemical Methods

2.2.3.1   Expression and Purification of Human Meprin β

Inactive Meprin β (Pro-Meprin β, containing the N-terminal propeptide) was produced in *Pichia pastoris* X33, basically as previously described (Schlenzig et al. 2015). In the present study, a C-terminally truncated Pro-Meprin β (T^{23}-Q^{595}), including the pro-, protease, MAM and TRAF domain, was cloned into pPICZαC-vector, applying standard cloning procedures (described in chapter 2.2.1, pp. 13). Two different constructs were generated: one included the Pro-Meprin β sequence according to human codon usage and the other construct contained the Pro-Meprin β sequence according to *Pichia pastoris* codon usage.

In general, Pro-Meprin β was cloned into the cloning site of pPICZαC downstream of the α-mating factor from *Saccharomyces cerevisiae*, which allows for secretion of Pro-Meprin β into the medium (Cereghino and Cregg 2000). The linearized expression vector was transformed in *P. pastoris* X33 cells (described in chapter 2.2.2.2, pp. 17). The integration of the linearized expression vector into the *P. pastoris* genome (AOX1 locus) is based on homologous recombination. As a consequence, the heterologous expression was driven by the AOX promoter, enabling the expression of Pro-Meprin β upon feeding of methanol (Cereghino and Cregg 2000). A high-density fermentation process in a 5 l reactor (xCUBIO twin, bbi-biotech), according to the 'Pichia Fermentation Process Guidelines' (Invitrogen™ life technologies, version B 053002) was performed, after the selection of a high expressing clone (clone #8, human codon usage) by determination of enzymatic activity (described in chapter 2.2.4.1, pp. 26). The recipes for the basal salts fermentation medium and the trace elemet solution are listed in the manual. Briefly, a 200 ml pre-culture (BMGY medium containing 200 µg/ml Zeocin) was inoculated with the high Pro-Meprin β expressing clone and grown at 30°C and 200 rpm (Multitron Standard, Infors HT) overnight until an OD_{600} of 3-4 was reached. The fermenter containing 2 l of fermentation medium was equilibrated for about 2 h to reach the fermentation temperature of 30°C and for saturation of the medium with air (equal to 100% O_2) for calibration. A pH of 5.5 was adjusted by addition of 28% ammonia solution. Additionally, 8 ml of trace element solution was added to the fermentation broth before inoculation with the pre-culture. During the first phase of the high-density fermentation (glycerol batch phase), glycerol within the fermentation medium served as nutrient source, leading to consumption of O_2. If, upon 12 h of glycerol batch phase, the O_2-level drops below 40% and increases again above 60%, which is a sign of complete consumption of glycerol, the glycerol fed batch phase was started. During this phase, 50% (v/v) glycerol (supplemented with 1.4% (v/v) of trace element solution) are delivered for 5 h (feeding profile shown in table 16, appendix, p. 125). After 4.5 h of glycerol fed batch phase, the methanol fed batch phase was initiated (feeding profile shown in table 16, appendix, p. 125). The feeding of methanol induces the protein production. The fermentation process was stopped after 72 h and the supernatant was harvested by centrifugation at 6000xg, 4°C for 20 min (Avanti J30I, Beckmann Coulter). The purification process of the fermentation supernatant started with affinity chromatography on immobilized Ni^{2+}-ions using the expanded bed adsorption technique (Streamline Chelating, GE Healthcare Life Science). Prior to purification, the pH of the expression media was adjusted to 7.4 by addition of sodium hydroxide. Additionally, TRIS buffer pH 7.4 was added to reach a final concentration of 30 mM. The first purification step was followed by Trypsin-mediated activation of Pro-Meprin β to mature Meprin β (1 mg bovine Trypsin to 15 mg of Pro-Meprin β in elution buffer supplemented with 10 mM calcium chloride).

For removal of Trypsin (previously inhibited with AEBSF) and denatured protein, hydrophobic interaction chromatography (HIC, butyl-Sepharose column, 25x100 mm, GE Healthcare) was carried out. Therefor, the activated Meprin β fraction was mixed with ammonium sulfate by dropwise addition of 3 M ammonium sulfate stock solution to a final concentration of 1.5 M. Finally, the mature Meprin β was desalted by size exclusion chromatography (Superdex 75 column, 26x850 mm, GE Healthcare). The buffers used during the purification process are listed in table 17 in the appendix (p. 125), for purification either an ÄKTAprime plus system or an ÄKTAavant system (GE Healthcare Life Science) was applied.

2.2.3.2 Expression and Purification of Human Meprin α Wild Type

Pro-Meprin α was expressed in Schneider-2 *Drosophila* cells (S2 cells) under the control of the MT (metallothionein) promoter, enabling an induction of expression by addition of copper sulfate. The expression vector pMT/BiP/V5 mediates the expression of a C-terminally truncated Pro-Meprin α (V^{22}-S^{600}) containing an N-terminal STREP-Tag (WSHPQFEK) and the pro, protease, MAM and TRAF domain. The signal sequence of BiP (immunoglobulin binding chaperone protein) from *Drosophila*, which is located upstream of the Pro-Meprin α sequence, enables the secretion of Pro-Meprin α into the medium. The expression vector encoding for wild type Meprin α (already available) was co-transfected with the selection vector pCoBlast, which harbors a blasticidine resistence gene (bsd). The co-transfection enables the generation of stable cell lines by passaging the transfected cells in blasticidine S hydrochloride containing medium, as described in chapter 2.2.2.3 (pp. 19). For production of Pro-Meprin α wild type, the stably transfected cells were seeded at $2*10^6$ cells/ml in three 175 cm^2 flasks (45 ml each, Sarstedt) and grown at 28°C in Schneider's Drosophila Medium supplemented with 10% (v/v) FBS and 25 µg/ml blasticidine S hydrochloride for four days. The cells were separated by centrifugation at 300xg for 7 min (Allegra X30R, Beckmann Coulter) and resuspended in Schneider's Drosophila Medium (containing 10% (v/v) FBS, 25 mg/ml blasticinde S hydrochloride and 0.1% (v/v) Pluronic™ F-68 (Non-ionic Surfactant 100x, Thermo Fisher Scientific)). Afterwards, they were seeded at $2*10^6$ cells/ml in three 500 ml shaking flasks (150 ml each) and incubated at 28°C and 80 rpm (Multitron Standard, Infors HT) for another three days. Finally, and to induce the expression of Pro-Meprin α, the cells were harvested by centrifugation at 300xg for 7 min, resuspended in Schneider's Drosophila Medium supplemented with 1 mM copper sulfate and 0.05% Pluronic™ F-68 and seeded at $4*10^6$ cells/ml in three 1 l shaking flasks (300 ml each, Corning). The cells were kept for protein expression at 28°C and 80 rpm for two days. Then, the supernatant was harvested by centrifugation at 800xg, 4°C for 20 min (Avanti J30I, Beckmann Coulter) and immediatly purified. The initial purification process for Pro-Meprin α from expression media was previously developed by colleagues at Fraunhofer IZI-MWT and further optimized by the author of the present study.

First, the expression media was purified by hydrophobic interaction chromatography (expanded bed adsorption). Therefor, ammonium sulfate and TRIS were added to reach final concentrations of 1.5 M and 30 mM, respectively, and a pH of 7.4. Due to a very low expression yield, three rounds of expressions were pooled, after purification by HIC, and subjected to affinity chromatography using Strep-Tactin® column (5 ml cartridge, GE Healthcare Life Science). Finally, Pro-Meprin α was activated to mature Meprin α by Trypsin cleavage applying immobilized Trypsin on magnetic beads. The cleavage was performed similar as described in the manual 'Mag-Trypsin User Manual' (PT3957-1, Clontech), except the denaturation step. In the present study, 4 ml of immobilized Trypsin (>150 U/ml) were mixed with 1 mg of Pro-Meprin α and the reaction proceeded at room temperature for 48 h. The buffer solutions applied for the purification are listed in table 18 in the appendix (p. 125). The purification was carried out using an ÄKTAprime plus system or an ÄKTAavant system (GE Healthcare Life Science).

2.2.3.3 Expression and Purification of Human Meprin α Mutants

The Pro-Meprin α variants C308A, R372T and R372A were expressed, basically as described for Pro-Meprin α wild type (chapter 2.2.3.2, pp. 22). The expression vectors for these constructs were generated by site-directed mutagenesis PCR (described in chapter 2.2.1.1, pp. 14), whereby the single/double point mutations were introduced in order to exchange the resulting amino acid sequence for the appropriate Pro-Meprin α variants. For production of Pro-Meprin α mutants, the stably transfected cells in supension were seeded at $2*10^6$ cells/ml in three 250 ml shaking flasks (50 ml each, Corning) and grown at 28°C (80 rpm Multitron Standard, Infors HT) for four days in Schneider's Drosophila Medium supplemented with 10% (v/v) FBS, 25 µg/ml blasticinde S hydrochloride and 0.1% (v/v) Pluronic™ F-68. The cells were centrifuged at 300xg for 7 min (Allegra X30R, Beckmann Coulter), resuspended in Schneider's Drosophila Medium (containing 10% (v/v) FBS, 25 mg/ml blasticinde S hydrochloride and 0.1% Pluronic™ F-68) and seeded at $3*10^6$ cells/ml in three 500 ml shaking flasks (150 ml each) and incubated at 28°C and 80 rpm for another three days. Finally, the cells were harvested by centrifugation at 300xg for 7 min, resuspended in Schneider's Drosophila Medium supplemented with 1 mM copper sulfate and 0.05% Pluronic™ F-68 and seeded at $4*10^6$ cells/ml in seven 1 l shaking flasks (300 ml each) to induce the expression of Pro-Meprin α variants. The expression was perfomed at 28°C and 80 rpm for two days. Then, the supernatant was harvested by centrifugation at 800xg at 4°C for 20 min and directly purified by affinity chromatography applying Strep-Tactin® column (5 ml cartridge, GE Healthcare Life Science). Finally, the Pro-Meprin α mutants were activated to mature Meprin α by Trypsin cleavage applying magnetic Trypsin beads. The cleavage reactions were performed as described in the manual 'Mag-Trypsin User Manual' (PT3957-1, Clontech).

Briefly, 1 ml of Trypsin beads were mixed with 1 mg of Pro-Meprin α mutant and incubated at room temperature for 60 min. The reaction was followed by dialysis against a buffer containing 30 mM TRIS pH 7.4 and 150 mM NaCl (Spectrapor, cutoff: 10 kDa, regenerated cellulose, Spectrum Laboratories) in order to remove the desthiobiotin, which is present in the elution buffer used for the Strep-Tactin® column.

2.2.3.4 Determination of Protein Concentration

The concentration of protein solutions was determined either by Bradford reagent, BCA assay or by measurement of absorption at 280 nm. The assessment of protein concentration was necessary during the purification of the proteases and before starting kinetic evaluation.

Bradford Assay (Bradford 1976): This assay is based on the change in absorption of Coomassie Brilliant Blue G250 at 595 nm depending on the protein concentration. Bradford reagent (750 µl, Sigma Aldrich) was mixed with 25 µl of protein solution and incubated in the dark for 10 min (room temperature). Afterwards, the absorption at 595 nm was measured and the protein concentration was calculated according to a calibration curve (bovine serum albumin (BSA)).

BCA Assay (Smith et al. 1985): In alkaline solution, proteins reduce Cu^{2+} to Cu^+. The complex of Cu^+ with bicinchoninic acid can be detected at 652 nm. The absorbance increases with increasing protein concentration. With the help of a standard curve (BSA), the protein concentration can be calculated. The assay was performed as described in the manual (Pierce™ BCA Assay Kit, Thermo Fisher Scientific).

Absorption at 280 nm: The protein concentration can be determined by absorption at 280 nm based on the Lambert-Beer-Law:

Equation 1

$$E = c * d * \varepsilon$$

$E = absorption\ at\ 280\ nm$ $c = protein\ concentration\ [M]$

$d = pathlength\ [cm]$ $\varepsilon = extinction\ coefficient\ [M^{-1}cm^{-1}]$

The molar extinction coefficients have been calculated using the ExPASy-Software (Gasteiger et al. 2003) and are listed in table 19 in the appendix (p. 126).

2.2.3.5 Electrophoretic Methods

The sodiumdodecylsulfate polyacrylamide gel electrophoresis (SDS-PAGE) was applied for analysis and visualization of Meprins after and during the expression and purification process, e.g to observe the purity of the protein, to check if the activation of zymogens or the deglycosylation was successful.

Native PAGE was performed to analyze Meprin α mutants regarding their oligomerisation properties and for investigation of endogenous Meprin α in murine urine. Protein detection by Western blot analysis was used to identify endogenously expressed Meprin α in murine urine and Caco-2 culture supernatant as well as for detection of recombinant Meprin α after text expression.

SDS-PAGE (Laemmli 1970)*:* For reducing conditions, the samples were mixed with 5-fold sample buffer (225 mM TRIS, pH 6.8; 50% (w/v) glycerol; 10% (w/v) SDS; 0.1% (w/v) bromphenol blue; 5% (v/v) β-mercaptoethanol) and heated to 95°C for 10 min (Dri-Block® DB-2D, Techne). For non-reducing SDS-PAGE, the samples were mixed 1:5 with 5-fold sample buffer without β-mercaptoethanol and without heating. The proteins were separated in an appropriate separating gel (table 20 in the appendix, p. 126) at 130 V for about one hour (running buffer: 25 mM TRIS, 1.92 M glycine, 1% (w/v) SDS). All electrophoretic separations were carried out using a Mini-PROTEAN 2-D electrophoresis cell equipped with a PowerPac™ 300/PowerPac™ Basic power supply (both BioRad). The separated proteins were stained with Coomassie-staining solution (Weber and Osborn 1969) (2.5 g/l Coomassie Brilliant Blue G250, 10% (v/v) acetic acid, 45% (v/v) methanol) for 30 min, following destaining with 10% (v/v) acetic acid. For higher sensitivity, the Pierce® Silver Stain kit (Thermo Fisher Scientific) was applied. Gradient gels, used for analysis of substrate cleavage reactions performed with Meprin α, were bought from Serva (Serva*Gel*™ TG PRiME™ 4-20%).

Native PAGE (Schägger et al. 1994): For separation of proteins in their native state, e.g. for investigations on the oligomerization state of Meprin α mutants, native PAGE was applied. Samples were mixed 1:5 with sample buffer (20% (w/v) sucrose, 0.1% (w/v) bromphenol blue). The components used for stacking and separating gel are listed in table 21 in the appendix (p. 126). The proteins were separated at 130 V for about 45 min (running buffer: 100 mM TRIS, 100 mM glycine).

Western Blot: For transfer of the proteins from the PAA-gel onto the nitrocellulose membrane (Protan™ NC, GE Healthcare Amersham™), the semi-dry-blot system (BioRad) was used. The blot was built, applying a discontinuous buffer system according to Kyhse-Andersen (1984). Two filter paper were equilibrated in anode buffer 1 (0.3 M TRIS, pH 10.4, 20% (v/v) methanol) and one filter paper in anode buffer 2 (25 mM TRIS, pH 10.4; 20% (v/v) methanol) for about 5 min, each. The membrane was shortly equilibrated in anode buffer 2 as well, and the last two filter paper in cathode buffer (25 mM TRIS, pH 9.4, 20% (v/v) methanol, 40 mM ε-aminocaproic acid). The PAA-gel was located on top of the membrane (in between the membrane and the last two filter paper, equilibrated in cathode buffer). The proteins were transferred at constant current of 0.8 mA/cm^2 for 1.5-2 h (depending on the size of the protein and the percentage of the separating gel).

The membrane was removed and subjected to blocking in appropriate buffer (5% (w/v) milk powder in TBS-T buffer (20 mM TRIS pH 7.5, 150 mM NaCl, 0.05% (v/v) Tween 20) at 4°C overnight. Afterwards, the appropriately diluted primary antibody was applied onto the membrane at room temperature (RT) for 1 h. Before application of the secondary antibody, the membrane was washed with TBS-T buffer four times for 5 min, each. The secondary antibody was used in an appropriate dilution applied at RT for 1 h. All antibodies were dissolved in blocking buffer. Then, the membrane was washed with TBS-T and TBS (20 mM TRIS pH 7.5, 150 mM NaCl), each twice for 5 min. For the detection based on chemiluminescence, the secondary antibody is coupled to horseradish peroxidase (HRP), enabling the turnover of luminol in its oxidative form, which leads to luminescence (Alegria-Schaffe et al. 2009). Therefor, two kits were used: SuperSignal™West Femto Maximum Sensitivity Substrate and SuperSignal™West Pico Chemiluminescent Substrate (Thermo Fisher Scientific). The substances were applied according to the appropriate manual and the signals were detected using the Fusion Fx7 fluorescence- and chemiluminescence imaging system (Peqlab). For colorimetric detection based on alkaline phosphatase (AP), the secondary antibody is coupled to AP, which catalyses the conversion of the colorimetric substrates BCIP (5-bromo-4-chloro-3-indoyl phosphate) and NBT (nitrotetrazolium blue chloride) (Blake et al. 1984). The reaction buffer (10 ml: 100 mM TRIS pH 9.5, 100 mM NaCl, 5 mM $MgCl_2$) was mixed with 66 µl NBT (5% (w/v) in 70% DMF) and 33 µl BCIP (5% (w/v) in DI water) and incubated on the blot until a violet precipitate (bands) occured. The reaction was stopped by addition of DI water.

2.2.4   Enzymological Methods

2.2.4.1   Determination of Meprin β Activity

For the determination of Meprin β activity during expression and purification, the Proenzyme-containing factions were activated using a Trypsin cleavage in 50 mM TRIS, 20 mM $CaCl_2$, pH 8.0 buffer (activation buffer) at 30°C for 30 min. Activation buffer (100 µl) was added to 50 µl of Pro-Meprin β solution (1:10 diluted in activation buffer in advance) and 50 µl of a 500 µg/ml Trypsin solution (stock solution 10 mg/ml in 1 mM HCl). After incubation, 50 µl of the Trypsin cleavage reaction were added into 150 µl of reaction buffer (40 mM TRIS, pH 8.0) and incubated at 30°C for about 5 min. The quenched substrate Abz-YVAEPK(Dnp)G-OH was diluted to a final concentration of 50 µM in reaction buffer and preincubated at 30°C for 5 min, as well. The Abz (2-Aminobenzoyl) fluorescence is quenched by Dnp (2,4-dinitrophenyl) until the Meprin-mediated cleavage between Alanine and Glutamic acid occurs. The fluorescence was recorded immediately after addition of the substrate Abz-YVAEPK(Dnp)G-OH to the preincubated Meprin β reaction. The increase of fluorescence was measured using a CLARIOstar Plus spectrophotometer (BMG LABTECH). All reactions were performed in NUNC™ F96 MicroWell™ polystyrene plates (black, clear bottom; Thermo Fisher Scientific).

The measurement parameters are listed below:

- Excitation wavelength: 340±15 nm, Emission wavelength: 410±20 nm

- Gain: 1700, bottom optic, number of cycles: min. 40

- Shaking before measurement: 20 s, double orbital.

The evaluation of the results (linear phase of fluorescence increase) was done using the MARS software (BMG LABTECH).

2.2.4.2 Determination of Meprin α Activity

The activity determination of Meprin α was performed as described before for Pro-Meprin β and active Meprin β (chapter 2.2.4.1, pp. 26). However, in case of Meprin α, the substrate (Abz-YVADPK(Dnp)G-OH) and a reaction buffer consisting of 50 mM HEPES pH 7.4 and 150 mM NaCl were used.

2.2.4.3 Determination of Kinetic Parameters

The test applied for determination of enzymatic activity of Meprins was also used for determination of the kinetic parametes K_m, k_{cat} and specific activity. First, a standard curve for the device and the appropriate substrate was recorded. Therefor, 150 µl of reaction buffer (50 mM HEPES pH 7.4, 150 mM NaCl), 50 µl of enzyme (at appropriate concentration) and 50 µl of substrate Abz-YVADPK(Dnp)G-OH at a concentration of 15, 13, 11, 9, 7, 5, 3 and 1 µM were mixed in a cavity of a 96-well plate. After one hour of incubation at 30°C the fluorescence was recorded (plate, measurement device and parameters as described in chapter 2.2.4.1, pp. 26). The relative fluorescent units (RFU) were plotted as a function of the substrate concentration, to determine the factor (slope of the plot) for the device and the substrate, in order to calculate the velocities of the reaction. The calculated velocities are required for the determination of the enzyme units [U]. One unit is defined as the amount of enzyme necessary for turnover of 1 µmol of substrate per minute. The units again are required for calculation of the specific activity of Meprins [U/mg].

For determination of the K_m-value, the turnover of the substrate Abz-YVADPK(Dnp)G-OH at various substrate concentrations (10 to 100 µM, ten steps) in reaction buffer was recorded (reaction volumes as described for activity measurement in chapter 2.2.4.1, pp. 26). The results were evaluated using GraphPad Prism 6 (GraphPad Software), applying the following equation 2, considering substrate inhibition, to determine V_{max} and K_m.

Equation 2 (Copeland 2000)

$$v = \frac{V_{max}[S]}{1 + \frac{K_m}{[S]} + \frac{[S]}{K_i}}$$

$v = velocity\ [\frac{\mu mol}{min}]$ $\qquad\qquad\qquad\qquad$ $V_{max} = maximum\ velocity\ [\frac{\mu mol}{min}]$

$[S] = substrate\ concentration\ in\ reaction\ [M]$ $\qquad$ $K_i = substrate\ inhibition\ constant$

$K_m = substrate\ concentration\ at\ half-maximal\ velocity\ of\ the\ enzymatic\ reaction$

For calculation of k_{cat}, equation 3 was applied.

Equation 3 (Copeland 2000)

$$k_{cat} = \frac{V_{max}}{[E]}$$

$k_{cat} = turnover\ number$ $\qquad$ $[E] = enzyme\ concentration\ in\ reaction$

For the determination of K_m and k_{cat}, the following concentrations of enzyme were used: $1.63*10^{-9}$ M (Meprin β), $5.20*10^{-10}$ M (wild type Meprin α), $7.73*10^{-10}$ M (Meprin α C308A) and $6.94*10^{-10}$ M (Meprin α R372T). For the determination of K_m, k_{cat} and the specific activity, v/S-characteristics were evaluated in duplicate at three independent days.

2.2.5 Biophysical Methods

2.2.5.1 Circular Dichroism (CD) Spectroscopy

In order to investigate differences in secondary structure elements between the three Meprin α variants, a CD spectroscopic analysis in the far-UV range (190-260 nm) was performed. The enzymes were assessed in native and denatured state (chemical denaturation by guanidinium hydrochloride). In general, for helical proteins minima at about 222 and 208 nm and a maximum at 195 nm are expected. For proteins mainly consisting of *β*-sheets, maxima at 190 and 200 nm as well as a minimum around 218 nm are detected. Usually, the *α*-helical signals dominate the CD-spectrum. Unfolded proteins show weaker signals above 210 nm with a minimum between 195 and 200 nm (Buchner and Kiefhaber 2005). The spectra for native proteins were recorded at a concentration of 0.1 mg/ml in 30 mM TRIS pH 7.4 buffer containing 100 mM NaCl. Spectra for denatured proteins were recorded at the same concentration in 30 mM TRIS pH 7.4 buffer containing 100 mM NaCl and 4 M guanidinium hydrochloride. The measurements were executed at 20°C using a Jasco J-710 spectral photometer (Jasco) equipped with a water bath (F25, Julabo) in a 0.1 cm cuvette.

The measurement parameters are listed below:

- Wavelength: 190-260 nm, data pitch: 1 nm

- Scanning mode: continuous, scanning speed: 50 nm/min

- Number of accumulations: 60.

All obtained spectra were normalized against the buffer. The mean residue ellipticity was calculated by usage of equation 4 and plotted as a function of the wavelength.

Equation 4

$$[\Theta]_{MRW} = \frac{\Theta * M}{10 * d * c * N}$$

$[\Theta]_{MRW} = mean\ residue\ ellipticity\ [deg * cm^2 * dmol^{-1}]$ $\Theta = measured\ ellipticity\ [mdeg]$

$M = molar\ mass\ [\frac{g}{mol}]$ $d = path\ length\ [cm]$

$c = concentration\ [\frac{mg}{ml}]$ $N = number\ of\ amino\ acids$

Also, the thermal stability of Meprins was analyzed using CD spectroscopy. For this purpose, far-UV spectra were recorded as described above, but in this case at different temperatures (20 to 90°C, five steps). After reaching the appropriate temperature and before starting the scan, a waiting time of 180 s was set. The mean residue ellipticity was calculated according to equation 4 and plotted as a function of wavelength. Thermal stability was calculated by change of CD signal at appropriate wavelength as a function of temperature. By fitting the data according to a sigmoidal dose-response model in GraphPad Prism 6 (GraphPad Software), the melting temperature of Meprins was calculated. Additionally, the resulting CD data were analyzed using the web server BeSTSel (Beta Structure Selection) (Micsonai et al. 2018; Micsonai et al. 2015) and the web server CAPITO (Wiedemann et al. 2013) in order to predict secondary structure elements.

2.2.5.2   SEC-MALS (Size Exclusion Chromatography – Multi-Angle Light Scattering)

The SEC-MALS analysis was applied for determination of the molar mass of the Meprin α mutants C308A and R372T. A typical SEC method is combined with multi-angle light scattering (MALS), UV$_{280}$ and differential refractive index (DRI) detectors. The UV detector allows a conclusion on the protein concentration by absorbance at 280 nm. The DRI detector is able to determine the concentration as well, by detecting the change in refractive index of the solution, because of the presence of the analyte. Finally, the MALS detector measures the amount of scattered light by the analyte into multiple angles relative to the incident laser beam. Thus, the molecular weight of an analyte can be determined independently of the elution time (Wyatt 1993). The determination was performed in 30 mM TRIS pH 7.4 buffer containing 100 mM NaCl.

Meprin α C308A (100 µl of 0.74 mg/ml) and Meprin α R372T (100 µl 0.44 mg/ml) were applied onto an AdvanceBio SEC column (300Å, 7.8x300 mm, Agilent Technologies) by means of a SIL-20AC autosampler (Shimadzu). The SEC-MALS system was equipped with a CBM 20A system controller (Shimadzu), a DGU-20A5 degassing system (Shimadzu) and a LC-20AD pump (Shimadzu). For detection of the protein sample a SPD-20A UV/Vis detector, an Optilab® DRI dector (Wyatt Technology) and an DAWN® MALS detector (Wyatt Technology) were used. The data evaluation was executed applying the software ASTRA® 6 (Wyatt Technology).

2.2.5.3   MALDI-TOF mass spectrometry

MALDI-TOF mass spectrometry was performed to examine the molecular mass of Meprins and for investigation of cleavage products of Elastin, generated by Meprin α wild type and Meprin α C308A (described in chapter 2.2.7, p. 34). All samples were purified using ZipTip® pipette tips (Merck) before analysis, essentially as described in the supplied manual. In a first step, the protein samples were mixed 1:2 (v/v) with 2% (v/v) TFA. The tip was equilibrated using acetonitrile, then the sample was applied and washed by pipetting 0.1% (v/v) TFA. Finally, proteins or peptides were eluted using 85% (v/v) acetonitrile, 0.1% (v/v) TFA-solution. For analysis of Meprins, C4 ZipTip® tips were used. The purified sample (1 µl) was mixed with 1 µl of DHAP-matrix (7 mg 2,5-dihydroxyacetophenone (DHAP), 375 µl ethanol, 125 µl of 16 mg/ml di-ammonium hydrogen citrate) and 1 µl of 0.1% TFA and applied onto a metal target plate. The samples were analyzed in linear positive mode (LP_30-210 kDa according to Bruker Daltonics) using an Autoflex™ speed MALDI-TOF/TOF device (Bruker Daltonics). Protein Calibration Standard I and II (Bruker Daltonics) were applied for calibration of the device. For analysis of Elastin cleavage reaction supernatants, the samples were purified as described above using C4 and C18 ZipTip® tips and analyzed using the linear positive mode (LP_5-20 kDa, Bruker Daltonics). The calibration of the device was performed with Protein Calibration Standard I and II (Bruker Daltonics). Samples purified with C18 ZipTip® tips were mixed with 1 µl of DHB-matrix (2 mg 2,5-dihydroxybenzoic acid (DHB) solubilized in 100 µl methanol) and 1 µl of 0.1% TFA, applied onto a metal target plate and analyzed using linear and reflector positive mode (LP_5-20 kDa and RP_900-4500Da, Bruker Daltonics). In this case, the Protein Calibration Standard I and the Peptide Calibration Standard II (Bruker Daltonics) were applied for calibration of the device.

2.2.6 Protein Structure Elucidation

2.2.6.1 Crystallography

The crystallography approach was performed to determine the structure of mature Meprin β in complex with its specific inhibitor MWT-S-270.

Protein Preparation-Deglycosylation and Stability Test: For the removal of flexible carbohydrates (N-glycosylations), which lead to heterogeneity of the sample and may interfere the crystal growth, a deglycosylation was performed. Therefor, 0.5 mg/ml purified, mature Meprin β was deglycosylated by EndoH (500 U/mg Meprin β) under non-denaturing conditions (50 mM sodium acetate pH 6.0) at 37°C for 4 h.

Afterwards, the deglycosylated Meprin β was concentrated by ultrafiltration using VivaSpin®6 centrifugal concentrators (cutoff:10 kDa, Sartoris). The protein concentration was determined by UV-absorption at 280 nm (described in chapter 2.2.3.4, p. 24). Finally, the stability of the concentrated Meprin β was tested for up to 15 days at 15°C in a 30 mM TRIS pH 7.4 buffer containing 100 mM NaCl, with and without inhibitor (unspecific inhibitor Actinonin, specific inhibitor MWT-S-270) and analyzed using SDS-PAGE (described in chapter 2.2.3.5, pp. 24).

Protein Crystallization: The protein crystallization was performed in the laboratory of Prof. Dr. Stubbs at Martin-Luther-University Halle-Wittenberg. Mature Meprin β (20 mg/ml and 8 mg/ml in 30 mM TRIS pH 7.4, 100 mM NaCl) was co-crystallized with the specific inhibitor MWT-S-270 at a molar ratio of 1:1.2 (10 mM stock solution of the inhibitor in DI water). First, a primary screen was performed by applying the sitting-drop vapor diffusion method (Russo Krauss et al. 2013). For the primary screen, the following commercial screening kits were used:

- JBScreen Classic, JBScreen JCSG++ (Jena Bioscience)
- Slice pH™; Crystal screen, Crystal screen 2 (Hampton Research)
- Low Ionic Strength kit and Extension kit (Sigma Aldrich)
- Morpheus® (Molecular Dimensions).

By usage of a pipetting robot (Mycrosys SQ, Zinsser-Analytic), 200 nl crystallization buffer were mixed with 200 nl of protein solution and equilibrated next to a reservoir of crystallization buffer (55 µl) in a 96-well-screening format. The screening plates were incubated in a crystal farm at 13°C (Minstrel DT UV Protein Crystal Imaging system, Rigaku). Also, the hanging-drop vapor diffusion method (Russo Krauss et al. 2013) was applied for generation of larger crystals. Therefor, 1 µl of protein solution was combined with 1 µl of crystallization buffer on top of a screwable cover, that was transferred upside down above a reservoir containing 500 µl of crystallization buffer.

Data Collection and Analysis: The data collection at an X-ray radiation generator (copper K-α radiation) at the Martin-Luther-University Halle-Wittenberg (Group of Prof. Dr. Stubbs) and model building was executed by Dr. Miriam Linnert (Fraunhofer IZI-MWT) and Dr. Christoph Parthier (Martin-Luther-University Halle-Wittenberg), who kindly provided the model and map files. The existing crystal structure of Meprin β 4GWN (Arolas et al. 2012) was used for the molecular replacement.

The model building was done using the program Coot from the CCP4 suite (Emsley et al. 2010), the refinement was performed applying Phenix (Liebschner et al. 2019). Images of the structure and map were created by the author of the present study, using the programs UCSF ChimeraX (Goddard et al. 2018) or UCSF Chimera (Pettersen et al. 2004).

2.2.6.2 Cryo-Electron Microscopy (Cryo-EM)

The cryo-electron microscopy (cryo-EM) single particle analysis approach was used for structural elucidation of Meprin α and Meprin β in complex with their specific inhibitors in the active site. Additionally, the transmission electron microscopy (TEM) was applied for screening of different Meprin α and Meprin β samples, in negative stain and for imaging in their native states by vitrification. Also, samples of murine urine and cell culture supernatants were investigated using cryo-TEM. In general, cryo-EM was part of a project including a cooperation of Fraunhofer IZI and the Monash University Melbourne, especially the group of Prof. James Whisstock. Sample preparation and screening were done with support of Dr. Christopher Lupton.

Sample Screening using Negative Stain and Cryo-EM: All grids (usually QUANTIFOIL® Cu R1.2/1.3, QUANTIFOIL® Cu R2/2, QUANTIFOIL® Au R1.2/1.3) were glow-discharged for 30 s in a PELCO easiGlow™ Glow Discharge Cleaning System (PLANO). For negative stain (Gallagher et al. 2019), 3 µl of sample were applied onto the glow-discharged grid. After 1 min of incubation, the sample was removed applying filter paper. Then, the grid was washed twice using 5 µl DI water, followed by negative staining (5 µl of 1% uranyl acetate) for 1 min. The samples were analyzed using a Tecnai 12 transmission electron microscope (Thermo Fisher Scientific, acceleration voltage 120 kV). If not stated otherweise, a Vitrobot II System (Thermo Fisher Scientific) was used for vitrification (Dubochet and McDowall 1981; Dubochet 2012). Usually, 3 µl of sample were applied to a glow-discharged grid, blotted for 2 s with a blot force of -8 at 4°C and 100% relative humidity. A wait time of 5 s (time before blotting) and a drain time of 1 s (time before plunging, after blotting) were applied. Plunge freezing was performed in liquid ethane. Alternatively, the blotting of the grid was executed manually using the hand-plotting technique. Thereby, the excess sample is soaked by filter paper applied onto the grid located in the Vitrobot II System. Finally, the grids were stored in liquid nitrogen until analysis using a Tecnai 12 transmission electron microscope.

Sample Preparation for Data Collection on Titan Krios: The samples for data collection were vitrified as described above. The sample conditions are listed below:

- Meprin β: 3 µl of 1 mg/ml Meprin β with specific inhibitor MWT-S-270 in 30 mM TRIS pH 7.4, 100 mM NaCl; glow-discharged QUANTIFOIL® Au R1.2/1.3 grid
- Meprin α: 3 ml of 0.94 mg/ml Meprin α with specific inhibitor MWT-S-698 in 30 mM TRIS pH 7.4, 100 mM NaCl, 0.2% DMSO; glow-discharged QUANTIFOIL® Cu R2/2 grid.

The same batch of Meprin β, that was used for crystallography was also applied for structural elucidation by cryo-EM (sample preparation described in chapter 2.2.6.1, pp. 31).

In case of Meprin α, the protein solution (in 30 mM TRIS pH 7.4, 100 mM NaCl) was mixed with the specific inhibitor MWT-S-698 in a molar ratio of 1:2. Because, the inhibitor was solubilized to 10 mM in DMSO, a DMSO concentration of about 0.2% remained within the sample applied for data collection.

Data Collection on Titan Krios and Single Particle Analysis Approach: For data collection, a Titan Krios (Thermo Fisher Scientific), equipped with a Quantum energy filter (Gatan) and Summit K2 direct electron detector (Gatan) was used. The data collection was done by Dr. Hariprasad Venugopal at the Monash Ramaciotti Centre for Electron Microscopy, Melbourne. For data processing, the cryo-EM single particle analysis approach was applied (Frank 1975, 2016). The data processing and optimization of the reconstructions of both Meprins, was performed at the Monash University by Dr. Charles Bayly-Jones and Dr. Christopher Lupton (laboratory of Prof. Whisstock), who kindly provided the map files. The model building and refinement, done by the author, was executed using the program Coot from the CCP4 suite (Emsley et al. 2010) and Phenix (Liebschner et al. 2019). In case of Meprin β, the crystal structure obtained in the present study was used as template-model for building. For Meprin α model building, a Swiss-model (Waterhouse et al. 2018) was created using the human Meprin α protein sequence (UniProt: Q16819, (The UniProt Consortium 2019)) and the published Meprin β structure 4GWN (Arolas et al. 2012).

The placement of the specific inhibitors into the cryo-EM structures was performed by docking experiments in cooperation with Christian Jäger (Vivoryon AG). The inhibitors for Meprin β (MWT-S-270) and Meprin α (MWT-S-698) were docked into the respective Model using GOLD 2020.1 (Jones et al. 1997) in combination with the scoring function ChemScore. This was followed by a refinement applying the electron density with MOE (Vilar et al. 2008). For the docking procedure of MWT-S-270 into the Meprin β cryo-EM structure, constraints regarding the binding of the hydroxamic acid to the zinc were set, a range between 1.5 and 3 Å was defined.

Afterwards, for the highest ranked docking solution the systemic rotation energies were minimized to obtain the final protein-ligand structure. In case of the docking into the Meprin α structure, no constraints were set.

Images of the structures and maps were created by the author of the present study, using the programs UCSF ChimeraX (Goddard et al. 2018) or UCSF Chimera (Pettersen et al. 2004).

2.2.7 Analysis of Substrate Cleavage by Different Meprin α Variants

For investigations on the impact of the oligomer formation of Meprin α on its activity, comparative substrate turnover studies were executed using Meprin α wild type and Meprin α mutant C308A. The known substrate Fibronectin (Kruse et al. 2004; Jefferson et al. 2013) and two other extracellular matrix proteins, Tropoelastin and Elastin, were used for the present study.

The substrates and both types of Meprin α were tested for stability during the reaction time in the appropriate buffer at 37°C. The stability was investigated using SDS-PAGE followed by Coomassie-staining (described in chapter 2.2.3.5, pp. 24). The Meprin α variants were additionally investigated by determination of enzymatic activity (described in chapter 2.2.4.2, p. 27).

Different enzyme-substrate ratios were tested in all cleavage reactions. In case of Tropoelastin, the reaction was carried out in 50 mM TRIS pH 7.4 buffer at 37°C and molar ratios of enzyme to substrate of $1:10^4$, $1:10^5$, $1:10^6$. Samples (10 µg) were removed every 30 min for a reaction time of 3 h.

The cleavage of Fibronectin was assessed in 50 mM HEPES pH 7.4 buffer containing 150 mM NaCl. Enzyme to substrate ratios of $1:10^3$, $1:10^4$, $1:10^5$, $1:10^6$ were tested, the reaction conditions were as described before. Finally, an evaluation of the cleavage reactions was performed using reducing SDS-PAGE, followed by Coomassie-staining (described in chapter 2.2.3.5, pp. 24).

Elastin consists of covalently crosslinked Tropoelastin molecules (Frantz et al. 2010). As a consequence, no defined molar mass of Elastin can be determined. Hence, a weight to weight ratio for the cleavage reaction was used. Elastin was shock frozen in liquid nitrogen and lyophilized. Then, the reaction was performed in 50 mM HEPES pH 7.4 buffer containing 150 mM NaCl (weight ratio 1:50), at 37°C for 24 h. Samples were taken after 1, 2, 4, and 24 h of reaction. Since Elastin is not soluble, 30 µl of reaction supernatant was analyzed using SDS-PAGE followed by Coomassie-staining (described in chapter 2.2.3.5, pp. 24). Additionally, the supernatant was analyzed using MALDI-TOF mass spectrometry (described in chapter 2.2.5.3, p. 30).

3 Results

3.1 Structure Elucidation of Meprin β in Complex with its Specific Inhibitor MWT-S-270

3.1.1 Heterologous Expression, Purification and Characterization of Meprin β

Meprin β and its isoenzyme Meprin α are multidomain metalloproteases requiring Trypsin-like proteinases for proteolytic removal of the N-terminal propeptide and thus activation (Sterchi et al. 2008). Both enzymes play a major role in fibrosis, but also nephritis and potentially neurodegeneration (Broder and Becker-Pauly 2013; Bien et al. 2012; Becker-Pauly and Pietrzik 2016). Accordingly, the development of selective inhibitors is in focus of research (Ramsbeck et al. 2017; Ramsbeck et al. 2018).

Pro-Meprin β was expressed as zymogen in *Pichia pastoris* X33 under the control of the AOX1 promoter, enabling an induction of expression by addition of methanol. A C-terminally truncated Pro-Meprin β (T^{23}-Q^{595}, figure 5) containing an N-terminal His-Tag, the pro, protease, MAM and TRAF domain, was cloned into the pPICZαC-vector. The α-mating factor from *Saccharomyces cerevisiae* upstream of the Pro-Meprin β serves as a signal, mediating the secretion of Pro-Meprin β and thus purification of the enzyme from the fermentation supernatant. To achieve a high expression rate of Pro-Meprin β, the coding sequence was adjusted to the codon usage of *Pichia pastoris* and the expression was compared to the native sequence (*Homo sapiens*). The linearized expression vector was transformed into *Pichia pastoris* X33 cells. A high-expressing clone was selected by a test expression in 2 ml scale and activity determination (described in chapter 2.2.3.1, pp. 20 and chapter 2.2.4.1, pp. 26).

A   Meprin β full length
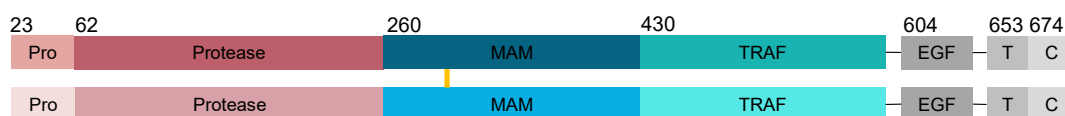
B   Meprin β
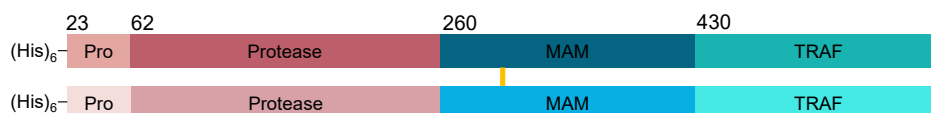
Figure 5: Schematic illustration of the expression construct of Pro-Meprin β, naturally occurring as dimer linked by a disulfide bridge in the MAM domain. A) *Wild type Pro-Meprin β full length, including the propeptide (Pro, T^{23}-R^{61}), protease domain (N^{62}-L^{259}), meprin A5 tryrosine phosphatase μ – MAM domain (S^{260}-H^{429}), the tumor-necrosis-factor-receptor-associated factor – TRAF domain (H^{430}-Q^{595}), the epidermal growth factor like-domain (EGF, V^{604}-E^{644}), the transmembrane domain (T, I^{653}-V^{673}) and the cytosolic tail (C, S^{674}-F^{701}).* ***B)*** *Heterologously expressed C-terminally truncated Pro-Meprin β, including the propeptide, protease, MAM and TRAF domain (N^{62}-Q^{595}).*
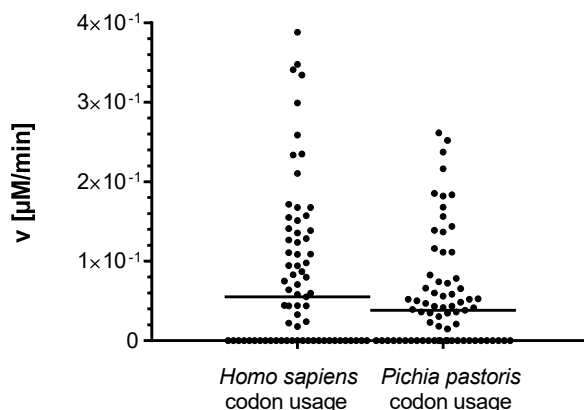
Figure 6: Investigation of the influence of the codon usage on the heterologous expression of Pro-Meprin β in P. pastoris X33, analyzed by determination of enzymatic activity. *Competent P. pastoris were transformed with two constructs, either featuring the native human coding sequence or a condon-optimized sequence to enable higher expression in P. pastoris. 72 clones of each construct were investigated by activity determination using the fluorescence substrate Abz-YVAEPK(Dnp)G-OH (assay buffer: 40 mM TRIS pH 8.0, described in chapter 2.2.4.1, pp. 26).*

The codon optimization did not improve the expression level of Pro-Meprin β in *P. pastoris* X33. Nevertheless, clones showing low, medium and high Pro-Meprin β expression could be identified (figure 6). The highest expressing clone #8 (native human nucleotide sequence) was used for a high-density fermentation process in a 5 l reactor (described in chapter 2.2.3.1, pp. 20).
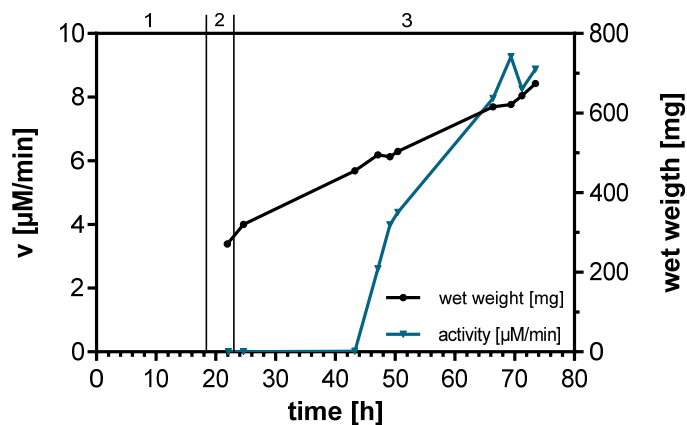
Figure 7: Dependence of biomass and enzymatic activity during a typical fermentation process of P. pastoris clone #8, expressing Pro-Meprin β. *Wet weight [mg] and Meprin β activity [µM/min] (both values assayed in duplicate and averaged) in relation to the fermentation time is displayed. 1: glycerol batch phase, 2: glycerol fed batch phase, 3: methanol fed batch phase (induction of protein production regulated by AOX1 promoter). Activity was determined using the fluorescence substrate Abz-YVAEPK(Dnp)G-OH, assay buffer: 40 mM TRIS, pH 8.0; 30°C).*

During the fermentation, a continuous increase of biomass wet weight was observed, as well as an increase of enzyme activity, following initiation of the methanol fed batch phase (figure 7). After 72 h, the fermentation process was stopped, since the activity of Meprin β was not increasing further.

The supernatant was harvested and Pro-Meprin β was purified by Ni^{2+}-IMAC (immobilized metal affinity chromatography) using the expanded bed adsorption technique (EBA). This was followed by the activation of Pro-Meprin β by Trypsin leading to cleavage of the propeptide. For removal of Trypsin and putatively denatured Meprin β, a hydrophobic interaction chromatography (HIC) was performed. Finally, the mature Meprin β was desalted by size exclusion chromatography and concentrated to about 0.9 mg/ml using an Amicon® stirred cell (cutoff: 30 kDa). The purification process was evaluated by SDS-PAGE (figure 8) and by determination of the specific activity, which is displayed in the purification table (table 6).
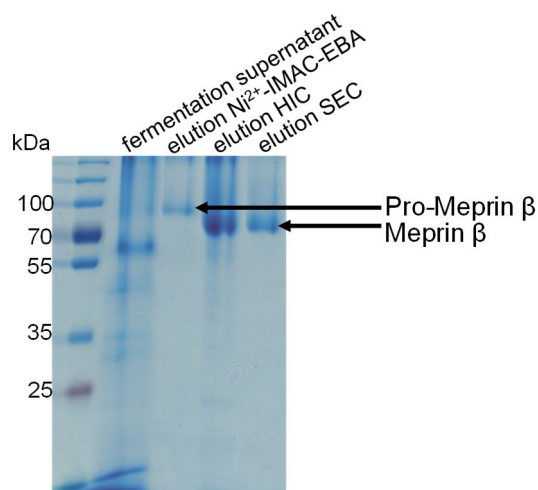
Figure 8: SDS-PAGE analysis illustrating the Meprin β purification process, visualized by Coomassie-staining. The starting material was the fermentation supernatant. The mass shift occurring after the Ni^{2+}-IMAC-EBA, is a result of activation of Pro-Meprin β by Trypsin cleavage. 12%T acrylamide gel, 5 μg of protein of each fraction was applied.

As shown in figure 8, virtually homogenous Pro-Meprin β could be observed in the gel already after the first column (Ni^{2+}-IMAC-EBA). The corresponding specific activity was 32 U/mg. Pro-Meprin β was activated by Trypsin after the initial column. The following purification by HIC and size exclusion chromatography (SEC) led to a further increase of the specific Meprin β activity. Finally, the specific activity of mature Meprin β was 36 U/mg (substrate Abz-YVAEPK(Dnp)G-OH; 40 mM TRIS, pH 8.0; 30°C), with an average yield of 7 mg per liter of fermentation broth. The diffuse bands, visible in figure 8, are a result of high protein glycosylation, which was known for Meprins (Marchand et al. 1994) and heterologously expressed proteins in yeast (Hamilton et al. 2003; Tanner and Lehle 1987; Tang et al. 2016).

Table 6: Purification of Pro-Meprin β from fermentation supernatant of P. pastoris. Activity determination was performed with the fluorescence substrate Abz-YVAEPK(Dnp)G-OH; assay buffer: 40 mM TRIS, pH 8.0; temperature: 30°C, as described in chapter 2.2.4.1, pp. 26. Before each activity determination, Pro-Meprin β was activated by Trypsin. This table represents a typical purification process after high density fermentation of clone #8.

Purification step	Protein concentration [mg/ml]	Protein amount [mg]	Total activity [U]	Specific activity [U/mg]	Yield [%]	Enrichment factor
Fermentation supernatant	0.33	568	2785	5	100	1
Elution Ni²⁺-IMAC-EBA	0.11	17	546	32	20	7
ElutionHIC	0.20	15	405	28	15	6
Elution SEC	0.33	10	356	36	13	7

3.1.1.1 Determination of the Kinetic Parameters for Conversion of a Fluorogenic Substrate by Meprin β

To characterize active Meprin β, the K_m and k_{cat} values were determined for turnover of substrate Abz-YVADPK(Dnp)G-OH in 50 mM HEPES pH 7.4 buffer containing 150 mM NaCl, (chapter 2.2.4.1, pp. 26). The resulting v/S-characteristic is displayed in figure 9. The analysis resulted in a K_m value of 44±3 µM. The k_{cat} value is 11.7±0.9 s⁻¹. An inhibition constant for the substrate Abz-YVADPK(Dnp)G-OH of 350±107 µM was determined. The catalytic efficiency k_{cat}/K_m is 265±0.04 µM⁻¹s⁻¹.
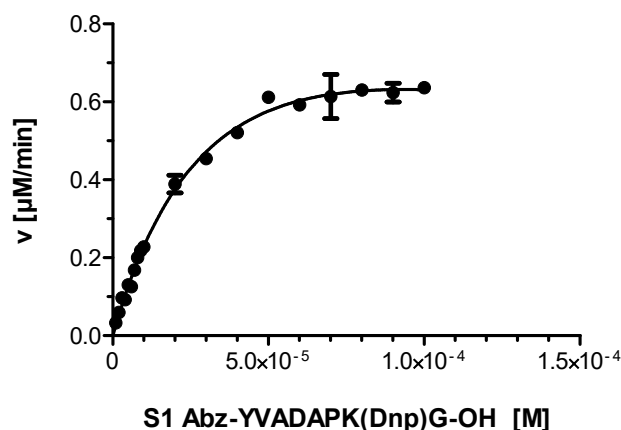
Figure 9: v/S-characteristic for turnover of substrate Abz-YVADPK(Dnp)G-OH by Meprin β in a buffer containing 50 mM HEPES pH 7.4 and 150 mM NaCl at 30°C. Measurements were performed in duplicate on three different days at the same instrument. The data was evaluated by substrate inhibition kinetics with the software GraphPad Prism 6. This graph represents one out of the three independent measurements in duplicate. The K_m and k_{cat} values determined from three individual measurements are 44±3 µM and 11.7±0.9 s⁻¹, respectively. A calatytic efficiency of 265±0.04 µM⁻¹s⁻¹ was determined.

3.1.1.2   Biophysical Characterization of Meprin β

In order to investigate the thermal stability of the recombinant Meprin β and to obtain information about the secondary structure of the protein, a CD spectroscopic analysis within the far-UV range was performed (see chapter 2.2.5.1, pp. 28). The resulting CD signals were normalized and the mean residue ellipticity was calculated. The far-UV spectrum of native and chemically denatured Meprin β is displayed in figure 10A. Although the data is only evaluable between 200 and 260 nm, due to background noise, the native Meprin β exhibits a typical *β*-sheet spectrum with a minimum at 218 nm and a maximum at 200 nm (figure 10 A). In comparison, the spectrum of chemically denatured Meprin β shows a strong minimum below 210 nm, indicating disordered protein structure. Finally, these investigations lead to the conclusion that Meprin β is properly structured in its native state, harboring a high *β*-sheet content.
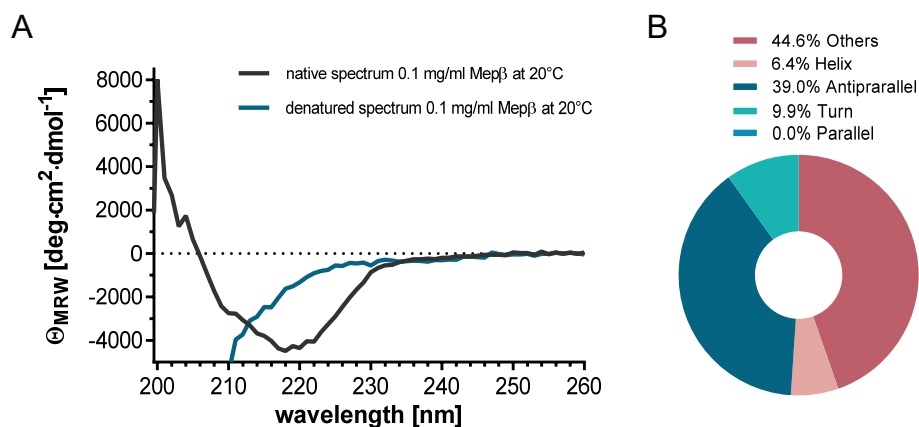
Figure 10: Far-UV CD spectrum of native (black) and denatured (blue) Meprin β. A) *The analysis was performed at a protein concentration of 100 µg/ml in a quartz cuvette with a path length of 0.1 cm at 20°C as described in chapter 2.2.5.1 (pp. 28). The data was baseline corrected (against buffer) and the mean residue ellipticity was calculated by the software GraphPad Prism 6.* *B)* *Analysis of CD signals by the web server BeSTSel for prediction of secondary structure.*

To prove these investigations, the CD data were analyzed by the web server BeSTSel (Beta Structure Selection), which is a method for prediction of secondary structures from CD signals (Micsonai et al. 2018; Micsonai et al. 2015). The results are depicted in figure 10 B. The evaluation suggests a significant degree of antiparallel *β*-sheets in the Meprin β secondary structure, whereas a percentage of 6.4% for helical structures was determined (figure 10 B). About 45% of other secondary structure elements were observed, these include 3_{10}-helix; π-helix; β-bridge; bend as well as loop or irregular regions of the structure (Micsonai et al. 2018). In order to obtain information on the thermal stability of Meprin β, a stepwise thermal denaturation was performed, whereby far-UV spectra were recorded.
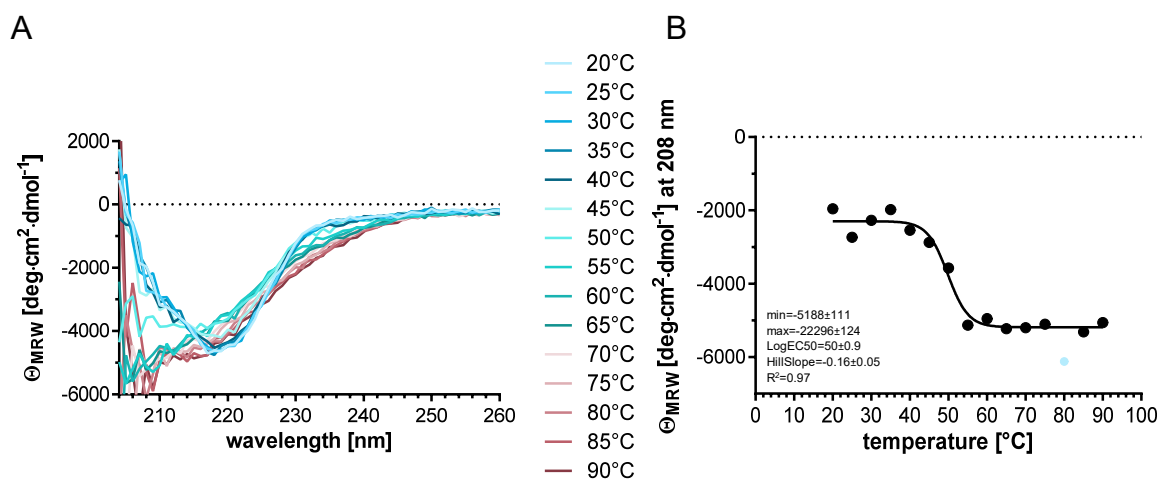
Figure 11: Analysis of Meprin β thermal stability using CD spectroscopy. A) *The enzyme was analyzed in 30 mM TRIS pH 7.4 buffer containing 100 mM NaCl, at a protein concentration of 100 µg/ml in a quartz cuvette with a path length of 0.1 cm as described in chapter 2.2.5.1 (pp. 28). For analysis of the thermal stability of Meprin β, scans at temperatures ranging from 20 to 90°C (5°C steps) were recorded. The mean residue ellipticity was calculated by the software GraphPad Prism 6.* ***B)*** *The CD signals at 208 nm were plotted against the temperatures and fitted by the sigmoidal dose-response model in GraphPad Prism 6. The light blue marked value was excluded from analysis.*

Significant changes of the mean residues ellipticity was observed upon temperature increase, especially within the wavelength range between 200-215 nm (figure 11 A). At temperatures up to 45°C, the native structure of the protease appears to be stable. A calculation of difference spectra revealed the most prominent change of the CD signal at 208 nm. Therefor, CD signals at this wavelength were plotted against the temperature (figure 11 B). By fitting the data according to a sigmoidal dose-response model, a melting temperature for active Meprin β of 49.8°C could be determined.

3.1.2 Deglycosylation of Meprin β in Its Native State and Stability test

Because the 3D-structure of active Meprin β should be determined by X-ray crystallography, the removal of the flexible glycosyl side chains appeared important. Glycosyl side chains may introduce heterogeneity and the conformational flexibility may interfere with crystal growth (Chang et al. 2007). Thus, a deglycosylation with EndoH at low Meprin β concentration under native conditions was performed. The treatment led to a mass shift of about 10 kDa as displayed in figure 12 A. Although the mass shift could be visualized using SDS-PAGE, still a smear above the deglycosylated protein band is observed, indicating partial deglycosylation of Meprin β. However, the specific activity of Meprin β was not altered due to the deglycosylation process and the enzyme did not show a tendency to aggregate. Consequently, the deglycosylated, active Meprin β was used for all analysis and characterization steps. After successful deglycosylation, Meprin β was concentrated using a centrifugal ultrafiltration column (cutoff: 10 kDa), to reach a high protein concentration, which is necessary for crystal growth (Dessau and Modis 2011). Since the crystals are grown at 15°C for several days up to months, the stability of the highly concentrated Meprin β solution is important.

Hence, a stability test of the concentrated Meprin β (13 mg/ml in 30 mM TRIS pH 7.4, 100 mM NaCl) at 15°C was executed, samples were taken after different times of incubation and analyzed using SDS-PAGE (figure 12 B).
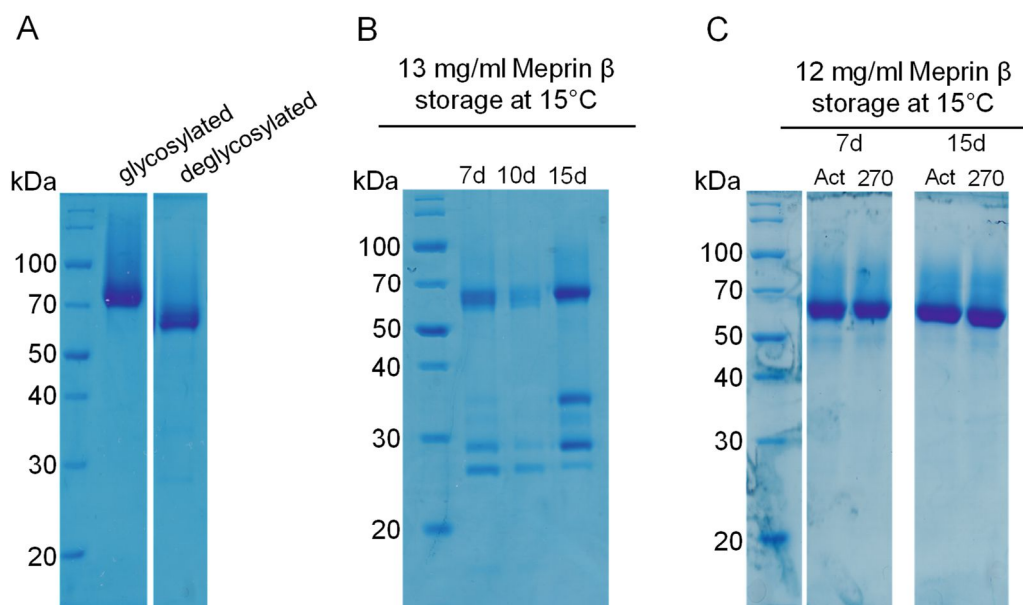
Figure 12: Analysis of stability of Meprin β (13 mg/ml) by SDS-PAGE. A) *Visualization of Meprin β before and after deglycosylation by EndoH under native conditions. The mass shift indicates a partial removal of glycan chains.* ***B)*** *Stability test of highly concentrated Meprin β for up to 15 days at 15°C (30 mM TRIS pH 7.4, 100 mM NaCl). A degradation of Meprin β after 7 days is visible.* ***C)*** *To increase the stability of the deglycosylated Meprin β, the commercial inhibitor Actinonin (IC$_{50}$ 574 nM) and the specific inhibitor MWT-S-270 (IC$_{50}$ 49 nM) were added in a molar ratio of 1:1.3 and 1:1.2, respectively. The inhibition of Meprin β leads to an increased stability at 15°C, which may indicate an autocatalytic activity of Meprin β as cause of instability.*

As shown in figure 12 B, Meprin β was degraded. To prevent degradation of Meprin β at high enzyme concentration, the commercial inhibitor Actinonin and the specific inhibitor MWT-S-270 were added at a molar ratio of 1:1.3 and 1:1.2, respectively. The stability of Meprin β at high enzyme concentration was improved due to the addition of inhibitors (figure 12 C). This result is in accordance with an autocatalytic cleavage of Meprin β.

3.1.3 Crystallization and Structure Elucidation of Mature Meprin β in Complex with MWT-S-270

After successful isolation and characterization, the co-crystallization of Meprin β with the specific inhibitor MWT-S-270 was initiated. First, a primary screen of 960 conditions at two enzyme concentrations was performed (8 mg/ml, 20 mg/ml), applying the sitting drop vapor diffusion method. The primary screen was followed by a fine screen of promising conditions in 15-well plates, whereby a hanging drop vapor diffusion method was used (chapter 2.2.6.1, p. 31). Meprin β crystallized at 8 and 20 mg/ml. Under most of the tested conditions crystals grew. The most promising crystals of the primary and fine screen are depicted in figure 13.

A Primary screen of Meprin β with MWT-S-270, vapor diffusion, sitting drop

condition 1	condition 2	condition 3	condition 4
0.1 M HEPES pH7.5 0.8 M NaH$_2$PO$_4$ 0.8 M KH$_2$PO$_4$ 20 mg/ml, 3 d growth Hampton Research Crystal Screen 1+2.C11	0.1 M sodium acetate pH4.6 30% (w/v) PEG 400 0.1 M CaCl$_2$ 20 mg/ml, 7 d growth JBScreen Classic 1-4.A8	0.1 M phosphate-citrate pH4.2 30% (v/v) PEG 300 20 mg/ml, 9 d growth JBScreen, JCSG++ 1-4.C6	0.1 M Tris pH8.5 32% (w/v) PEG 800 0.2 M CsCl 2.8% (v/v) glycerol 8 mg/ml, 98 d growth JBScreen Classic 1-4.A1

B Fine screen of Meprin β with MWT-S-270, vapor diffusion, hanging drop

condition 1f	condition 2f	condition 3f
0.1 M HEPES pH7.7 0.8 M NaH$_2$PO$_4$ 0.8 M KH$_2$PO$_4$ 20 mg/ml, 12 d growth	0.1 M sodium acetate pH4.7 35% (w/v) PEG 400 0.1 M CaCl$_2$ 20 mg/ml, 12 d growth	0.1 M phosphate-citrate pH4.0 40% (v/v) PEG 300 20 mg/ml, 12 d growth

Figure 13: Microscopic images of Meprin β crystals grown in presence of the specific inhibitor MWT-S-270.
A) Four conditions from the primary screen. Crystals obtained using the vapor diffusion method and sitting drop technique. With crystals of conditions 1-3, diffraction patterns of 3-4 Å were achieved. For improvement of the diffraction pattern, a fine screen was performed. The crystal of condition 4 was analyzed using a laboratory X-ray diffractometer (copper K-α radiation). This crystal diffracted to a resolution of about 2.4 Å. B) Fine screen of conditions 1-3, reached by application of the vapor diffusion method using the hanging drop technique.

The crystals obtained under conditions 1-3 (figure 13 A) were observed within the first two weeks after initiation of crystallization. Screening applying the laboratory X-ray diffractometer (copper K-α radiation) resulted in a diffraction pattern with a resolution of 3-4 Å. For improvement of the resolution and to obtain larger crystals, a fine screen in 15-well format (vapor diffusion, hanging drop) was performed (figure 13 B). The resolution could not be improved after fine screening. However, a large crystal grown in 0.1 M TRIS pH 8.5, 32% (w/v) PEG 800, 0.2 M CsCl, 2.8% (v/v) glycerol (JBScreen Classic 1-4.A1, Jena Bioscience) at an enzyme concentration of 8 mg/ml was first observed after 37 days and analyzed after 96 days of growth. For the respective crystal an improved diffraction pattern and resolution was observed. Thus, further analysis was done with crystals grown under these conditions. A further fine screen was not perfomed. The data collection and model building were done by Dr. Miriam Linnert (Fraunhofer IZI-MWT) and Dr. Christoph Parthier (Martin-Luther-University Halle-Wittenberg), who kindly provided the model and map files.

The diffraction pattern was recorded at the laboratory X-ray diffractometer at the Martin-Luther-University Halle-Wittenberg (Group of Prof. Stubbs). The previously published structure of Meprin β without inhibitor (PDB: 4GWN) was used for molecular replacement (Arolas et al. 2012). The statistics of the data collection and refinement are listed in table 22 in the appendix (p. 127).

3.1.4 Structure of Meprin β in Complex with the Inhibitor MWT-S-270 elucidated by X-ray crystallography

The evaluation of the diffraction pattern resulted in a Meprin β structure with a resolution of 2.41 Å. One dimeric Meprin β of C2 symmetry was observed per unit cell (figure 51 in the appendix, p. 128). Meprin β consists of the three subunits: protease domain, MAM domain and TRAF domain, according to the expression construct. The two monomers are linked by a disulfide bridge within the MAM domain (figure 14). The disulfide linkage is, as shown for the first time, clearly defined by electron density.

Chain A

Intermolecular disulfide bridge
C^{305}/chain A and C^{305}/chain B

Chain B

▬ Protease domain/chain A	▬ Protease domain/chain B
▬ MAM domain/chain A	▬ MAM domain/chain B
▬ TRAF domain/chain A	▬ TRAF domain/chain B

▬ Solvent/chain A and B	
▬ Calcium ion/chain A and B	
▬ Zinc ion/chain A and B	
▬ Inhibitor MWT-S-270/chain A and B	
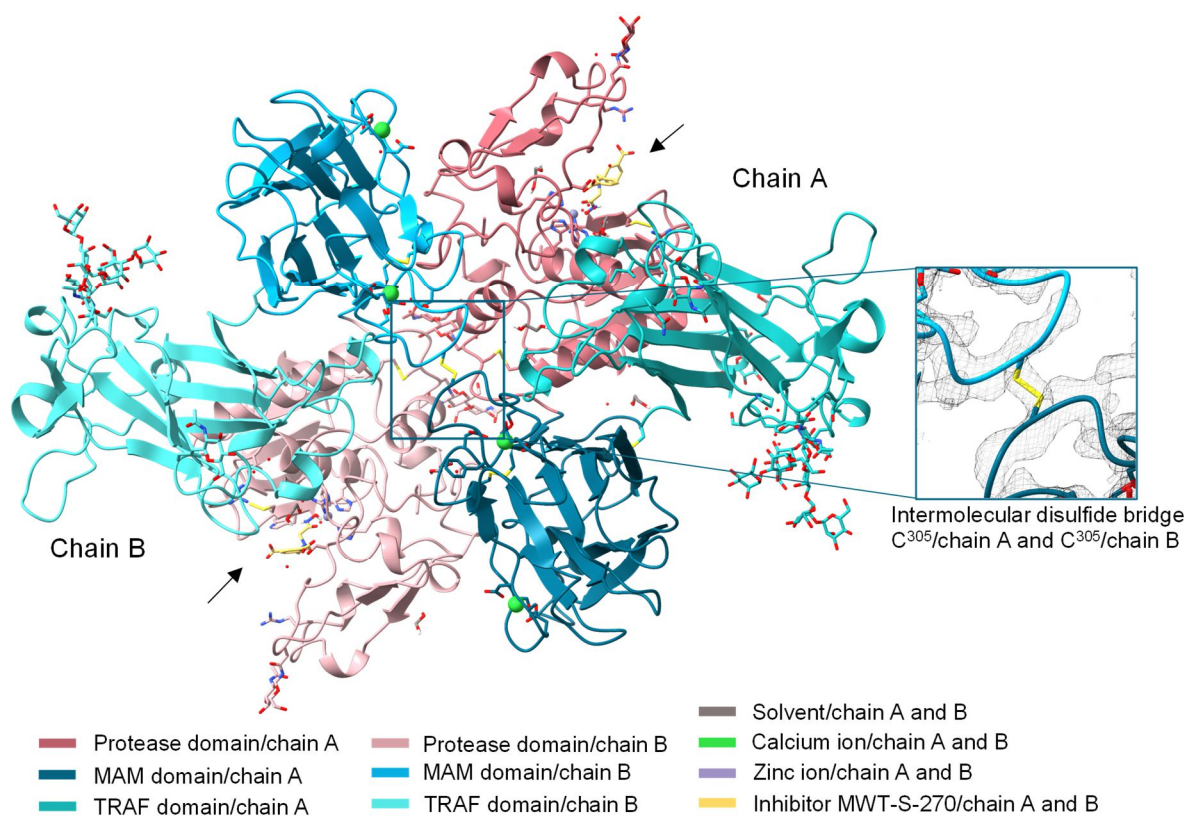
Figure 14: Structure of Meprin β, elucidated by crystallization and X-ray diffraction analysis. Meprin β crystallized as dimers (chain A and B) with a resolution of 2.41 Å. The model includes the TRAF domain P^{428}-Q^{595}, MAM domain Q^{260}-C^{427} and protease domain N^{62}-L^{259} within both chains. Chain A and B are linked by an intermolecular disulfid bridge mediated by C^{305} within both chains. The active site of chain A and chain B is highlighted by an arrow. The inhibitor is highlighted in yellow. Glycolsyations are shown as sticks.

The TRAF domain spans the residues P^{428}-Q^{595} in both chains (figure 14 and figure 52 in the appendix, p. 128). For the last amino acid, Q^{595}, no electron density could be observed.

The TRAF domain mainly consists of a β-sandwich including two four-stranded antiparallel β-sheets (figure 14). A large glycosylation tree in both chains at N^{547} was observed, although the protein underwent a deglycosylation by EndoH. Additionally, single N-acetylglucosamine residues at positions N^{445} and N^{592} were noted within chain A. EndoH cleaves between the two N-acetylglucosamine residues within the diacetylchitobiose core of the oligosaccharide (Freeze and Kranz 2010). The remaining N-acetylglucosamine suggests the presence of an N-linked glycosylation tree before the deglycosylation.

The MAM domain of both chains includes the residues Q^{260}-C^{427} and is stabilized by two intramolecular disulfide bridges between C^{265}-C^{273} and C^{340}-C^{427} (figure 15 and figure 53 in the appendix, p. 129). The intermolecular disulfide bridge between C^{305}/chain A and C^{305}/chain B, connecting the two monomers of Meprin β, is also present within the MAM domain. The overall secondary structure of the MAM domain in chain A and chain B is characterized by a β-sandwich composed of two four-stranded antiparallel β-sheets. Two tentative calcium ions in each chain are coordinated within the MAM domain (figure 53 in the appendix, p. 128). One calcium ion within chain A shows square planar geometry. It is coordinated by the backbone carbonyls of S^{278} and A^{283}, as well as by the hydroxyl group of D^{284}. Additionally, bidentate binding to the side chain carboxyl group of D^{281} is observed. Within chain B, this calcium ion shows octahedral coordination, involving the same interactions as described for chain A and an interaction with a water molecule. The second calcium ion bound within chain A and B shows octahedral coordination involving the backbone carbonyls of S^{266} and F^{310}, the hydroxyl group of S^{300} and the carboxyl groups of E^{268} and D^{298}. In addition to these monovalent coordinative bonds, a bivalent interaction to the side chain carboxyl residue of D^{418} is observed.

The protease domain includes the residues N^{62} to L^{259} (figure 14 and figure 54 in the appendix, p. 130). The active site harboring the zinc subdivides the protease domain into an upper and lower subdomain ("standard orientation"). The upper subdomain is crosslinked by two disulfide bridges between C^{103}-C^{255} and C^{124}-C^{144}. It is characterized by a four-stranded antiparallel β-sheet and three α-helices. The lower subdomain has little secondary structure elements (figure 14). At N^{218} in chain A and chain B, one N-acetylglucosamine residue and at N^{254} (both chains) two N-acetylglucosamine residues could be determined. As described for metzincins, also the mature Meprin β harbors the conserved zinc-binding motif HExxHxxGxxH (x can be any amino acid) and the 1,4-β-type Met-turn close to the active site (Sterchi et al. 2008; Gomis-Rüth 2009). The zinc within the active site is complexed by the three Histidine residues H^{152}, H^{156} and H^{162}. The three subpockets S1, S1' and S2', belonging to the active site cleft of Meprin β, are shaped by the residues R^{184} (S1), R^{238} (S1') and R^{146} (S2'). These provide the rational for the preference of Meprin β to cleave negatively charged substrates (Sterchi et al. 2008; Broder and Becker-Pauly 2013).

In particular, the subpocket S1 (R^{184}) shows high flexibility, as suggested by the B-factor staining (figure 54 in the appendix, p. 130), and mediates a slightly more 'opened' or more 'closed' position of the active site. Within the active site of chain A and chain B, the inhibitor MWT-S-270 could be determined (figure 15). MWT-S-270 consists of a tertiary amine connecting the hydroxamic acid and two benzoic acid moieties (*meta*-positioned). Docking experiments predicted, that the hydroxamic acid of the inhibitor complexes the zinc ion within the active site. Furthermore, charged interactions were predicted between R^{184} (S1) and R^{238} (S1') and the two benzoic acid moieties of the inhibitor (Ramsbeck et al. 2018).
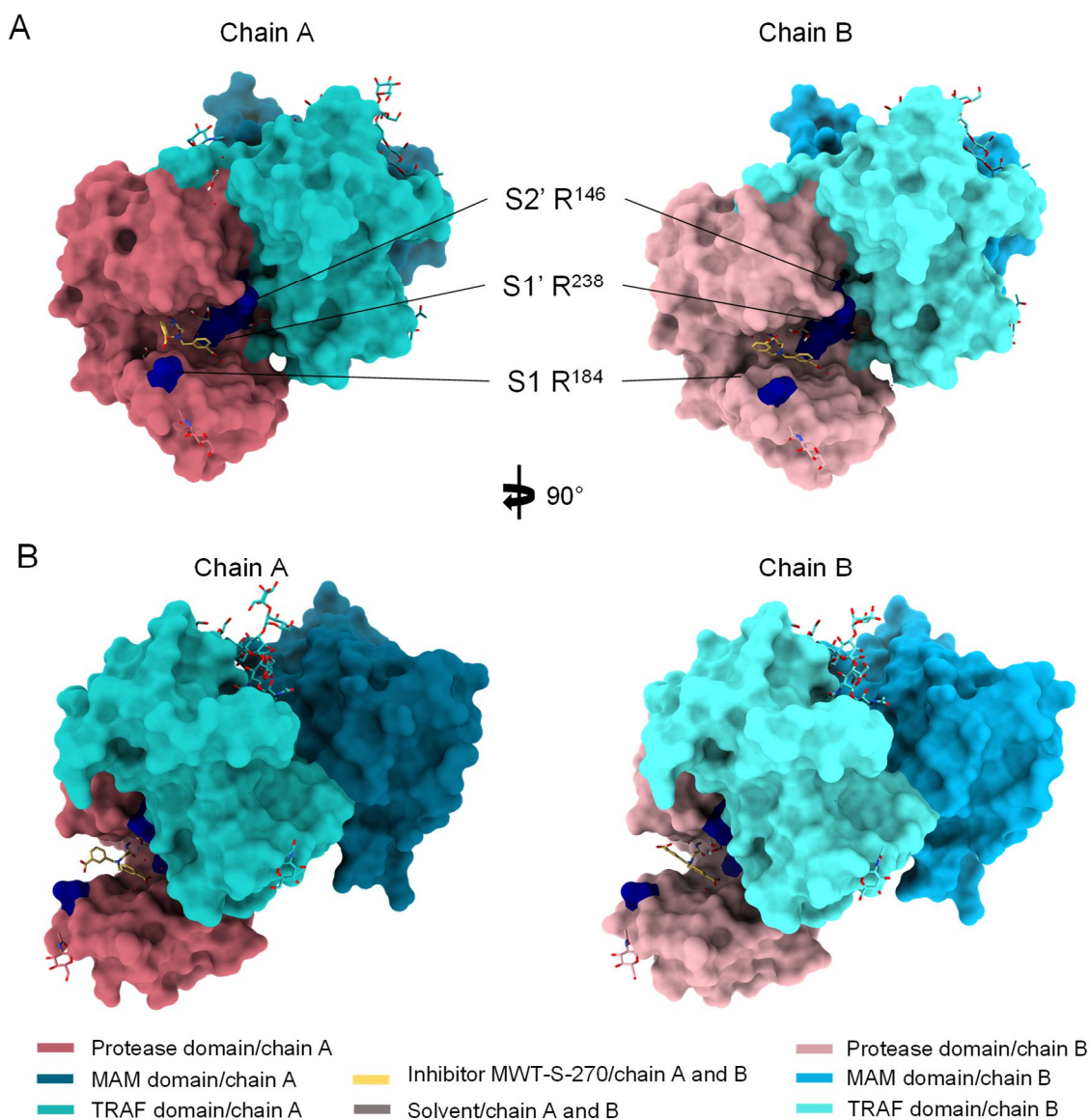
Figure 15: Structure of dimeric Meprin β, elucidated by crystallization and X-ray diffraction analysis, colored according to domain structure. A) *'Standard orientation' of chain A and chain B, representation of surface structure with view into the active site cleft. The Arginine residues R^{184}, R^{238} and R^{146}, shaping the subpockets S1, S1' and S2', are colored in dark blue. The inhibitor is highlighted in yellow.* **B)** *Chain A and chain B rotated by 90° on the vertical axis.*

Within the crystal structure, the hydroxamic acid moiety of MWT-S-270 chelates the catalytic zinc in both chains. Additionally, the hydroxamate amide forms a hydrogen bond with the backbone carbonyl of C^{124} (2.9 Å). The hydroxyl group of the hydroxamic acid coordinates the zinc and forms a hydrogen bond to the carboxylate of E^{153} (3.0 Å). The interactions of the inhibitor side chains are depicted in figure 16. Only one benzoic acid moiety of the inhibitor within chain A, could be elucidated (benzoic acid 1, figure 16). This meta-carboxylate 1 forms a hydrogen bond with the hydroxyl group of S^{212} and with the backbone amide of S^{212} as well as a water molecule (3.2 Å). Because of the ambiguous electron density, also an ionic interaction of the guanidine moiety of R^{238} with the carboxylate 1 cannot be excluded. Additionally, the spacer carbon between the tertiary amine and the benzoic acid moiety 1 might form a hydrophobic interaction with the side chain aromatic ring of F^{216}. The second carboxylate group of MWT-S-270 might interact with the guanidine group of R^{184} at a distance of 3.8 Å (figure 16), but the electron density of R^{184} is ambiguous as well, most likely due to the high flexibility of this residue. A staining of the protease domain according to B-factor, as depicted in figure 54 in the appendix (p. 130), indicates a high flexibility of R^{184} within chain A and chain B. Within chain B, the interactions of the hydroxamic acid and benzoic acid moiety 1 are similar to the described interactions within chain A (figure 16). For the benzoic acid moiety 2 within chain B, the electron density observed is sparse.

Summarizing, in the present study the structure of mature Meprin β in complex with an inhibitor at a resolution of 2.41 Å is described. Both monomers of Meprin β are linked by a well-resolved disulfide bridge, as shown in the present study for the first time. However, the electron density of the inhibitor appears ambiguous in both monomers of the crystal structure. As expected, the hydroxamic acid complexes the zinc and benzoic acid moiety 1 might interact with S^{212} or R^{238}. Benzoic acid moiety 2 seems to form an ionic interaction with the R^{184}, which could be shown at least within chain A (figure 16). But, based on the B-factor staining (figure 54 in the appendix, p. 130), the residue of subpocket S1, R^{184}, shows high flexibility and consequently might achieve different conformations, which might lead to different binding modes of the inhibitor within the actice site. Because of these observations, conclusions on the primary interactions providing the rationale for the extraordinary specificity of the inhibitor for Meprin β, could not be drawn. Therefore, a second approach for an analysis of the inhibitor binding was undertaken.
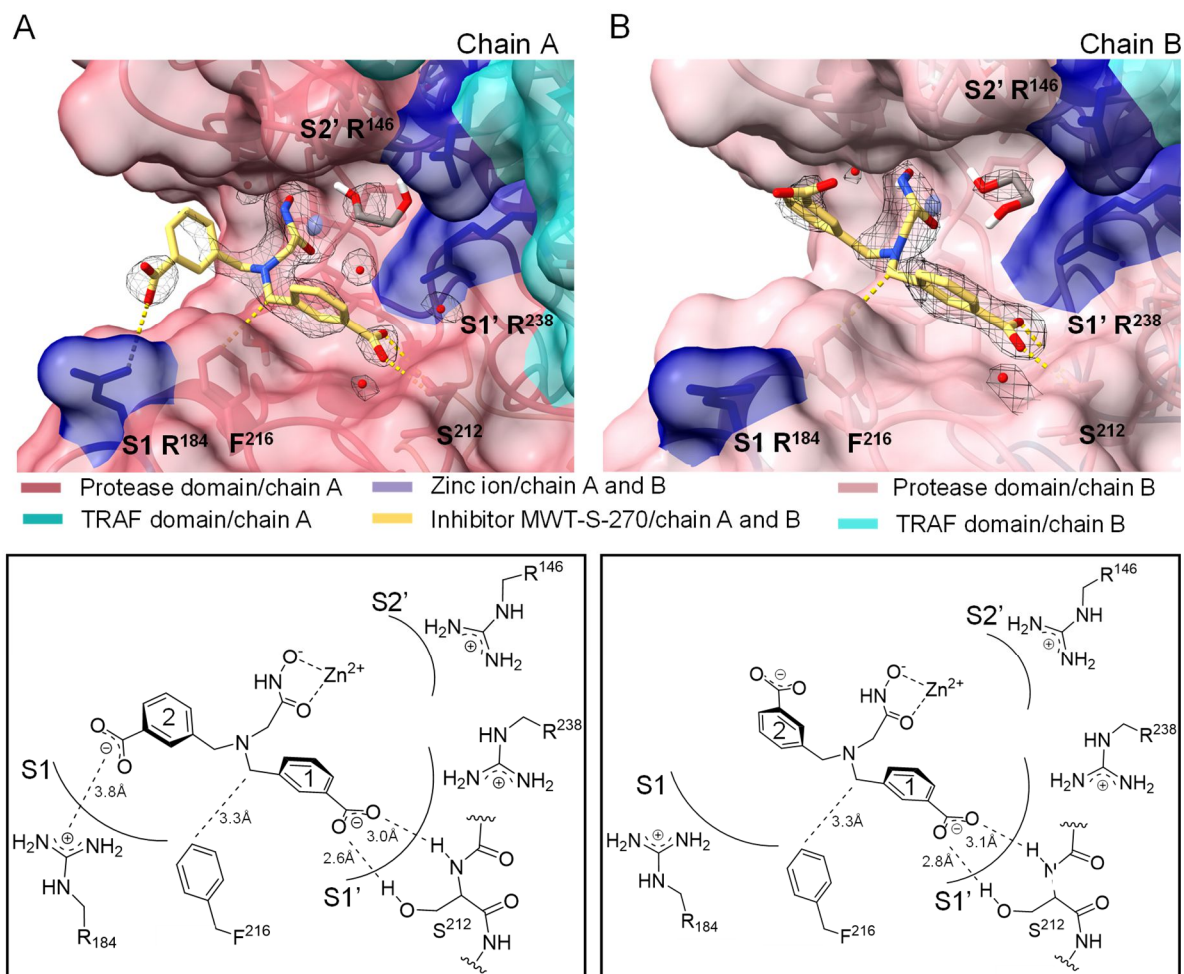
Figure 16: The inhibitor MWT-S-270 bound to the active site of Meprin β (crystal structure). *Comparison of the different orientations of MWT-S-270 within the active site of chain A and chain B. Inhibitor side chain interactions are displayed in a 2D-plot.* **A)** *Benzoic acid moiety 1 forms a hydrogen bond with the hydroxyl group of S^{212} and with the backbone amide of S^{212}. Also, an ionic interaction with R^{238} could be possible. The benzoic acid moiety 2 might form an ionic interaction with R^{184} of subpocket S1.* **B)** *The benzoic acid moiety 1 forms the same interactions as observed for chain A. In case of benzoic acid moiety 2, no conclusions on an interaction could be drawn due to ambiguous electron density.*

3.1.5 Structure of Meprin β in Complex with MWT-S-270 elucidated by Cryo-Electron Microscopy

An X-ray crystallography approach leads to resolution of a snapshot of a protein and its inhibitor or ligand. Additionally, packing effects within the crystal might affect the conformation of the protein and the orientation of the inhibitor within the active site cleft. By applying the cryo-electron microscopy approach (cryo-EM) the sample is vitrified and visualized in its native state (Wang and Wang 2017). So, the resulting structure is not impaired by packing effects. As a consequence, the cryo-electron microscopy single particle analysis approach was performed to determine the structure of Meprin β with the inhibitor MWT-S-270 in its active site.

The samples were prepared as described in chapter 2.2.6.2 (pp. 32). A homogenous protein could be observed, showing triangle and diamond shape (figure 17). Different protein concentrations were tested, as well as several sample preparation techniques. Dose-fractioned movies were recorded. The data processing and optimization of the reconstruction was done at the Monash University by Dr. Charles Bayly-Jones and Dr. Christopher Lupton (laboratory of Prof. Whisstock), who kindly provided the map. The model building and refinement was done by the author of the present study. The parameters for data collection and statistics of the model building are summarized in table 23 in the appendix (p. 131).
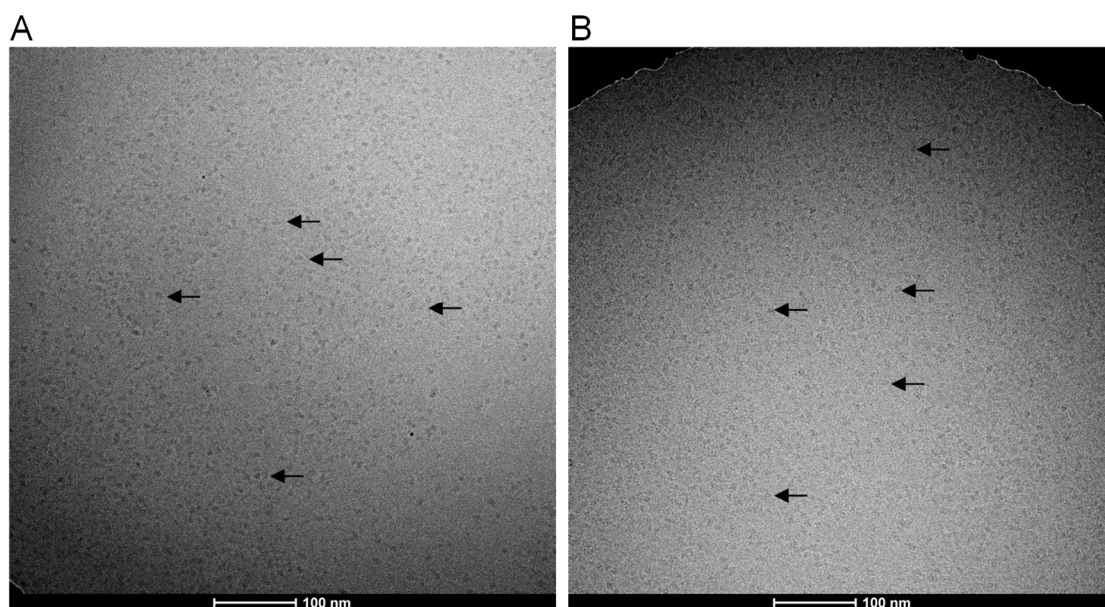
Figure 17: Cryo-EM micrographs of mature Meprin β in complex with MWT-S-270. Some Meprin β dimers are highlighted by arrows. A) Representative image of Meprin β (1 mg/ml) frozen using the Vitrobot System (glow-discharged QUANTIFOIL® Au R1.2/1.3 grid; 4°C; 100% humidity; blot force: -8, blot time: 2 s; wait time: 5 s, drain time: 1 s) recorded at a Tecnai 12 electron microscope. Data set was collected using a Titan Krios. *B)* Representative image of Meprin β (4 mg/ml) frozen using the Vitrobot System (glow-discharged QUANTIFOIL Au R1.2/1.3 grid; 4°C; 100% humidity; hand-blotted) recorded at aTecnai 12 electron microscope.
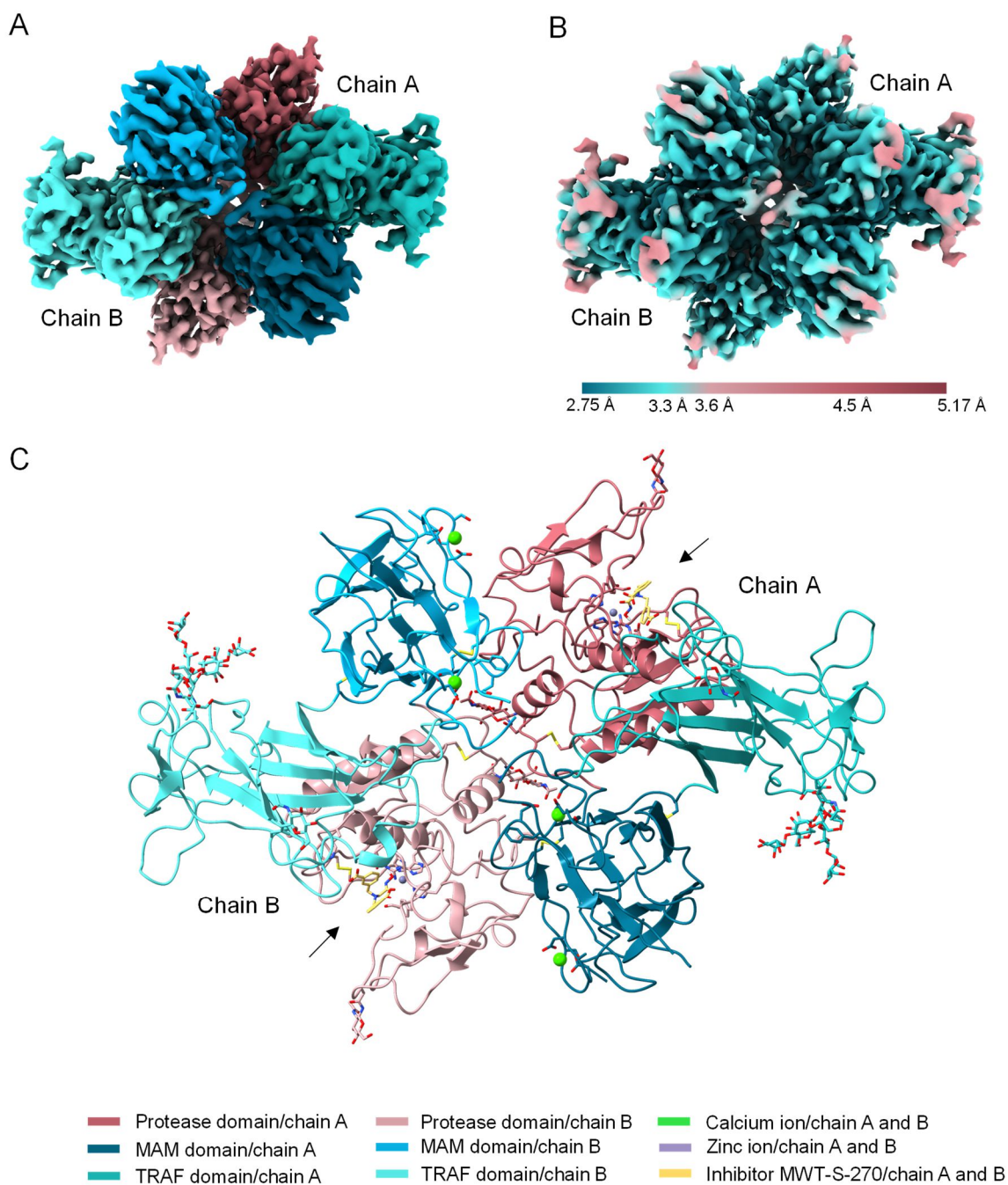
***Figure 18: Structure of Meprin β obtained by cryo-EM single particle analysis. The enzyme was vitrified in complex with MWT-S-270. The resolution of the structure is 3.0 Å. A)** Map is colored according to domain structure of Meprin β: TRAF domain P^{428}-Q^{595}, MAM domain Q^{260}-C^{427}, protease domain N^{62}-L^{259}. **B)** Reconstruction colored according to local variation in resolution by gold-standard Fourier shell correlation at 0.143. **C)** 3.0 Å structure of Meprin β colored according to domains. The active site of chain A and chain B is highlighted by an arrow. The inhibitor is highlighted in yellow. Glycolsyations are shown as sticks.*

A global resolution of 3.0 Å could be achieved. The reconstruction, consisting of two Meprin β monomers is, shown in figure 18. The domain structure of each Meprin β monomer and the local resolution are visualized by color (figure 18 A/B). As depicted in figure 18 B, the reconstruction of Meprin β shows a local resolution of 2.75-5.17 Å. The generated 3D-structure of Meprin β, colored according the domain structure, is shown in figure 18 C.

A superposition of the crystal structure and the cryo-EM structure revealed the same secondary, tertiary and quaternary structure elements of the overall structure, which is already described in chapter 3.1.4 (pp. 43). Figure 55 to 57 in the appendix (pp. 132) depict the single domains of the Meprin β structure elucidated by cryo-EM single particle analysis. Due to the lower resolution of this structure, some loop regions and the intermolecular disulfide bridge could not be determined. However, the electron density of the inhibitor MWT-S-270 within the active site is well resolved and the inhibitor was placed into the model by docking, followed by a refinement using the reconstruction of Meprin β. The placement of the inhibitor was performed in cooperation with Christian Jäger (Vivoryon AG) (figure 19) as described in chapter 2.2.6.2 (p. 33).
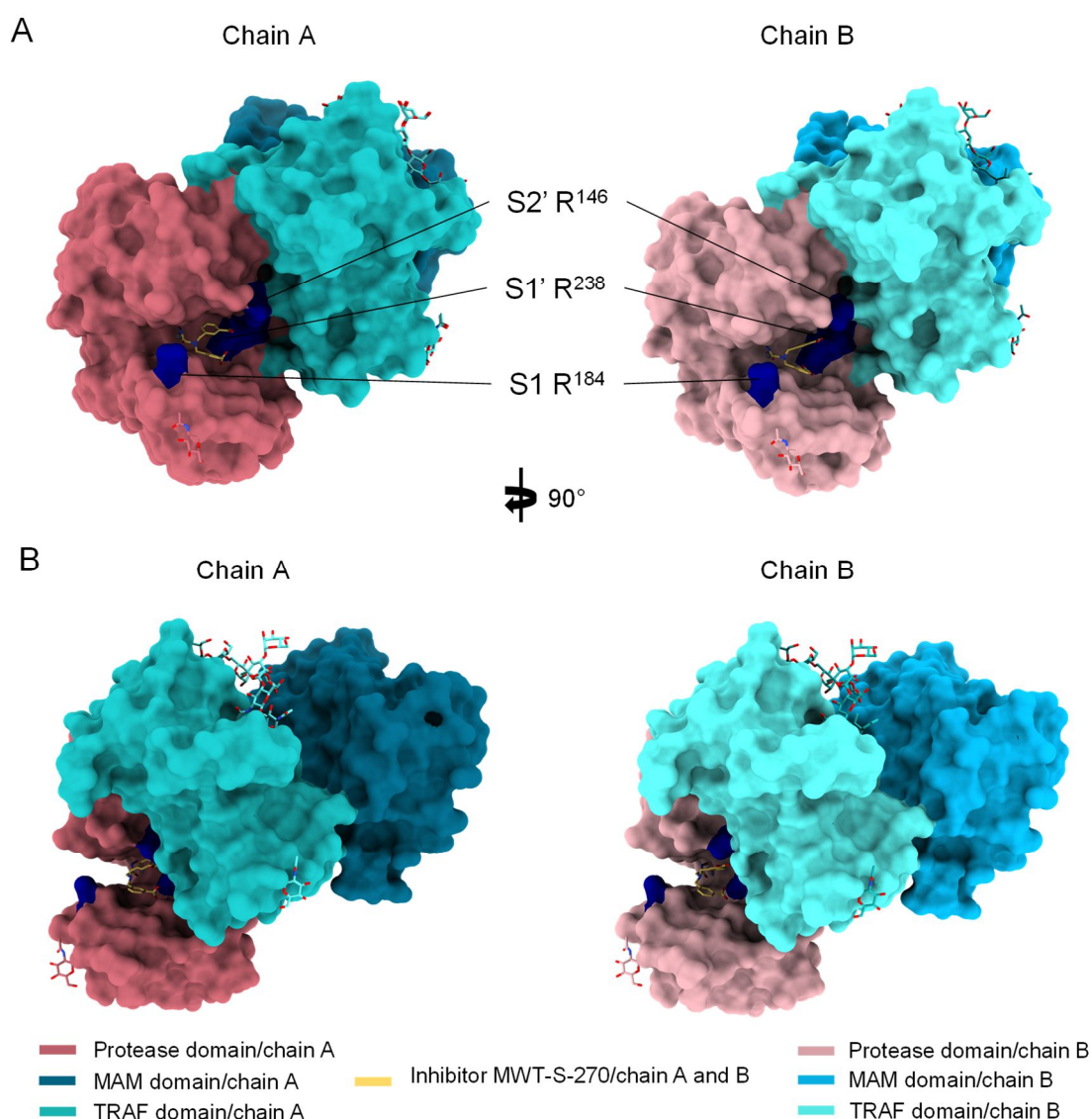
Figure 19: Structure of dimeric Meprin β, elucidated by cryo-EM single particle analysis, colored according to domain structure. A) *'Standard orientation' of chain A and chain B, representation of surface structure with view into the active cleft. The Arginine residues R^{184}, R^{238} and R^{146}, shaping the subpockets S1, S1' and S2', are colored in dark blue. The inhibitor is highlighted in yellow.* **B)** *Chain A and chain B rotated by 90° on the vertical axis.*
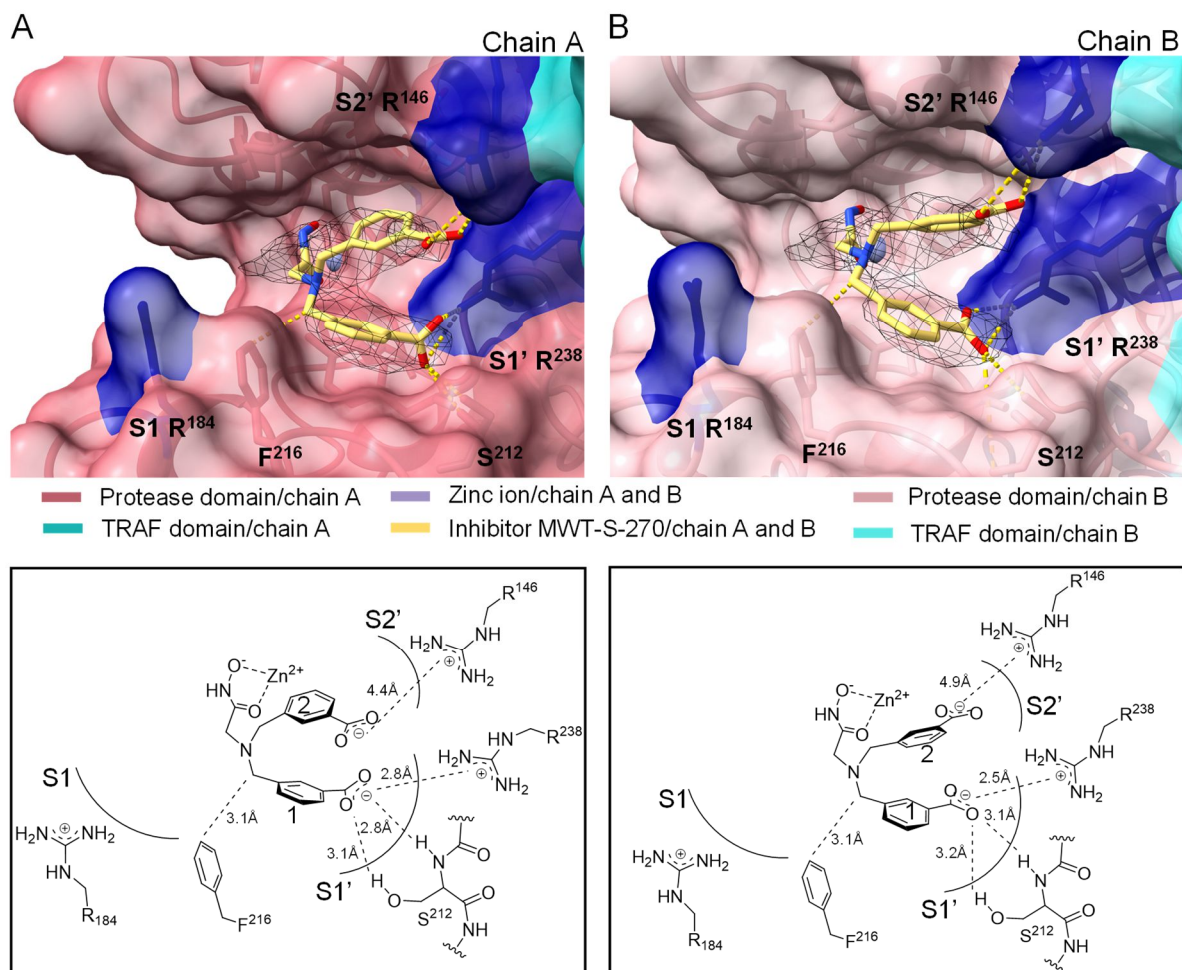
Figure 20: Active site of Meprin β in complex with its specific inhibitor MWT-S-270 as deduced from cryo-EM analysis. *Orientation of MWT-S-270 within the active site of **A)** chain A and **B)** chain B. Interactions of MWT-S-270 within chain A and chain B are also displayed in a 2D-plot. Carboxylate 1 forms an ionic interaction with R^{238} of subpocket S1', as well as a hydrogen bond with carbonyl and the backbone amide of S^{212}. Benzoic acid 2 forms an ionic interaction with R^{146} of subpocket S2'.*

The orientation of the inhibitor MWT-S-270 within chain A and chain B was elucidated (figure 19 and figure 20). In both chains, the zinc is complexed by the hydroxamic acid. The hydroxamate amide interacts with the carbonyl of C^{124} via a hydrogen bond at a distance of 3.1 Å in chain A and 3.2 Å in chain B. Additionally, the hydroxyl group of the hydroxamic acid coordinates the zinc and forms a hydrogen bond to the carboxylate of E^{153} (2.8 Å/chain A; 2.7 Å/chainB). This binding mode corroborates the results obtained by X-ray crystallography (chapter 3.1.4, pp. 43). However, the interactions of the two benzoic acid moieties differs, and is virtually identical in both chains of the cryo-EM structure. These interactions are depicted as 2D-plot in figure 20. Meta-carboxylate 1 forms an ionic interaction with the guanidine group of R^{238} (S1') and a hydrogen bond with the hydroxyl group of S^{212} within both chains. Additionally, an interaction between the meta-carboxylate 1 and the backbone amide of S^{212} within chain A and B is observed. The interactions of the benzoic acid 1 to S^{212} are also present in the crystal structure of Meprin β.

The second carboxylate group of MWT-S-270 (benzoic acid 2, figure 20) might rather interact with the guanidine group of R^{146} (S2') than with the R^{184} (S1), as it was assumed from the crystal structure.

Summarizing, significantly different conformations of the inhibitor MWT-S-270 within the crystal and the cryo-EM structure of Meprin β were observed. Generally, the electron density of the inhibitor appears better defined in cryo-EM analysis, compared to crystallography. Hence, the crystal packing might affect the conformation of the inhibitor. Additionally, within the cryo-EM Meprin β structure, R^{184} of subpocket S1 shows a different orientation as compared to the crystal structure, possibly caused by inhibitor binding. The orientation of R^{184} leads to a more 'closed' position of the active cleft (figure 19 C and figure 58 in the appendix, p. 135), again substantiating the high flexibility of R^{184} (B-factor staining, figure 57 in the appendix, p. 134).

Finally, by elucidation of the Meprin β structure in complex with its specific inhibitor by crystallography and cryo-EM, the overall structure of dimeric mature Meprin β could be determined and the interactions of the specific inhibitor MWT-S-270 within the active site were identified for the first time.

3.2 Investigations on the Structure of Meprin α

3.2.1 Heterologous Expression, Purification and Initial Characterization of Wild Type Meprin α

The binding of the selective inhibitor MWT-S-270 to Meprin β was analyzed by elucidation of the crystal and cryo-EM structures. For its isoenzyme Meprin α, such structural information is not available so far, most likely due to formation of higher order aggregates, which hampers crystallization. Upon shedding of Meprin α from the membrane during passage of the secretory pathway, oligomers (1-8 MDa) are formed by non-covalent associations of Meprin α dimers (Ishmael et al. 2006; Bertenshaw et al. 2003; Ishmael et al. 2001). Due to the high molecular mass of Meprin α oligomers, the crystal growth could be hindered. Nevertheless, endeavors were initiated to determine the structure of Meprin α in complex with its specific inhibitor MWT-S-698 and to investigate its oligomerization propensity.

Meprin α (Pro-Meprin α) was expressed as zymogen in Schneider-2 *Drosophila* cells under the control of the MT (metallothionein) promoter, enabling an induction of expression by addition of copper sulfate. The expression vector pMT/BiP/V5 harbors a C-terminally truncated Pro-Meprin α (V^{22}-S^{600}, figure 21), containing an N-terminal STREP-Tag (WSHPQFEK), the pro, protease, MAM and TRAF domain. The signal sequence of BiP (immunoglobulin binding chaperone protein) from *Drosophila* upstream of the Pro-Meprin α enables the secretion of the zymogen and immediate purification from the culture media. The expression vector was already available, the expression and purification strategy needed to be established and optimized.
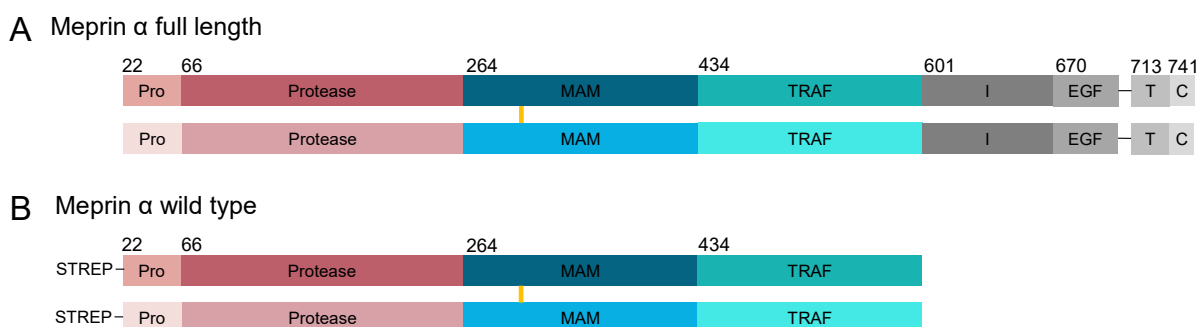
***Figure 21: Schematic illustration of the expression construct of Pro-Meprin α, naturally occurring as dimer linked by a disulfide bridge in the MAM domain. A)** Wild type Pro-Meprin α full length, including the propeptide (Pro, V^{22}-R^{65}), protease domain (N^{66}-H^{263}), meprin A5 tryrosine phosphatase µ – MAM domain (T^{264}-T^{433}), the tumor-necrosis-factor-receptor-associated factor – TRAF domain (G^{434}-S^{600}), the so called 'inserted domain' with a furin cleavage site (I, Q^{601}-Y^{669}), the epidermal growth factor like domain (EGF, F^{670}-Q^{710}), the transmembrane-domain (T, Q^{713}-L^{740}) and the cytosolic tail (C, S^{741}-K^{746}). **B)** The expressed construct was a C-terminally truncated Pro-Meprin α, including the propeptide, protease, MAM and TRAF domain (N^{66}-S^{600}).*

The expression vector was co-transfected with the selection vector pCoBlast, which harbors a blasticidine resistence gene (bsd), enabling the generation of stable cell lines by passaging the transfected cells in blasticidine containing media (described in chapter 2.2.3.2, pp. 22).

For production of Pro-Meprin α, the stably transfected cells were grown to high density in shaking flaks and the expression was induced by addition of copper sulfate. After 48 h of expression, the media was harvested and immediatly purified by hydrophobic interaction chromatography (HIC) applying the expanded bed adsorption technique (EBA). Due to a very low expression yield, three pools of protein after expression and purification by HIC were combined and subjected to affinity chromatography using a Strep-Tactin® column. Finally, Pro-Meprin α was activated using magnetic beads containing Trypsin protease. As a consequence, no further purification step for removal of Trypsin was required. The purification process was evaluated by SDS-PAGE (figure 22), protein concentration and the specific activity, as displayed in the purification table (table 7).
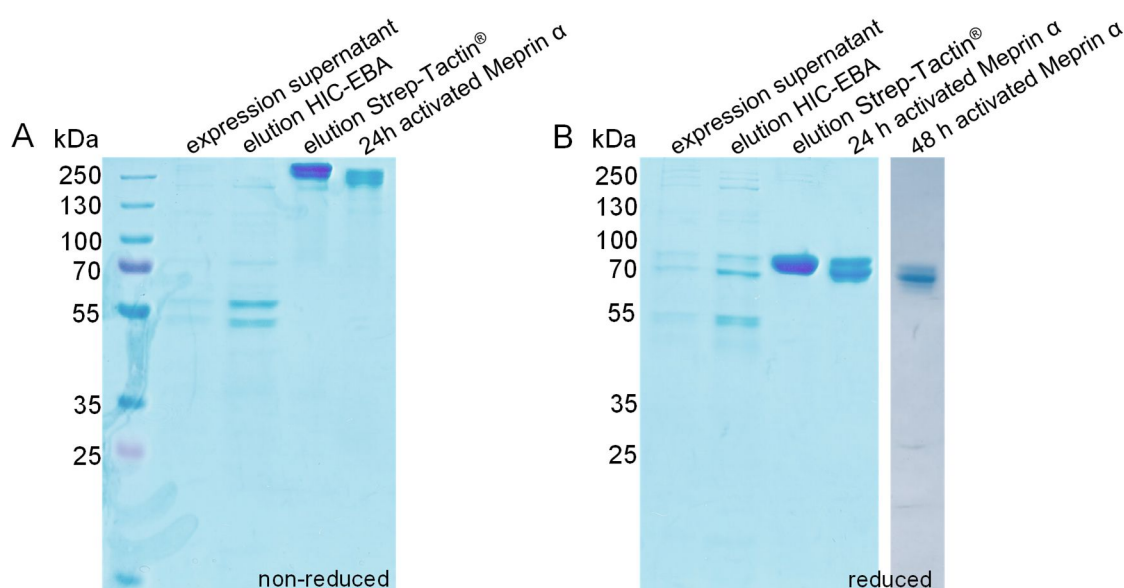
Figure 22: SDS-PAGE analysis illustrating the Meprin α purification process starting from the S2 culture medium, visualized by Coomassie-staining. *The mass shift occurring after the Strep-Tactin® column is a result of activation of Pro-Meprin α by Trypsin cleavage. 10%T acrylamide gel, 40 µl of the expression supernatant and 3 µg of protein for all other lanes were applied.* **A)** *non-reducing denaturing conditions.* **B)** *reducing denaturing-conditions.*

Table 7: Progress of purification of Pro-Meprin α from S2 culture medium (purification table). *Activity determination was performed using the fluorescence substrate Abz-YVADPK(Dnp)G-OH; assay buffer: 50 mM HEPES pH 7.4 containing 150 mM NaCl; temperature: 30°C as described in chapter 2.2.4.2 (p. 27). Before each activity determination, Pro-Meprin α was activated by Trypsin. This table represents a typical purification process after 48 h shaking flask expression of stable Pro-Meprin α expressing S2 cell line.*

Purification step	Protein concentration [mg/ml]	Protein amount [mg]	Total activity [U]	Specific activity [U/mg]	Yield [%]	Enrichment factor
Expression media (equal to three expressions)	0.04	208	46	0.2	100	1.0
Elution HIC	0.30	110	33	0.3	72	1.4
Elution Strep-Tactin®	0.32	0.6	2.4	3.7	5	17.1

As shown in figure 22 and table 7, the first column (HIC) has no positive impact on specific activity and enrichment factor. However, since the yield of Pro-Meprin α expression is very low, this column was used for capture of Meprin α. Furthermore, it was observed that the freezing of the expression media leads to reduced activity, consequently, an immediate purification after harvesting of the expression media was necessary. After purification by HIC and affinity chromatography (Strep-Tactin®), a specific activity of 3.7 U/mg and a pure Pro-Meprin α was obtained, as shown in figure 22. Finally, Pro-Meprin α was activated by Trypsin cleavage. The activation process did not result in a loss of activity. Meprin α is migrating in reducing SDS-PAGE at a mass of about 70 kDa (figure 22). The expected molecular mass of active monomeric Meprin α is 61.3 kDa (calculated by ExPASy, ProtParam tool). The difference is likely caused by glycosylation of Meprin α. Under non-reducing conditions the dimeric Meprin α should migrate at about 123 kDa to 130 kDa, but in figure 22 a band above 250 kDa is visible. This might indicate formation of non-covalently associated oligomeric Meprin α structures, as described in the literature (Bertenshaw et al. 2003; Ishmael et al. 2006).

In order to investigate the molecular state and to prove, whether non-covalently associated oligomers are formed, Pro-Meprin α and mature Meprin α were investigated by negative stain electron microscopy and cryo-EM. The micrographs are depicted in figure 23. Large flexible, helical particles were observed, which are of different length and shape (figure 23). In general, no differences between activated and Pro-Meprin α could be identified. The formation of these oligomers hampers the crystallization process, due to heterogeneity, i.e. in size of the oligomers and flexibility. In addition, the yield of heterologous expression and purification is low, which makes crystallographic approaches ineffective. Therefore, attemps were undertaken to modify the primary sequence of the protein in order to isolate dimeric Meprin α for crystallization. These are described in the following chapter 3.2.2.

A

0.05 mg/ml Meprin α wild type 0.05 mg/ml Meprin α wild type

B

0.94 mg/ml Meprin wild type 0.94 mg/ml Pro-Meprin α wild type
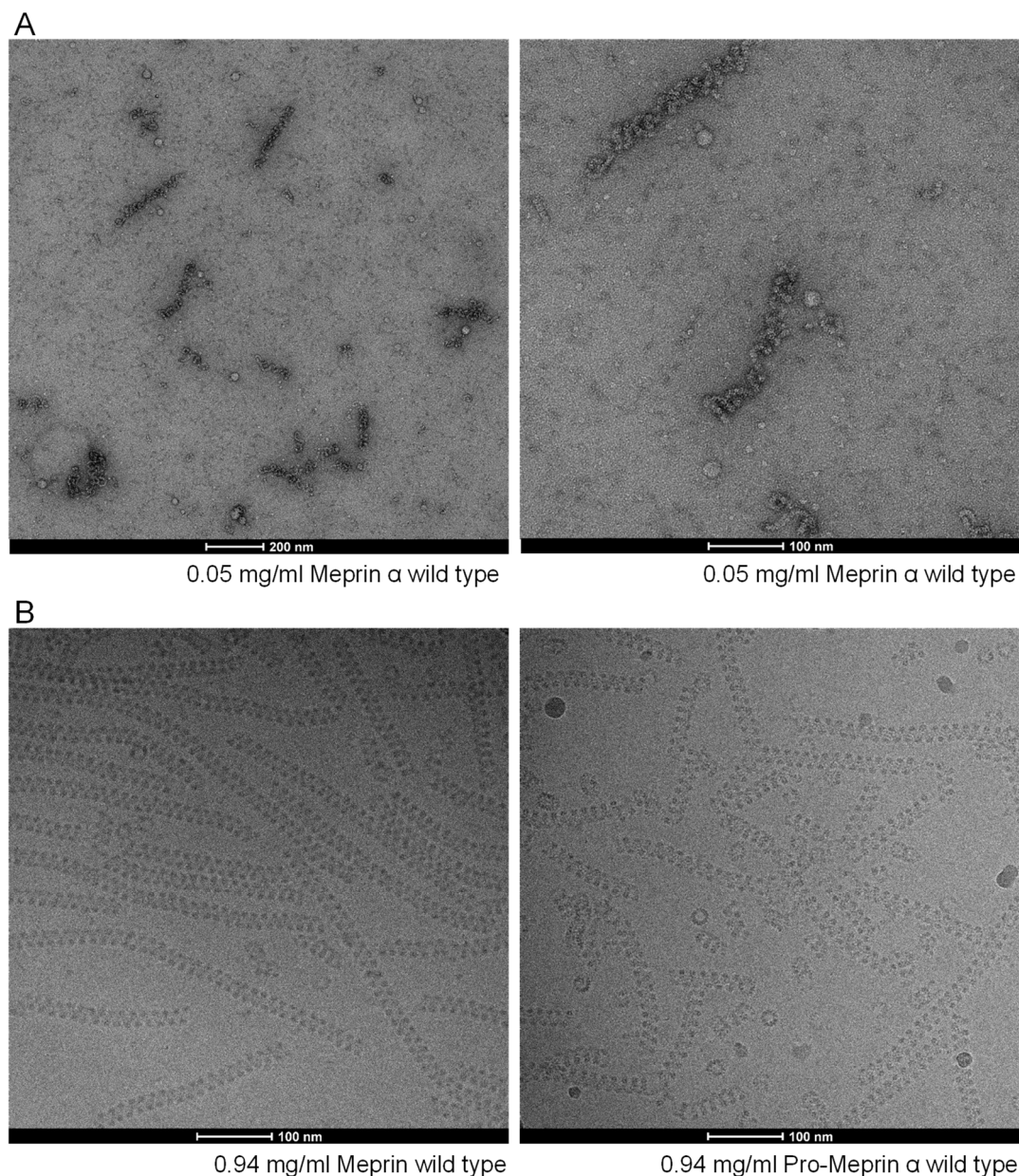
Figure 23: Electron micrographs of mature Meprin α and Pro-Meprin α. Images were recorded at a Tecnai 12 electron microscope. Glow-discharged QUANTIFOIL® Cu R2/2 grids were used. A) Representative image of negatively stained mature Meprin α (0.05 mg/ml Meprin α, 1% uranyl acetate), large helical particles were observed. B) Representative image of mature Meprin α (left) and Pro-Meprin α (right) (0.94 mg/ml) frozen using the Vitrobot System (glow-discharged; 4°C; 100% humidity; blot force: -8, blot time: 2 s; wait time: 5 s, drain time: 1 s). Large Meprin α helices were observed as well, no single molecules noted. Helices are of flexible length and shape.

3.2.2 Heterologous Expression, Purification and Initial Characterization of Meprin α Variants

As described in chapter 3.2.1 (pp. 53), mature Meprin α and Pro-Meprin α were investigated using cryo-EM. The observed oligomeric structures may occur through non-covalent association of Meprin α dimers, as stated in the literature (Bertenshaw et al. 2003; Broder and Becker-Pauly 2013). At least for recombinant murine Meprin α, different reasons for the oligomerization were stated, among those intermolecular disulfide bonds in the MAM domain (Ishmael et al. 2001; Marchand et al. 1996) and glycosylations (Ishmael et al. 2006).

The isoenzyme Meprin β is not forming oligomers in the MDa range, as proven by cryo-EM (chapter 3.1.5, figure 17, p. 48) and described in the literature previously (Bertenshaw et al. 2003). The analysis of the Meprin β structures described in chapter 3.1.4/3.1.5 (pp. 43) and the previously published observations (Arolas et al. 2012), suggest Meprin β as being a highly glycosylated protease. Possibly, these flexible and bulky glycan chains prevent Meprin β from oligomerization. Consequently, a sequence alignment of human Meprin α and human Meprin β using the webserver Clustal Omega (McWilliam et al. 2013) was performed to identify differences in the protein sequence. The analysis was primarily focused on identification of different glycosylations sites. The result is depicted in figure 24.

```
MepB:  MDLWNLSW-FLFLDAL------LVISGLATPENFDVDGGMDQDIFDINEGLGLDLFEGDI    53
MepA:  -MAWIRSTCILFFTLLFAHIAAVPIKYLPEENVHDADFGEQKDISEINLAAGLDLFQGDI    59
         *   *   :**:   *         : *. *     : .*.* * ::** :**  . *****:***
MepB:  RLDRAQIRNSIIGEKYRWPHTIPYVLEDSLEMNAKGVILNAFERYRLKTCIDFKPWAGET   113
MepA:  LLQKS--RNGLRDPNTRWTFPIPYILADNLGLNAKGAILYAFEMFRLKSCVDFKPYEGES   117
         *::::   **.:  .  : **  : ***:* *.* :**** .** *** :***:*:****: **:
MepB:  NYISVFKGSGCWSSVGNRRVGKQELSIGANCDRIATVQHEFLHALGFWHEQSRSDRDDYV   173
MepA:  SYIIFQQFDGCWSEVGDQHVGQ-NISIGQGCAYKAIIEHEILHALGFYHEQSRTDRDDYV   176
         .**  . :  .****.**::**: ::*** .*   *  ::**:*****:*****:******
MepB:  RIMWDRILSGREHNFNTYSDDISDSLNVPYDYTSVMHYSKTAFQN-GTEPTIVTRISDFE   232
MepA:  NIWWDQILSGYQHNFDTYDDSLITDLNTPYDYESLMHYQPFSFNKNASVPTITAKIPEFN   236
         .* **:**** :***:**.*.:  .**.**** *:***.  .  :*::  .:  ***.::* :*:
MepB:  DVIGQRMDFSDSDLLKLNQLYNCSSSLSFMDSCSFELENVCGMIQSSGDNADWQRVSQVP   292
MepA:  SIIGQRLDFSAIDLERLNRMYNCTTTHTLLDHCTFEKANICGMIQGTRDDTDWAHQDSAQ   296
         .:****:***   ** :**::***::   :::* *:**  *:*****.: *::** :  ...
MepB:  RGPESDHSNMGQCQGSGFFMHFDSSSVNVGATAVLESRTLYPKRGFQCLQFYLYNSGSES   352
MepA:  -AGEVDHTLLGQCTGAGYFMQFSTSSGSAEEAALLESRILYPKRKQQCLQFFYKMTGSPS   355
          . *  **: :*** *.:.**:*.:** ..  :*:**** ***** *****:   :** *
MepB:  DQLNIYIREYSADNVDGNLTLVEEIKEIPTGSWQLYHVTLKVTKKFRVVFEGRKGSG-AS   411
MepA:  DRLVVWVRRDDSTGNVRKLVKVQTFQGDDDHNWKIAHVVLKEEQKFRYLFQGTKGDPQNS   415
         *:*  :::*. .: .   :*. *: ::    .*:: **.** :*** :*:* **.   *
MepB:  LGGLSIDDINLSETRCPHHIWHIRNFTQFIGS--PNGTLYSPPFYSSKGYAFQIYLNLAH   469
MepA:  TGGIYLDDITLTETPCPTGVWTVRNFSQVLENTSKGDKLQSPRFYNSEGYGFGVTLYPNS   475
         ** : :****.*:** ** :* :***:*.:  .   ...* ** **.*:**.* : *
MepB:  VTN---AGIYFHLISGANDDQLQWPCPWQQATMTLLDQNPDIRQRMSNQRSITTDPFM--   524
MepA:  RESSGYLRLAFHVCSGENDAILEWPVENRQVIITILDQEPDVRNRMSSSMVFTTSKSHTS   535
         .    : **: ** **  *:** :*. :*:***:**:*:***.. .:**.
MepB:  TTDNGNYFWDRPSKVGTVALFSNGTQFRRGGGYGTSAFITHERLKSRDFIKGDDVYILLT   584
MepA:  PAINDTVIWDRPSRVGTYHTD---CNCFRSIDLGWSGFISHQMLKRRSFLKNDDLIIFVD   592
         : *.. :*****:*** :   * .    * .. * *.**:*: ** *.*:*.**: *::
MepB:  VEDISHLNSTQ   595
MepA:  FEDITHLS     600
         .***:**.
```

Propeptide   Protease domain   MAM domain   TRAF domain

Figure 24*: **Sequence alignment of human Meprin α (MepA, UniProt: Q16819, amino acids M¹ to S⁶⁰⁰) and human Meprin β (MepB, UniProt: Q16820, amino acids M¹ to Q⁵⁹⁵) using the webserver Clustal Omega (McWilliam et al. 2013)**. Identical amino acids are marked by ***, amino acids with similar feature are marked by :, amino acids with less similarity are marked by ... Amino acids are colored according to the domain structure: All potential glycosylation sites are highlighted in red, the underlined and bold glycosylation sites are present in Meprin β, but not in Meprin α. Glycosylation sites with grey background have been introduced in Meprin α to generate the two mutants: R372T and F560T.*

A sequence identity of 46% for human Meprin α and human Meprin β was determined. Analyzing the sequence alignment with regard to N-linked glycosylation sites (N-X-T/S motif, highlighted in red, figure 24), obviously most of the glycosylation sites occur in both enzymes. By paying attention to the glycosylations present in Meprin β, but not in Meprin α, three potential glycosylation sites are determined, two in the MAM domain and one in the TRAF domain:

- N^{370} (MAM domain) in Meprin β, corresponding asparagine in Meprin α N^{370}
- N^{421} (MAM domain) in Meprin β, no corresponding asparagine in Meprin α
- N^{547} (TRAF domain) in Meprin β, corresponding asparagine in Meprin α N^{558}.

The glycosylation site N^{421}, present in Meprin β, is in the 3D-structures (chapter 3.1.4/3.1.5, pp. 43 and PDB: 4GWM) located within the MAM domain and not exposed to the surface of the protein, in accordance this potential glycosylation site is not glycosylated. Since the homology model of Meprin α seems to be very similar to the structures of Meprin β (Tan et al. 2018), it can be assumed that the same region in Meprin α is buried within the structure as well, and consequently can not be involved in non-covalent interactions between Meprin α dimers. In contrast, the glycosylation sites N^{370} (MAM domain) and N^{547} (TRAF domain) are actually glycosylated in the Pro-Meprin β structure 4GWM (Arolas et al. 2012). Thus, it was hypothesized, that the introduction of these two glycosylation sites in Meprin α, at N^{370} in the MAM domain and N^{558} in the TRAF domain, may interfere with its the oligomerization propensity.

Additionally, C^{308}, which is most likely responsible for dimer formation will be exchanged to Alanine in order to obtain Meprin α monomers. This was previously described for murine Meprin α (Marchand et al. 1996). Consequently, three different mutants of human Meprin α were produced. The expression constructs for these protein variants are depicted in figure 25.
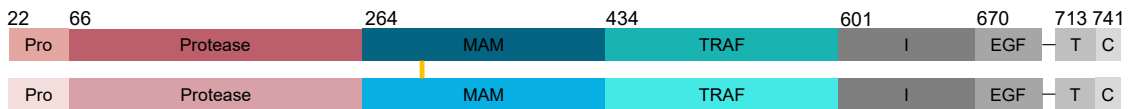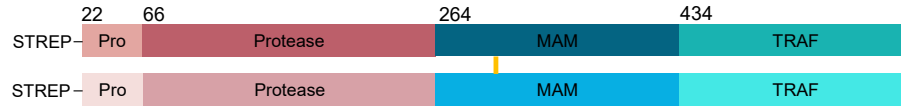
Figure 25: Scheme of wild type Meprin α and Meprin α variants for heterologous expression. *Three mutations were introduced in order to prevent oligomer formation of Meprin α. Variant C308A may lead to formation of monomers. The other two mutants introduce N-glycosylation sites, which should lead to generation of dimers similar to Meprin β.*

Two mutants were generated by insertion of glycosylation sites (by mutation, to obtain the motif for N-linked glycosylation: N-X-T) and one by exchange of the Cysteine responsible for disulfide bond formation between two Meprin α monomers:

- C308A, prevention of the intermolecular disulfide formation, may result in monomeric Meprin α

- R372T, insertion of a glycosylation site at N^{370}; corresponding to the glycosylation site N^{370} in Meprin β

- F560T, insertion of a glycosylation site at N^{558}; corresponding to the glycosylation site N^{547} in Meprin β.

In order to heterologously express the Meprin α mutants, a site-directed mutagenesis PCR of the previously described expression vector pMT-hMepA-NStrep was performed (chapter 3.2.1, pp. 53; appendix table 15, p. 124). For each construct, a stable S2 cell line was established by co-transfection with the selection vector pCoBlast and passaging the transfected cells in blasticidine containing media. An initial test expression in small scale was executed to prove the heterologous expression and secretion of the Meprin α variants (described in chapter 2.2.2.3, p. 20). As a positive control, the C-terminally truncated Meprin α without mutations, referred to as wild type Meprin α, was used (expression and purification described in chapter 3.2.1, pp. 53). The media were harvested and investigated using Western blot analysis under reducing denaturing, non-reducing denaturing and native conditions. The results are depicted in figure 26.
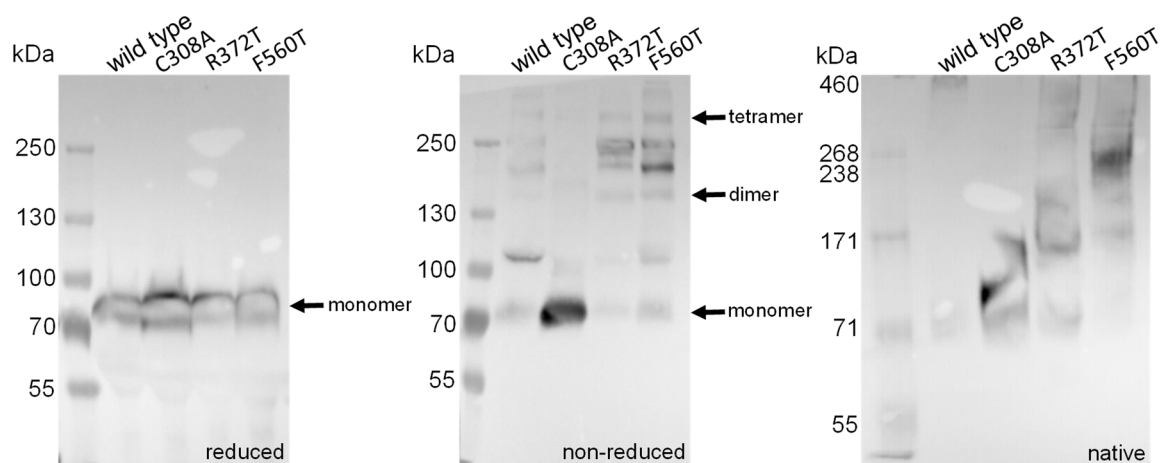
Figure 26: Western blot analysis of Pro-Meprin α variants after small-scale expression. *Samples were seprated in 7%T SDS-PAGE under reducing denaturing, non-reducing denaturing and native conditions, followed by Western blot, detection with primary antibody goat-anti-human Meprin α and secondary antibody anti-goat-HRP using chemiluminescence. Meprin α monomers and putative dimers and tetramers are highlighted by arrows. In each lane 40 µl of expression supernatant were applied.*

In reducing SDS-PAGE (figure 26), the monomeric Pro-Meprin α at an expected molecular mass of about 70 kDa is observed for all expressed Pro-Meprin α variants. Consequently, the introduced mutations did not interfere with secretion of Pro-Meprin α into the medium. In order to prove, if dimeric or oligomeric forms of Pro-Meprin α were secreted, a non-reducing SDS-PAGE was performed. The wild type Pro-Meprin α exhibits several bands at high molecular mass, most likely caused by oligomerization, as already observed for purified wild type Pro-Meprin α (chapter 3.2.1, figure 22, p. 54) and cryo-EM (chapter 3.2.1, figure 23, p. 56). As a consequence of the exchange of the Cysteine at position 308 to Alanine, a monomeric form of Pro-Meprin α seemed to be expressed, due to the single band at 70 kDa, visible in the non-reducing SDS-PAGE. For the mutants R372T and F560T, which led to the introduction of glycosylation sites at N^{370} and N^{558}, several bands at high molecular mass could be observed, similar to the pattern observed for wild type Pro-Meprin α.

To obtain information about the migration behavior of the different variants in comparison to the wild type Pro-Meprin α, which forms large helical structures, a native-PAGE was performed. For wild type Pro-Meprin α a very faint band at the top of the separating gel was obtained (figure 26, native, wild type). The C308A mutant shows the fastest migration within the gel, followed by R372T and F560T. It was assumed, that because of the exchange of the Cysteine, involved in intermolecular disulfide bridge formation, a monomeric form of Pro-Meprin α is expressed (C308A). Due to the different migration behavior of mutant R372T and F560T in native-PAGE it was further assumed, that the R372T mutation may led to a dimeric or tetrameric Pro-Meprin α and the F560T mutation to a Pro-Meprin α tetramer or higher order structure.

Because of these assumptions, the mutant C308A and R372T were selected for further investigations on activity and stability. For production of Pro-Meprin α C308A and Pro-Meprin α R372T, stably transfected cells were grown to high density in shaking flaks and the expression was induced by addition of copper sulfate. After 48 h of expression, the medium was harvested and immediatly purified by one affinity column, the Strep-Tactin® column, leading to pure Pro-Meprin α. Finally, Pro-Meprin α C308A and Pro-Meprin α R372T, were activated to mature Meprin α by Trypsin cleavage. Followed by a dialysis in 30 mM TRIS pH 7.4 buffer containing 150 mM NaCl, in order to exchange the desthiobiotin, which is present in the elution buffer used for the Strep-Tactin® column. The purification process was evaluated by SDS-PAGE (figure 27), protein concentration and determination of the specific activity, as displayed in the purification table (table 8).
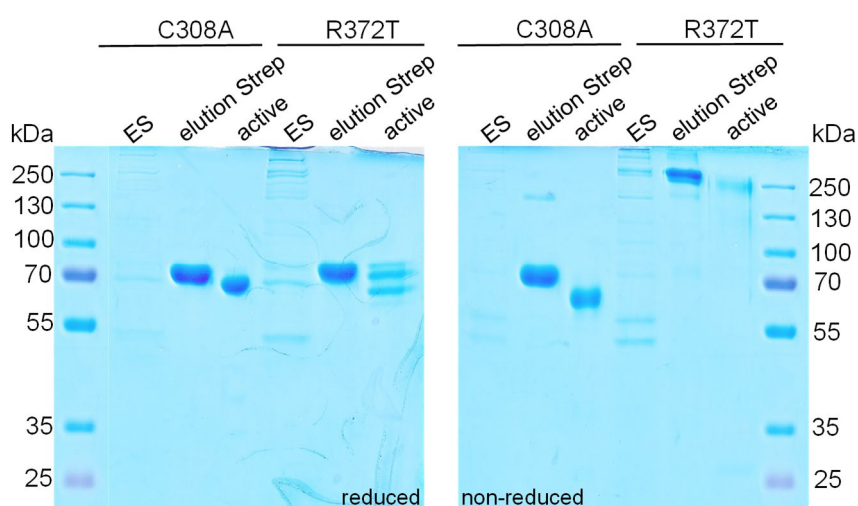
Figure 27: SDS-PAGE analysis illustrating the Meprin α C308A and R372T purification process starting from the expression media. *Samples were separated in 10%T SDS-PAGE under reducing and non-reducing conditions. 40 µl of the expression supernatant and 3 µg of protein for all other samples were applied. Mass shift occurring after Strep-Tactin® eluted fractions is due to activation of Pro-Meprin α by Trypsin cleavage. ES: expression supernatant, elution Strep: elution fraction of Strep-Tactin® column, active: activated, mature Meprin α variant (after Mag-Trypsin cleavage).*

Table 8: Progress of purification of Pro-Meprin α C308A and R372T from S2 expression media (purification table). Determination of enzymatic activity was performed using the fluorescence substrate Abz-YVADPK(Dnp)G-OH, assay buffer: 50 mM HEPES pH 7.4 containing 150 mM NaCl; temperature: 30°C. Before each activity determination, the Pro-Meprin α variants were activated by Trypsin. This table represents a typical purification process after expression of Pro-Meprin α C308A and R372T in shake flasks for 48 h.

Purification step C308A	Protein concentration [mg/ml]	Protein amount [mg]	Total activity [U]	Specific activity [U/mg]	Yield [%]	Enrichment factor
Expression media	0.05	80.99	26.4	0.3	100	1
Elution Strep-Tactin®	0.34	0.31	0.9	3.0	4	9
Dialysis	0.29	0.26	1.5	5.7	6	17
Purification step R372T	Protein concentration [mg/ml]	Protein amount [mg]	Total activity [U]	Specific activity [U/mg]	Yield [%]	Enrichment factor
Expression media	0.11	195.2	28.4	0.1	100	1
Elution Strep-Tactin®	0.18	0.6	1.3	2.1	5	14
Dialysis	0.09	0.4	2.0	4.8	7	33

After one-step purification, as shown in figure 27, both variants were pure and appeared as a single band in the SDS-PAGE under reducing as well as non-reducing conditions. For the mutant C308A, a single band at 70 kDa in reducing and non-reducing SDS-PAGE is observed. This confirms the results obtained from the test expression, as described above, and led to the assumption that a monomeric Pro-Meprin α was secreted. The mutant R372T shows a single band at 70 kDa in reducing SDS-PAGE, and a band above 250 kDa under non-reducing-denaturing conditions. This may corresponds to a tetrameric form of Pro-Meprin α.

The next step included the activation of the Pro-Meprin α C308A and R372T with magnetic Trypsin beads for 60 min at room temperature, followed by a dialysis in 30 mM TRIS pH 7.4 buffer containing 150 mM NaCl. The Trypsin treatment resulted in a single band of activated Meprin α C308A (figure 27). For activated Meprin α R372T, three bands were observed (figure 27, reducing), which may indicate a heterogeneity of R372T due to different glycoforms, an incomplete activation by Mag-Trypsin or partial degradation of Meprin α R372T during the Trypsin digest. Finally, the specific activity of Meprin α C308A and R372T is 5.7 U/mg and 4.8 U/mg, respectively.

For determination of the molecular mass of both Meprin α mutants, a MALDI-TOF mass spectrometry (MS) analysis was performed. For comparison, the wild type Meprin α was investigated as well. The purified samples (ZipTip® C4) were analyzed in linear positive mode, the spectra are depicted in figure 28. The calculated and experimentally determined molecular masses (MW) of the Pro-Meprin α and mature Meprin α variants are listed in table 9.
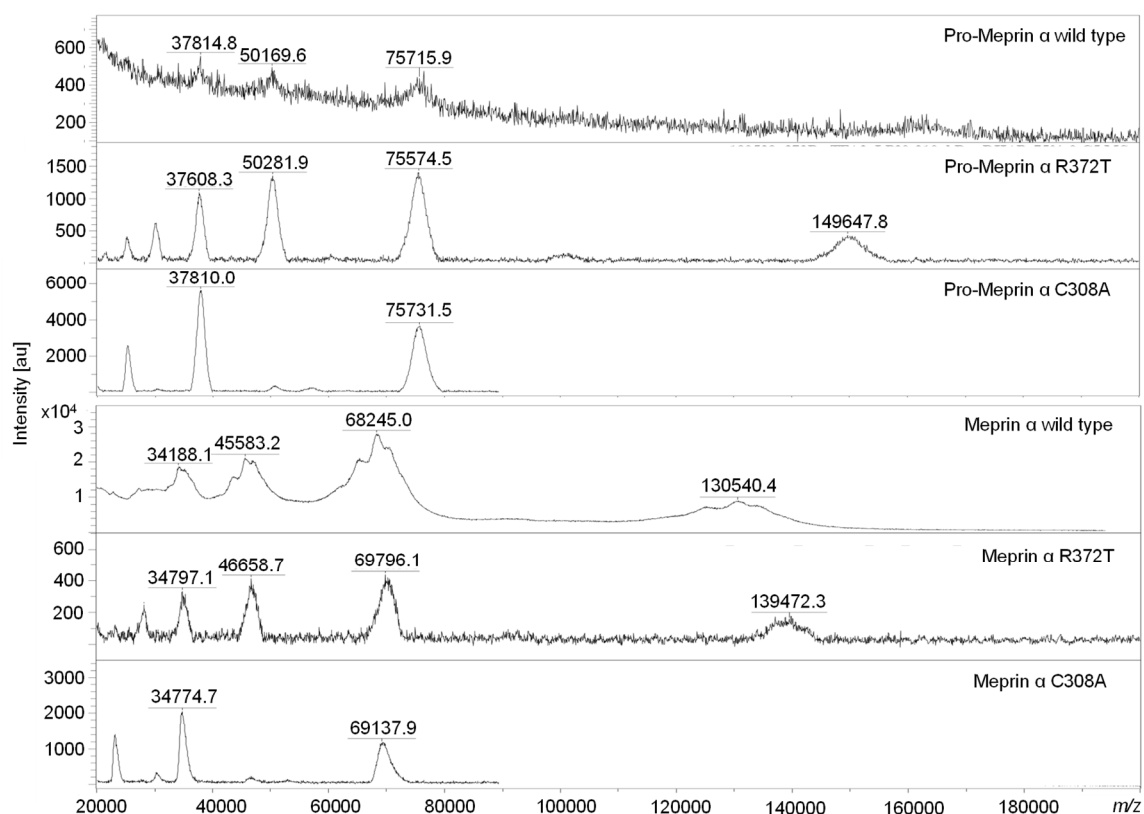
Figure 28: MALDI-TOF analysis of Meprin α wild type, Meprin α C308A and Meprin α R372T, before (zymogen) and after Trypsin cleavage (mature form). *The samples were purified before analysis using ZipTip® C4. Peaks of about 75 kDa (Pro-Meprin α variants) and 69 kDa (active Meprin α variants) equal [M+H]+ or [M+2H]+, peaks of about 38 kDa (Pro-Meprin α variants) and 35 kDa (Meprin α variants) equal [M+2H]2+. A spectrum for Meprin α C308A covering the mass range from 90 to 200 kDa was determined as well and no peaks could be observed (not shown).*

Table 9: Tabular summary of the MALDI-TOF MS analysis results. *The inactive and mature Meprin α wild type (Pro-wt, wt), R372T (Pro-R372T, R372T) and C308A (Pro-C308A, C308A) were investigated in linear positive mode after purification using ZipTip® C4. The m/z values interpreted for monomeric and dimeric zymogen and active Meprin α variants are listed.*

Pro-Meprin α/ Meprin α variant	m/z values of monomeric Meprin α					m/z values of dimeric Meprin α		
Variant	MW [Da]	[M+H]+ [Da]	[M+2H]2+ [Da]	[2M+H]+ [Da]	[M+3H]3+ [Da]	[M+H]+ [Da]	[M+2H]2+ [Da]	[M+3H]3+ [Da]
Pro-wt	67783.8	75715.9	37814.8	-	50169.6	-	75715.9	50169.6
Pro-R372T	67728.7	75574.5	37608.3	149647.8	50281.9	149647.8	75574.5	50281.9
Pro-C308A	67751.7	75731.5	37810.0	-	-	-	-	-
wt	61250.4	68245.0	-	130540.4	45583.2	130540.4	68245.0	45583.2
R372T	61195.3	69796.1	34797.1	139472.3	46658.7	139472.3	69796.1	46658.7
C308A	61218.4	69137.9	34774.7	-	-	-	-	-

The putative single charged ion peak of all Pro-Meprin α variants shows a mass of about 75 kDa. The corresponding single charged ion peak for mature Meprin α variants is at about 69 kDa. In case of active Meprin α wild type and active Meprin α R372T, an additional peak was observed at about 130 kDa, which most likely represents the single charged ion peak of dimeric Meprin α ([M+H]$^+$). Hence, the peaks at 75/69 kDa could be caused by [M+2H]$^{2+}$. The peak at 130 kDa peak was not observed in the spectrum of Meprin α C308A, as a measurement up to 200 kDa was performed. For all variants of Pro-Meprin α and active Meprin α the determined molecular mass is about 8 kDa higher than the calculated mass (Expasy, Prot Param tool). This is likely caused by glycosylations present on the enzymes, because the same mass difference is observed for the zymogen and the mature Meprin α. A deglycosylation of Meprin α C308A was executed and resulted in a mass shift of about 8 kDa, observed using SDS-PAGE (data not shown), unfortunately the deglycosylated enzyme could not be detected in MALDI-TOF MS analysis. For approvement of the obtained MALDI-TOF results and to determine a mass or mass range of the variants C308A and R372T, a SEC-MALS (Size exclusion chromatography – Multi-angle light scattering) analysis was performed. The results are shown in figure 29.
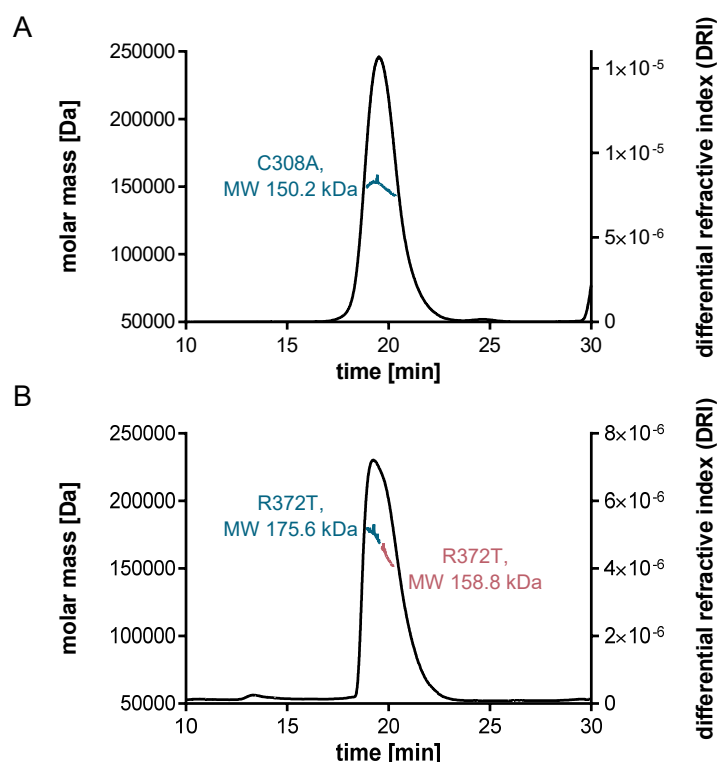
Figure 29: SEC-MALS analysis of Pro-Meprin α variants C308A and R372T. *Molecular masses [Da] and DRI are plotted against time [min]. Pro-Meprin α C308A and R372T form dimeric structures, whereas for C308A a homogenous peak was observed, for R372T a heterogenous peak was detected, including two forms of dimeric Pro-Meprin α R372T. For mutant C308A a molar mass of 150.2 kDa was determined. For mutant R372T a mass range between 175.6 to 158.8 kDa was obtained. The data was analyzed by Astra 6 software (Wyatt Technology Corporation).*

For each variant a major peak, eluting at 18.5 min, was detected. However, in SEC-MALS analysis the molecular mass is determined independently of the elution time, by taking multi-angle light scattering, UV_{280} and the change in differential refractive index (DRI) into account. For Pro-Meprin α C308A, a molecular mass of 150.2 kDa±0.657% was determined. The sample seemed to be homogenous, since one major peak was detected. In case of Pro-Meprin α R372T one broad peak with two maxima was observed, leading to the assumption, that the sample is heterogenous. The first part of the peak was evaluated and a molecular mass of 175.6 kDa±0.94% was determined. For the second part of the peak a molecular mass of 158.8 kDa±0.85% was determined. Consequently, a mass range of 176 to 159 kDa can be assumed for Pro-Meprin α R372T. Both Pro-Meprin α variants seemed to occur as dimers, although the SDS-PAGE analysis of Meprin α C308A indicated that a monomeric form of Meprin α was secreted (figure 26 and figure 27, pp. 60). Possibly, C308A forms non-covalently associated dimers in solution.

For further investigations on the molecular state of both variants, Meprin α C308A and R372T were investigated by cryo-EM, images are shown in figure 30. According to the electron micrographs of Meprin α C308A and R372T, both variants do not form helical structures, as observed for the Meprin α wild type (figure 30). Consequently, the mutation at C308A, in order to delete the intermolecular disulfide bridge, and the mutation R372T, to introduce the glycosylation site at N^{370}, lead to dimeric forms of Meprin α, confirmed by the SEC-MALS results. This can be further verified, because the size of both mutants in cryo-EM images appears to be the same size observed for the isoenzyme Meprin β, which is known to occur as dimer (chapter 3.1, pp. 35). Nevertheless, as shown in figure 30 B, Meprin α C308A dimers are still associating with each other, forming ring like structures, especially at higher concentrations. The association of the dimeric structure is also observed for Meprin α R372T, but less pronounced (figure 30 D), which might be due to lower protein concentration.

A
0.12 mg/ml Meprin α C308A

B
0.77 mg/ml Meprin α C308A

C
0.15 mg/ml Meprin α R372T

D
0.15 mg/ml Meprin α R372T

E
0.94 mg/ml Meprin α wild type
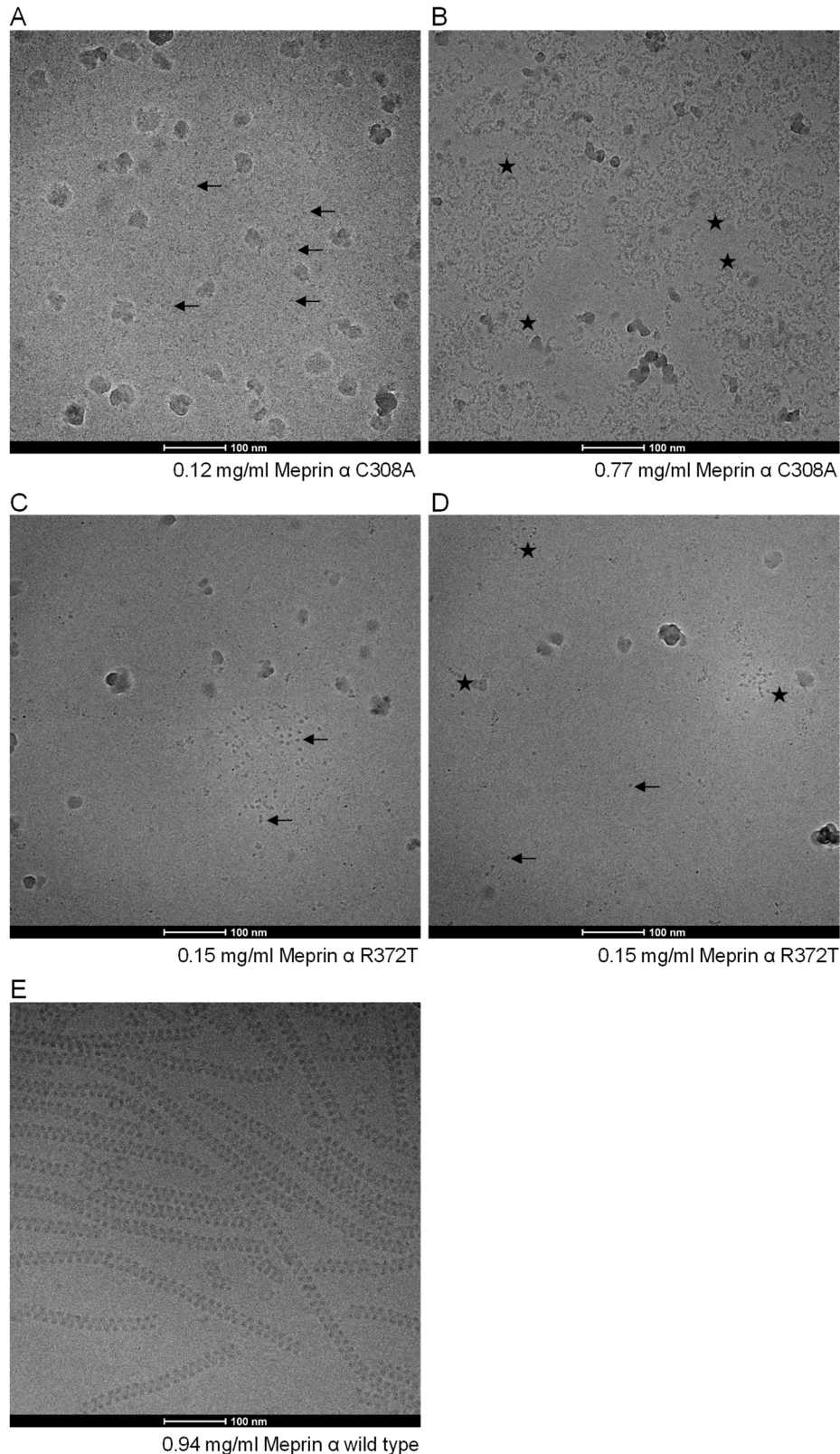
Figure 30: Electron micrographs of mature Meprin α C308A and R372T. *Images were recorded at a Tecnai 12 electron microscope. Glow-discharged QUANTIFOIL® Au R1.2/1.3 grid used for A, C and D; Cu R2/2 grid used for B and E. The samples were frozen using the Vitrobot System (4°C, 100% humidity). Both Meprin α variants occur as putative dimers (marked by arrows), which have the tendency to associate (marked by asterisks).* **A)** *0.12 mg/ml Meprin α C308A (blot force: -8, blot time: 2 s; wait time: 5 s, drain time: 1 s).* **B)** *0.77 mg/ml Meprin α C308A (blot force: -5, blot time: 2.5 s; drain time: 1 s).* **C)** *0.15 mg/ml Meprin α R372T (blot force: -8, blot time: 2 s; wait time: 5 s, drain time: 1 s).* **D)** *0.15 mg/ml Meprin α R372T (blot force: -8, blot time: 2 s; wait time: 5 s, drain time: 1 s).* **E)** *0.94 mg/ml wild type Meprin α (blot force: -8, blot time: 2 s; wait time: 5 s, drain time: 1 s).*

Summarizing, by introducing the mutations C308A and R372T, the helix formation of wild type Meprin α could be prevented and dimeric structures for both mutants were observed (SEC-MALS data, figure 29 and cryo-EM images, figure 30). Whereas R327T dimers are linked by the intermolecular disulfide bridge at C^{308}, Meprin α C308A dimers are most likely formed by non-covalent interactions. Both variants still have the tendency to associate in ring-like structures, which leads to the assumption, that more interaction sites between Meprin α dimers are involved in the formation of the oligomeric helical structures, than the ones exchanged within these mutants. This leads to heterogeneity within the quaternary structures of the variants R372T and C308A, as shown by cryo-EM (figure 30). Additonally, by SEC-MALS analysis inhomogeneity of the variant R372T was detected, maybe caused by heterogenous glycosylation of the protease (figure 29).

Although the crystallography approach might lead to higher resolution of Meprin α in complex with its specific inhibitor MWT-S-698, the heterogeneity of the sample might interfere with the crystallization process. Additonally, the expression yield of both variants is still very low.

Hence, single particle analysis cryo-electron microscopy, which is a method suitable for proteins of high molecular mass (Zanotti 2016), was chosen for structural elucidation of Meprin α. Additionally, a low protein amount is required for this method. Furthermore, cryo-electron micrographs were recorded in advance and this technique was applicable for imaging of wild type Meprin α. As a consequence, and to determine the structure of mature wild type Meprin α in complex with its specific inhibitor, different sample preparation conditions were tested. Several data sets were collected on a Titan Krios (Meprin α-MWT-S-698, Pro-Meprin α, mature Meprin α, Meprin α-MWT-S-959). Dose-fractioned movies were processed, the parameters for data collection and model building are summarized in the appendix in table 24 (p. 136), the structure is presented in the following chapter 3.2.3.

3.2.3 Structure Elucidation of Meprin α Wild Type in Complex with the Specific Inhibitor MWT-S-698 by Single Particle Cryo-Electron Microscopy

Since Meprin α wild type forms helical oligomeric structures, which hamper the crystallization process, endeavors to produce a crystallizable dimeric Meprin α were undertaken and led to the generation of Meprin α dimers. Both Meprin α variants show heterogeneity in their quaternary structures mediated by formation of ring-linke structures at higher protein concentration. Furthermore, the expression yield is very low. Hence, both variants were not applied for crystallography. As a consequence, oligomeric Meprin α wild type was used for structural elucidation by cryo-EM single particle analysis, which is a suitable approach for large protein samples (Zanotti 2016).

For the structure of Meprin α with the specific inhibitor MWT-S-698 in the active site, a global resolution of 2.42 Å could be achieved. By particle extraction within 400 pixel boxes, including four monomers of Meprin α, the reconstruction of this helical particle could be generated by a single particle analysis approach (figure 31). The data processing and optimization of the reconstruction was done at the Monash University by Dr. Charles Bayly-Jones and Dr. Christopher Lupton (laboratory of Prof. Whisstock), who kindly provided the map. The model building and refinement was done by the author of the present study. The statistics of the data collection and refinement are listed in table 23 in the appendix (p. 136).

The obtained cryo-EM reconstruction is shown in figure 31 A-B. The composite map includes the helical particle of Meprin α wild type, colored according to the domain structure of chain A and chain B (figure 31 B) as well as according to local resolution (figure 31 C). The reconstruction of Meprin α shows a local resolution of 2.35-3.50 Å. The generated structure of Meprin α, colored according to the domain structure, is depicted in figure 32. The dimeric Meprin α is linked by a disulfide bridge within the MAM domain. The protease consists of the three subunits: protease domain, MAM domain and TRAF domain.

A

B

Protease domain/chain A   Protease domain/chain B
MAM domain/chain A   MAM domain/chain B
TRAF domain/chain A   TRAF domain/chain B
Chain G   Chain H

C

2.35 Å   2.6 Å   2.9 Å   3.1 Å   3.5 Å
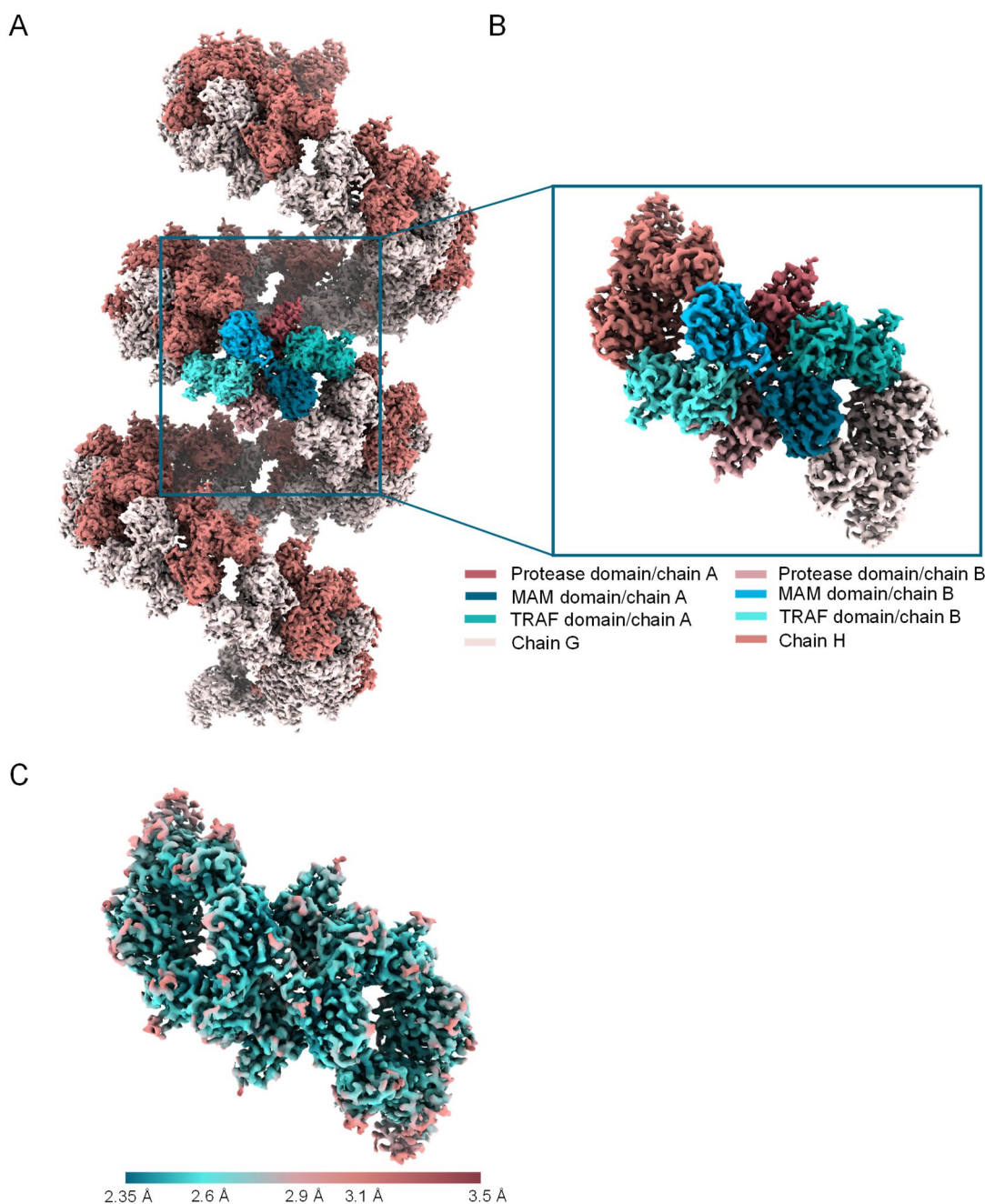
Figure 31: Cryo-EM reconstruction of Meprin α wild type, extraction of 400 pixel boxes to reach a reconstruction including four monomers of Meprin α. A) Composite map of obtained reconstruction, depicting the helical particle observed in electron micrographs (figure 30 E). B) Reconstruction colored according to Meprin α domain structure of chain A and chain B. Chain H and chain G are colored individually. C) Reconstruction colored according to local variation in resolution by gold-standard Fourier shell correlation at 0.143.

The TRAF domain spanning the residues G^{434}-S^{600} in both chains is characterized by a β-sandwich including one four-stranded and one three-stranded antiparallel β-sheet and some α-helical segments (figure 32 and figure 59 in the appendix, p. 137). At N^{440} (both chains), one N-acetylglucosamine residue was determined, suggesting N-glycosylation.

The MAM domain of both chains includes the residues T^{264}-T^{433} and is stabilized by two intramolecular disulfide bridges between C^{269}-C^{277} and C^{343}-C^{431} (figure 32 and figure 60 in the appendix, p. 138).
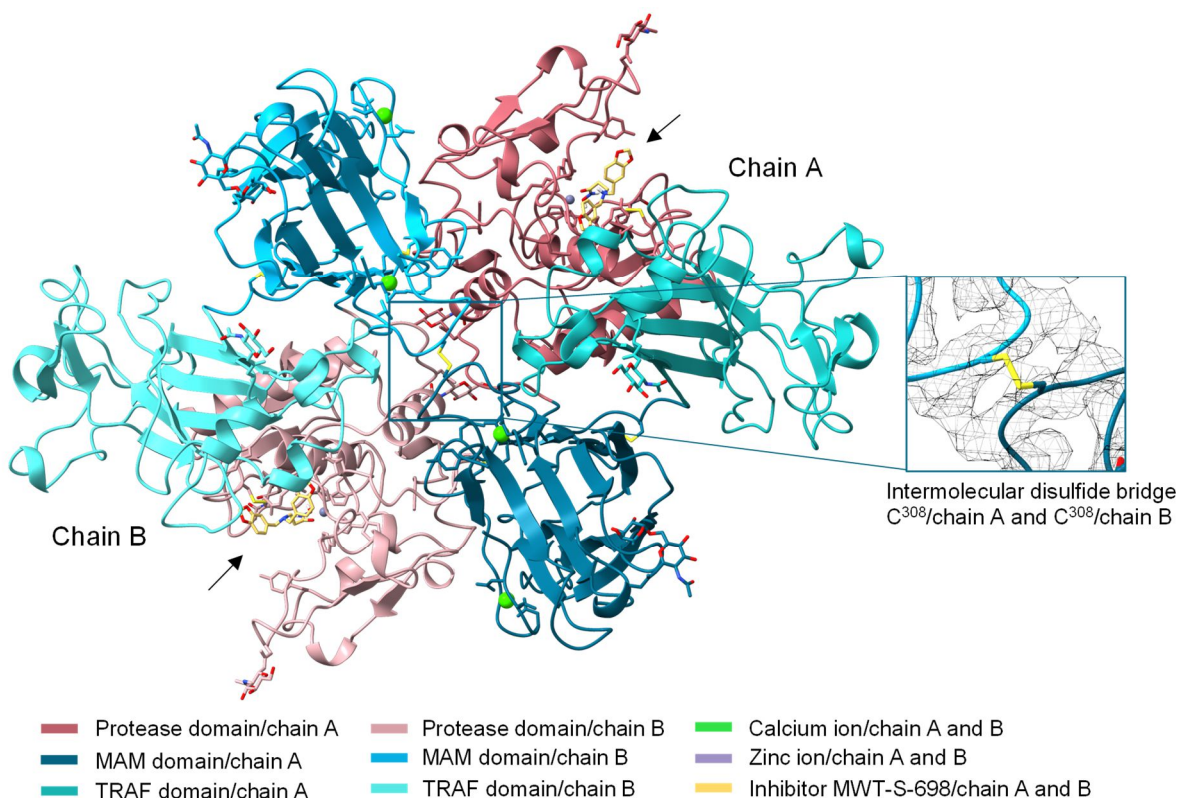
Figure 32: Dimeric Meprin α, linked by intermolecular disulfid bridge mediated by C^{308} within chain A and chainB, determined by cryo-EM single particle analysis (2.42 Å). The model includes the TRAF domain G^{434}-S^{600}, MAM domain T^{264}-T^{433} and protease domain N^{66}-H^{263} within both chains. Chain A and B are linked by an intermolecular disulfid bridge mediated by C^{308} within both chains. The active site of chain A and chain B is highlighted by an arrow. The inhibitor is highlighted in yellow. Glycolsyations are shown as sticks.

Chain A and chain B are connected by an intermolecular disulfide bridge between C^{308}/chain A and C^{308}/chain B. The overall secondary structure of the MAM domain in chain A and chain B includes a *β*-sandwich composed of two four-stranded antiparallel *β*-sheets. Two ions in each chain are coordinated within the MAM domain. Those have been interpreted as two calcium ions, due to the coordination geometry as well as preferences of Ca^{2+}-binding sites in proteins (Zheng et al. 2008; Harding 2006). The calcium ions E1 in chain A and F1 in chain B might be also interpretable as sodium ions, due to their penta-coordination (Harding 2002). Monodentate coordinations to carbonyl backbone of G^{282}, and with the hydroxyl group of T^{287} as well as D^{288} are observed. Additionally, a bidentate coordination to the carboxyl moiety of D^{285} is present. The second calcium ion within chain A and chain B shows octahedral geometry, characterized by monovalent connections to the hydroxyl moieties of T^{270}, E^{272}, T^{303} and Y^{313}, as well as by a bivalent interaction with the carboxyl group of D^{422}. Glycosylations within the MAM domain were modeled as well. At N^{414} in chain A and chain B one N-acetylgucosamine residue with an 1,6-linked fucose was determined.

The protease domain includes the residues N^{66} to H^{263} (figure 32 and figure 61 in the appendix, p. 139). As shown for Meprin β, the protease domain is subdivided by the active site cleft into an upper and lower subdomain ("standard orientation").

Whereas the lower subdomain has little secondary structure elements, the upper subdomain of both chains is characterized by a four-stranded antiparallel β-sheet and three α-helices. Additionally, it is crosslinked by one intramolecular disulfide bridge between C^{128} and C^{147}. At N^{140}, N^{222} and N^{258} in both chains, one N-acetylglucosamine residue each could be observed, suggesting N-glycosylation. As described for metzincins, also mature Meprin α harbors the conserved zinc-binding motif HExxHxxGxxH (x can be any amino acid) and the 1,4-β-type Met-turn close to the active site (Sterchi et al. 2008; Gomis-Rüth 2009). The zinc within the active site is complexed by the three Histidine residues H^{152}, H^{156} and H^{162}. The active site cleft is divided into three subpockets S1, S1' and S2', formed by the residues Y^{187} (S1), R^{242} (S1') and Y^{149} (S2') (figure 33), mirroring the preference of Meprin α for neutral aliphatic and aromatic residues (Bertenshaw et al. 2001; Sterchi et al. 2008; Becker-Pauly et al. 2011).
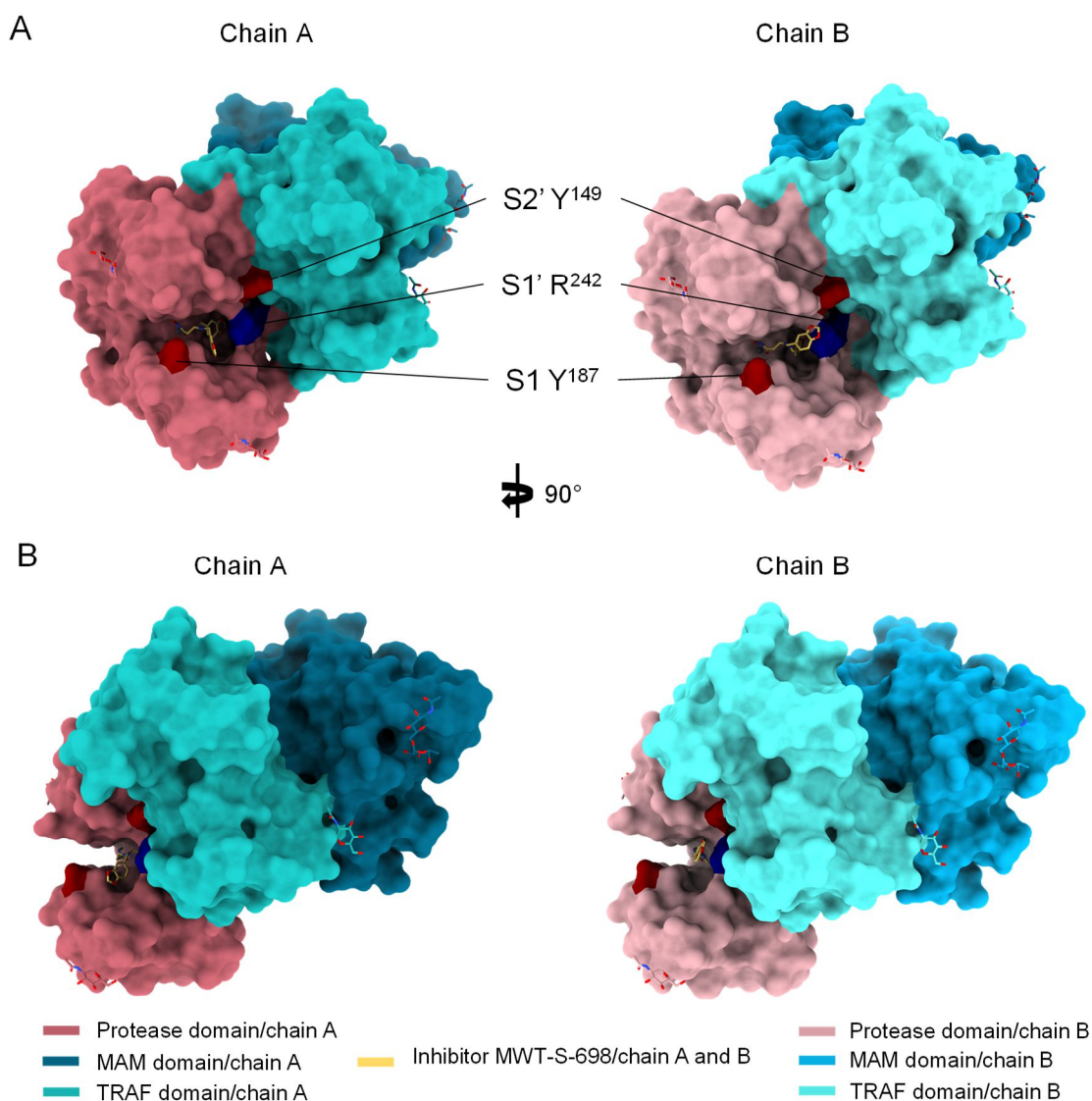
Figure 33: Representation of dimeric Meprin α, elucidated by cryo-EM single particela analysis, colored according to domain structure. A) 'Standard orientation' of chain A and chain B, representation of surface structure with view into the active cleft. The two Tyrosine residues $Y^{187}$and Y^{149}, shaping the subpockets S1 and S2', are colored in red. The Arginine residue R^{242} shaping the subpocket S1' is colored in dark blue C) Chain A and chain B rotated 90° on the vertical axis.

Within the active site cleft of chain A and chain B the placement of the inhibitor MWT-S-698 was performed by docking experiments as described in chapter 2.2.6.2 (p. 33). Therefor, the inhibitor was docked into the model, which was followed by a refinement using the reconstruction of Meprin α. The inhibitor MWT-S-698 consists of a tertiary amine connecting the hydroxamic acid and two benzodioxolane moieties. The hydroxamic acid of the inhibitor MWT-S-698 complexes the zinc ion within the active site. Furthermore, it was assumed that Y^{187} might interact with one benzodioxolane moiety and R^{242} might form a hydrogen bond or a cation-π interaction with the other benzodioxolane moiety (Tan et al. 2018).

Within both chains of Meprin α, similar binding modes of the hydroxamic acid of inhibitor within the active site cleft were observed (figure 33). In particular, the hydroxamate amide forms a hydrogen bond with the carbonyl of C^{126} at a distance of 3.1 Å. The hydroxyl group of the hydroxamate interacts via a hydrogen bond to the carboxylate of E^{156} (3.0 Å) and chelates the zinc (2.3 Å).

Focusing on the interactions of the inhibitor side chains, within chain A and chain B the electron density of one benzodioxolane moiety is well defined (benzodioxolane 1, figure 34), for the other moiety the electron density could not be elucidated (benzodioxolane 2, figure 34). Possible interactions within chain A and chain B are illustrated in a 2D-plot in figure 34. Within chain A, the benzodioxolane 1 forms a cation-π interaction with the guanidine group of R^{242} in subpocket S1' (5.6 Å). The benzodioxolane moiety 2 of chain A seemed to form a π-π interaction via F^{219} (4.1 Å) with Y^{187} in subpocket S1 (4.1 Å). For the π-π stacking interaction, a parallel-displaced geometry is observed. For chain B three possible conformations of MWT-S-698 were obtained by the docking experiments. In case of the highest ranked conformation of MWT-S-698, a cation-π interaction of the guanidine group of R^{242} to either the benzodioxolane moiety 1 or moiety 2 could be possible at a distance of 4.9 Å or 3.9 Å. For two of the three determined conformations, the benzodioxolane moiety 1 shows the same orientation. Nevertheless, all three orientations allow a possible cation-π interaction with the guanidine group of R^{242}. The orientation of the benzodioxolane moiety 2 is different in the three determined conformations of MWT-S-698 within chain B (data not shown). Except for the highest ranked conformation, no specific interactions of the benzodioxolane moiety 2 with the amino acid side chains within the active site cleft could be observed. These observations led to the assumption, that the inhibitor MWT-S-698 obviously binds in different conformations within the active site of Meprin α. However, within both chains an interaction with R^{242} of subpocket S1' was determined.
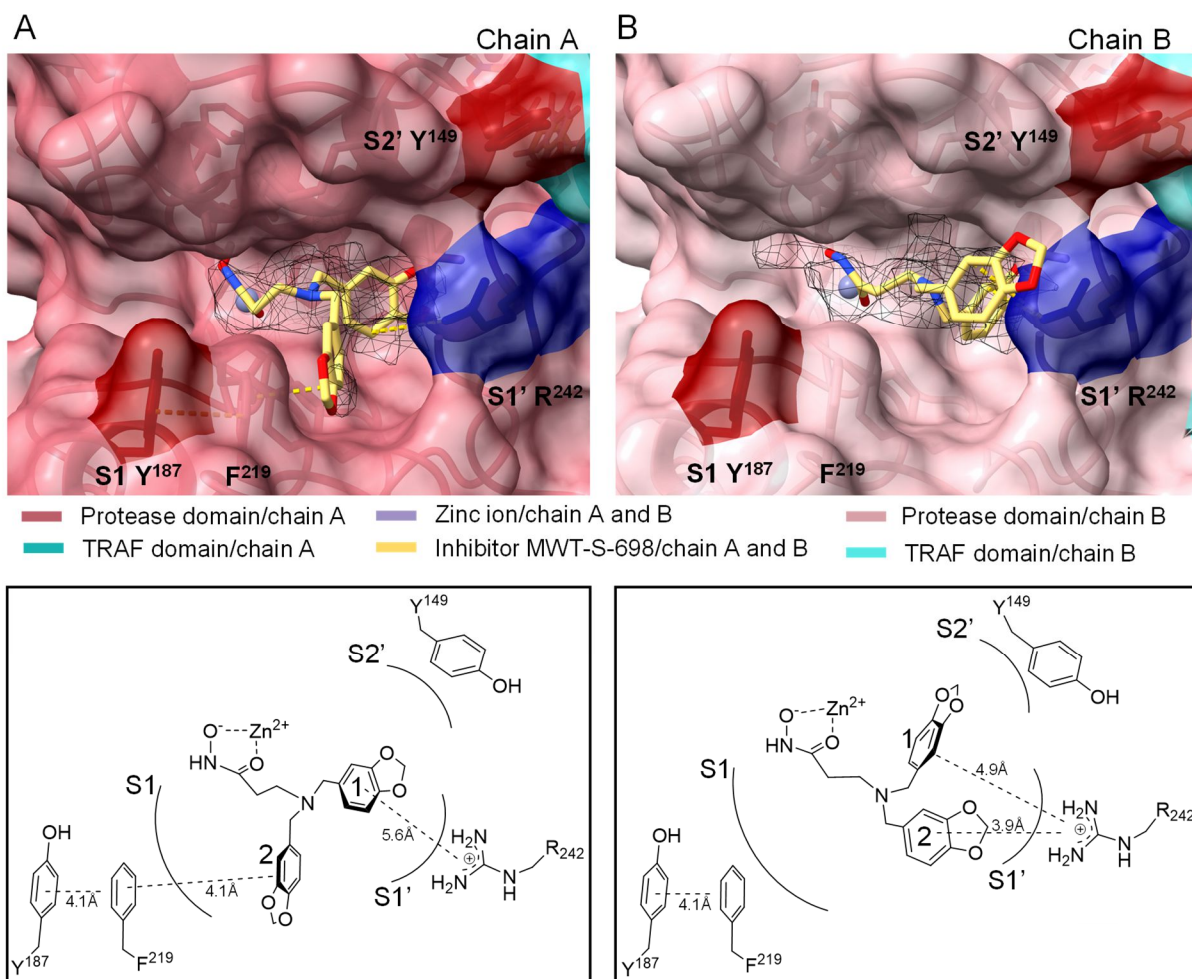
Figure 34: Active site of Meprin α in complex with the specific inhibitor MWT-S-698. *Orientation of MWT-S-698 within the active site of chain A and chain B. Inhibitor sidechain interactions are displayed in a 2D-plot.* **A)** *Within chain A a cation-π interaction is formed between benzodioxolane 1 and R^{242} of subpocket S1'. The benzodioxolane moiety 2 interacts via a π-π stacking with F^{219} and further with Y^{187} of subpocket S1.* **B)** *Possible cation-π interaction of R^{242} with either benzodioxolane 1 or 2.*

Summarizing, the structure of mature Meprin α could be elucidated by single particle cryo-EM for the first time. A resolution of 2.42 Å could be achieved. Within both monomers of Meprin α, which are linked by a well resolved disulfide bridge, the specific inhibitor MWT-S-698 is bound. Based on the described data, first insights into the binding mode of the inhibitor could be presented. The data imply, similar as concluded for Meprin β before, that the inhibitor binds in flexible mode within the active site.

In addition, the structural determinants for the helix formation were analyzed on the basis of the cryo-EM structure. A particle extraction within 400 pixel boxes enabled the reconstruction of parts of the Meprin α helix and the placement of four monomers of Meprin α within the map. The refinement statistics are listed in table 24 in the appendix (p. 136). Two monomers are linked by an intermolecular disulfide bridge and interact with the other two monomers, each on one site, via non-covalent interactions. In the following, the amino acids involved in these non-covalent associations of dimeric Meprin α molecules and according to this the amino acids responsible for helix formation are analyzed.

Obviously, four interfaces between the dimeric Meprin α are present (figure 35 and figure 62 in the appendix, p. 139). Within all four interfaces the same amino acids are involved in interactions between the dimeric Meprin α molecules, these are listed in table 10. Apparently, ionic interactions contribute to the helix formation of dimeric Meprin α. The amino acids involved are situated within the MAM (T^{264}-T^{433}) and TRAF domain (G^{434}-S^{600}). The most prominent interaction involves the amino acids R^{372} and D^{595}. Additionally, E^{492} interacts either with K^{376} via an ionic interaction or with R^{357} via a hydrogen bond, at least within interface 2 and 3. For interface 1 and 4, the distance between these amino acids might be too far. Unfortunately, the density for E^{498} is ambiguous. Because, it is located close to R^{284}, it is tempting to speculate that a charged interaction occurs between the carboxylate of E^{498} and the guanidine group of R^{284}.

Thus, the presented cryo-EM structure provides clues for the non-covalent association of Meprin α dimers into helical particles. To investigate the impact of the helical structure on the activity and stability was the aim of the following studies and is described in the chapters 3.3 and 3.4.

*Table 10: Residues possibly involved in non-covalent association of Meprin α dimers leading to formation of helical oligomers. Each residue is characterized by chain (A, B, H or G), in which the residue is harbored. *poor density for this residue, **interaction with backbone-carbonyl, italics: distance might be too far for the appropriate type of interaction.*

Interface 1			Interface 2		
R^{372}/B ↔ D^{595}/H	2.7 Å	Ionic interaction	R^{372}/H ↔ D^{595}/B	2.7 Å	Ionic interaction
K^{376}/B ↔ E^{492}/H	3.7 Å	Ionic interaction	K^{376}/H ↔ E^{492}/B	2.9 Å	Ionic interaction
R^{357}/B ↔ E^{492}/H	3.6 Å	Ionic interaction	R^{357}/H ↔ E^{492}/B	3.8 Å	Ionic interaction
**R^{357}/B ↔ E^{492}/H*	*3.6 Å*	*Hydrogen bond*	**R^{357}/H ↔ E^{492}/B	3.0 Å	Hydrogen bond
*R^{284}/B ↔ *E^{498}/H	3.4 Å	Ionic interaction	*R^{284}/H ↔ *E^{498}/B	2.7 Å	Ionic interaction
Interface 3			Interface 4		
R^{372}/G ↔ D^{595}/A	2.8 Å	Ionic interaction	R^{372}/A ↔ D^{595}/G	2.3 Å	Ionic interaction
K^{376}/G ↔ E^{492}/A	4.2 Å	Ionic interaction	K^{376}/A ↔ E^{492}/G	3.8 Å	Ionic interaction
R^{357}/G ↔ E^{492}/A	3.7 Å	Ionic interaction	*R^{357}/A ↔ E^{492}/G*	*4.4 Å*	*Ionic interaction*
**R^{357}/G ↔ E^{492}/A	2.8 Å	Hydrogen bond	**R^{357}/A ↔ E^{492}/G*	*3.5 Å*	*Hydrogen bond*
*R^{284}/G ↔ *E^{498}/A	4.0 Å	Ionic interaction	*R^{284}/A ↔ *E^{498}/G	3.9 Å	Ionic interaction
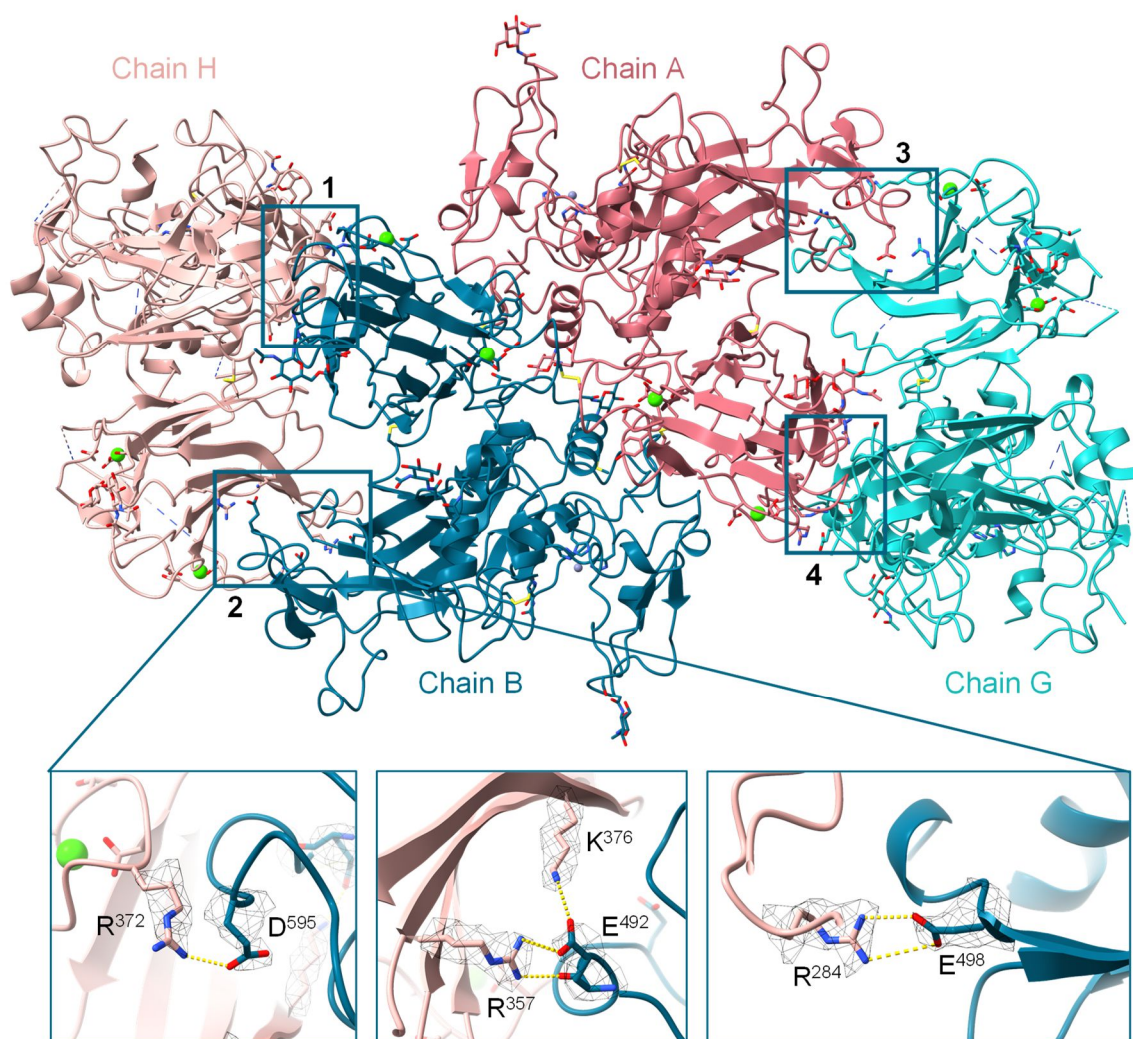
Figure 35: Schematic representation of the non-covalent interactions between Meprin α dimers. The helix formation depends on ionic interactions within the MAM and TRAF domains. Chains are labeled as A/B/G/H. Four interfaces (labeled 1-4) observed between dimeric Meprin α and adjacent Meprin α monomers. Within in all four interfaces the same amino acids are involved in helix formation. Exemplary, the interactions of interface 2 are displayed.

3.3   Investigations on Stability and Activity of Meprin α Helical Oligomers

3.3.1   Influence of Helical Formation on Stability of Meprin α

In additional studies, the question should be addressed, whether the helix formation of Meprin α might affect its stability and activity. For these investigations, three variants of Meprin α were available: i) wild type Meprin α, forming helical structures up into the MDa range, ii) Meprin α R372T, generating dimeric structures and ring-like small oligomers, as well as iii) Meprin α C308A, which is secreted as monomer and interacts non-covalently to form ring-like small oligomers.

For investigations on the thermal stability of the three Meprin α variants and to obtain information about the secondary structure, a CD spectroscopic analysis in far-UV range was performed. The resulting CD signals were normalized and the mean residue ellipticity was calculated. In figure 36, the far-UV CD spectra of native and denatured wild type Meprin α, Meprin α R372T and Meprin α C308A are shown. In general, for helical proteins minima at about 222 and 208 nm and a maximum at 195 nm are expected. For proteins mainly consisting of *β*-sheets maxima at 190 and 200 nm as well as a minimum around 218 nm are detected. Usually, the *α*-helical signals dominate the CD-spectrum. Unfolded proteins show weaker signals above 210 nm with a minimum between 195 and 200 nm (Buchner and Kiefhaber 2005).
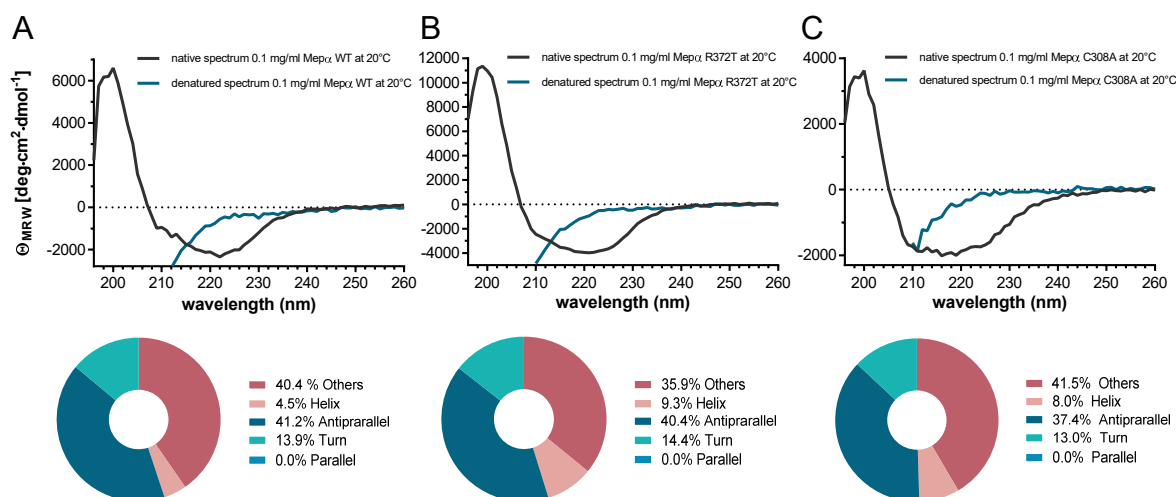
Figure 36: Far-UV CD spectra of native (black) and denatured (blue) A) Meprin α wild type, B) Meprin α R372T and C) Meprin α C308A. The enzymes were assessed in 30 mM TRIS pH 7.4 buffer containing 150 mM NaCl, at a concentration of 100 µg/ml in a quartz cuvette with a path length of 0.1 cm at 20°C as described in chapter 2.2.5.1 (pp. 28). Chemical denaturation of Meprin α was performed in 30 mM TRIS pH 7.4 buffer containing 4 M guanidinium hydrochloride and 150 mM NaCl. The data was baseline corrected (against the appropriate buffer) and the mean residue ellipticity was calculated by the software GraphPad Prism 6.

All three Meprin α variants exhibit a *β*-sheet spectrum, although for Meprin α C308A subtle differences were observed, in comparison to Meprin α wild type and Meprin α R372T (figure 36). For Meprin α wild type and Meprin α R372T, the same characteristics within the CD spectra were observed, showing a minimum around 220-222 nm and a maximum at 200 nm, indicating a high number of *β*-sheets. Meprin α C308A shows a minimum around 216-218 nm and a maximum at 200 nm. The CD data were analyzed by the web server BeSTSel (Beta Structure Selection), in order to predict the secondary structure elements from the CD signals (Micsonai et al. 2018; Micsonai et al. 2015). A high number of antiparallel *β*-sheets seemed to be present in all variants of Meprin α (wild type: 41.2%, C308A: 37.4% and R372T: 40.4%). The major difference was observed for the predicted number of *α*-helices, whereas for Meprin α wild type 4.5% were calculated, for the other two variants about 8 to 9% *α*-helix content was predicted. A turn content of about 13 to 14% for all three variants was predicted. By analysis of the CD spectra using another web server, called CAPITO (Wiedemann et al. 2013), again a higher *α*-helix content for the Meprin α mutants R372T and C308A was predicted in comparison to the wild type Meprin α. Although the CD spectrum of the Meprin α C308A appears to be different than those of the other two Meprin α variants, no significant difference with respect to the secondary structure elements was calculated by the webserver BeSTSel and CAPITO. However, the analysis of the PDB-file of the elucidated Meprin α cryo-EM structure using the web server STRIDE (Heinig and Frishman 2004), revealed an antiparallel *β*-sheet content of 32% and an *α*-helix content of 10%.

In order to obtain information on the thermal stability of the Meprin α variants, and if the oligomeric state of Meprin α wild type has an impact on its stability, a stepwise thermal denaturation was performed and monitored by far-UV CD. In figure 37, the far-UV spectra recorded with increasing temperature of Meprin α wild type and its mutants R372T and C308A are depicted. For analysis of the melting temperature, the CD signals showing the highest difference at a certain wavelength were plotted against the temperature. By fitting the data according to a sigmoidal dose-response model, the melting temperature or rather a transition in secondary structure was calculated. As visible in figure 37 A/B, a transition of the minimum at 218 nm to 208 nm occurs at a temperature of 45-55°C for wild type Meprin α and at a temperature of 35-45°C in case of Meprin α R372T. Since the minimum at 218 nm disappears, the *β*-sheet structure might be lost. The CD spectra of Meprin α wilde type and R327T do not show typical features as observed for unfolded proteins and as it was recorded for the chemical denatured proteases (figure 36 A/B). The calculated transition temperature for Meprin α wild type and Meprin α R372T was 46°C and 40°C, respectively, indicating a higher stability of the helical particle. Nevertheless, on the basis of this data, it is difficult to judge, whether Meprin α wild type and R372T show different thermostability or may aggregate upon temperate increase.
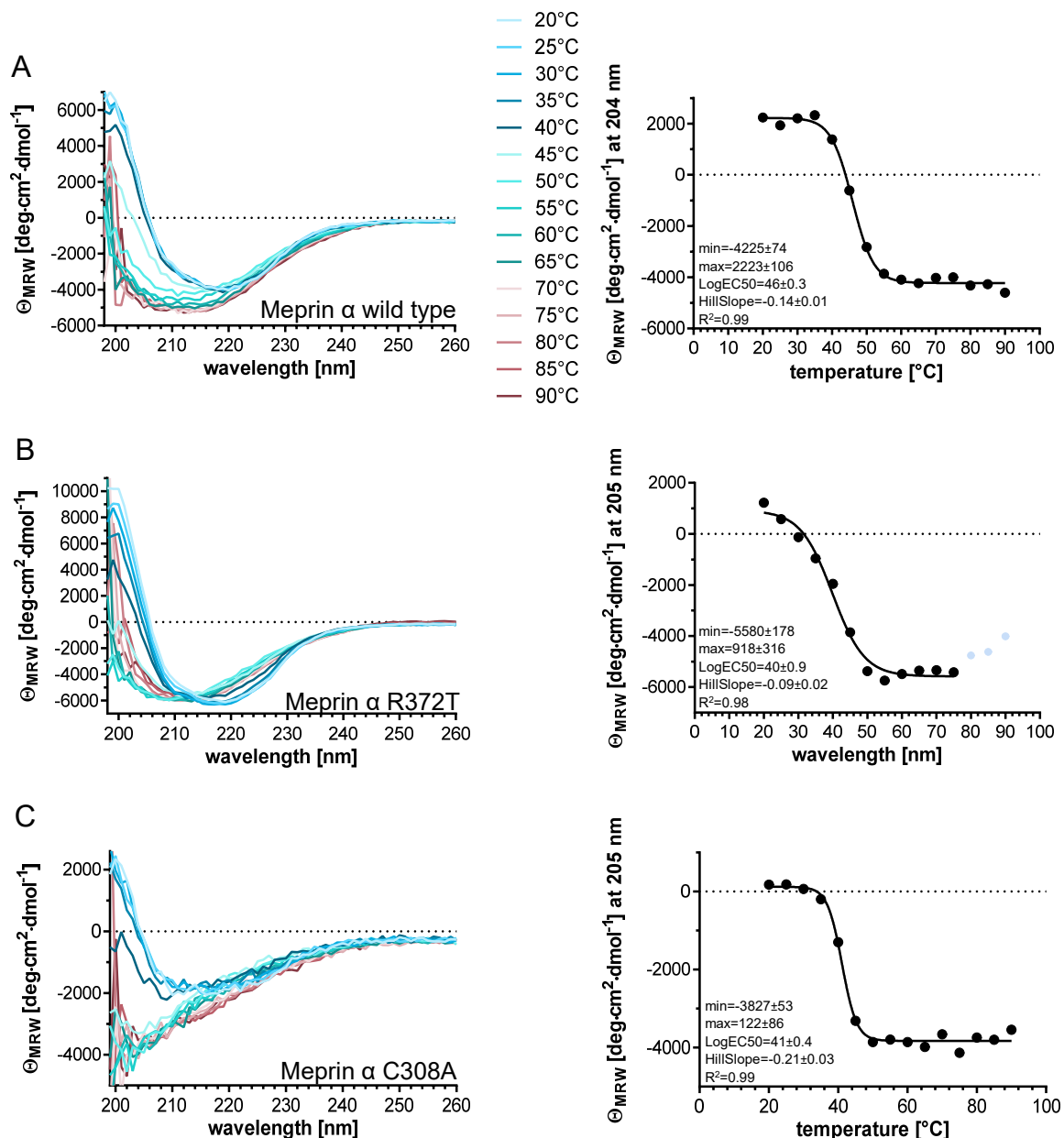
Figure 37: Far-UV CD spectrum of Meprin α wild type, R372T and C308A for analysis of thermal stability. *The enzymes were measured in 30 mM TRIS pH 7.4 buffer containing 100 mM NaCl at a concentration of 100 µg/ml in a quartz cuvette with a path length of 0.1 cm as described in chapter 2.2.5.1 (pp.28). For analysis of the thermal stability scans at temperatures from 20 to 90°C (5°C steps) were recorded. The mean residue ellipticity was calculated by the software GraphPad Prism 6. The CD signals at a specific wavelength were plotted against the temperatures and fitted by the sigmoidal dose-response model in GraphPad Prism 6.* ***A)*** *Far-UV spectra of Meprin α wild type.* ***B)*** *Far-UV spectra of Meprin α R372T. The light blue marked values were excluded from analysis.* ***C)*** *Far-UV spectra of Meprin α C308A.*

In comparison to Meprin α wild type and R372T, for the mutant C308A a clear change in CD signal with increasing temperature is visible (figure 37 C). In the range between 20 and 35°C the protease seemed to be stable and folded, above 45°C Meprin α C308A is denatured, as depicted in figure 37 C. By fitting the obtained data with the sigmoidal dose-response model a melting temperature for Meprin α C308A of 41°C could be determined (figure 37 C).

Consequently, it can be stated, that the helical formation has little effect on thermal stability. Additionally, the formation of dimeric molecules, linked by an intermolecular disulfide bridge at C^{308}, contributes to thermal stability of the protease.

3.3.2   Influence of Helical Formation on Proteolytic Activity of Meprin α

To investigate, if the helix formation has an impact on the proteolytic activity of Meprin α, the kinetic parameters K_m and k_{cat} of Meprin α wild type, C308A and R372T were determined for turnover of the fluorogenic substrate Abz-YVADPK(Dnp)G-OH in 50 mM HEPES pH 7.4 buffer containing 150 mM NaCl. The resulting v/S-characteristics are shown in figure 38, the kinetic parameters determined applying a model considering substrate-inhibition kinetics are listed in table 11.
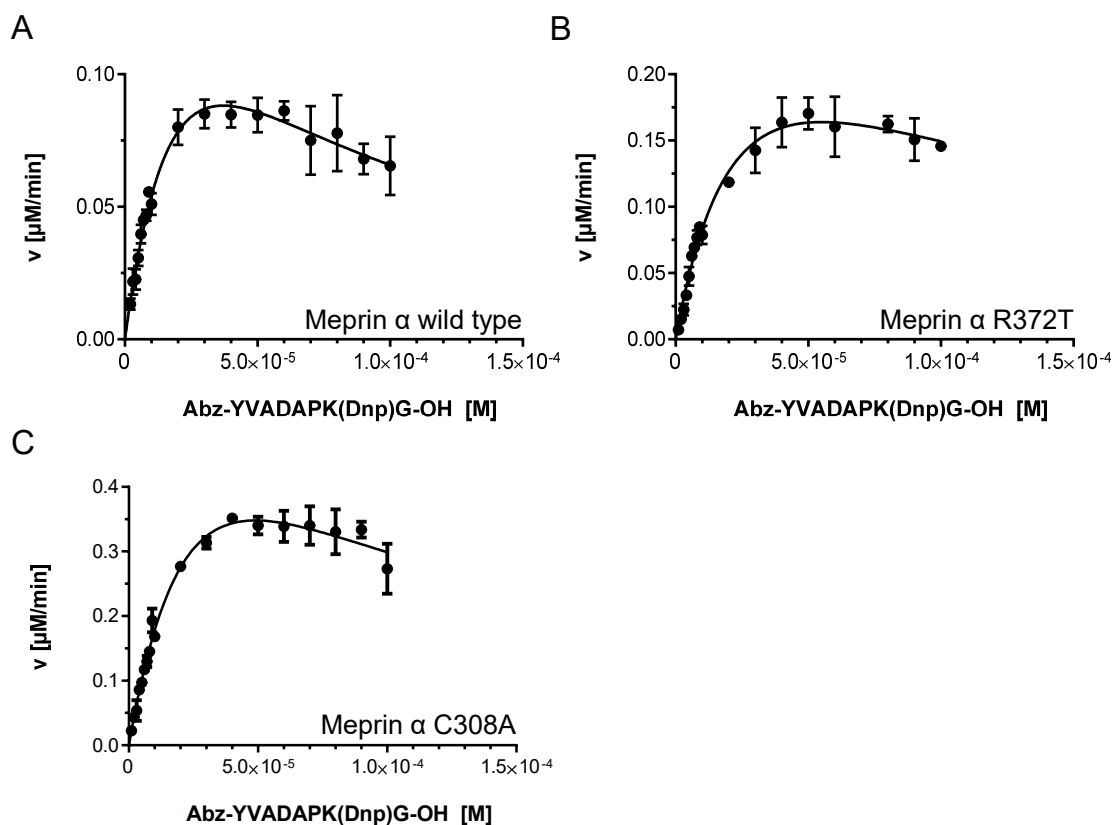
Figure 38: v/S-characteristics for turnover of substrate Abz-YVADPK(Dnp)G-OH in 50 mM HEPES pH 7.4 buffer containing 150 mM NaCl, at 30°C by Meprin α wild type, R372T and C308A. The determination was performed in duplicate on three different days at the same instrument. The data were evaluated using the software GraphPad Prism 6. The applied model considers substrate inhibition, as described in chapter 2.2.4.3 (pp. 27.). The graphs represent one out of three independent measurements in duplicate. A) v/S characteristics of Meprin α wild type. The K_m and k_{cat} value determined by three individual measurements are 33±2 µM and 9±1 s⁻¹, respectively. A catalytic efficiency k_{cat}/K_m of 271±22 mM⁻¹s⁻¹ was obtained. B) v/S characteristics of Meprin α R372T. The K_m and k_{cat} value determined by three individual measurements are 55±19 µM and 18±7 s⁻¹, respectively. A catalytic efficiency k_{cat}/K_m of 329±14 mM⁻¹s⁻¹ was obtained. C) v/S characteristics of Meprin α C308A. The K_m and k_{cat} value determined by three individual measurements are 33±7 µM and 15±4 s⁻¹, respectively. A catalytic efficiency k_{cat}/K_m of 453±17 mM⁻¹s⁻¹ was obtained.

Table 11: Kinetic parameters for the turnover of the substrate Abz-YVADPK(Dnp)G-OH by the three Meprin α variants in 50 mM HEPES pH 7.4 buffer containing 150 mM NaCl at 30°C. The determination was performed in duplicate on three different days at the same instrument. The data was evaluated by substrate inhibition kinetics using the software GraphPad Prism 6.

Meprin α variant	K_m [µM]	k_{cat} [s^{-1}]	k_{cat}/K_m [$mM^{-1}s^{-1}$]	K_i for substrate [µM]
Meprin α wild type	33±2	9±1	271±22	14±5
Meprin α R372T	55±19	18±7	329±14	49±9
Meprin α C308A	33±7	15±4	453±17	113±47

Based on the turnover of the fluorogenic, small substrate Abz-YVADPK(Dnp)G-OH and assuming the enzymes are homogenous and fully active, for the applied conditions it can be stated that Meprin α C308A exhibits the highest catalytic efficiency (k_{cat}/K_m=453±17mM^{-1}s^{-1}) in comparison to Meprin α R372T (k_{cat}/K_m=329±14 mM^{-1}s^{-1}) and Meprin α wild type (k_{cat}/K_m=271±22 mM^{-1}s^{-1}). Hence, this might indicate that the helix formation leads to reduced catalytic efficiency of Meprin α wild type, at least for the turnover of the utilized small substrate.

Consequently, the impact of the helix formation on the Meprin α activity towards large, native substrates needed to be investigated as well. Therefor, Meprin α wild type (helical variant) and Meprin α C308A (secreted as monomer, but non-covalently associates into dimers) were applied. The extracellular matrix proteins Fibronectin, Tropoelastin and Elastin were investigated as substrates. Fibronectin is a known substrate of Meprins (Kruse et al. 2004; Jefferson et al. 2013), Tropoelastin and Elastin have not been investigated before, but it is known that both proteins are substrates for matrix metalloproteinases (MMPs) (Heinz et al. 2010; Miekus et al. 2019). For the cleavage reactions, different enzyme-substrate ratios were tested. They were incubated at 37°C for different time points in 50 mM TRIS buffer pH 7.4 for Tropoelastin and 50 mM HEPES pH 7.4 buffer containing 150 mM NaCl for Fibronectin and Elastin as described in chapter 2.2.7 (p. 34). An evaluation of the cleavage reaction was performed by reducing SDS-PAGE, followed by Coomassie-staining (described in chapter 2.2.3.5, pp. 24). The results are depicted in figures 39 to 41.
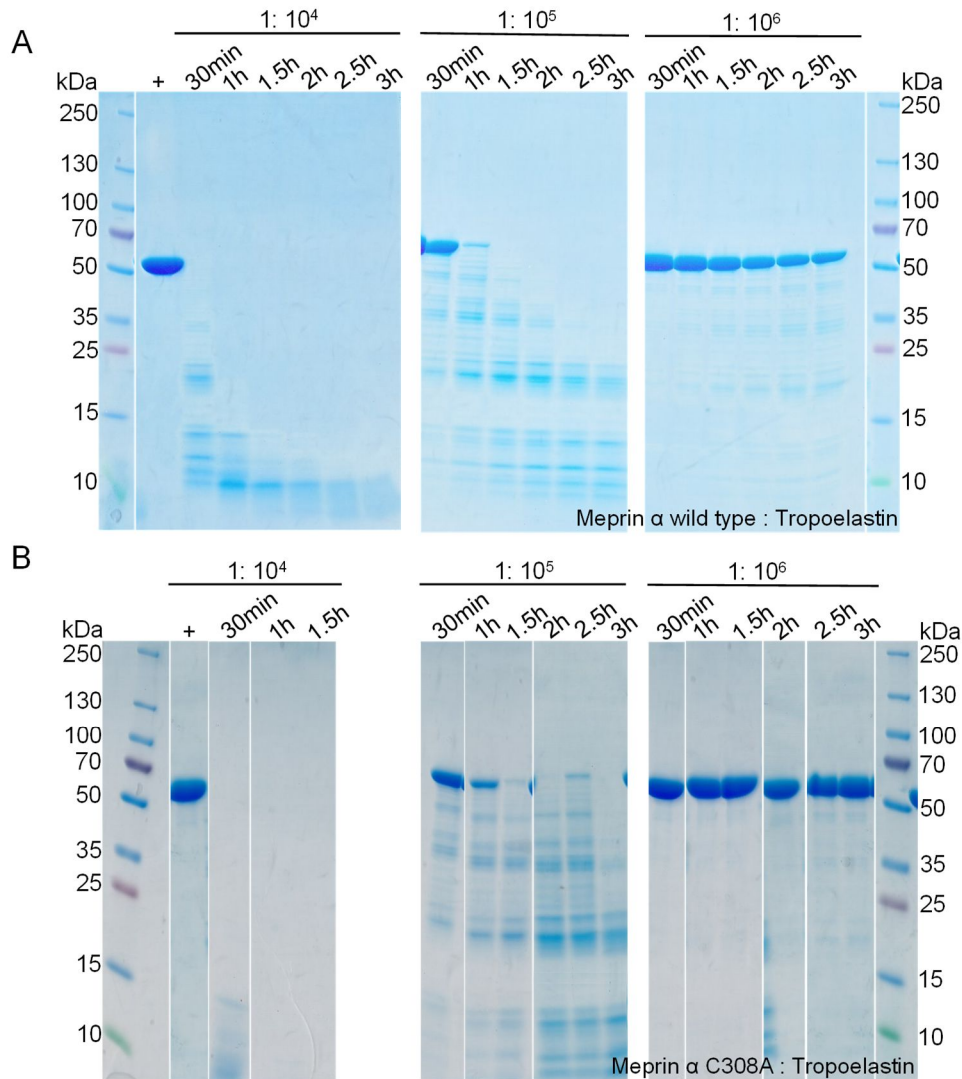
Figure 39: Cleavage of human Tropoelastin by Meprin α wild type and Meprin α C308A. *Analyzed using reducing SDS-PAGE (4-20% gradient gel), visualized by Coomassie-staining. In each sample 10 µg Tropoelastin were applied, + positive control (Tropoelastin incubated for 3 h at 37°C). **A)** Cleavage of Tropoelastin by Meprin α wild type, complete degradation of Tropoelastin after 3 h at a molar ratio of 1:10⁴ (Meprin α:Tropoelastin). **B)** Cleavage of Tropoelastin by Meprin α C308A, complete degradation of Tropoelastin after 30 min at a molar ratio of 1:10⁴ (Meprin α:Tropoelastin).*

First, the cleavage of recombinant Tropoelastin (61 kDa) by Meprin α wild type and Meprin α C308A was tested. Topoelastin is the soluble precursor molecule of Elastin (Wise et al. 2014). As depicted in figure 39, Tropoelastin is completely degraded by both Meprin α variants. Applying the same molar ratio of 1:10⁴ Meprin α to Tropoelastin, Meprin α C308A seems to degrade Tropoelastin faster than Meprin α wild type.

The second extracellular matrix protein investigated was Fibronectin. Fibronectin exits as a dimer of two 250 kDa monomers linked by a pair of disulfide bridges, it mediates several cellular interactions within the extracellular matrix (Pankov and Yamada 2002).

According to figure 40, a specific cleavage of Fibronectin by Meprin α wild type and Meprin α C308A occurs, since a defined band pattern is visible in the SDS-PAGE, depending on the molar ratio applied for the cleavage reaction. Obviously, both proteases cleave at the same sites, no differences in the resulting products are observed.
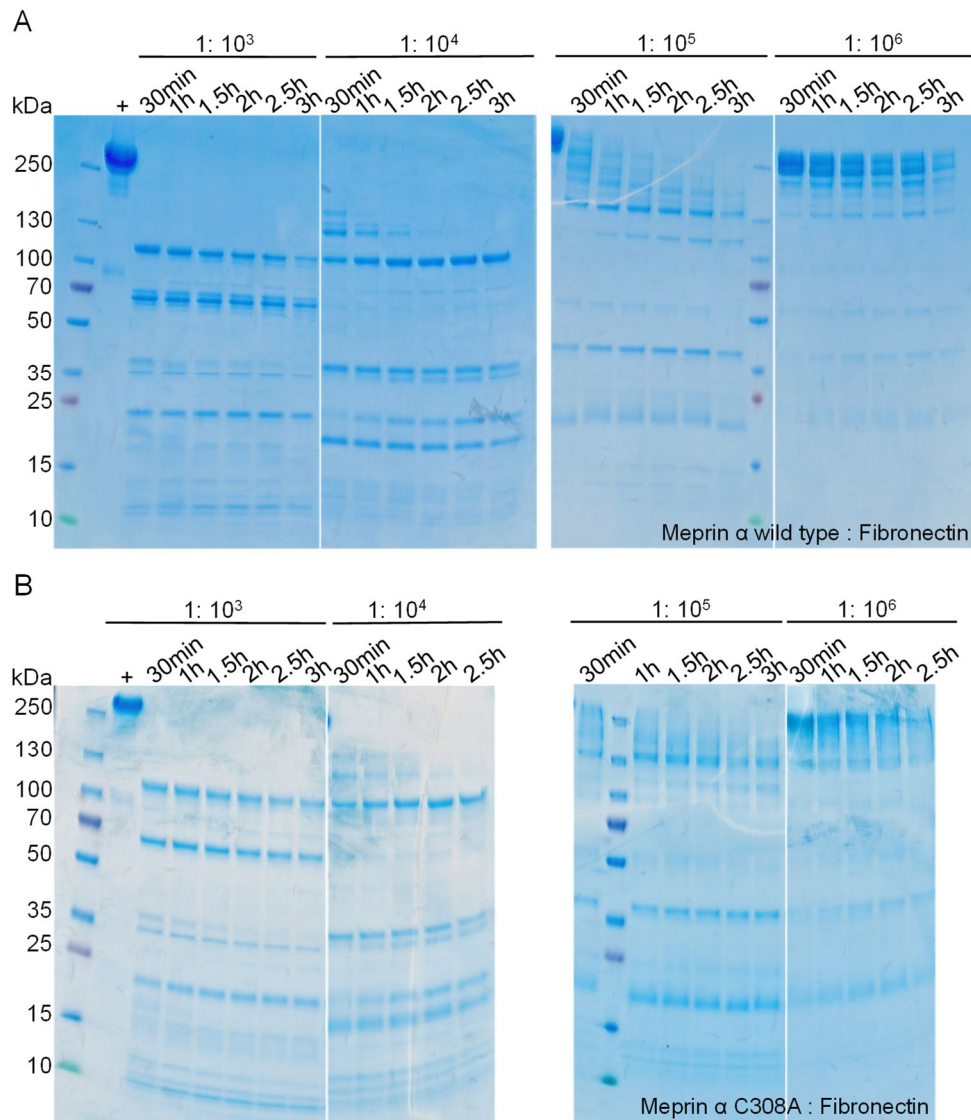
Figure 40: Cleavage of human Fibronectin by Meprin α wild type and Meprin α C308A. *Analyzed using reducing SDS-PAGE (4-20% gradient gel), visualized by Coomassie-staining. In each sample 10 µg Fibronectin were applied, + positive control (Fibronectin incubated for 3 h at 37°C).* **A)** *Specific cleavage of Fibronectin by Meprin α wild type.* **B)** *Specific cleavage of Fibronectin by Meprin α C308A.*

As a third extracellular substrate Elastin was used. The cleavage of Elastin by MMPs was described previously (Miekus et al. 2019), but if Elastin is a substrate of Meprin α was not investigated so far. Elastin provides elasticity and tensile strength to the extracellular matrix (Frantz et al. 2010). The protein consists of covalently crosslinked Tropoelastin molecules and contributes up to 90% of elastic fibers. Thus, no defined molecular mass can be determined for Elastin. As a consequence, a mass ratio for the cleavage reaction was applied.

Because the isolated Elastin is not soluble, only the supernatant of the cleavage reaction was analyzed applying reducing SDS-PAGE, followed by Coomassie-staining. The result is shown in figure 41.
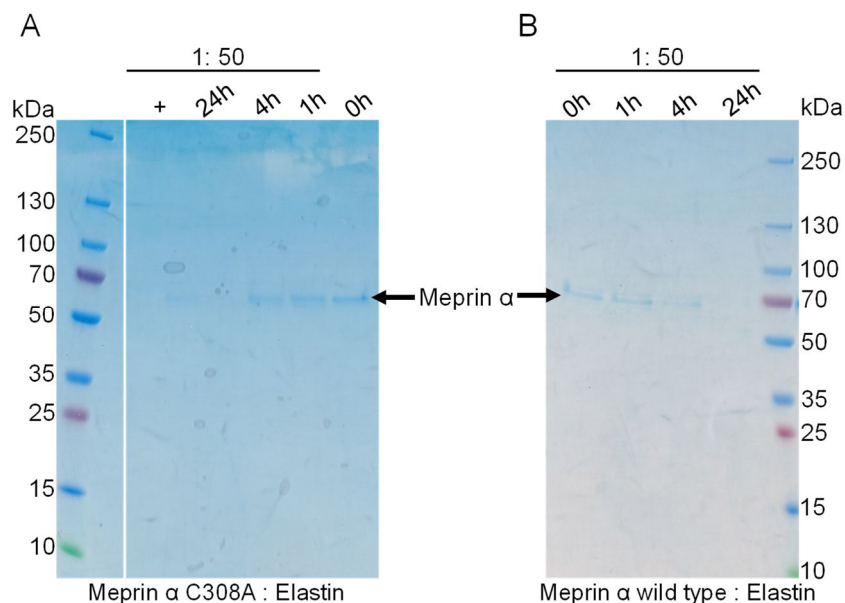
Figure 41: Cleavage of bovine Elastin by Meprin α wild type and Meprin α C308A. *Analyzed using reducing SDS-PAGE (4-20% gradient gel), visualized by Coomassie-staining. Elastin was incubated at 37°C for 24 h, 30 µl of supernatant were applied onto the gel, + positive control.* *A) Cleavage of Elastin by Meprin α wild type, bands at about 65 kDa result from Meprin α.* *B) Cleavage of Elastin by Meprin α C308A, bands at about 65 kDa result from Meprin α C308A.*

As shown in figure 41, no cleavage products of Elastin could be observed by SDS-PAGE analysis. The band at about 65 kDa results from Meprin α. The supernatants of the cleavage reaction were also analyzed by MALDI-TOF MS. Applying this method small cleavage products can be identified, which are not visible in SDS-PAGE. The results are depicted in figure 63 in the appendix (p. 140). For the cleavage of Elastin by Meprin α wild type, the MALDI-TOF MS analysis revealed two potential cleavage products: 740.4 Da and 1127.6 Da. For the turnover of Elastin by Meprin α C308A, three possible cleavage products were determined using MALDI-TOF MS analysis: 740.4 Da, 1070.6 Da and 1213.6 Da. A mass range of 500 to 50000 Da was covered by this MS analysis, but only the mentioned cleavage products could be identified.

For further identification of cleavage products of Elastin and to obtain their sequence, the samples were additionally analyzed using nanoLC-MS/MS. The analysis was perfomed by Tobias Hedtke (laboratory of Dr. Christian Schmelzer, Fraunhofer IMWS). By this analysis it was confirmed that Elastin serves as a substrate for Meprin α wild type and Meprin α C308A. The determined Elastin cleavage products generated by both proteases are listed in table 25 in the appendix (pp. 141).

The turnover of Elastin by Meprin α C308A revealed about five times more cleavage products, as compared to Meprin α wild type, which might indicate a higher activity of the mutant C308A towards Elastin. All cleavage products identified from the Meprin α wild type cleavage reaction could be also found in case of Elastin turnover by Meprin α C308A. Preferred amino acids of both Meprin α variants in P1 are Glycine and Alanine and in P1' Valine, Glycine and Alanine.

Using nanoLC-MS/MS, the peptide sequences of the cleavage products were identified and the peptide representing the *m/z* value of 740.4, previously determined using MALDI-TOF MS, corresponds to the sequence: G↓LPGVYPGGVLPGAGAR, whereby the *m/z* value 740.6 represents [M+2H]$^{2+}$. In addition, the sequence G↓VYPGGVLPGAGAR was identified, which corresponds to the *m/z* value of 1213.6, observed in MALDI-TOF MS analysis previously. The other two *m/z* values found using MALDI-TOF MS (1127.6, 1070.6) could not be assigned to peptide sequences identified using nanoLC-MS/MS.

In conclusion, two new potential substrates of Meprin α were identified: Tropoelastin and Elastin. In general, the turnover of both substrates by Meprin α C308A seemed to be faster than by Meprin α wild type. Based on these results and assuming both proteases are homogenous and fully active, it can be stated that the helix formation of Meprin α has little effect on its activity towards large, native substrates, at least for the tested conditions and substrates *in vitro*. This is in accordance with previous results, whereby the helix formation seems to lead to reduced catalytic efficiency towards the small fluorogenic substrate Abz-YVADPK(Dnp)G-OH (chapter 3.3.2, figure 38, p. 79). Consequently, the rather unstable Meprin α variant C308A appears to have higher catalytic activity than the more stable helical Meprin α wild type.

Nevertheless, the helix formation could be an artifact of concentration or recombinant protein production. Investigations on this assumption are presented in the next chapter 3.4.

3.4 Do Meprin α Helices Occur *In Vivo*?

According to the results obtain in chapter 3.3 (pp. 76), it is questionable whether the observed Meprin α helices are an artifact of concentration or recombinant protein production. To address the first point, an investigation was performed, applying Meprin α wild type in a concentration range from 15.3 µM to 15.3 nM, followed by cryo-EM analysis (figure 42).

A   15.3 µM Meprin α wild type

B   1.53 µM Meprin α wild type

C   153 nM Meprin α wild type

D   15.3 nM Meprin α wild type
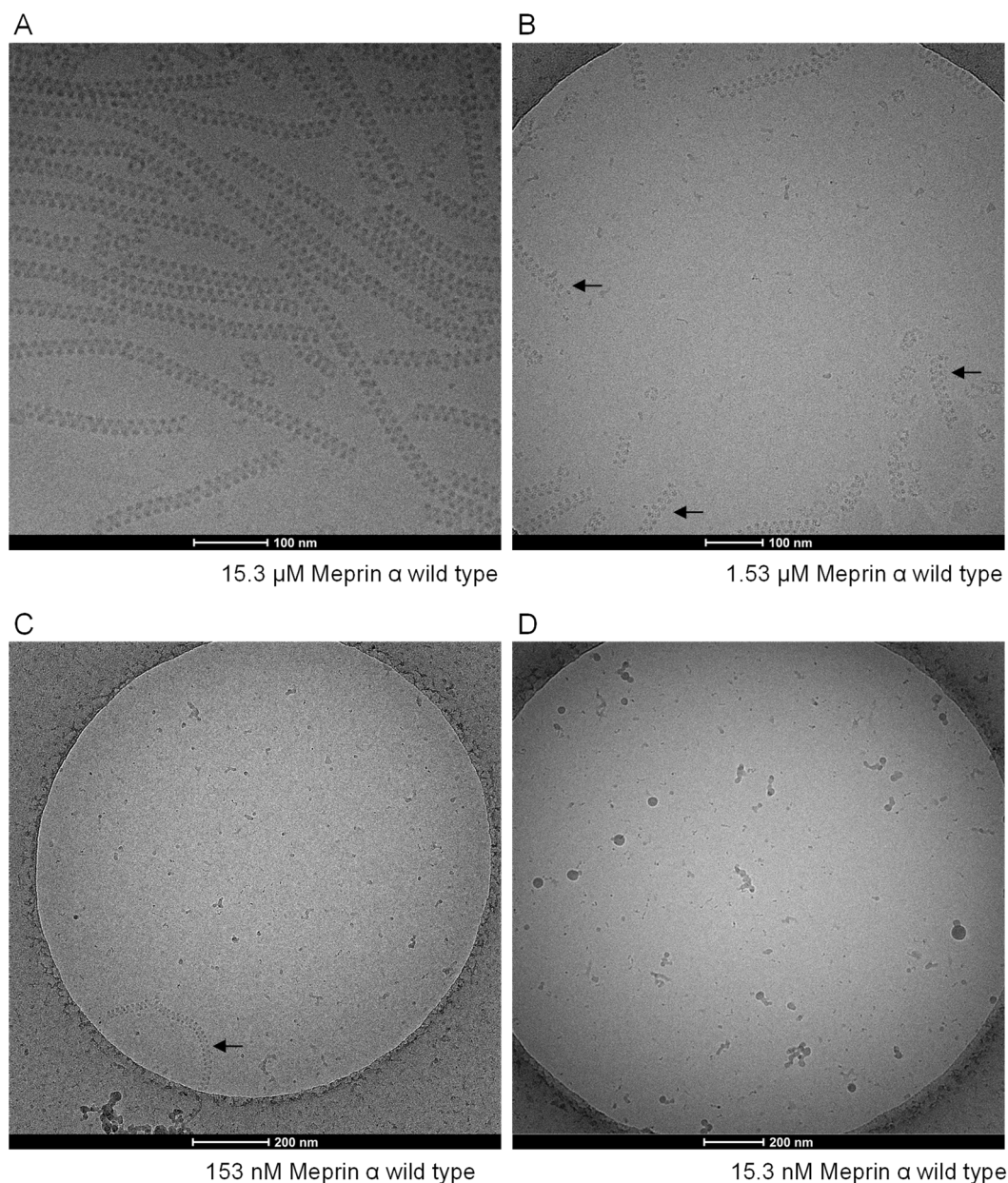
Figure 42: Electron micrographs of mature Meprin α wild type at different concentrations. *Images were recorded at a Tecnai 12 electron microscope. The samples were frozen on a glow-discharged QUANTIFOIL® Cu R2/2 using the Vitrobot System (4°C, 100% humidity, blot force: -5, blot time: 2.5 s; drain time: 1 s). Meprin α helical oligomers are highlighted by arrows.* ***A)*** *15.3 µM Meprin α wild type.* ***B)*** *1.53 µM Meprin α wild type.* ***C)*** *153 nM Meprin α wild type.* ***D)*** *15.3 nM Meprin α wild type.*

At a concentration of 153 nM, still helical particles were observed, diluting further to 15.3 nM no particles could be observed anymore, which is most likely due to the low number of remaining particles on the grid, that have not been detected by imaging.

But, a higher number of small particles were observed correlating with decreased concentration of Meprin α, which might indicate a dissociation of the helical particle at lower enzyme concentrations.

In an attempt to determine the presence of oligomeric Meprin α *in vivo*, an analysis of urine from mice, which were challenged with Cisplatin, was performed. Cisplatin-treated mice serve as a model for acute kidney injury (Perše and Večerić-Haler 2018). Upon IR-injury and Cisplatin-induced acute kidney injury in rodents, Meprins undergo a redistribution from apical brush-border membrane to basolateral tubular basement membrane. Hence, they are in contact with their substrates, which leads to degradation of basement membrane components (Carmago et al. 2002; Norman et al. 2003; Kaushal et al. 2013) and finally enables the detection of Meprins in urine. Additonally, the culture supernatant of the cell line Caco-2, a heterogeneous human epithelial colorectal adenocarcinoma cell line, was investigated regarding endogenous expression of Meprin α. The presence of Meprin α in urine was already stated in the literature (DeGuzman et al. 2004; Beynon et al. 1996). It was also reported that Caco-2 cells express endogenous Meprin α post-confluence (Lottaz et al. 1999; Rösmann et al. 2002; Thul et al. 2017; Pontén et al. 2008).

The Western blot analysis of urine from mice and Caco-2 supernatant are depicted in figure 43. Urine of two wild type mice, challgend with Cisplatin, were investigated in reducing, non-reducing SDS-PAGE and native PAGE. Recombinantly expressed Meprin α wild type served as positive control. For the two urine samples, bands above 100 kDa in reducing SDS-PAGE and bands above 250 kDa in non-reducing SDS-PAGE were obtained. The bands detected for the samples are slightly slower migrating than the bands observed for the positive control, most likely due to C-terminal truncation of recombinatly expressed Meprin α. In native PAGE, a similar migration behaviour of murine urine Meprin α and recombinant human Meprin α was observed. Analyzing the Caco-2 supernatant at different time points, it was observed, that from 3 d to 32 d post-confluence endogenous Meprin α is expressed by Caco-2 cells. Samples were analyzed in reducing and non-reducing SDS-PAGE, the detected bands comply with the bands observed in urine from mice. These results indicate that an oligomeric form of Meprin α or rather tetramers might be present *in vivo*. However, further investigations of the samples using cryo-EM and immunogold-labeling on negative stained grids did not led to visualization of endogenous helical particles.

Consequently, it can be summarized, that the investigated samples are suitable for detection of endogenously expressed Meprin α. But, based on these results it just can be speculated that the large, helical Meprin α structures exist *in vivo*. For prove of endogenous Meprin α helices, further analyses are required.
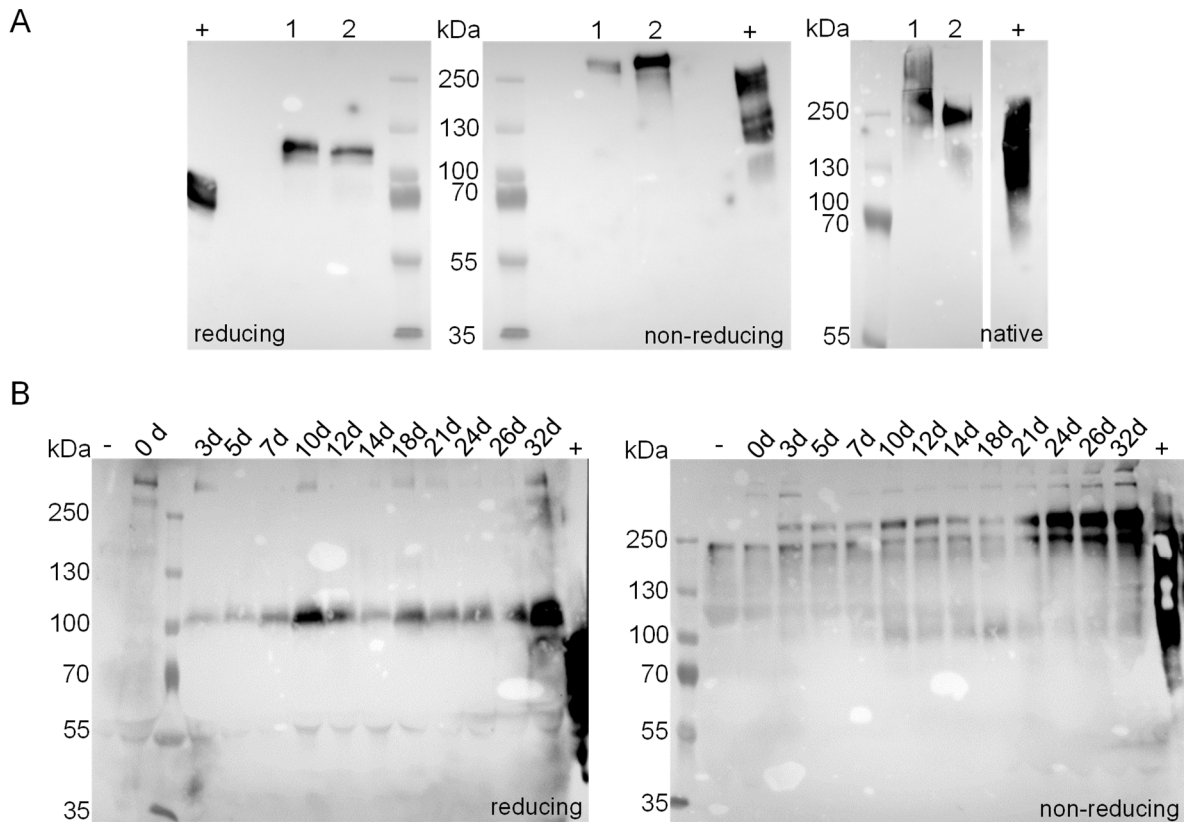
Figure 43: Western blot analysis of Meprin α from murine urine (Cisplatin-treated mice) and Caco-2 tissue culture supernatant. *SDS-PAGE analysis (7%T) using reducing denaturing and non-reducing denaturing conditions, followed by Western blot, detection with primary antibody goat-anti-human Meprin α and secondary antibody anti-goat-HRP applying chemiluminescence. **A)** 30 µl of urine collected from two different Cisplatin-treated wild type mice were applied onto the gel. + positive control: 1 µg recombinant Meprin α wild type. Additionally, a native PAGE was performed. **B)** 30 µl of collected supernatant at certain time points post-confluence from Caco-2 cell culture (0 d equals 100% confluence) were applied onto the gel. + positive control: 1 µg recombinant Meprin α wild type, - negative control: 30 µl of pure culture media (MEM) supplemented with 10% FBS.*

4 Discussion

The enzymes Meprin α and Meprin β are metalloproteinases, which are involved in proteolytic cleavage of several protein substrates of the extracellular matrix, among those Collagen IV, Fibronectin and Procollagens, but also Cytokines such as TGF-β and IL-18 (Walker et al. 1998; Bertenshaw et al. 2001; Kruse et al. 2004; Vadon-Le Goff et al. 2015; Banerjee and Bond 2008). The proteases are characterized by a quite unique substrate specificity, which differs from that of e.g. MMPs. Hence, specific inhibitors could be discovered, which might represent future drugs for treatment of fibrosis, cancer and inflammatory disorders.

In particular, the isoenzymes Meprin α and Meprin β belong to the astacin family of metalloproteases (Beynon et al. 1981; Barnes et al. 1989). They are expressed as zymogens (Sterchi et al. 2008). The propeptide at the N-terminus is connected with the protease domain followed by the MAM domain, TRAF domain, EGF-like domain, transmembrane domain and the cytosolic tail (Arolas et al. 2012). The major structural difference between the two proteases is the 'inserted domain' in Meprin α, which causes the release of Meprin α into the extracellular space, whereas Meprin β remains at the membrane (Marchand et al. 1995; Tang and Bond 1998; Broder and Becker-Pauly 2013). Upon shedding of Meprin α from the membrane, oligomers in the MDa range are built by non-covalent interactions of Meprin α dimers, as shown for recombinant mouse and rat and Meprin α *in vitro* (Ishmael et al. 2001; Bertenshaw et al. 2003).

Whereas Meprin α cleaves at neutral aliphatic (A, V), aromatic (Y, W) and negatively charged side chains (D, E), Meprin β has a striking preference for negatively charged amino acids (Bertenshaw et al. 2002; Villa et al. 2003; Becker-Pauly et al. 2011; Sterchi et al. 2008). The reason is the difference of the amino acids shaping the subpockets of the active site cleft. Three Arginine residues are located in the active site cleft of Meprin β: R^{184} (S1), R^{238} (S1') and R^{146} (S2'), which correspond to two Tyrosine and one Arginine residue within the subpockets of the Meprin α active site cleft: Y^{187} (S1), R^{242} (S1') and Y^{149} (S2'). The substrate specificity reasons the key role of Meprins in fibrosis and keloids, but also in nephritis and neurodegeneration (Bien et al. 2012). Selective inhibitors based on a tertiary amine scaffolds were developed (Ramsbeck et al. 2018; Tan et al. 2018). For further drug design and optimization, the determination of the binding modes of the inhibitors in the active site would be helpful. Accordingly, the first goal of the present work was to elucidate the structures of Meprin α and Meprin β in complex with inhibitors. The structure of Meprin β was determined by X-ray crystallography at a resolution of 2.41 Å. However, the electron density for the specific inhibitor bound to the active site is ambiguous. Because, a crystal structure is a snapshot of one conformation, additionally the cryo-EM structure of Meprin β was determined, which finally provided additional information on the interactions of the specific inhibitor within the active site.

In case of Meprin α, the expression yield was too low for crystallography. Additionally, Meprin α forms large oligomeric structures, which could prevent the crystal growth. By generation of Meprin α mutants a dimeric Meprin α should be produced. Since the expression yield was still too low for crystallography and the quaternary structures of the dimeric Meprin α variants seemed to be heterogenous, the cryo-EM single particle analysis approach was used to elucidate the structure of Meprin α (2.42 Å). Cryo-electron micrographs, obtained from human Meprin α, revealed large helical oligomers, which have been described before (Beynon et al. 1981; Köhler et al. 2000; Bertenshaw et al. 2003). Consequently, the second goal of the present work was to investigate the structural basis for the helix formation and if this has an impact on stability and activity of the protease.

4.1 Heterologous Expression, Purification and Characterization of Meprins

Several expression systems were used for heterologous expression of Pro-Meprin β, such as Baculovirus (Becker-Pauly et al. 2011; Arolas et al. 2012) and HEK 293 cells (Bien et al. 2012). In the present study, Pro-Meprin β was expressed using the methylotrophic yeast strain *Pichia pastoris* X33*,* which offers high-level expression similar to procaryotes, and introduces post-translational modifications, such as disulfide bonds, N-glycosylation, and enables secretion of the protein of interest into the media (Macauley-Patrick et al. 2005). The ability of *P. pastoris* to form N-linked glycosylations and disulfide bonds enables the correct folding, stability and activity of the expressed proteins (Cereghino et al. 2002). Also, the limited endogenous expression of secreted proteins facilitates the purification of the protein of interest from the media (Cereghino and Cregg 2000; Tachioka et al. 2016). Additionally, the media applied for growth of *P. pastoris* and high-density fermentation for protein production is relatively cheap, which makes this expression system even more attractive.

The expression of Pro-Meprin β in *P. pastoris* was previously described (Schlenzig et al. 2015). An N-terminally and C-terminally His-tagged Pro-Meprin β was expressed, spanning the amino acids T^{23} to T^{652} (propeptide to EGF-like-domain). In the present study, a C-terminally truncated Pro-Meprin β (T^{23}-Q^{595}) was cloned and expressed, including the propeptide, protease, MAM and TRAF domain. The flexible C-terminal domains were not expressed, because they could interrupt the crystal growth and, as it has been proven, are not necessary for activity (chapter 3.1.1.1, p. 38). Although it was reported, that the C-terminally His-tagged Meprin β shows a higher expression rate than the N-terminally His-tagged variant (Schlenzig et al. 2015), in the present study a Tag was fused to the N-terminus in order to remove the Tag after activation of Pro-Meprin β. Tag removal was intended to facilitate the crystallization.

The optimization of the codon usage to the expression system can lead to increased production of the recombinant protein (Gustafsson et al. 2004; Bai et al. 2011; Wang et al. 2015a). In order to obtain high expression rates, two constructs of Pro-Meprin β, either harboring the native coding sequence or a codon optimized open reading frame, were used. The expression rate was analyzed by activity determination. In contrast to the results described in the literature, no increased expression rate was obtained after codon-optimization for *P. pastoris*. Nevertheless, clones of low, medium and high Pro-Meprin β expression levels were identified, which is likely a result of different numbers of gene copies integrated into the genome of *P. pastoris* after transformation (Cereghino and Cregg 2000). This was previously shown for other proteins expressed in *P. pastoris,* e.g. porcine Insulin precursor and Proteinase K (*Tritirachium album Limber*) (Zhu et al. 2009; Yang et al. 2016). In general, the isolation of multi-copy integrants is desired. In consequence, the clone with the highest expression rate (human codon usage) was used for production and finally secretion of Pro-Meprin β into the fermentation supernatant.

The purification process for Pro-Meprin β from yeast fermentation supernatant was previously described (Schlenzig et al. 2015). After the last step (SEC), a specific activity of 36 U/mg for mature Meprin β could be determined (assay conditions: 40 mM TRIS pH 8.0 at 30°C using the substrate Abz-YVAEPK(Dnp)G-OH). A yield of about 7 mg/L was obtained for the expression and purification of mature Meprin β, which is five-fold higher in comparison to the yield of 1.3 mg/L described by Schlenzig et al. (2015). A comparable yield of 10 mg/L cell culture medium was reported for the expression of Meprin β using insect cells applying the Baculovirus system (Becker et al. 2003). In order to increase the yield of the heterologously expressed Meprin β, an exchange of the secretion signal might be helpful. The signal peptide of the invertase from *S. cerevisiae* (SUC-2) (Tschopp et al. 1987) or the *Phaseolus vulgaris* agglutinin (PHA) secretion signal sequence (Raemaekers et al. 1999) were described for recombinant protein production in *P. pastoris*. Additionally, the yeast serine endoprotease Kex2 might lead to degradation of Pro-Meprin during secretory pathway through the trans-Golgi network, and therefore leading to reduced yield in case of Pro-Meprin β. This protease cleaves C-terminally of the dibasic motif RR or KR (Diane Hopkins et al. 2000; Yang et al. 2013; Pyati et al. 2014), Pro-Meprin β comprises three potential cleavage sites.

Whereas the generation of a Pro-Meprin β expressing *P. pastoris* clone and subsequent purification was successful, Pro-Meprin α could not be expressed using yeast. In previous work several attempts were done to obtain recombinant Pro-Meprin α from *P. pastoris*. Beside the expression using *P. pastoris* X33, also the strain SMD1168H, which is deficient in Protease A, was used.

Additionally, the variation of the expression conditions, i.e. temperature, pH, time and amount of methanol for induction, did not improve the expression and led to a secreted 30 kDa fragment of Pro-Meprin α, most likely due to degradation (Tüting 2015). As already described for Pro-Meprin β, Pro-Meprin α harbors four potential Kex2 cleavage sites, which might contribute to degradation. Furthermore, for the expression of full-length triple helical collagen type I and III in *P. pastoris* it was shown, that the molecules accumulate within the endoplasmatic reticulum (Vuorela et al. 1997; Nokelainen et al. 2001). The expression of single polypeptide chains and fragments of those was successful (Pakkanen et al. 2006). This indicates, that the secretion system of *P. pastoris* might not be suitable for secretion of large protein complexes, as those formed by Meprin α. Since, the expression trials in *P. pastoris* were performed with a Meprin α constructs lacking the membrane anchor, maybe the oligomerization of Meprin α dimers occurred within the cell, which led to accumulation in the endoplasmatic reticulum and further to degradation of the protease. Consequently, the expression of full length Meprin α in yeast and shedding from the membrane by endogenous furin (Huang et al. 2018) might lead to successful expression and secretion of the protease. Interestingly, for the production of recombinant human, mouse or rat Meprin α only insect cells or mammalian cell lines are described, an overview is shown in table 12.

Table 12: Overview about described expression systems used for production of recombinant Meprin α.
AA: amino acids, COS-1: fibroblast cell line derived form monkey kindey, HEK 293: human embryonic kidney cell line, SF21: Spodoptera frugiperda 21.

Meprin α primary sequence	Expressionsystem	Reference
Mouse, wild type fulllength and mutants w/o or modified 'inserted'domain	COS-1	Marchand et al. 1995
Mouse, wild type fulllength and C-terminally truncated mutants C302A and C289A (AA1-570)	HEK 293	Marchand et al. 1996
Mouse, wild type fulllength	HEK 293	Ishmael et al. 2001
Mouse, wild type fulllength and single N-linked glycosylation mutants	HEK 293	Ishmael et al. 2006
Rat, wild type C-terminally truncated (AA1-603)	HEK 293	Bertenshaw et al. 2002, 2003
Human, wild type fulllength, wild type C-terminally truncated (AA1-263)	SF21, Baculovirus system	Köhler et al 2002
Human, wild type fulllength	See Köhler et al. 2002	Becker et al. 2003 Becker-Pauly et al. 2011

Because all the attempts for the heterologous expression of human Meprin α in yeast failed, insect cells, i.e. Schneider's *Drosophila* S2 cells, were used and tested previously (Tüting 2015). The S2 cells are an easy-to-use expression system providing the ability to grow as adherent culture or in suspension (Schneider 1972). The suspension culture enables a growth to high density and the S2 cells can be cultured in serum-free media.

Additionally, the generation of a stably transformed cell line simplifies the expression and by the help of the secretion signal of the Immunoglobulin-binding protein (BiP) the protein of interest will be secreted into the media (Kirkpatrick et al. 1995). The expression of functional human Meprin α in insect cells, applying the Baculovirus system, was successfully described before (Köhler et al. 2000). In the present study, a C-terminally truncated Pro-Meprin α was expressed, including the propeptide, protease, MAM and TRAF domain (V^{22}-S^{600}). The MAM domain is necessary for the correct folding and transport through the secretory pathway and the TRAF domain might be responsible for correct folding of an activable zymogen (Tsukuba and Bond 1998). The C-terminal domains were not expressed, because they are not necessary for activity and proper folding (Marchand et al. 1996). Moreover, it was assumed that these domains might interfere with crystal growth. The cloning of an N-terminal STREP-Tag should simplify the purification and has the advantage that it is removed by activation of the protease. The usage of a STREP-Tag was preferred over a His-Tag, because the amino acid Histidine shows higher prevalence in insect and human proteins and thus immobilized metal affinity chromatography is frequently less efficient for purification of recombinant proteins (Kimple et al. 2013). In general, for purification of proteins from yeast supernatants, the STREP-Tag is not preffered, because the media contain biotin, which also binds to the column material (Strep-Tactin®) and is usually used for elution of the protein of interest during purification. Consequently, the binding of the STREP-tagged protein would be impaired.

The purification process of Pro-Meprin α from S2 cell expression media was previously developed by colleagues at Fraunhofer IZI-MWT. In the present study, a noticeably high yield loss of >90% after the affinity column (Strep-Tactin®) could be identified. Several attempts to optimize the expression and purification were undertaken. However, these did not improve the process, which might be due to reduced accessibility of the Tag to the column material, because it may be buried within the Pro-Meprin α oligomeric structures. The complete activation of Pro-Meprin α by immobilized Trypsin on magnetic beads took about 48 h at room temperature, which also indicates a buried N-terminus of Pro-Meprin α, either within the structure or within the helical oligomers built up by Pro-Meprin α dimers. In line with this, is the fact that the activation of dimeric Meprin α mutants (C308A, R372T) is much faster (60 min), although only 150 U immobilized Trypsin per mg Meprin α mutants were used instead of 600 U/mg, which was applied to activate Meprin α wild type. This corresponds to a 4-fold higher amount of immobilized Trypsin required to activate Meprin α wild type. Marchand et al. also described that the wild type helical murine Meprin α is more stable against proteolytic degradation than the monomeric mutants (Marchand et al. 1996). For activation of wild type murine Meprin α Marchand et al. applied about a 4-fold higher amount of free Trypsin (40 ng Trypsin per µl Meprin α) in comparison to the activation of the monomeric mutants (5-10 ng Trypsin per µl Meprin α), which confirms the results obtained in the present study.

Analyzing the composite map of the obtained Meprin α reconstruction (chapter 3.2.3, figure 31, p. 69), obviously the protease domain and especially the active site cleft points towards the inner site of the helical particle.

Despite the low yield and a long activation time by magnetic Trypsin beads, homogenous Meprin α with a specific activity of 3.2 U/mg was isolated (assay conditions: 50 mM HEPES pH 7.4 buffer containing 150 mM NaCl at 30°C using the substrate Abz-YVADPK(Dnp)G-OH). Using the PABA-peptide (N-benzoyl-tyrosyl-p-amino-benzoic acid), a specific activity of 0.7 U/mg was determined previously for human Meprin α expressed using the Baculovirus system (Köhler et al. 2000). For murine Meprin α expressed in mammalian cells, a specific activity of 6.1 U/mg was determined, which is similar to the specific activity of isolated Meprin α from mouse kidney (6.8 U/mg, substrate BK$^+$: Abz-RPPGFSPFRK(Dnp)G-OH) (Marchand et al. 1996). However, application of the short peptide substrate Abz-YVADPK(Dnp)G-OH for the determination of the kinetic parameters for both Meprins, revealed a v/S-characteristic showing substrate inhibition.

For the tested conditions (50 mM HEPES pH 7.4, 150 mM NaCl, 30°C) a catalytic efficiency k_{cat}/K_m for Meprin α of $0.271\pm0.02\ \mu M^{-1}s^{-1}$ and for Meprin β of $0.265\pm0.00004\ \mu M^{-1}s^{-1}$ was determined. Thus, the determined catalytic efficacy towards the substrate Abz-YVADPK(Dnp)G-OH, which is cleaved between Alanine and Aspartate, is almost equal for both Meprins and consistent with the observed preference for Alanine in P1 and for Aspartate in P1' position (Becker-Pauly et al. 2011).

For the turnover of peptides by human Meprin β catalytic efficiencies of $3.3\pm0.1\ \mu M^{-1}s^{-1}$ (substrate: Abz-YVAEPK(Dnp)G-OH, measurement without salt in the buffer) and $1.3\pm0.03\ \mu M^{-1}s^{-1}$ (substrate OCK$^+$: Abz-MGWMDEIDK(Dnp)SG-OH, measurement without salt in the buffer) were reported (Schlenzig et al. 2015). Using the substrate OCK$^+$, for rat Meprin β a k_{cat}/K_m of $12\pm1\ mM^{-1}s^{-1}$ was determined (Bertenshaw et al. 2002). According to Bertenshaw et al. the increase of salt (>1M NaCl) within the reaction buffer leads to inactivation of rat Meprin β (subtrate: OCK$^+$). The reason for this observation might be that in presence of salt electrostatic interactions are reduced (Zhang et al. 2007; Zhou and Pang 2018), this means that the affinity of Meprin β to its substrates might be decreased and consequently a substrate turnover does not take place. It might be also possible, that the catalytic zinc was exchanged in presence of high amounts of NaCl (>1M) and consequently, Meprin β was inactivated. Additionally, it can be stated that the C-terminal truncation of Meprin β and also Meprin α did not led to inactive proteases, consequently the EGF-like domain, the 'inserted' domain (Meprin α) and the cytosolic tail are not required for catalytic efficiency.

Investigation on the molecular mass of deglycosylated, native Meprin β by analytic ultracentrifugation (AUC, executed by Prof. Hauke Lilie, Martin-Luther-University Halle-Wittenberg) revealed a homogenous sample with a size of 158 kDa, which is higher than the calculated mass of 121.5 kDa (ExPASy, ProtParam tool, data not shown). The difference in predicted and determined molecular mass are a result of N-linked glycosylation at Meprin β produced by the expression system *P. pastoris* (Hamilton et al. 2003; Tanner and Lehle 1987; Tang et al. 2016). Since the deglycosylation was done under native conditions, not all glycosyl chains were removed. It was reported that Meprins are highly glycosylated and that about 15% of the molecular mass is due to glycosylation (Bertenshaw et al. 2003; Schlenzig et al. 2015). About 26% of those glycosylations could not be removed by deglycosylation (Schlenzig et al. 2015). Additionally, the diffuse bands of glycosylated and deglycosylated, native Meprin β in SDS-PAGE are an indication of glycosylations still present on the enzyme (chapter 3.1.2, figure 12, p. 41), which was also previously shown for Meprin (Marchand et al. 1994).

However, the high degree of glycosylation typically generates disadvantages for crystallization. Therefore, Meprin β was partially deglycosylated in its native state. However, the protease was unstable under conditions applied for crystallization, i.e. at high protein concentration and in partially deglycosylated state. Already after seven days of incubation the protease was degraded, most likely due to a previously unkown autocatalytic activity, which was prevented by addition of the specific inhibitor MWT-S-270 or the commercial inhibitor Actinonin. Autocatalytic activity was already described for Pro-Astacin (Yiallouros et al. 2002; Guevara et al. 2010), but also for the metzincin Pro-ADAM 8 (Schlomann et al. 2002) and for Thermolysin-like proteases (Gao et al. 2010). This is the first time an autocatalytic activity has been observed for Meprin β. Possibly, this was not observed in previous studies, because a deglycosylation and concentration (to 13 mg/ml) was not performed. Consequently, the glycosylations may also contribute to the stability of Meprin β and abolish autocatalytic activity. The contribution of glycosylations on protein stability is already described (Lee et al. 2015; Jayaprakash and Surolia 2017). Also, for Meprin α wild type and its mutant C308A autocatalytic activity was observed. The nanoLC-MS/MS analysis, performed during substrate cleavage analysis (chapter 3.3.2, pp. 83), identified peptides of Meprin α, after incubation at 37°C for 24 h. Apparently, self-cleavage of astacin proteases is a common feature *in vitro*.

4.2 Structures of Meprin α and Meprin β in Complex with Selective Inhibitors

4.2.1 Comparison of the Protein Fold of Meprin α and Meprin β

On the basis of the succesful isolation of Meprin α and Meprin β, a structural investigation of enzyme-inhibitor complexes was performed. The crystal and cryo-EM structures of mature Meprin β with the inhibitor MWT-S-270 (IC_{50} 49±11 nM) were elucidated to a resolution of 2.41 Å and 3.00 Å, respectively (chapter 3.1.4/3.1.5, pp. 43). A resolution of 2.42 Å could be obtained for the cryo-EM structure of Meprin α in complex with the inhibitor MWT-S-698 (IC_{50} 160±1 nM, chapter 3.2.3, pp. 68). The applied synthetic inhibitors are shown in chapter 1.3 (figure 4, p. 10). The X-ray structure of mature Meprin β without inhibitor was previously determined to a resolution of 3.00 Å (PDB:4GWM) (Arolas et al. 2012). A structure of Meprin α was not described before. These novel achievements allow a comparison of the protein fold of Meprin β and Meprin α, also within the context of other astacin proteases. Additionally, a comparison of the cryo-EM and crystal structure of Meprin β is discussed with respect to the different binding of the inhibitor within the active site cleft. An overview about main features of the here obtained and previously published Meprin structures is listed in table 13.

Table 13: Overview of main features of Meprin structures obtained in the present study and previously published (Arolas et al. 2012).

Feature	Meprin α (present study)	Meprin β (present study)	Meprin β (present study)	Meprin β 4GWM	Meprin β 4GWN
Method used for structural elucidation	Cryo-EM chain A/B: N^{66}-S^{600}	X-ray chain A/B: N^{62}-T^{594}	Cryo-EM chain A/B: N^{62}-N^{592}	X-ray chain A: E^{25}-Q^{597} chain B: P^{23}-S^{593}	X-ray N^{62}-T^{594}
Active/inactive protease	Active	Active	Active	Inactive	Active
Inhibitor in active site	MWT-S-698	MWT-S-270	MWT-S-270	-	-
Chains	A/B	A/B	A/B	A/B	A
Number of intermolecular disulfide bridges	1	1	0	0	0
Intramolecular disulfide bridges in protease domain	2/chain	2/chain	2/chain	2/chain B 1/chain A	2/chain
Intramolecular disulfide bridges in MAM domain	2/chain	2/chain	2/chain	2/chain	2/chain
Ions within MAM domain	$2 \times Ca^{2+}$/chain	$2 \times Ca^{2+}$/chain	$2 \times Ca^{2+}$/chain	$1 \times Na^{2+}$	$1 \times Na^{2+}$
Catalytic ion	Zinc	Zinc	Zinc	Zinc	Cadmium

Feature	Meprin α (present study)	Meprin β (present study)	Meprin β (present study)	Meprin β 4GWM	Meprin β 4GWN
Glycosylations within protease domain	N^{140}/A+B N^{222}/A+B N^{258}/A+B	N^{218}/A+B N^{254}/A+B	N^{218}/A+B N^{254}/A+B	N^{218}/A+B N^{254}/A+B	N^{218}, N^{254}
Glycosylations within MAM domain	-	-	-	N^{370}/A+B	N^{370}
Glycosylations within TRAF domain	N^{440}/A+B	N^{445}/A+B N^{547}/A+B N^{592}/A	N^{445}/A+B N^{547}/A+B	N^{436}/A+B N^{445}/A+B N^{547}/A+B	N^{436}, N^{547}, N^{592}

The sequence alignment between human Meprin α and human Meprin β revealed a sequence identity of 46% (chapter 3.2.1, p. 57). The superposition of the cryo-EM structure of Meprin α and the crystal structure of Meprin β reveals a very similar fold, including the protease, MAM and TRAF domain (figure 44). Both 3D-structures colored according to their domains are shown in figure 14 (chapter 3.1.4, p. 43) and figure 18 (chapter 3.1.5, p.49) for Meprin β and figure 32 (chapter 3.2.3, p.70) for Meprin α.
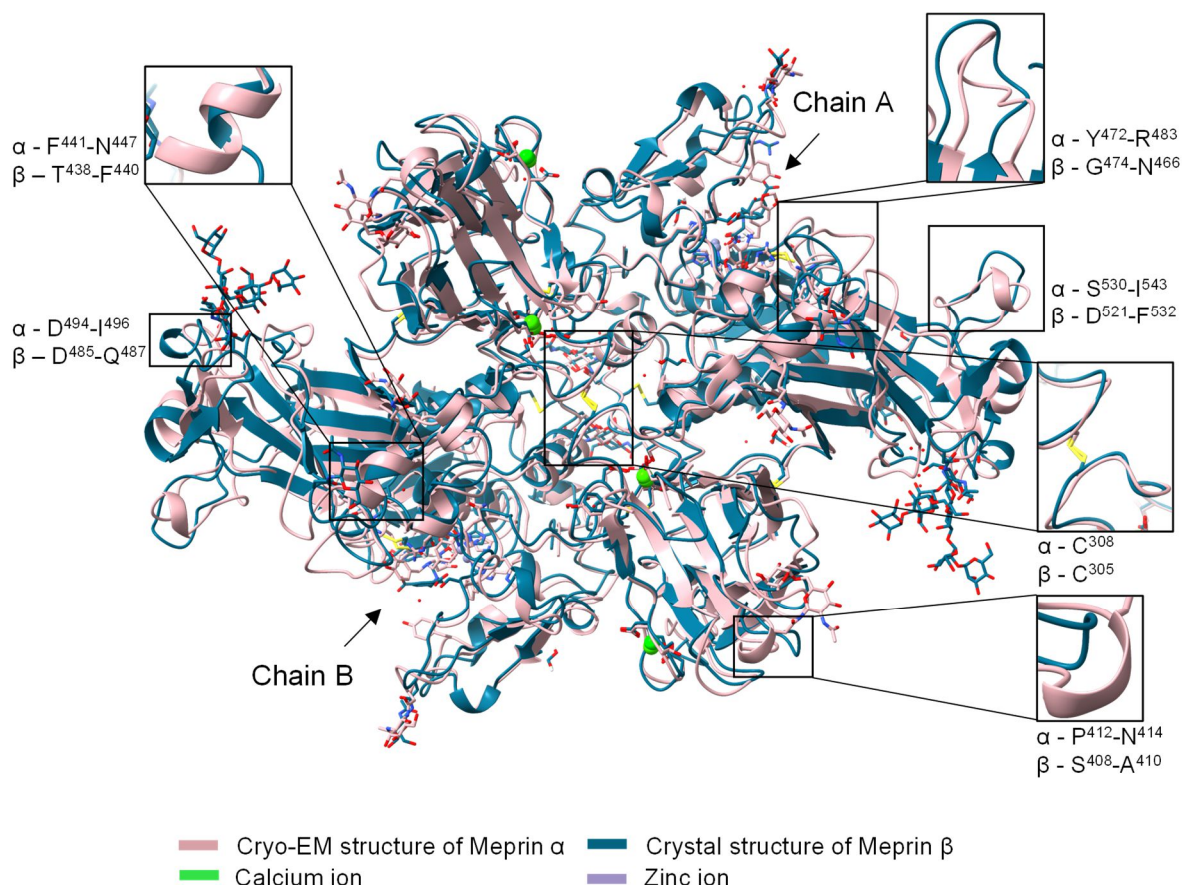
Figure 44: Comparison of Meprin β and Meprin α structures. Superposition of the Meprin β structure obtained by crystallography and the Meprin α structure obtained by cryo-EM single particle analysis (RMSD 1.997 Å). The inhibitors, glycosyl chains and solvent molecules are presented as sticks. The arrow highlights the active cleft of chain A and chain B of both proteases. Major differences in fold are highlighted in boxes.

Both proteases occur as dimeric molecules (chain A and chain B) linked by a disulfide bridge within the MAM domain. Based on *in vitro* studies performed with recombinant murine Meprin α, the MAM domain was previously reported to be involved in the interaction of two Meprin α monomers (Marchand et al. 1996). The 3D-structures of Meprin α and Meprin β, shown in the present study, now provide evidence for the intermolecular disulfide bond, enabling the formation of Meprin dimers. In Meprin α the intermolecular disulfide bridge is formed by C^{308} and in Meprin β by C^{305}, of chain A and chain B, respectively. In general, minor differences of the architecture of the MAM domain are observed between mature Meprin α and mature Meprin β. At P^{412}-N^{414} a 3_{10}-helix is observed in Meprin α, in Meprin β (crystal structure of the present study and 4GWM, S^{408}-A^{410}) a loop is found, which shows different orientation than the 3_{10}-helix in Meprin α (figure 44). The two intramolecular disulfide bonds within the MAM domain are observed in both enzymes. These are also existing within the Meprin β structure 4GWM described previously (Arolas et al. 2012). Two coordinated tentative calcium ions are observed in the Meprin α cryo-EM structure and both Meprin β structures within the MAM domain. The MAM domain was first discovered in Meprin α, Meprin β, A5 protein and receptor protein tryrosine phosphatase μ (Beckmann and Bork 1993) and was described to be involved in protein-protein interaction and cell adhesion (Cismasiu et al. 2004). In fact, the oligomerization of Meprin α is mainly mediated by electrostatic interactions via the MAM-TRAF interfaces (further discussed in chapter 4.3, pp. 105).

Comparing the TRAF domain of both proteases, some differences of the secondary structure elements are observed. The overall structure of the TRAF domain in Meprin α is characterized by one four-stranded and one three-stranded antiparallel *β*-sheet. In the Meprin β crystal structure elucidated within the present study and the previously described structure 4GWM (Arolas et al. 2012) two four-stranded antiparallel *β*-sheets are found. Additionally, some loop regions differ, these are in Meprin α Y^{472}-R^{483} and S^{530}-I^{543}, corresponding to G^{474}-N^{466} and D^{521}-F^{532} in Meprin β. The amino acids F^{441}-N^{447} form an α-helix in Meprin α, in Meprin β a 3_{10}-helix is observed (T^{438}-F^{440}). In case of the Meprin β crystal structures (of the present study and 4GWM) a 3_{10}-helix is observed including the amino acids D^{485}-Q^{487}, whereas in Meprin α the corresponding amino acids form a loop (D^{494}-I^{496}). Overall, the TRAF domains of both proteases are structurally similar to C-terminal domain of the tumor-necrosis factor-associated factor 6 (PDB: 1LB6) (Ye et al. 2002). In comparison to the MAM and protease domain, the TRAF domains of Meprin α and Meprin β, represent the domains owing most of the differences in secondary structure. This is based on the lower sequence identity of the TRAF domains of both Meprins (40%) in comparison to the MAM and the protease domain, which show a sequence identity of 44% and 56%, respectively. Both domains were previously described to be involved in association to mediate function of certain proteins.

It is shown that the MAM domain of Receptor-like Protein-tyrosine Phosphatase μ is involved in homophilic binding to form dimers (Cismasiu et al. 2004). This was also described for Neuropilin-2. Here, the homodimer formation mediated by the MAM domain is important for semaphoring-dependent signal transduction (Barton et al. 2015). Also, for Meprin α it was mentioned that the MAM domain is necessary for correct folding and transport through the secretory pathway. For the TRAF domain is was stated that it might be responsible for correct folding of an activable zymogen (Tsukuba and Bond 1998). Interestingly, the tumor-necrosis-factor-receptor-associated factor 2 and 6 (TRAF2/TRAF6) are transducers of e.g. TNF-α, TGF-β and IL-1 receptors (Walsh et al. 2015). This process is based on the oligomerization of the C-terminal domains of TRAF2 and 6, which are homologue to the TRAF domain in Meprins (Cheng et al. 1995; Baud et al. 1999). This supports the adhesive function of the C-terminal TRAF domain. Moreover, in the present study it could be shown that the MAM and TRAF domains are involved in oligomerization of dimeric Meprin α.

However, comparing the MAM and TRAF domains of the Meprin β structures obtained by cryo-EM and crystallography, as shown in the superposition depicted in figure 45, obviously in both structures these domains appear virtually identical, although the resolution of the cryo-EM structure is lower. Within the TRAF domain of the Meprin β crystal structure, three 3_{10}-helices are present that are not observed within the cryo-EM structure, including the residues T^{438}-F^{440}, D^{485}-Q^{487} and I^{508}-Q^{510}. Additionally, two α-helices were observed within the crystal structure, but not in the cryo-EM structure, including the residues P^{536}-V^{539} and S^{589}-N^{592}. Nevertheless, although the resolution of the cryo-EM structure is lower, all glycosylations identified from the crystal structure are also defined within the cryo-EM structure, except at N^{592}.

Within the MAM domain of the Meprin β cryo-EM structure, as already described for Meprin α and the crystal structure of Meprin β, two ions are coordinated and the two stabilizing disulfide bridges are also defined within the reconstruction. In contrast to the crystal structure, the intermolecular disulfide bridge at C^{305} could not be modelled within the cryo-EM structure, due to low resolution. Again, one 3_{10}-helix of the MAM domain (V^{272}-G^{274}), that is present in the crystal structure was not observed in the cryo-EM structure of Meprin β. In general, the MAM domain of the crystal structure of Meprin β is characterized by a *β*-sandwich composed of two four-stranded antiparallel *β*-sheets. In case of the cryo-EM structure the *β*-sandwich is composed of one four-stranded and one three-stranded antiparallel *β*-sheet. Here, the amino acids T^{324}-E^{328} occur as loop instead of a *β*-sheet. For the previously elucidated Meprin β crystal structure 4GWM a five-stranded *β*-sheet was observed (Arolas et al. 2012).
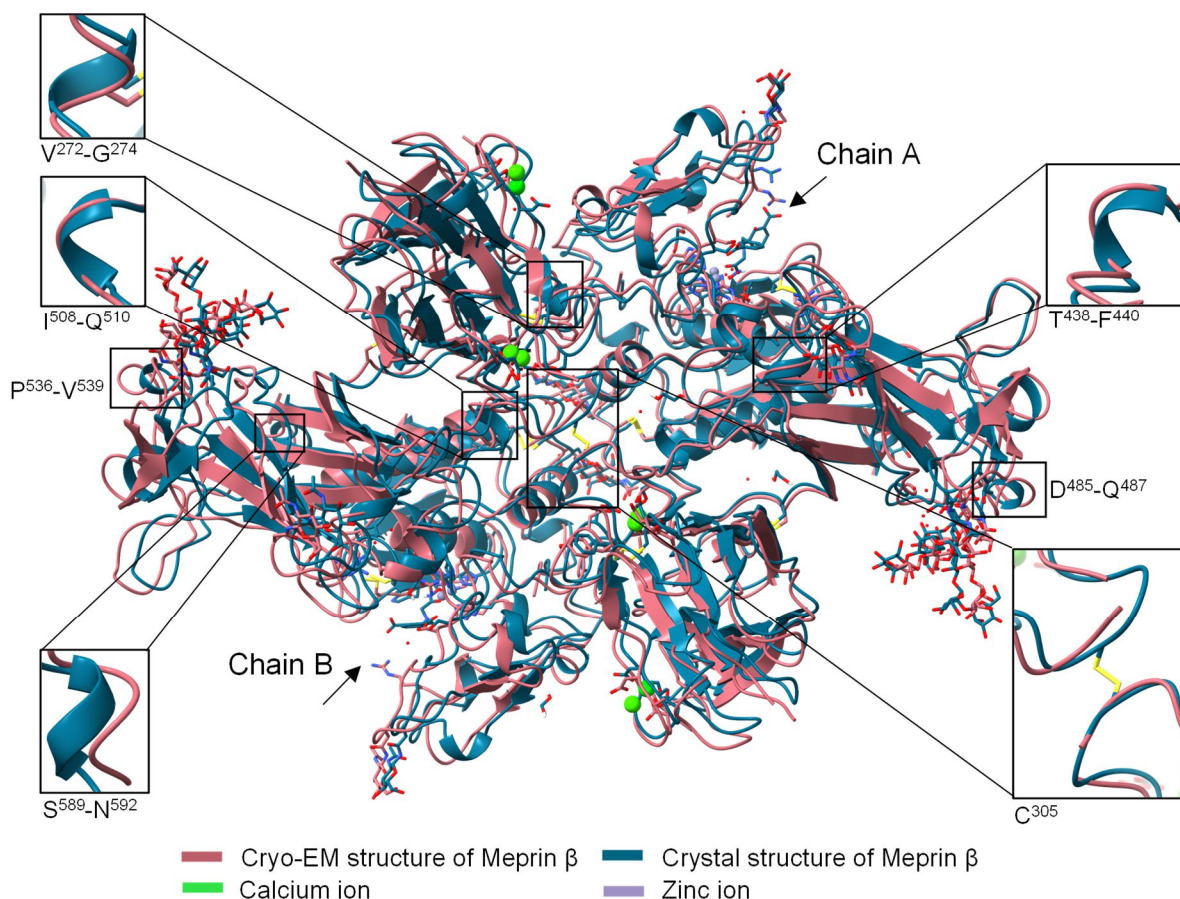
Figure 45: Comparison of Meprin β structures elucidated by cryo-EM and crystallography. *Superposition of the Meprin β structures obtained by crystallography and cryo-EM single particle analysis (RMSD 1.329 Å). The inhibitors, glycosyl chains and solvent molecules are presented as sticks. The arrow highlights the active cleft of chain A and chain B of both proteases. Major differences in fold are highlighted in boxes.*

Also the 3_{10}-helices within the MAM and TRAF domains, observed for the Meprin β crystal structure but not for the cryo-EM structure, are present in the previously published crystal structure 4GWM. These structural differences within the MAM and TRAF domains of the Meprin β cryo-EM and crystal structures might indicate the influence on the secondary structure by packing effects within the crystal or even due to the crystal growth conditions (Eyal et al. 2005). Especially in flexible regions of the protein, conformational changes occur due to packing within the crystal (Brito and Archer 2020). Nevertheless, most of these differences were observed on the surface of the protein, where the local resolution of the cryo-EM structure is even lower than 3.0 Å. As a consequence, the less defined electron density in these regions, might contribute to slightly different positions of the appropriate amino acids, which in turn lead to small differences within the secondary structure.

The superposition performed for the protease domains of the Meprin α cryo-EM structure, the Meprin β cryo-EM, crystal structure and 4GWN crystal structure, as well as for Astacin (PDB: 1AST) is shown in figure 46 A. The protease domains are virtually identical in secondary structure and are subdivided into an upper and lower subdomain ('standard orientation' (Gomis-Rüth et al. 2012)).

The upper subdomain is crosslinked by two disulfide bridges in Meprin β (C[103], C[255] and C[124], C[144]) and in Astacin protease (C[42], C[198] and C[64], C[84]), but in Meprin α (C[128], C[147]) only one disulfide bridge is observed, although both Cysteine residues are in proximity. The upper subdomain is characterized by a four-stranded antiparallel *β*-sheet as well as three α-helices. Within the Meprin β cryo-EM structure a three-straned β-sheet is observed, additionally loop regions instead of 3_{10}-helices are observed (E[67]-Y[69], W[177]-R[179]). The lower subdomain contains little secondary structure elements. Among all three domains of the Meprins expressed in the present study, the protease domain shows the highest sequence identity (56%), thus the secondary structure elements of the presented Meprin α and Meprin β structures are almost identical (figure 46).

In general, for all metzincins the conserved zinc-binding motif HExxHxxGxxH is characteristic (Bode et al. 1992; Stöcker et al. 1993; Stöcker et al. 1995; Gomis-Rüth 2003, 2009). The first part of this consensus sequence is harbored within an α-helix, which ends with a Glycine allowing for a sharp turn to enter the lower protease subdomain ('standard orientation'). Within the lower subdomain, the third Histidine residue and adjacent Glutamate, which was described to be specific for astacins (Bode et al. 1992; Stöcker et al. 1993; Arolas et al. 2012), is located and in agreement with the superposition in the same orientation in Meprin α, Meprin β and Astacin. In Astacin, besides an additional water molecule, Y[149] serves as a fifth zinc-binding ligand, as long as no substrate or inhibitor is bound, which results in a penta-coordinated zinc ion (Bode et al. 1992; Stöcker et al. 1993). This Tyrosine does never serve as a fifth zinc-binding ligand within Meprin α (cryo-EM structure of Meprin α with and without inhibitor (data not shown)) and Meprin β (4GWN, cryo-EM and crystal structure). The position of Y[149] is similar in Astacin with or without inhibitor (PDB: 1QJJ and 1AST), but based on the superposition different in Meprin α and Meprin β (figure 46 B). Considering the very similar fold of the protease domains, it is tempting to speculate that the substrate conversion (i.e. chemical step) occurs similarly. However, their substrate specificity differs, due to the different amino acids shaping the S1, S1' and S2' subpockets of the active site cleft. Meprin β, but also Meprin α show a preference for negatively charged amino acids in P1', in contrast Astacin favors small uncharged residues in P1' (Sterchi et al. 2008). For Meprin β three Arginine residues are located within the subpockets (S1: R[184], S1': R[238], S2': R[146]), in Meprin α two Tyrosine residues and one Arginine are found (S1: Y[187], S1': R[242], S2': Y[149]). Consequently, a broader substrate specificity for Meprin α than Meprin β was observed by PICS and TAILS analysis, which includes also a strong preference of T>A>V in P1' (Becker-Pauly et al. 2011). Derived from the sequence alignment (figure 64 in the appendix, p. 141), the corresponding subpockets in the Astacin protease are M[124] in S1, K[179] in S1' and Y[86] in S2' (figure 46 B).
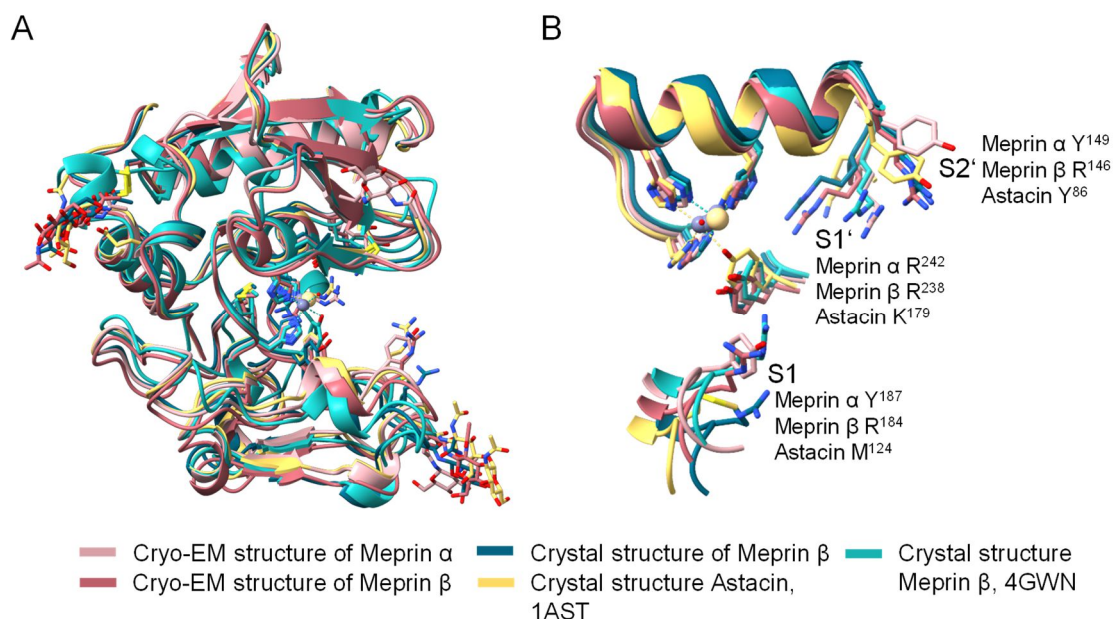
Figure 46: Superposition of the protease domains of Meprin β (present study and 4GWN (Arolas et al. 2012)) and Meprin α (present study) as well as Astacin protease (Bode et al. 1992). A) *Superposition of the whole protease domains (inhibitors not shown).* ***B)*** *Superposition of the active site motif, including three Histidine residues chelating the catalytic zinc and Tyrosine, serving as fifth zinc binding ligand in Astacin, as well as the amino acids within the S1,S1' and S2' subpockets (for Meprin β: S1, R^{184}; S1', R^{238}; S2', R^{146}; for Meprin α: S1, Y^{187}; S1', R^{242}; S2', Y^{149}; for Astacin: S1, M^{124}; S1', K^{179}; S2', Y^{86}).*

4.2.2   Analysis of the Binding Modes of the Specific Inhibitors

The inhibitors MWT-S-270 and MWT-S-698 have been developed on the basis of hydroxamic acid. Hydroxamate-containing compounds, among those the natural metalloprotease inhibitor actinonin, are typical for inhibition of zinc-dependent enzymes (Wu et al. 2011; Jani et al. 2005; Jacobsen et al. 2010; Kawai and Nagata 2012). In Meprin α and β, the zinc is chelated and the hydroxamic acid is further involved in two hydrogen bonds. The hydroxamate amide forms a hydrogen bond to the backbone of a close Cysteine residue (C^{124} Meprin β and C^{126} Meprin α). Additonally, the hydroxyl group of the hydroxamic acid interacts with the carboxyl side chain of Glutamic acid (E^{153} Meprin β and E^{156} Meprin α). This binding motif of the hydroxamic acid within metalloproteases was also observed for MMP-10 (Bertini et al. 2004). It is also mentioned in the literature that the hydroxamic acid at physiological pH is protonated enabling the binding of the hydroxyl group of the hydroxamic acid to the carboxyl side chain of E^{153}/E^{156}, but upon binding to the zinc deprotonation occurs for efficient chelation (Ducháčková and Roithová 2009). According to this assumption, the hydrogen bond between E^{153}/E^{156} and the hydroxyl group of the hydroxamic acid would not be possible, upon chelating of the zinc. Furthermore, the possibility of a proton transfer was described enabling a hydrogen bond between the acid proton of a Glutamic acid and the hydroxyl oxygen of the hydroxamate anion (Cross et al. 2002).

Based on the electron density obtained by X-ray crystallography for Meprin β and the reconstructions of Meprin α and Meprin β obtained by cryo-EM it can not be judged, whether such a hydrogen bond is formed, but indeed the Glutamic acid is close to the hydroxyl group of the hydroxamic acid.

Major differences between the cryo-EM and crystal structure of Meprin β were observed for the inhibitor interaction within the active site cleft. In contrast to the electron density obtained by crystallography, the electron density of MWT-S-270 within the cryo-EM reconstruction is well defined. Based on these results, the specific inhibitor MWT-S-270 addresses the subpockets S1' and S2'. This is in contrast to the assumed binding modes to the subpockets S1 and S1', predicted by docking experiments (Ramsbeck et al. 2018). Analyzing the Meprin β crystal structure it was suspected, that one benzoic acid moiety binds to the hydroxyl group of S^{212}, additionally an ionic interaction to the guanidine group of R^{238} within subpocket S1' was supposed. But due to the ambiguos electron density this interaction was an assumption, which was also observed before by docking experiments (Ramsbeck et al. 2018). By the help of the cryo-EM structure the binding of this benzoic acid moiety to S^{212} and R^{238} was confirmed. For the second benzoic acid moiety the electron density obtained by crystallography is weak and the inhibitor moiety was placed close to R^{184} of subpocket S1. Based on the cryo-EM reconstruction of Meprin β, this benzoic acid forms an ionic interaction with R^{146} of subpocket S2'. Within the active site of the crystal structure an ethylene glycol was placed as well, since electron density is present. Interestingly, this solvent molecule is situated close to the benzoic acid moiety of the cryo-EM structure pointing towards the subpocket S2' (R^{146}, yellow circle in figure 47 A). Possibly, the densities within the active site were misinterpreted and instead of the inhibitor moiety a solvent molecule was placed within the Meprin β crystal structure. Another reason for the different binding modes of the inhibitor within the cryo-EM and crystal structure might be the flexibility of the inhibitor and the structure itself, leading to different orientations of MWT-S-270 within the active site cleft. Especially, for the Arginine residue 184 in subpocket S1 a high flexibility was observed by B-factor staining of the protease domain (figure 57 in the appendix, p. 134). For example, within the Meprin β cryo-EM structure, obtained in the present study, and the crystal structure 4GWN, the orientation of R^{184} is similar and has a slightly 'closed position'. But within the Meprin β crystal structure of the present study, R^{184} shows a more 'open' conformation, which might be mediated by the bound inhibitor (figure 47 B, highlighted by arrow). Additionally, different orientations of R^{238} in subpocket S1' were observed. Whereas R^{238} shows a similar orientation within the cryo-EM and crystal structure of Meprin β, the orientation within the crystal structure 4GWN is different, but similar to the orientation of R^{242} within Meprin α.

A

Chain A   Chain B

— Cryo-EM structure of Meprin β   — Crystal structure of Meprin β

B

Meprin β, chain A, crystal   Meprin β, chain A, cryo   Meprin α, chain A, cryo

— Protease domain   — MAM domain   — TRAF domain   — Specific Inhibitor
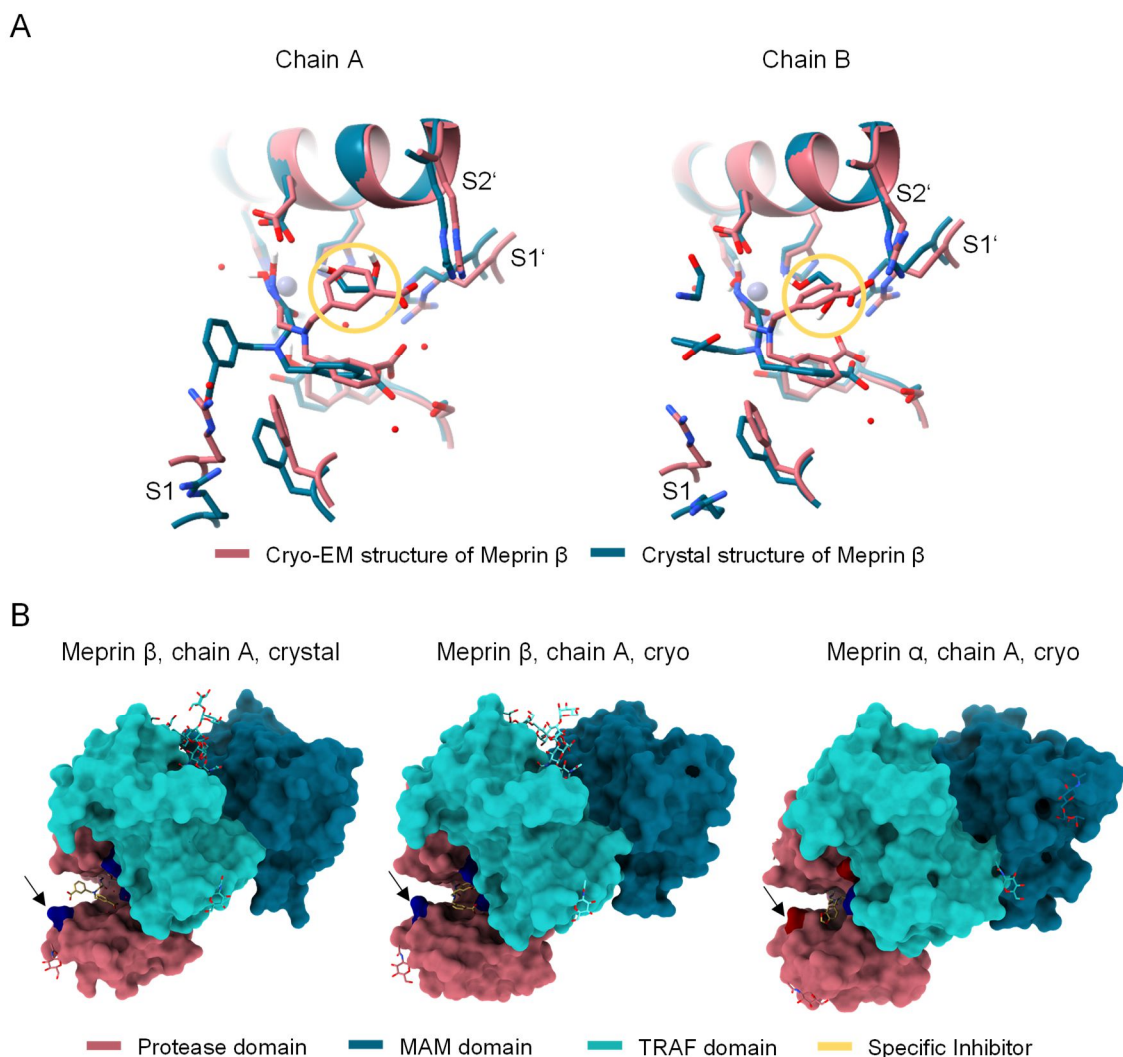
Figure 47: Comparison of Meprin β structures obtained by cryo-EM single particle analysis and crystallography. A) *Superposition of active site motif, including three Histidine residues chelating the catalytic zinc and amino acids within the subpockets of S1 (R^{184}),S1' (R^{238}) and S2'(R^{146}) as well as the placed inhibitor MWT-S-270.Chain A and chain B are displayed.* *B)* *'Standard orientation', rotated 90° on the vertical axis of the active site cleft of Meprin β (cryo-EM and crystal structure) and Meprin α structure. Exemplary, just chain A is displayed. The Arginine residues R^{184} (highlighted by arrow), R^{238} and R^{146}, located in the subpockets S1, S1' and S2' of Meprin β, are colored in dark blue. The two Tyrosine residues Y^{187} (highlighted by arrow), Y^{149}, located in the subpockets S1 and S2 of Meprin α, are colored in red and the R^{242}, located in the subpocket S1' is colored in dark blue.*

Taken together, these results may be interpreted by a flexibility of binding, i.e. occupation of different binding modes, in the active site of Meprin β. Thereby, the cryo-EM analysis clearly supports a binding mode, in which the Arginine residues in subpockets S1' and S2' are serving as interaction partners for the benzoic acid moieties of MWT-S-270. Such an orientation of MWT-S-270 was also identified by molecular dynamics simulations as potential binding mode (personal communication Christian Jäger). Hence, the molecular dynamics simulations are supporting flexibility of binding. However, it remains unclear, why electron density is only ambiguous in case of the crystal structure of Meprin β. Possibly, in solution a highly preferred binding mode exists, which is not occupied in the crystal due to additional interaction forces.

However, a significant contribution of ionic forces for binding of MWT-S-270 is supported by isothermal titration calorimetry analysis. The binding affinities of the inhibitor MWT-S-270 and variants thereof were determined. Interestingly, at higher salt concentration the binding affinity decreased significantly, supporting that the binding of MWT-S-270 is driven by ionic interactions (Fritz, Linnert et al. 2021). This provides also a rationale for the higher selectivity of MWT-S-270 to Meprin β than to Meprin α, which was already determined by enzyme kinetic determinations. An IC_{50} value for Meprin β of 49±11 nM and for Meprin α of 16050±212 nM was determined. By the help of the present study, this selectivity is now explainable and substantiated.

Additionally, by the help of the cryo-EM structure of Meprin α a first insight into the binding of the selective inhibitor MWT-S-698 to the active site cleft of Meprin α could be gained. It was assumed that Y^{187}, within subpocket S1, might interact with one benzodioxolane moiety and that R^{242}, within subpocket S1', might form a hydrogen bond or a cation-π interaction with the other benzodioxolane moiety (Tan et al. 2018). Based on the elucidated structure, an cation-π interaction of one benzodioxolane moiety with R^{242} of subpocket S1' could be confirmed within chain A and B, at a distance of 5.6 Å and 4.9 Å, respectively. Although the distances appear to be far, for cation-π interactions, including especially Arginine-arene complexes, long distances up to 6 Å were described (Gallivan and Dougherty 1999; Kumar et al. 2018). Additionally, within chain B a π-π stacking of the second benzodioxolane moiety to F^{219} and further to Y^{187}, of subpocket S1, was identified. But the electron density for the second benzodioxolane moiety is ambiguous, which might imply a flexible binding mode of the inhibitor. Based on the IC_{50} values of this inhibitor for Meprin α and Meprin β of 160±1 nM and 2950±350 nM, respectively, it is obvious that MWT-S-698 is not as selective as the inhibitor MWT-S-270 for Meprin β. Thus, this inhibitor needs to be further optimized to obtain a higher selectivity, thereby the elucidated Meprin α cryo-EM structure is a helpful tool.

Recently, cryo-EM emerges as a structural technique, not just applicable for large protein complexes, in the meantime also suitable for smaller proteins and drug discovery studies (Johnson et al. 2019; van Drie and Tong 2020). In case of Meprin β the overall structure was elucidated and even more important the binding modes of the specific inhibitor within the active site were determined. By this technique the drawbacks of crystallography, such as packing effects, requirement of high protein amount and concentration, or effects on the protein structure due to crystal growth conditions, are overcome. Cryo-EM enables the mapping of a protein in its native state using physiological and optimal conditions, harboring glycosylations and without the need for high protein concentration. Nevertheless, cryo-EM might not yet be well suited for drug screening campaigns, because the process is 2-3 orders of magnitude slower than using X-ray crystallography, as long as the protein crystallizes well (Renaud et al. 2018; Johnson et al. 2019; van Drie and Tong 2020).

4.3   On the Structural Basis of Helix Formation of Meprin α

The formation of MDa-conglomerates of Meprin α was already mentioned previously (Beynon et al. 1981; Köhler et al. 2000; Bertenshaw et al. 2003). In the present study, these results have been corroborated and first insights into the structural determinants of helix formation could be obtained. Different reasons for the oligomerization were presented, at least for recombinant murine and rat Meprin α, such as intermolecular disulfide bonds in the MAM domain (Ishmael et al. 2001; Marchand et al. 1996) or glycosylations within the MAM domain (Ishmael et al. 2006). Consequently, especially the MAM domain was supposed to be involved in protein-protein interaction (Beckmann and Bork 1993) and in the formation of oligomeric Meprin α (Bertenshaw et al. 2003; Ishmael et al. 2001).

Although Meprin β shares a 46% sequence identity with Meprin α formation of oligomers was not reported, because Meprin β is found as stable dimer *in vitro* and *in vivo*, but also heterodimers or heterotetramers with Meprin α are described *in vivo* (Marchand et al. 1994; Bertenshaw et al. 2003; Peters and Becker-Pauly 2019; Peters et al. 2019). The structural reasons for this difference have not been elucidated so far, but may be related to a different number of glycosylation sites. Consequently, the sequence alignment between human Meprin α and Meprin β was performed (chapter 3.2.2, figure 24, p. 57). Analyzing the glycosylation sites, three of them were identified, that are present in non-oligomerizing Meprin β, but not in oligomerizing Meprin α, two of them within the MAM-domain:

- N^{370} (MAM domain) in Meprin β, corresponding to N^{370} in Meprin α
- N^{421} (MAM domain) in Meprin β, no corresponding asparagine in Meprin α
- N^{547} (TRAF domain) in Meprin β, corresponding to N^{558} in Meprin α.

Considering the elucidated structures of Meprin β (chapter 3.1.4, pp. 43), the glycosylation site N^{421} is buried within the MAM domain and not exposed to the surface of the protein. In accordance this potential glycosylation site is not glycosylated in the elucidated structures.

Based on the homology model of Meprin α described by Tan et al., which seems to be very similar to the structures of Meprin β, it was assumed that the same region in Meprin α is located within the structure as well (Tan et al. 2018), and consequently may not be involved in non-covalent interactions between Meprin α dimers. These assumptions were confirmed by the elucidated cryo-EM structure of Meprin α (chapter 3.2.3, pp. 68). The remaining glycosylation sites N^{370} (MAM domain) and N^{547} (TRAF domain) are glycosylated in the Pro-Meprin β structure 4GWM (Arolas et al. 2012) and were observed in the Meprin β structures described in the present study (chapter 3.1.4, pp. 43).

In order to set base for crystallization of Meprin α, two glycosylation sites at N^{370} in the MAM domain and N^{558} in the TRAF domain were introduced to reduce the oligomerization propensity In addition, monomers should be produced by exchange of C^{308} to A^{308}, which could be already shown for murine Meprin α (Marchand et al. 1996).

Hence, three different mutants of human Meprin α were produced: two by insertion of glycosylation sites and one by exchange of the Cysteine responsible for intermolecular disulfide bond formation between two Meprin α monomers:

- C308A, deletion of the intermolecular disulfide bridge, may result in monomeric Meprin α

- R372T, insertion of a glycosylation site at N^{370}; corresponding to the glycosylation site N^{370} in Meprin β

- F560 T, insertion of a glycosylation site at N^{558}; corresponding to the glycosylation site N^{547} in Meprin β.

The mutant F560T was not further investigated, since the results of the test expression revealed that this variant is of higher molecular mass, than the mutant R372T, thus potentially forming tetrameric or higher order oligomeric Meprin α.

The analysis of human Meprin α C308A led to detection of monomeric Pro-Meprin α C308A and mature Meprin α C308A in reduced and non-reduced SDS-PAGE at about 70 kDa and 65 kDa, respectively. This is an approval of the results obtained with murine Meprin α at C^{320} (Marchand et al. 1996) and it confirms that the Cysteine at position 308 in human Meprin α is responsible for covalent interaction of two Meprin α monomers through a disulfide bridge. This intermolecular disulfid bridge at C^{308} was also observed by cryo-EM (chapter 3.2.3, pp. 68). The analysis of Meprin α C308A by cryo-EM revealed single particles of the same size as the mutant R372T and the dimeric Meprin β. A further analysis on the molecular mass of Pro-Meprin α C308A by SEC-MALS revealed a homogenous sample with a molecular mass of 150.2 kDa±0.7%. This indicates dimer formation, since the calculated molecular mass of a Pro-Meprin α C308A monomer is 67.7 kDa. The results fit very well, but indicate that the mutant C308A is dimeric Meprin α in solution. This result asserts that Meprin α C308A still has the tendency of association with other monomers to form non-covalently interacting dimers at higher protein concentration (~0,8 mg/ml, chapter 3.2.2, figure 30, p. 66). According to the determined structure of mature Meprin α, probably non-covalent interactions within the MAM-TRAF interface are responsible for association of Meprin α C308A monomers, most likely mediated by formation of an ionic bond between R^{372} and D^{595}.

In general, the higher masses observed in both analyses are a result of glycosylations, since they could be removed by deglycosylation (data not shown). Furthermore, it was reported that the contribution of glycosylations sum up to 25% of the total mass of Meprins (Kadowaki et al. 2000).

For the mutant R372T, introducing a potential glycosylation site, a band at 70 kDa in reducing SDS-PAGE was observed. In non-reducing SDS-PAGE, several bands at high molecular mass were detected, similar to the migration pattern observed for wild type Meprin α. But, in native PAGE the R372T mutant showed an intermediate migration behavior. Consequently, it was assumed that the introduction of the glycosylation site at N^{370} leads to a dimeric or tetrameric form of Meprin α R372T and abolished oligomerization. The prevention of protein oligomerization and aggregation due to especially N-linked glycosylations was already described (Mitra et al. 2006; Jayaprakash and Surolia 2017; Yi et al. 2018; Nakamura et al. 2020). This was confirmed by SEC-MALS analysis after purification of Pro-Meprin α R372T. Due to inhomogeneity of the detected peak, a molecular mass range of 159-176 kDa could be determined, indicating a dimeric Meprin α. This result is in accordance with the molecular mass of 149.6 kDa $[M+H]^+$, obtained by MALDI-TOF analysis of Pro-Meprin α R372T. Again, the experimentally determined molecular masses are higher than the calculated molecular mass of 135.4 kDa for the Pro-Meprin α R372T dimer, due to N-glycosylation. These glycosylations most likely also contribute to the heterogeneity of Pro-Meprin α R372T (Rudd and Dwek 1997; Moremen et al. 2012), observed by SEC-MALS analysis and in SDS-PAGE after the activation of Pro-Meprin α R372T during the purification process (chapter 3.2.2, figure 29 (p. 64) and figure 27 (p. 61)). Furthermore, the analysis by cryo-EM revealed that no helical structures are formed by Meprin α R372T. Consequently, the results suggest that the region close to R^{372} is involved in the formation of the helical particles. This was proven by the elucidated structure of mature human Meprin α. Based on this structure, several possible interaction points, predominantly based on ionic interactions, were observed (described in chapter 3.2.3, pp. 74). These interactions, responsible for the oligomerization, involve the same amino acids within all four interfaces between Meprin α dimers. But the most relevant interaction, responsible for the formation of helical particles, observed within the structure of mature Meprin α, seemed to be the ionic interaction formed by R^{372} of one dimer with D^{595} of another dimer. Additionally, the interactions between E^{492} of one Meprin α dimer to K^{376} or R^{357} of another dimer might contribute to the helix formation. As known from the literature, electrostatic interactions between positively and negatively charged amino acids are frequently important for the stability of oligomeric structures (Petrauskas et al. 2015).

Summarizing, both Meprin α mutations led to interruption of the oligomerization, although subtle differences were observed. A scheme of the produced Meprin α variants depicting their possible associations to form helices and ring-like structures is depicted in figure 48.

A Meprin α wild type

B Meprin α C308A

C Meprin α R372T
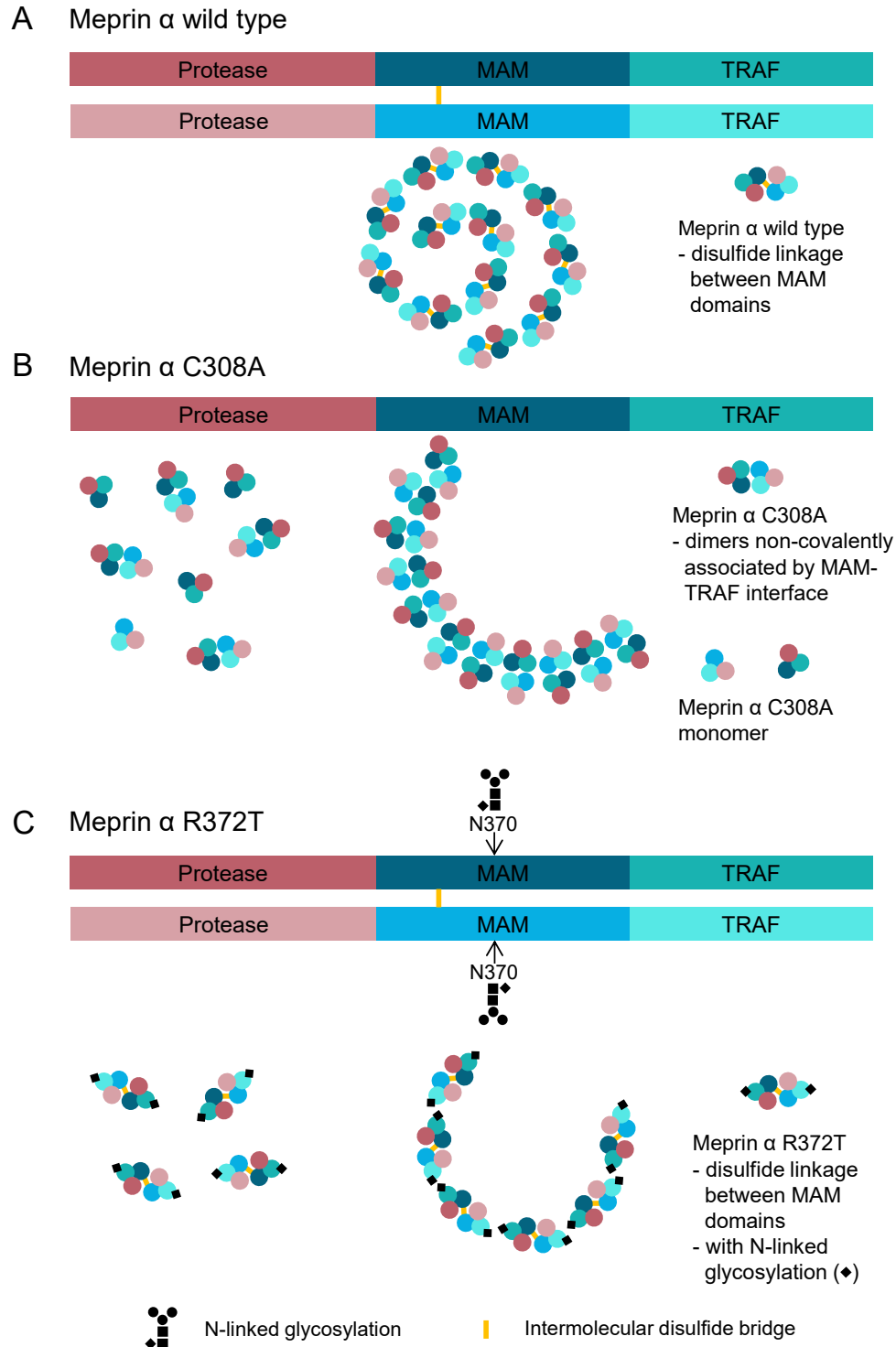
*Figure 48: Scheme of Meprin α variants and possible interactions between monomers forming dimers and dimers building up oligomeric structures. Each domain of Meprin α is symbolized by a circle in the appropriate colour. The black square symbolizes the introduced glycosylation site at R372T. The yellow line symbolizes the intermolecular disulfide bridge. **A)** Heterologously expressed Meprin α wild type, illustration of dimers non-covalently associating into large helical structures. **B)** Heterologously expressed Meprin α C308A, illustration of monomers, dimers and associated dimers, forming ring-like structures. The dimer formation and association in ring-like structures is most likely mediated by the amino acids R^{372}, D^{595} and E^{492}, K^{376} located within the MAM-TRAF interface. **C)** Heterologously expressed Meprin α R372T, illustration of dimers linked by a disulfide bridge, in solution single dimers and associated dimers, forming ring-like structures, were observed, but no helices.*

In an additional attempt it should be clarified, wheter the glycosylation in R372T or the interruption of the ionic interaction between R^{372} and D^{595} is causing the prevention of helix formation. Therefor, another variant, R372A, was generated and analyzed as before. Also, the mutation of Arginine at position 372 to Alanine leads to formation of homogenous dimeric Meprin α, as shown in figure 49. Thus, the ionic interaction of R^{372} with D^{595} seems to be crucial for the formation of Meprin α oligomers. Nevertheless, the dimeric mutant R372A still has tendency to associate with each other, but does not form large helical oligomers. The tendency of association of the R372A dimers could be still due to other interactions that are additionally involved in the formation of oligomeric Meprin α, such as those of negatively charged E^{492} with positively charged K^{376} (described in chapter 3.2.3, pp. 74). Typically, the ionic interactions formed by Arginine are of higher affinity than those formed by Lysine (Petrauskas et al. 2015), consequently the exchange of the positively charged R^{372} was sufficient to produce Meprin α dimers.

According to the sequence alignment (chapter 3.2.2, figure 24, p. 57) the positively charged R^{372} in human Meprin α corresponds to neutral G^{369} in human Meprin β and the negatively charged E^{492} (Meprin α) corresponds to neutral A^{483}. Moreover, the regions in the MAM and TRAF domains, responsible for oligomer formation in Meprin α, are covered in Meprin β by glycosylations derived from N^{370} and N^{547}. These glycosyl chains are orientated to the MAM-TRAF lumen and were named 'sugar channel' by Arolas et al. (2012). It was stated that the 'sugar channel' may assists substrate binding during Meprin β-mediated shedding at the plasma membrane (Arolas et al. 2012). In general, glycosylations were identified to be critical for physiological and pathophysiological cellular functions, i.e. many autoimmune diseases were associated with abnormal glycosylation (Reily et al. 2019). N-linked glycosylations were also described as molecular insulators, which enable the reduction of macromolecular environment by retarding intermolecular interactions (Jayaprakash and Surolia 2017). This is in accordance with the observed dimeric structure of Meprin β and in turn, the reduced degree of glycosylation of Meprin α seems to induce interaction to form helical oligomers stabilized by electrostatic interactions.

A   0.44 mg/ml Meprin α R372A

B   0.15 mg/ml Meprin α R372T

C   4 mg/ml Meprin β

D   0.94 mg/ml Meprin α wild type
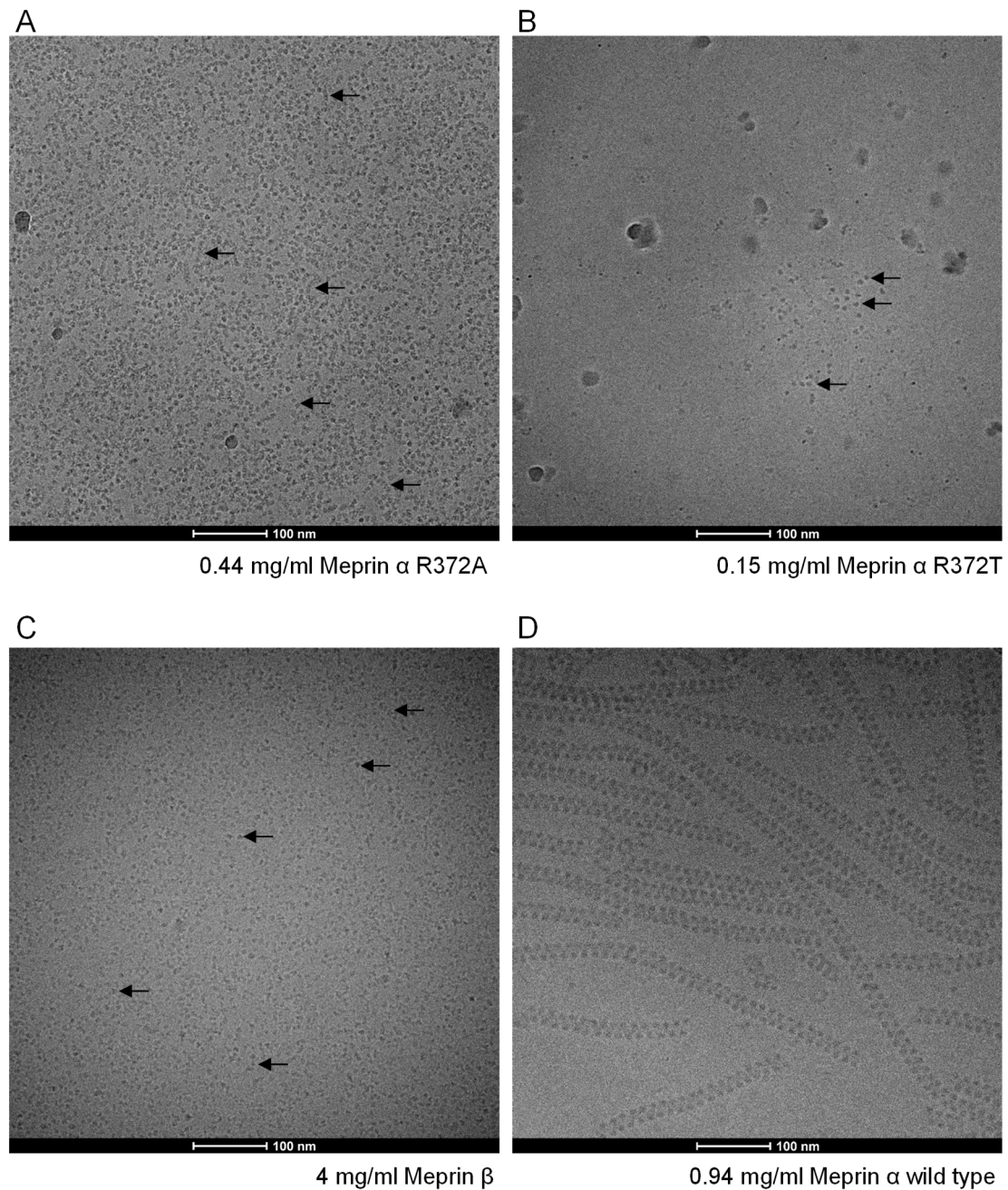
Figure 49: Electron micrographs of mature Meprin α R372A, R372T, wild type and mature Meprin β. *Proteins are highlighted by arrows. Images recorded at Tecnai 12 electron microscope. Glow-discharged QUANTIFOIL® Au R1.2/1.3 grid used for A, B and C. Cu R2/2 grid used for D. The samples were frozen using the Vitrobot System (4°C, 100% humidity). Both Meprin α mutants occur as dimers, in similar size as Meprin β dimers. **A)** 0.44 mg/ml Meprin α R372A (blot force: -8, blot time: 2 s; wait time: 5 s, drain time: 1 s). **B)** 0.15 mg/ml Meprin α R372T (blot force: -5, blot time: 2.5 s; drain time: 1 s). **C)** 4.0 mg/ml Meprin β (blot force: -8, blot time: 2 s; wait time: 5 s, drain time: 1 s). **D)** 0.94 mg/ml Meprin α wild type (blot force: -8, blot time: 2 s; wait time: 5 s, drain time: 1 s).*

The above-mentioned observations could be hints why Meprin β dimers do not associate non-covalently, at least *in vitro*, because *in vivo* Meprin β is mostly membrane bound or associated with Meprin α (Bertenshaw et al. 2003; Marchand et al. 1994; Peters et al. 2019). In fact, electrostatic interactions were shown to be involved in i.e. interaction of spliceosomal protein U1A and its RNA target (Law et al. 2006), but are also crucial for thermal stability and assembly of large complexes, like virions (Carrillo et al. 2018). In general, electrostatic interactions are dependent on salt concentration: at high salt concentrations, repulsive forces occur und in presence of low salt concentrations ionic interactions are formed (Zhang et al. 2007; Zhou and Pang 2018). If considering that the oligomerization of human Meprin α is based on ionic interactions, dependent on salt concentration, it could be assumed that depending on the localization of Meprin α *in vivo*, the protease is of dimeric or oligomeric quaternary structure. Because during the passage of secreted Meprin α within the nephron, it is subjected to a large variation of salt concentration from proximal tubule to the urine. Where isotonic conditions are present in the proximal tubule fluid (300 mOsm/l equal to 150 mM NaCl), hyperosmotic conditions occurring in the descending loop of Henle and in the urine (1400 mOsm/l) and hypoosmotic conditions are present in the ascending loop of Henle (80 mOsm/l) (Bertenshaw et al. 2002).

To address this fact, follow-up studies might be performed to investigate wild type Meprin α in presence of low and high salt concentration using cryo-EM. In addition, it might be interesting to introduce mutations in Meprin β to induce oligomerization, i.e. by deletion of N-linked glycosylation sites.

Although the crucial determinants of the oligomer formation of Meprin α could be elucidated, it demained open, whether the aggregation might influence the stability or activity of Meprin α. Therefore, investigations on differing activity and stability were initiated. In a first approach, for the three variants, including Meprin α wild type, C308A and R372T, far-UV spectra were recorded while a stepwise thermal denaturation was performed. For the non-covalently linked dimeric Meprin α mutant C308A, a melting temperature of 41°C was determined, which is in accordance with the murine Meprin α mutant C^{320} described by Marchand et al., who showed that half of the activity was lost after two minutes at 40°C (Marchand et al. 1996). Interestingly, the half-life of wild type murine Meprin α at 40°C was about 90 min. Accordingly, the stepwise thermal denaturation revealed that wild type Meprin α and the mutant R372T seemed to be more stable and seemed to not unfold with increasing heat up to 90°C. Nevertheless, no activity of the three Meprin α variants could be determined anymore after this treatment. According to the CD spectra both variants undergo a thermal transition, between 45°C and 55°C for wild type Meprin α and between 40°C and 50°C for Meprin α R372T, this was also observed for other proteins (Simons et al. 1969; Ranjbar and Gill 2009). Possibly, a change in secondary structure with increasing temperature occurs.

The active site including the zinc, which is coordinated by three Histidine residues (H[155], H[159], H[165]) (Sterchi et al. 2008), is characterized by an α-helix, harboring H[155] and H[159]. Changes in CD spectra upon removing of zinc from fibrolase, a metalloprotease showing a high homology with the metal binding site of e.g. thermolysin, was reported (Pretzer et al. 1992). Furthermore, it was described that the α-helix formation in zinc finger peptides is crucial for the complex binding of the zinc (Kluska et al. 2018). In accordance with the thermal transition observed in the generated CD data, maybe the loss of α-helices led to removal of the zinc in the active site of Meprin α wild type and R372T, which would explain the loss of activity, but the remaining secondary structure.

Finally, from this data it can be further concluded, that the disulfide bridge contributes significantly to the increased stability of the protease. The oligomerization of Meprin α showed an effect on thermal stability, as concluded from the comparison of the results with those of R372T. Because, the mutant R372T still has the tendency to associate, it would be advisable to produce a Meprin α variant including mutations at the major four amino acids, that are involved in the oligomerization: R[372], D[595], E[492], K[376] in order to prove if this mutant is less thermostable then the Meprin α wild type. Overall, the expression of a Meprin α mutant, whereby the majority of amino acids involved in helix formation is mutated to Alanine, might lead to intact Meprin α dimers, which again would be suitable for crystallization. The expression of such a mutant might be also successful in yeast and consequently could result in higher yields.

An investigation of the substrate conversion by Meprin α wild type and the variants suggests some influence of the oligomerization on enzymatic activity. First, the turnover of a small fluorogenic peptide substrate Abz-YVADPK(Dnp)G-OH was investigated. Although the mutant C308A is less stable than the mutant R372T and wild type Meprin α, it exhibits the highest catalytic efficiency ($k_{cat}/K_m = 453\pm17$ mM^{-1}s^{-1}) in comparison to Meprin α R372T ($k_{cat}/K_m = 329\pm14$ mM^{-1}s^{-1}) and Meprin α wild type ($k_{cat}/K_m = 271\pm22$ mM^{-1}s^{-1}). For wild type Meprin α, the lowest catalytic efficiency towards this small peptide substrate was determined, at least for the tested conditions (50 mM HEPES pH 7.4, 150 mM NaCl, 30°C). A similar result was obtained for murine Meprin α wild type, which is about 47% less active towards the small peptide substrate BK$^+$ (Abz-RPPGFSPFRK(Dnp)G-OH), in comparison to the C320A mutant, a murine Meprin α monomer (Marchand et al. 1996). Furthermore, Marchand et al. described that the activity of monomeric murine Meprin α mutant C320A towards the small protein substrate Azocasein, which consists of casein conjugated to an azo-dye with a molecular weight of 23.6 kDa, is markedly decreased in comparison to wild type Meprin α (Marchand et al. 1996).

The investigation of protein substrates within the current study, again showed differences between the Meprin α variants. The studies revealed new potential substrates Tropoelastin and Elastin. Tropoelastin is the precursor protein of Elastin and consists of alternating hydrophobic and hydrophilic regions. Whereas the hydrophilic regions are rich in Lysine and Alanine, the hydrophobic regions mainly bear non-polar amino acids, such as Glycine, Valine, Leucine and Proline (Wise et al. 2014). Because, Meprin α prefers Proline residues, especially in P2' and P3', and Alanine, Valine and Glycine in P1' (Broder and Becker-Pauly 2013; Bertenshaw et al. 2003; Bertenshaw et al. 2001), it was assumed that Tropoelastin is degraded by Meprin α.

The identification of Tropoelastin cleavage by Meprin α triggered the investigation of bovine Elastin, consisting of covalently crosslinked Tropoelastin molecules (Wise et al. 2014). Using SDS-PAGE followed by Coomassie-staining, no cleavage products could be observed. However, using nanoLC-MS/MS, Elastin cleavage products were identified (table 25 in the appendix, pp. 141). For the cleavage of Elastin by Meprin α C308A, about five times more peptides were identified, than for the Meprin α wild type cleavage reaction, which is in accordance with the faster degradation of Tropoelastin by Meprin α C308A in comparison to the wild type. Preferred amino acids of both Meprin α variants in P1 are Glycine>Alanine and in P1' Valine>Glycine>Alanine. This corresponds to the observed cleavage specificity of Meprin α (Becker-Pauly et al. 2011).

Both Meprin α variants released a variety of peptides containing a bioactive motif, e.g. VPGVG, which was described to be involved in the stimulation of cell proliferation and autogregulation of elastin expression, or GVYPG, GVLPG which were identified to be involved in the stimulation of pro-MMP-1 expression (Heinz 2020). Interestingly, a reduced amount of elastin is observed in vascular aging (Freitas-Rodríguez et al. 2017), leading to vascular stiffness and reduced resiliency of these tissues (Duca et al. 2016). Additionally, the enhanced activity of metalloproteinases in aortic walls was shown to be related to aging (Wang et al. 2015b). Because, Tropoelastin and Elastin were identified as new substrates for Meprin α it might be possible that Meprins are involved in aging as well. Consequently, investigations on the overexpression of Meprins with ageing or changes of the balance between Meprin expression and expression of endogenous Meprin inhibitors with ageing would be interesting, maybe suggesting a new function of Meprins within humans.

Fibronectin was already described as substrate of Meprins (Kaushal et al. 1994; Bertenshaw et al. 2001; Bertenshaw et al. 2002; Kruse et al. 2004; Jefferson et al. 2013) and specific cleavage sites for human Meprin α in Fibronectin[2] between $Y^{294}{\downarrow}Q^{295}$ and $N^{709}{\downarrow}T^{710}$ could be determined by N-terminal sequencing of bands from Coomassie-stained PVDF membranes (Kruse et al. 2004). In the present study, a specific cleavage pattern of Fibronectin generated by both Meprin α variants was observed. Depending on concentration and time, bands of high molecular masses and of low molecular masses were detected. According to the resultant cleavage pattern, it can be stated, that both Meprin α variants specifically cleave Fibronectin. Since no kinetic data of the cleavage reactions are available, it cannot be stated, which Meprin α variant exhibits higher catalytic efficiency towards Fibronectin. From the obtained cleavage pattern in Coomassie-stained gels, it can be estimated, that both variants cleave Fibronectin to the same extent. However, distinct bands were analyzed by N-terminal sequencing and cleavage sites could be determined. The results are kindly provided by Tobias Hedtke (laboratory of Dr. Christian Schmelzer, Fraunhofer IMWS). Several cleavage sites were obtained throughout the protein, consequently the N- and C-terminus of the cleavage products observed in SDS-PAGE could not be identified. The cleavage sites already described were observed as well (Kruse et al. 2004).

An interesting observation was made, while imaging Meprin α wild type with Fibronectin in cryo-EM (in 50 mM HEPES pH 7.4 buffer containing 150 mM NaCl). First, only Fibronectin was imaged and at 2 mg/ml small thin filament-like particles could be observed (figure 50 A). Second, Meprin α wild type, inactivated by EDTA, mixed with Fibronectin (mass ratio of 1:1, 0.5 mg/ml:0.5 mg/ml) (figure 50 B) and active Meprin α wild type mixed with Fibronectin (mass ratio of 1:1, 0.5 mg/ml:0.5 mg/ml) were investigated (figure 50 C/D). These samples were mixed just before freezing on the EM-grid. By imaging mature, inactive Meprin α wild type with Fibronectin, the characteristic large helical oligomers of Meprin α wild type were ascertained. But imaging mature, active Meprin α wild type with Fibronectin, it seems that the helical oligomers almost completely disappeared and smaller ring-like structures result (figure 50 C/D). As a consequence, it can be supposed that wild type Meprin α oligomeric structures may dissociate in presence of substrates, in this case Fibronectin. These observations might be in contrast to the structural basis of Meprin α oligomerization that was observed in the present study and described above.

---

[2] labeling according to UniProt entry P02751

A

2.0 mg/ml Fibronectin

B

0.5 mg/ml Meprin α wild type+ 4.5 mM EDTA
+ 0.5 mg/ml Fibronectin

C

0.5 mg/ml Meprin α wild type
+ 0.5 mg/ml Fibronectin

D

0.5 mg/ml Meprin α wild type
+ 0.5 mg/ml Fibronectin
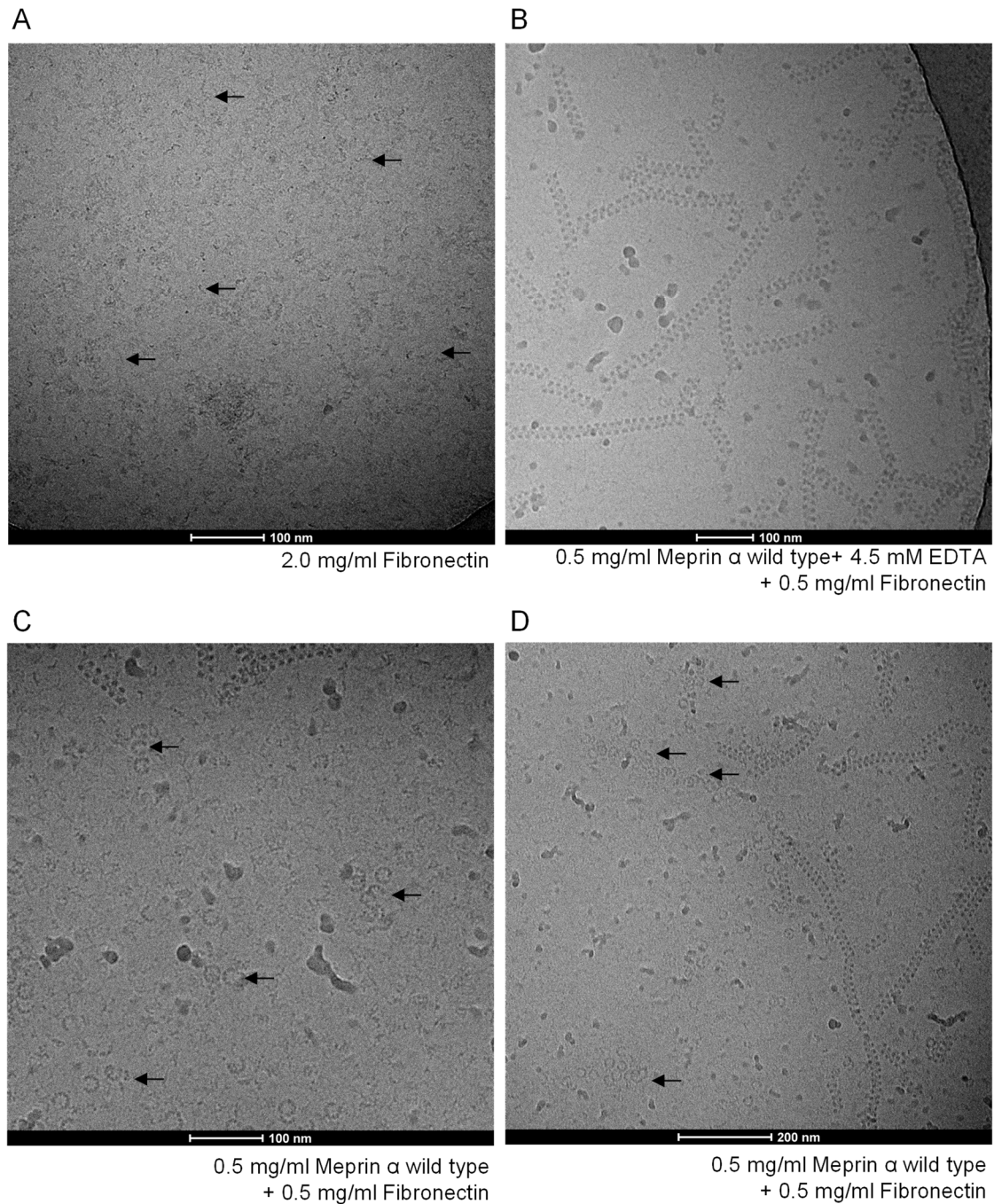
Figure 50: Electron micrographs of Fibronectin in presence of active and inactivated Meprin α wild type. *Images recorded at Tecnai 12 electron microscope. Glow-discharged QUANTIFOIL® Cu R2/2 grid. The samples were immediately frozen, after mixture of Fibronectin and Meprin α (in 50 mM HEPES, 150 mM NaCl pH 7.4), using the Vitrobot System (4°C, 100% humidity, blot force: -8, blot time: 2 s; wait time 5 s, drain time: 1 s). A) 2 mg/ml Fibronectin B) 0.5 mg/ml Meprin α wild type, previously inactivated by addition of EDTA (to 4.5 mM), mixed with 0.5 mg/ml Fibronectin C) 0.5 mg/ml Meprin α wild type mixed with 0.5 mg/ml Fibronectin D) 0.5 mg/ml Meprin α wild type mixed with 0.5 mg/ml Fibronectin, at lower resolution.*

According to the determined structure of mature Meprin α, the amino acids R^{372}, D^{595}, E^{492}, L^{376} are involved in the oligomerization by formation of ionic interactions, which are dependent on salt concentration. Supportingly, the relation of quaternary structure to activity was already described for other proteins. For instance, the spontaneous dissociation of oligomeric proteins was observed for Tripeptidyl-peptidase II. In this case the non-associated form is inactive (Tomkinson 2000; Tomkinson et al. 2002). In addition, Interleukin-1β Converting Enzyme associates in different quaternary structures and oligomerization is required for activity (Gu et al. 1995). Furthermore, for the collagenase Cathepsin K, the requirement of a dimerization for collagenolytic activity was reported (Aguda et al. 2014). Aguda et al. described the organization of Cathepsin K into elongated C-shaped protease dimers. By the help of glycosaminoglycans these dimers build a potential collagen-binding interface and enable collagen fiber degradation. Mutation studies revealed that the interruption of the dimeric structure or removal of the glycosaminoglycans abolished the Cathepsin-K mediated collagen fiber degradation completely, but without affecting the hydrolysis of Gelatin or a synthetic peptide (Aguda et al. 2014). Consequentliy, a vague assumption would be that in presence of especially large protein substrates, Meprin α protease domain undergoes conformational changes, which may lead to changes in the overall structure and with this, conformational changes of the Meprin α helix itself. This could further lead to interruption of some of the ionic bonds, involved in helix formation, and finally to dissociation of the large helical structures into ring-like structures, consisting of up to seven dimers (figure 50 C/D). In theory, this would mean that Meprin α in high oligomeric state is not active, but *in vitro* activity can be measured, since the oligomers dissociate in presence of large substrates. These suggestions can be supported by the reduced catalytic efficiency observed towards the small peptide substrate Abz-YVADPK(Dnp)G-OH of Meprin α wild type in comparison to the determined catalytic efficiency of Meprin α C308A and R372T towards this peptide substrate. Because small substrates may not lead to intense conformational changes within the protease domain and consequently of the helical oligomers.

Also, it could be possible that the conformational changes of the oligomeric structures take longer during the turnover of small substrates, as indicated by the 2-fold lower k_{cat} value determined for turnover of the small substrate Abz-YVADPK(Dnp)G-OH (chapter 3.3.2, pp. 79). The turnover number, k_{cat}, describes the velocity of the rate-limiting step of an enzyme catalzed reaction (Copeland 2000; Michaelis et al. 2011). Consequently, the catalytic step is slower during the turnover of small substrates by Meprin α wild type, than by dimeric Meprin α C308A, maybe mediated by the conformational change of the helical particle into ring-like structures, as described above.

However, to address this point and solve this issue, it would be recommended to perform a study in which Meprin α wild type is imaged using cryo-EM in presence of several small and large substrates, since the described result was obtained from one experiment and just by usage of one substrate.

In conclusion, it is unclear so far if the Meprin α helical oligomers, as observed here in cryo-EM, are occurring *in vivo* or if those might be an artifact of concentration or recombinant protein production. The existence of secreted, oligomeric human Meprin α has not been proven, yet. Most studies indicating oligomeric Meprin α were executed *in vitro* with heterologously expressed human, mouse and rat Meprin α or purified Meprin α from mouse or rat kidney (Köhler et al. 2000; Marchand et al. 1994; Bertenshaw et al. 2003; Bertenshaw et al. 2002; Becker et al. 2003; Marchand et al. 1996; Kadowaki et al. 2000; Ishmael et al. 2001; Ishmael et al. 2006). Bertenshaw et al. reported Meprin α oligomers (up to 1.6 MDa) in rat urine (Bertenshaw et al. 2003). The presence of secreted Meprin α in murine urine was also stated, but no oligomers were observed, after desalting of the urine using MonoQ or a Sephadex column (Beynon et al. 1996). The analysis of human urine revealed the secretion of a Meprin α at a size below 85 kDa, in this case the urine was concentrated before analysis by Western blot (DeGuzman et al. 2004). The murine urine analyzed in the present study was not treated before application onto the SDS-PAGE, in order to not interrupt the helical oligomers of Meprin α. In non-reduced SDS-PAGE, a single band above 250 kDa was observed, similar to the recombinant wild type Meprin α, and also similar to results observed in mice (Beynon et al. 1996). In reducing SDS-PAGE, a single band between 100 and 130 kDa was detected in case of urine samples of two individual mice. Native PAGE revealed similar migration behaviour of murine Meprin α and recombinant human Meprin α wild type. However, no helical particles could be observed by imaging the urine using cryo-EM, which could be explained by a low concentration of Meprin α within the urine than that the oligomers do not exist. Recently, it was reported that human Meprin α is tethered to the membrane as heterooligomer with human Meprin β (Peters et al. 2019), consequently the concentration of soluble Meprin α might be very low. This was also previously described for rat Meprins (Bertenshaw et al. 2003). However, for the Meprin α oligomers detected in rat urine a concentration of 20 nM was supposed (Bertenshaw et al. 2003). Imaging the recombinant wild type Meprin α at the same concentration no helices could be observed, most likely caused by low concentration of the helical particles. At a concentration of 153 nM, still some oligomers of recombinant wild type Meprin α could be detected by cryo-EM, which additionally led to the assumption that the concentration might not contribute to the helix formation.

Nevertheless, no oligomeric particles in urine were observed, although attempts were undertaken to increase the concentration by pulldown with anti-Meprin α antibody and ultracentrifugation, which should lead to sedimentation of the large helical particles. These efforts were performed with media collected from Caco-2 culture as well. But Meprin α oligomers could not be observed. Previously the endogenous expression of Meprin α in Caco-2 post confluence was described, bands at a size of 95 kDa were observed in reducing SDS-PAGE (Lottaz et al. 1999), but no higher order structures of Meprin α.

Finally, it could not be evidenced that the large, flexible, oligomeric particles of recombinant human Meprin α wild type are also existing *in vivo*. By analysis of murine urine and Caco-2 media, bands in Western blot at about 120 kDa (reducing conditions) and above 250 kDa (non-reducing conditions) were detected which could represent monomers and dimers, or even oligomers of native Meprin α. Further analyses are required to understand the potential physiological role of Meprin α oligomerization. In a first attempt, urine of Cisplatin-challenged wild type and Meprin β knockout mice could be separated by analytical SEC and fractions analyzed by Western blot. The generated Meprin α variants C308A, R372T or R372A serve as a positive control for dimeric Meprin α. Similarily, such analysis could be done to investigate a concentration-dependence of the oligomers in solution. Both investigations might address, if an oligomerization is occurring in tissue, or wheter this is just a unique structure-driven peculiarity of recombinant Meprin α.

5 Summary

The isoenzymes Meprin α and Meprin β represent multidomain metalloproteases of the astacin family. Both Meprins consist of an N-terminal propeptide, the protease, MAM (Meprin A5 protein tyrosine phosphatase μ) and TRAF domain (tumor-necrosis-factor-receptor-associated factor), the EGF-like domain (epidermal growth factor), a transmembrane domain and a cytosolic tail. Additonally, Meprin α harbors an 'inserted domain', which contains a furin cleavage site (Broder and Becker-Pauly 2013). This enables the shedding of the protease from the membrane, followed by the release of Meprin α into the extracellular space. Upon shedding from the membrane, Meprin α oligomers up to the Mega-Dalton range are formed by non-covalent interactions between Meprin α dimers (Ishmael et al. 2001; Bertenshaw et al. 2003). Homo- and heterocomplexes of Meprin α and Meprin β were described, which are situated at the membrane or released in the extracellular space (Peters et al. 2019). Meprin substrates are e.g. Procollagen I and III, Fibronectin, Nidogen-1, E-cadherin and different Interleukin species. Whereas Meprin α cleaves at neutral, aliphatic (A, V), aromatic (Y,W) and negatively charged side chains (D, E), Meprin β has a striking prefernce for negatively charged amino acids (Becker-Pauly et al. 2011). This is probably caused by the different amino acids shaping the subpockets of Meprin α (S1: Y^{187}, S1': R^{242}, S2': Y^{149}) and Meprin β (S1: R^{184}, S1': R^{238}, S2': R^{146}). Driven by their substrate cleavage specificity, Meprins are key players in fibrosis and keloids, but also in nephritis and neurodegeneration (Broder and Becker-Pauly 2013; Prox et al. 2015). Consequently, Meprin α and Meprin β are within focus of current drug discovery. Selective inhibitors for Meprins were developed, based on a tertiary amine scaffold linking a hydroxamic acid to the specific inhibitor moieties targeting the subpockets of the active site cleft of Meprins (Ramsbeck et al. 2018; Tan et al. 2018). For further drug design and optimization, the 3D-structures of Meprins in complex with inhibitors would be useful.

In the present study, for the first time, the structures of Meprin α and Meprin β in complex with specific inhibitors were elucidated. For the 3D-structure of Meprin β, a resolution of 2.41 Å was achieved using X-ray crystallography approach. By the analysis of this structure the orientation of the inhibitor within the active site could not be clarified due to missing electron density for a major part of the inhibitor. Hence, the complex-structure was also elucidated using cryo-electron microscopy (cryo-EM) single particle analysis approach (3.0 Å). In both Meprin β structures, the catalytic zinc ion is complexed by three Histidine residues, the fourth coordination site is occupied by the hydroxamic acid of the specific inhibitor MWT-S-270 (3-[[(3-Carboxyphenyl)methyl-[2-(hydroxyamino)-2-oxo-ethyl]amino]methyl]benzoic acid, IC_{50} 49±11 nM).

Based on the Meprin β cryo-EM structure the benzoic acid moieties of the inhibitor address the Arginine residues of the subpockets S1' (R^{238}) and S2' (R^{146}). This is in contrast to the docking results described in the literature, where an interaction with the subpockets S1 (R^{184}) and S1' was assumed (Ramsbeck et al. 2018). Moreover, the data suggest that different binding modes of the inhibitor within the active site are possible. The results indicate that the selectivity of MWT-S-270 to Meprin β is mediated by electrostatic interactions of the negatively charged benzoic acid moieties to the subpockets S1' and S2' or S1 harboring positively charged Arginine residues.

Because of the oligomerization propensity (formation of helical structures) of the recombinant human Meprin α and its high flexibility in size *in vitro*, the structural elucidation by a crystallography approach was inappropriate. In order to obtain a dimeric Meprin α, different Meprin α mutants were heterologously expressed, purified and investigated concerning their size and oligomerization propensity. The mutant C308A led to interruption of the intermolecular disulfid bridge formed by Meprin α monomers. With the second Meprin α mutant, R372T, an additional N-linked glycosylation site at N^{370} was introduced. This glycosylation site is present in Meprin β, which is not forming oligomers *in vitro* and might contribute to prevention of Meprin α oligomerization. In fact, both Meprin α mutants, C308A and R372T, do not form helical structures as observed for Meprin α wild type, but still have the tendency to associate in ring-like structures (small oligomers of up to seven dimers). These mutants might be suitable for crystallization, but the expression yield was too low to set up a crystallization trail. Hence, an alternative method for structural elucidation was applied and for the first time the structure of mature Meprin α in complex with its specific inhibitor was elucidated to a resolution of 2.42 Å using cryo-EM single particle analysis. Based on this structure, a first insight into the binding mode of the inhibitor MWT-S-698 (3-[bis(1,3-benzodioxol-5-ylmethyl)amino]propane-hydroxamic acid, IC_{50} 160±1 nM) within the active site could be determined. A primary interaction appears to be formed between one benzodioxolane moiety of MWT-S-698 and R^{242} of subpocket S1'. Other binding partners, which could provide a rationale for the selectivity and affinity of the inhibitor, could not be unambiguously identified. Consequently, it might be reasonable to optimize the structure of this inhibitor to increase its selectivity. Therefor, the determined Meprin α structure provides a helpful tool for further drug design, optimization and potential screening studies.

Moreover, insights into the structural determinants for oligomerization of Meprin α were obtained. It turned out that the helical particles are stabilized by electrostatic interactions within the MAM and TRAF domains of dimeric Meprin α molecules, involving the amino acids R^{372}, D^{595}, E^{492}, K^{376}. The impact of the oligomerization of Meprin α on its stability and activity in comparison to non-oligomerizing forms of Meprin α (C308A, R372T) was examined.

The helix formation has little effect on the thermostability, but the intermolecular disulfide bridge contributes significantly to the stability of protease.

Only subtle differences were observed between the Meprin α variants in terms of substrate specificity. The non-oligomerizing variants C308A and R372T showed about 1.5-fold higher specifcity constants towards the small peptide substrate Abz-YVADPK(Dnp)G-OH in comparision to Meprin α wild type. The determined specific activities (k_{cat}/K_m) of Meprin α wild type, C308A and R372T are 271±22, 453±17 and 329±14 mM^{-1}s^{-1}, respectively.

Two new substrates for Meprin α could be identified: Tropoelastin and Elastin. The cleavage of Elastin by Meprin α C308A, resulted in higher number of products compared to Meprin α wild type. But no difference in cleavage specificity was observed between oligomerizing Meprin α and the non-oligomerizing mutant C308A. Preferred amino acids of both Meprin α variants in P1 are Glycine>Alanine and in P1' Valine>Glycine>Alanine, this is in accordance with the observed cleavage specificity of Meprin α (Becker-Pauly et al. 2011). By the turnover of Elastin both Meprin α variants released a variety of peptides containing a bioactive motif, e.g. VPGVG, GVYPG or GVLPG. Since these new Meprin α substrates were identified it might be possible that Meprins are involved in the aging process.

Additionally, the already described Meprin α substrate, Fibronectin; was investigated. Meprin α wild type and Meprin α C308A specifically cleave Fibronectin, as shown by SDS-PAGE analysis. By imaging Meprin α wild type in presence of Fibronectin, using cryo-EM, a depolymerization of the Meprin α helical particles were observed and smaller ring-like structures resulted. A vague assumption would be that in presence of especially large substrates the Meprin α protease domain undergoes a conformational change, may leading to changes of the overall quarternary structure and consequently dissociation of the Meprin α helical oligomer. It remains elusive, however, whether the oligomerization of Meprin α conveys a physiological function. Maybe the oligomerization serves as a tissue-protective mechanism in order to prevent pathological effects. However, it cannot be excluded that the oligomerization represents only a peculiarity of Meprin α *in vitro*, because attempts to provide evidence of oligomers in urine of Cisplatin-treated mice and Caco-2 cell supernatant did not result in an observation of the large helical structures. Further studies on the role of Meprin α oligomerization are thus required.

6. Appendix

Table 14: Summary of applied oligonucleotides.

Oligonucleotide	Sequence 5' to 3'	Information
pPICZαC_pro_mepb_f	atatatCGATTACTCCAGAAAACTTTG	5' coding site of mep1B for cloning in pPICZαC
pPICZαC_his_pro_mepb_f	aatatCGATTCATCATCATCACCATCATGGTAGCACTCCAGAAAACTTTGATG	5' coding site of mep1B, including N-terminal His-Tag, for cloning in pPICZαC
pPICZαCmepbStoNot1_r	atatatGCGGCCGCGCTACCTTATTGTGTAGAGTTGAGGTG	3' coding site of mep1B, for cloning in pPICZαC
pPICZαC_mepb_TEV_2rev	atatatAGATTGGAAGTACAAGTTTTCTTGTGTAGAGTTGAGGTG	3' coding site of mep1B, including C-terminal TEV cleavage site, for cloning in pPICZαC
pPICZαCmepbHStNot2_r	atatatGCGGCCGCTTAATGATGGTGATGATGATGAGATTGGAAGTACAA	3' coding site for TEV cleavage site, including C-terminal His-Tag, for cloning in pPICZαC
pPICZαC_strep_mepb_f	aatatCGATTTGGTCCCACCCCCAGTTCGAGAAGACTCCAGAAAACTTTGATGTAG	5' coding site of mep1B, including N-terminal STREP-Tag, for cloning in pPICZαC
PIC_promepb_pas_f	tattatGCATCGATTGGCACGACTCCAGAGAACTTCGATGTTGAT	5' coding site of mep1B (*P. pastoris* codon usage), for cloning in pPICZαC
PIC_Spromepb_pas_f	tattatGCATCGATTGGCACGTGGTCCCACCCCCAGTTCGAGAAGACTCCAGAGAACTTCGATGTTGAT	5' coding site of mep1B (*P. pastoris* codon usage), including N-terminal STREP-Tag, for cloning in pPICZαC
PIC_promepb_pas_r	atatatGCGGCCGCGCTACCTTACTGAGTGGAGTTCAAGTGGGA	3' coding site of mep1B (*P. pastoris* codon usage), for cloning in pPICZαC
PIC_Hpromepb_pas_f	tattatGCATCGATTGGCACGCATCACCATCACCATCATACTCCAGAGAACTTCGATGTTGAT	5' coding site of mep1B (*P. pastoris* codon usage), including N-terminal His-Tag, for cloning in pPICZαC
PIC_Hpromepb_pas_r	atatatGCGGCCGCGCTACCTTAATGATGGTGATGATGATGCTGAGTGGAGTTCAAGTGGG	3' coding site of mep1B (*P. pastoris* codon usage), including C-terminal His-Tag, for cloning in pPICZαC

Oligonucleotide	Sequence 5' to 3'	Information
hMepB_1	TTGAATCAACTGTATAACTGC	Sequencing primer
hMepB_2	ATAACTACAGACCCATTTATG	Sequencing primer
pPICZaC_3'AOX_r	GCAAATGGCATTCTGACATCC	3' coding site for AOX, sequencing primer
pPICZaC_5'AOX_f	GACTGGTTCCAATTGACAAGC	5' coding site for AOX, sequencing primer
hMepA_ R372T_f	AGCACAGGCAATGTTACCAAGTTGGTGAAGGTG	5' mutagenesis primer, introducing mutation at R372T
hMepA_ R372T_r	CACCTTCACCAACTTGGTAACATTGCCTGTGCT	3' mutagenesis primer, introducing mutation at R372T
hMepA_F560T_f	ACGGACTGTAATTGTACTAGAAGCATCGACTTG	5' mutagenesis primer, introducing mutation at F560T
hMepA_F560T_r	CAAGTCGATGCTTCTAGTACAATTACAGTCCGT	3' mutagenesis primer, introducing mutation at F560T
hMepA_R372A_f	AGCACAGGCAATGTTGCCAAGTTGGTGAAGGTG	5' mutagenesis primer, introducing mutation at R372A
hMepA_R372A_r	CACCTTCACCAACTTGGCAACATTGCCTGTGCT	3' mutagenesis primer, introducing mutation at R372A
hMepA_C308A_f	ACCTTGTTGGGACAAGCCACAGGTGCCGGC TAC	5' mutagenesis primer, introducing mutation at C308A
hMepA_C308A_r	GTAGCCGGCACCTGTGGCTTGTCCCAACAAGGT	3' mutagenesis primer, introducing mutation at C308A
hMepA_1	TTCCATTGGCCAAGGATG	Sequencing primer
hMepA_2	AGTCCTTGAGAACACCAG	Sequencing primer

Table 15: Commercially available and in the present study produced plasmids.

Plasmids	Characteristics	Supplier
pPICZαC	Zeo^R, α-mating factor secretion signal, AOX1 promoter	Thermo Fisher Scientific, available in the lab
pPICZαC-hMepB-NHis	For heterologous expression of human Meprin β in *P. pastoris*, human codon usage, N-terminal His-Tag	Present study
pPICZαC-hMepB-CHis	For heterologous expression of human Meprin β in *P. pastoris*, human codon usage, C-terminal TEV cleavage site, C-terminal His-Tag	Present study
pPICZαC-hMepB-NStrep	For heterologous expression of human Meprin β in *P. pastoris*, human codon usage, N-terminal STREP-Tag	Present study
pPICZαC-PichaMepB-NHis	For heterologous expression of human Meprin β in *P. pastoris*, *P. pastoris* codon usage, N-terminal His-Tag	Present study
pPICZαC-PichaMepB-CHis	For heterologous expression of human Meprin β in *P. pastoris*, *P. pastoris* codon usage, C-terminal His-Tag	Present study
pPICZαC-PichaMepB-NStrep	For heterologous expression of human Meprin β in *P. pastoris*, *P. pastoris* codon usage, N-terminal Strep-Tag	Present study
pMT/BiP/V5-His	Amp^R, BiP secretion signal, pMT promoter	Thermo Fisher Scientific, available in the lab
pMT-hMepA-NStrep	For heterologous expression of human Meprin α wild type in S2 cells, human codon usage, N-terminal Strep-Tag	Available in the lab
pMT-hMepA-C308A-NStrep	See above, but heterologous expression of human Meprin α C308A	Present study
pMT-hMepA-R372T-NStrep	See above, but heterologous expression of human Meprin α R372T	Present study
pMT-hMepA-F560T-NStrep	See above, but heterologous expression of human Meprin α F560T	Present study
pMT-hMepA-R372A-NStrep	See above, but heterologous expression of human Meprin α R372A	Present study
pCoBlast	Amp^R, Bsd^R, selection vector for heterologous protein expression in S2 cells	Thermo Fisher Scientific, available in the lab

Table 16: Feeding rates for glycerol and methanol fed batch during high-density fermentation of Pro-Meprin β clone#8.

Glycerol fed batch		Methanol fed batch	
Time [min]	Feeding rate [%]	Time [min]	Feeding rate [%]
0	7	0	0
60	16	120	6
200	21	660	9
300	21	1380	10
-	-	4320	11

Table 17: Buffers used for purification of Pro-Meprin β.

Ni^{2+}-chelating chromatography	
Equilibration buffer	30 mM TRIS, 300 mM NaCl, pH 7.4
Wash buffer	30 mM TRIS, 300 mM NaCl, 20 mM imidazole, pH 7.4
Elution buffer	30 mM TRIS, 100 mM NaCl, 200 mM imidazole, pH 7.4
Hydrophobic interaction chromatography	
Equilibration buffer	30 mM TRIS pH7.4, 1.5 M ammonium sulfate
Elution buffer	30 mM TRIS, 100 mM NaCl, pH 7.4
Size exclusion chromatrography	
Running buffer	30 mM TRIS, 100 mM NaCl, pH 7.4

Table 18: Buffers used for purification of Pro-Meprin α.

Hydrophobic interaction chromatography	
Equilibration buffer	30 mM TRIS, pH 7.4, 1.5 M ammonium sulfate
Elution buffer	30 mM TRIS, 100 mM NaCl, pH 7.4
Strep-Tactin® chromatography	
Equilibration buffer	30 mM TRIS, 100 mM NaCl, pH 7.4
Elution buffer	30 mM TRIS, 100 mM NaCl, 2.5 mM desthiobiotin, pH 7.4

Table 19: Molar masses and extinction coefficients of Meprins. Calculated using the ProtParam tool by ExPASy.

Protein	Molecular mass (g mol^{-1})	ε (M^{-1} cm^{-1})
Pro- Meprin β	65117.4	96885
Mature Meprin β	60724.7	96885
Pro-Meprin α wild type	66699.5	102510
Mature Meprin α wild type	61250.4	95520
Pro-Meprin α C308A	66667.5	102385
Mature Meprin α C308A	61218.4	95395
Pro-Meprin α R372T	66644.5	102510
Mature Meprin α R372T	61195.3	95520
Pro-Meprin α R372A	66614.4	102510
Mature Meprin α R372A	61165.3	95520

Table 20: Components for SDS polyacrylamide (PAA)-gel.

Substances	12% separating gel	10% separating gel	7% separating gel	4% stacking gel
30% (37.5:1) Acrylamide/bisacrylamide	4.0 ml	3.35 ml	2.35 ml	1.33 ml
1.5 M TRIS, pH 8.8; 0.4% (w/v) SDS.	2.5 ml	2.5 ml	2.5 ml	-
0.5 M TRIS, pH 6.8; 0.4% (w/v) SDS	-	-	-	2.5 ml
DI water	3.4 ml	4.1 ml	5.1 ml	6.1 ml
TEMED	15 µl	15 µl	15 µl	20 µl
20% (w/v) APS	75 µl	75 µl	75 µl	50 µl

Table 21: Components for native PAA-gel.

Substances	7% separating gel	4% separating gel
40% (19:1) Acrylamide/bisacrylamide	2.1 ml	0.4 ml
2.5 M TRIS, pH 8.5	0.4 ml	0.4 ml
DI water	8.6 ml	3.2 ml
TEMED	10 µl	4 µl
20% (w/v) APS	80 µl	30 µl

Table 22: Statistics for data collection and structure refinement of Meprin β co-crystallized with the specific inhibitor MWT-S-270. Highest resolution shell is shown in parenthesis. Data provided by Dr. Miriam Linnert and Dr. Christoph Parthier.

Statistics of data collection	Meprin β with specific inhibitor MWT-S-270
Radiation source	Rotating anode
Wavelength [Å]	1.5418
Space group	C 1 2 1
Unit cell length [Å]	
a	162.25,
b	72.44,
c	135.47
Unit cell angles [°]	
α	90.0,
β	118.4,
γ	90.0
Resolution range [Å]	50 – 2.41
Highest resolution range [Å]	2.47 – 2.41
Rmerge [%]	13.1 (112.9)
I/σI	11.48 (1.79)
Completeness [%]	99.1 (95.5)
Multiplicity	5.5 (5.3)
Solvent content/Meprin β per ASU	58%/2
Wilson B factor	41.01
Data processing	XDS
Model for molecular replacement	4GWN
Refinement statistics	**Meprin β with specific inhibitor MWT-S-270**
Software used for building	COOT
Software used for refinement	Phenix
Validation	MolProbity
Number of reflections	53257
(working/test set)	2665
R_{work}/R_{free}	0.20/0.23
No. atoms	8542
Protein	449
Ligands	363
Water	
Average B-factors [Å^2]	
Protein	50.3
Ligand	67.6
Water	45.5
R. M. S. deviation	0.006
Bond length [Å]	0.868
Bond angles [°].	
Ramachandran plot [%]	
Favored	97.18
Allowed	2.54
Disallowed	0.28
Clash score	5.86
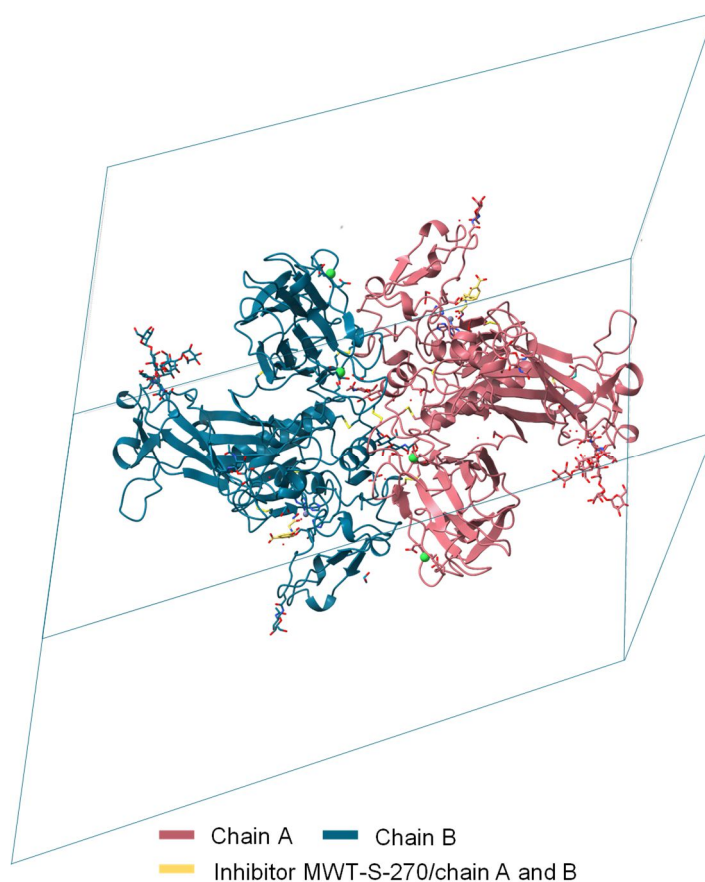
Figure 51: Crystal structure of homodimeric Meprin β within the unit cell (2.41 Å). *Meprin β monomers, consisting of protease, MAM and TRAF domain, are linked by disulfide bridge within MAM domain.*
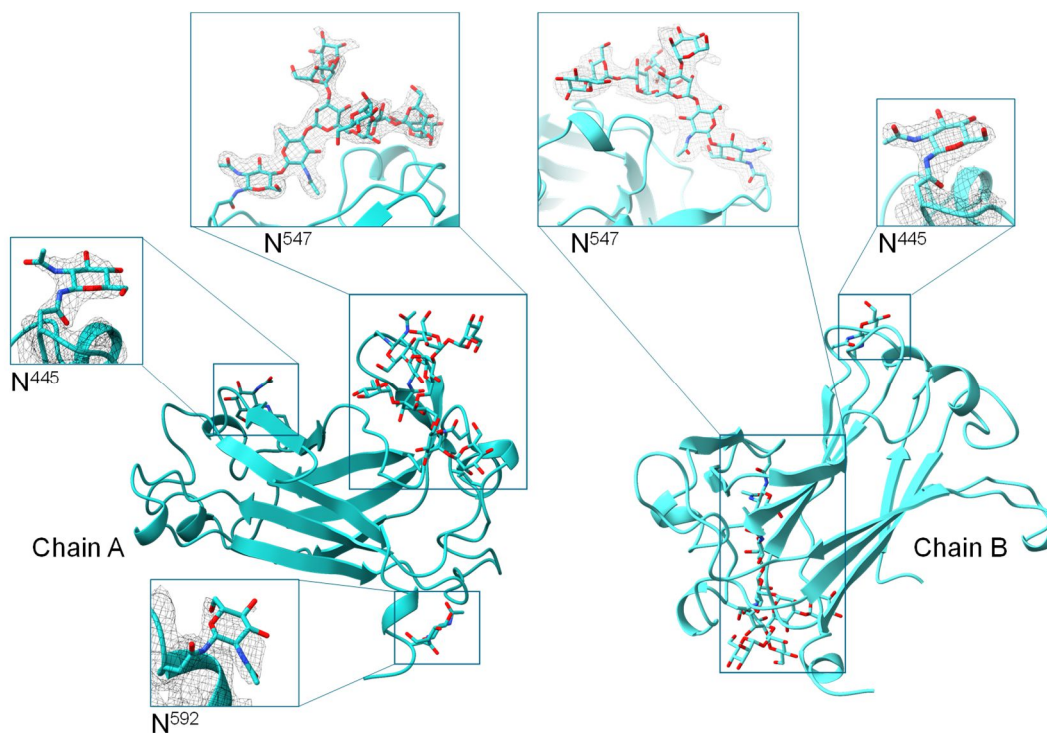
Figure 52: TRAF domain of crystal structure of Meprin β in complex with the specific inhibitor MWT-S-270, spanning the amino acids P^{428}-Q^{595}. *In both chains a large glycosylation tree was identified at N^{547}, still present after deglycosylation with EndoH under native conditions. Additionally, in chain A two N-acetylglucosamine residues were determined at N^{445} and N^{592}. In chain B one additional N-acetylglucosamine residue was identified at N^{445}.*
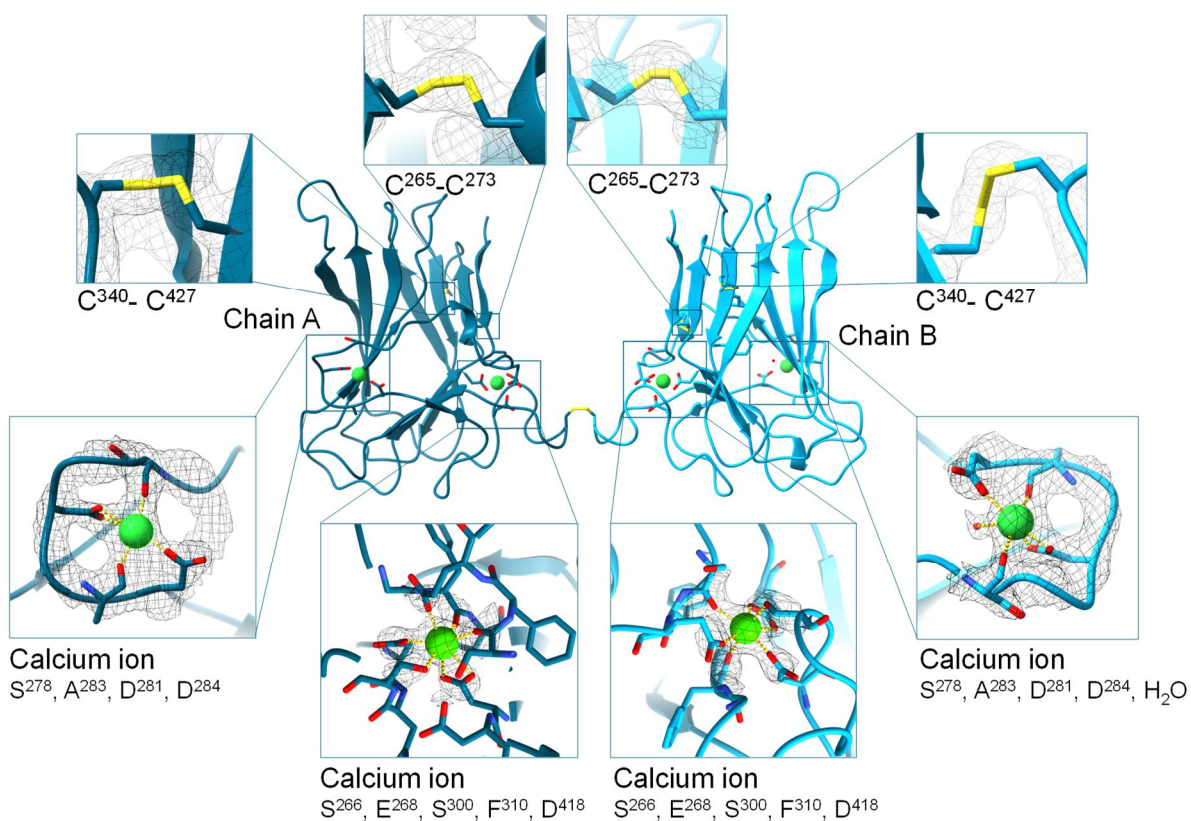
Figure 53: MAM domain of crystal structure of Meprin β in complex with the specific inhibitor MWT-S-270, spanning the amino acids Q^{260}-C^{427}. *Chain A and chain B are linked by an intermolecular disulfide bridge. In both chains two ions are coordinated, one calcium ion in chain A is complexed by S^{278}, A^{283}, D^{284} and a bidentate coordination to D^{281}. In chain B this calcium ion is coordinated by S^{278}, A^{283}, D^{284} and a water molecule as well as a bidentate coordination to D^{281}. The second calcium ion in chain A and chain B is coordinated by S^{266}, E^{268}, D^{298}, S^{300}, F^{310} as well as a bivalent interaction with D^{418}. Additionally, the MAM domains of chain A and chain B are stabilized by intramolecular disulfide bridges between C^{265}-C^{273} and C^{340}-C^{427}.*
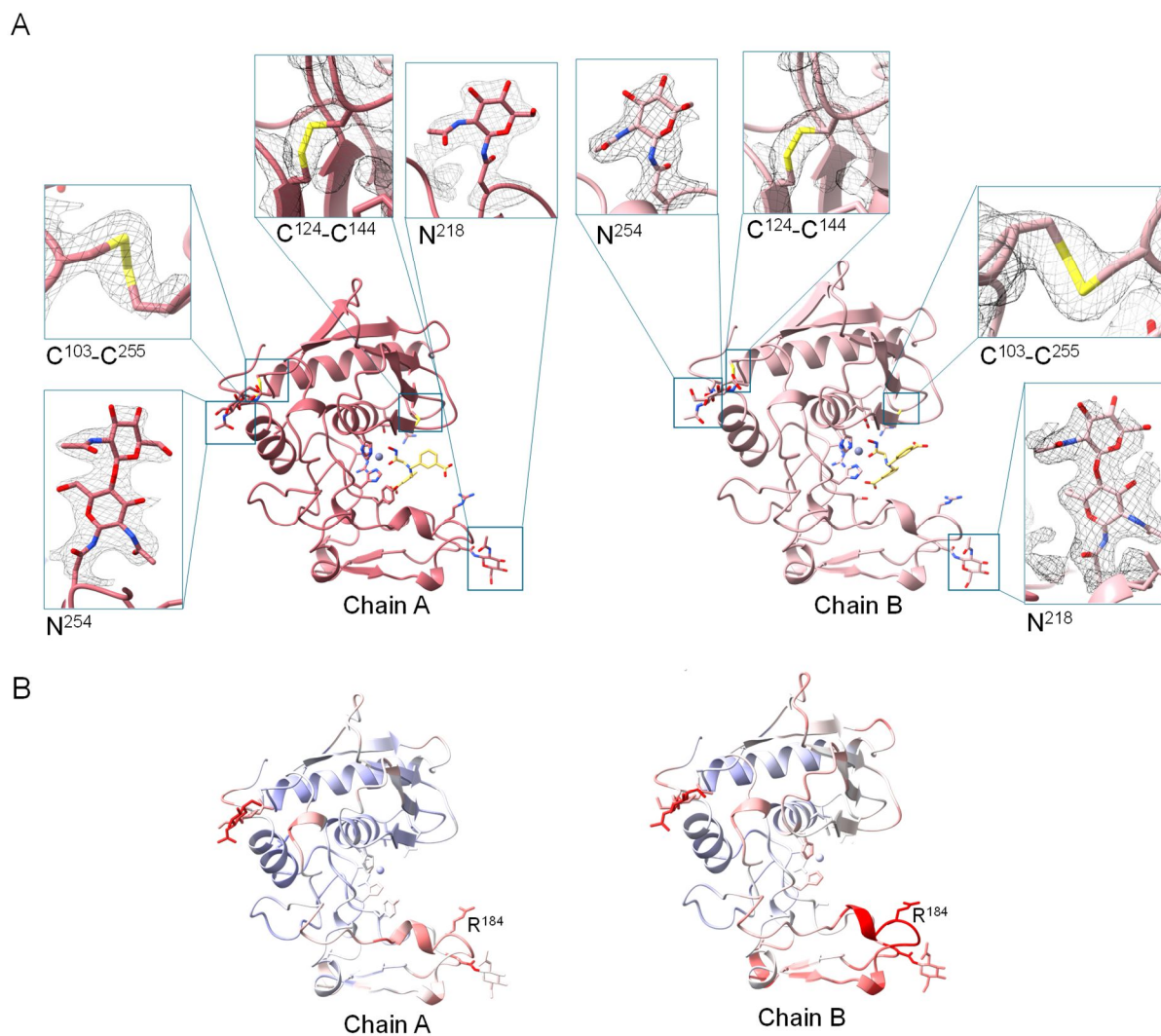
Figure 54: Protease domain of crystal structure of Meprin β in complex with the specific inhibitor MWT-S-270, spanning the amino acids N^{62}-L^{259}. A) Both chains are stabilized by intramolecular disulfide bridges between C^{103}-C^{255} and C^{124}-C^{144}. Two glycosylation sites were elucidated within chain A and chain B at N^{218} and N^{254}. The specific inhibitor could be determined within both chains, although ambiguous density of one of the two benzoic acid moieties. **B)** B-factor staining of the protease domains of chain A and chain B approved high flexibility, especially in proximity to the residue R^{184} within subpocket S1 of the active site cleft.

Table 23: Statistics of cryo-electron microscopy data collection, data processing and structure refinement of Meprin β with the specific inhibitor MWT-S-270. Statistics on data collection and processing provided by Dr. Charles Bayly-Jones and Dr. Christopher Lupton (Monash University Melbourne).

Statistics of data collection and processing	Meprin β with specific inhibitor MWT-S-270
Magnification	165k ×
Voltage [kV]	300
Electron exposure [e$^-$ Å^{-2}]	50
Set defocus range [μm]	-0.5 to -2.0
Measured defocus (μ ± σ) [μm]	1.3±0.5
Camera mode	EFTEM
Frames	50
Pixel size [Å pix^{-1}]	0.86
Micrographs	1808
Particles (total)	74,926
Particles (final)	45,850
Binning factor	1
Symmetry imposed	C2
Global resolution [Å] 0.143 (unmasked/masked)	3.7/3.0
Local resolution range [Å]	2.75 to 5.17
Sphericity of 3DFSC	0.986
Map sharpening B factor [Å^2]	86.1

Refinement statistics	Meprin β with specific inhibitor MWT-S-270
Software used for building	COOT
Software used for refinement	Phenix
Initial model	Crystal structure described in chapter 3.1.4
Model-to-map resolution	
CC [volume]	0.86
[Å, FSC 0.143/0.5, masked]	3.0/3.1
Average B-factors [Å^2]	
Protein	64.48
Ligand	97.36
R. M. S. deviation	
Bond length [Å]	0.003
Bond angles [°]	0.532
Ramachandran plot [%]	
Favored	96.15
Allowed	3.85
Disallowed	0.00
Cβ deviations [%]	0.00
Validation	
MolProbity score	1.60
Clash score	2.26
Poor rotamers [%]	2.73

Figure 55: TRAF domain of cryo-EM structure of Meprin β in complex with the specific inhibitor MWT-S-270, spanning the amino acids P^{428}-Q^{595}. *In both chains a large glycosylation tree was modeled at N^{547}, still present after deglycosylation with EndoH under native conditions. Additionally, in chain A and chain B one N-acetylglucosamine residue was determined at N^{445}.*
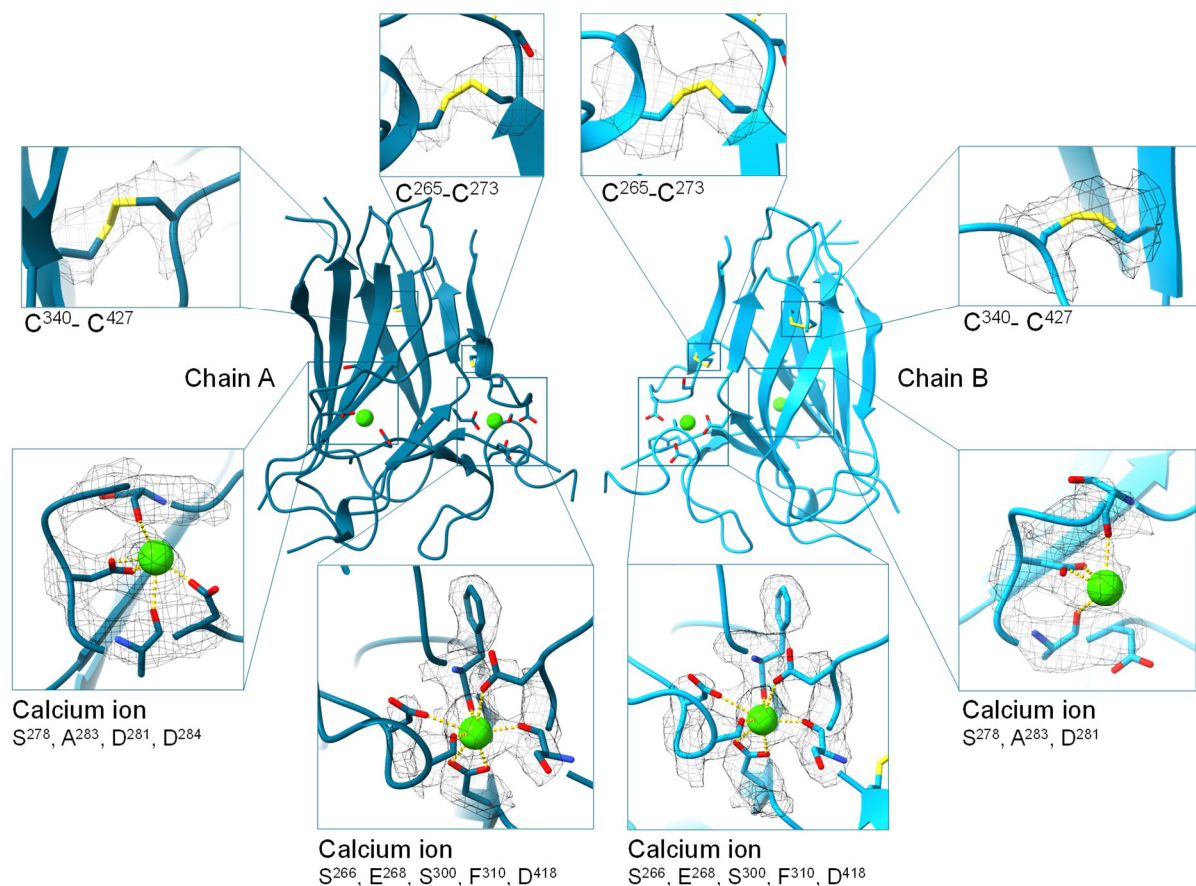
Figure 56: MAM domain of cryo-EM structure of Meprin β in complex with the specific inhibitor MWT-S-270, spanning the amino acids Q^{260}-C^{427}. In both chains two ions are coordinated. The first calcium ion within chain A is complexed by S^{278}, A^{283}, D^{284} and a bidentate coordination to D^{281}, within chain B D^{284} seemed to have another orientation (poor density) and therefore do not interact with the calcium. The second calcium ion within chain A and chain B is coordinated by S^{266}, E^{268}, S^{300}, D^{298}, F^{310} as well as a bivalent interaction with D^{418}. Additionally, the MAM domains of chain A and chain B are stabilized by intramolecular disulfide bridges between C^{265}-C^{273} and C^{340}-C^{427}.
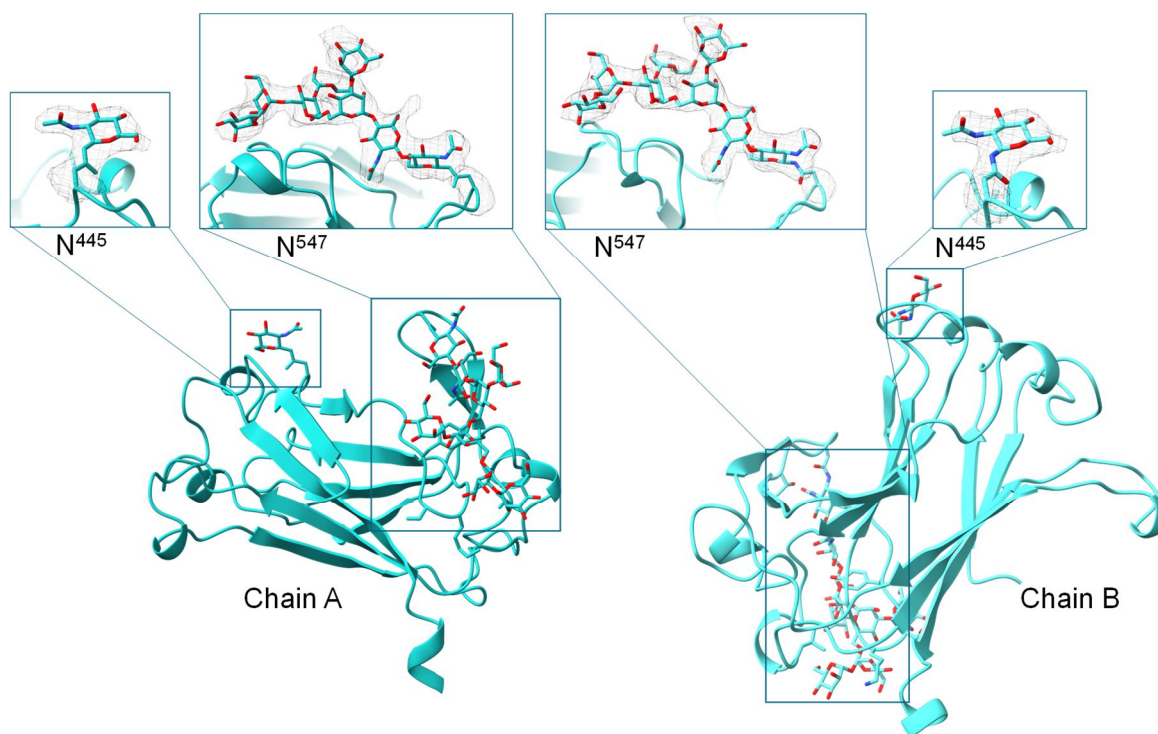
Figure 57: Protease domain of cryo-EM structure of Meprin β in complex with the specific inhibitor MWT-S-270, spanning the amino acids N^{62}-L^{259}. A) Both chains are stabilized by intramolecular disulfide bridges between C^{103}-C^{255} and C^{124}-C^{144}. Two glycosylation sites were elucidated within chain A and chain B at N^{218} and N^{254}. The specific inhibitor is well defined within both chains. B) B-factor staining of the protease domains of chain A and chain B approved high flexibility, especially close the residue R^{184} within subpocket S1 of the active cleft.

Meprin β, cryo-EM structure   Meprin β, crystal structure

A   Chain A   Chain A

S2' R^{146}

S1' R^{238}

S1 R^{184}

90°

B   Chain A, cryo   Chain A, crystal

■ Protease domain/chain A   ■ TRAF domain/chain A
■ MAM domain/chain A   ■ Inhibitor MWT-S-698/chain A and B

Figure 58: Comparison of Meprin β cryo-EM and crystal structure, with respect to the shape of the active site. Showing 'closed' and 'opened' position, mediated by the orientation of R^{184} of subpokcet S1. A) 'Standard orientation' of chain A of cryo-EM and crystal structure, representation of surface structure with view into the active cleft. The Arginine residues R^{184}, R^{238} and R^{146}, shaping the subpockets S1, S1' and S2', are colored in dark blue. B) Chain A rotated 90° on the vertical axis. Distinct difference of the orientstion of R^{184} between cryo-EM and X-ray generated structure, leading to 'closed' active cleft in cryo-EM Meprin β structure and 'opened' active cleft in Meprin β crystal structure, representing high flexibility.

Table 24: Statistics of cryo-electron microscopy data collection, data processing and structure refinement of Meprin α data sets. Statistics on data collection and processing provided by Dr. Charles Bayly-Jones and Dr. Christopher Lupton (Monash University Melbourne).

Statistics of data collection and processing	Meprin α with specific inhibitor MWT-S-698
Magnification	75k ×
Voltage [kV]	300
Electron exposure [e⁻ Å⁻²]	50
Set defocus range [μm]	-0.5 to -1.5
Measured defocus (μ ± σ) [μm]	1.0±1.3
Camera mode	EFTEM
Frames	50
Pixel size [Å pix⁻¹]	1.06
Micrographs	2,366
Particles (total)	925,458
Particles (final)	325,162
Binning factor	1
Symmetry imposed	C1
Global resolution [Å] 0.143 (unmasked/masked)	3.0/2.4
Local resolution range [Å]	2.35-3.50
Sphericity of 3DFSC	0.978
Map sharpening B factor [Å²]	47.4

Refinement statistics	Meprin α with specific inhibitor MWT-S-698 (two monomers)	Meprin α with specific inhibitor MWT-S-698 (four monomers)
Software used for building	COOT	COOT
Software used for refinement	Phenix	Phenix
Initial model	4GWN	4GWN
Model-to-map resolution		
CC [volume]	0.81	0.82
[Å, FSC 0.143/0.5 masked]	2.2/2.6	2.3/2.6
Average B-factors [Å²]		
Protein	48.64	41.31
Ligand	63.01	53.86
R. M. S. deviation		
Bond length [Å]	0.008	0.009
Bond angles [°]	0.665	0.700
Ramachandran plot [%]		
Favored [%]	95.46	94.22
Allowed [%]	4.54	5.87
Disallowed [%]	0.00	0.00
Cβ deviations [%]	0.00	0.00
Validation		
MolProbity score	2.04	2.31
Clash score	3.61	6.05
Poor rotamers [%]	5.62	5.83

Figure 59: TRAF domain of cryo-EM structure of Meprin α in complex with the specific inhibitor MWT-S-698, spanning the amino acids G^{434}-S^{600}. In both chains an N-acetylglucosamine residue was modeled at N^{440}.
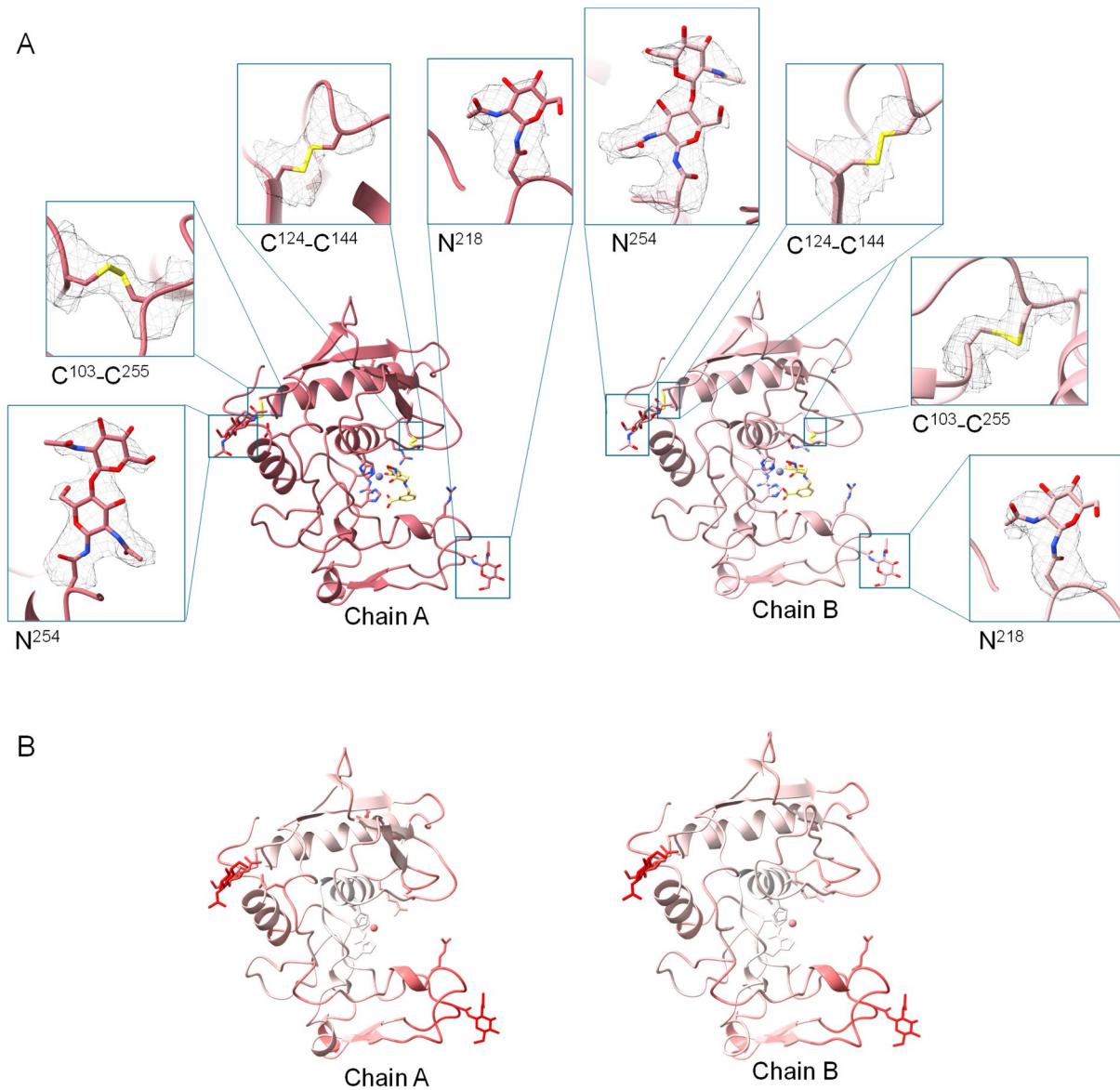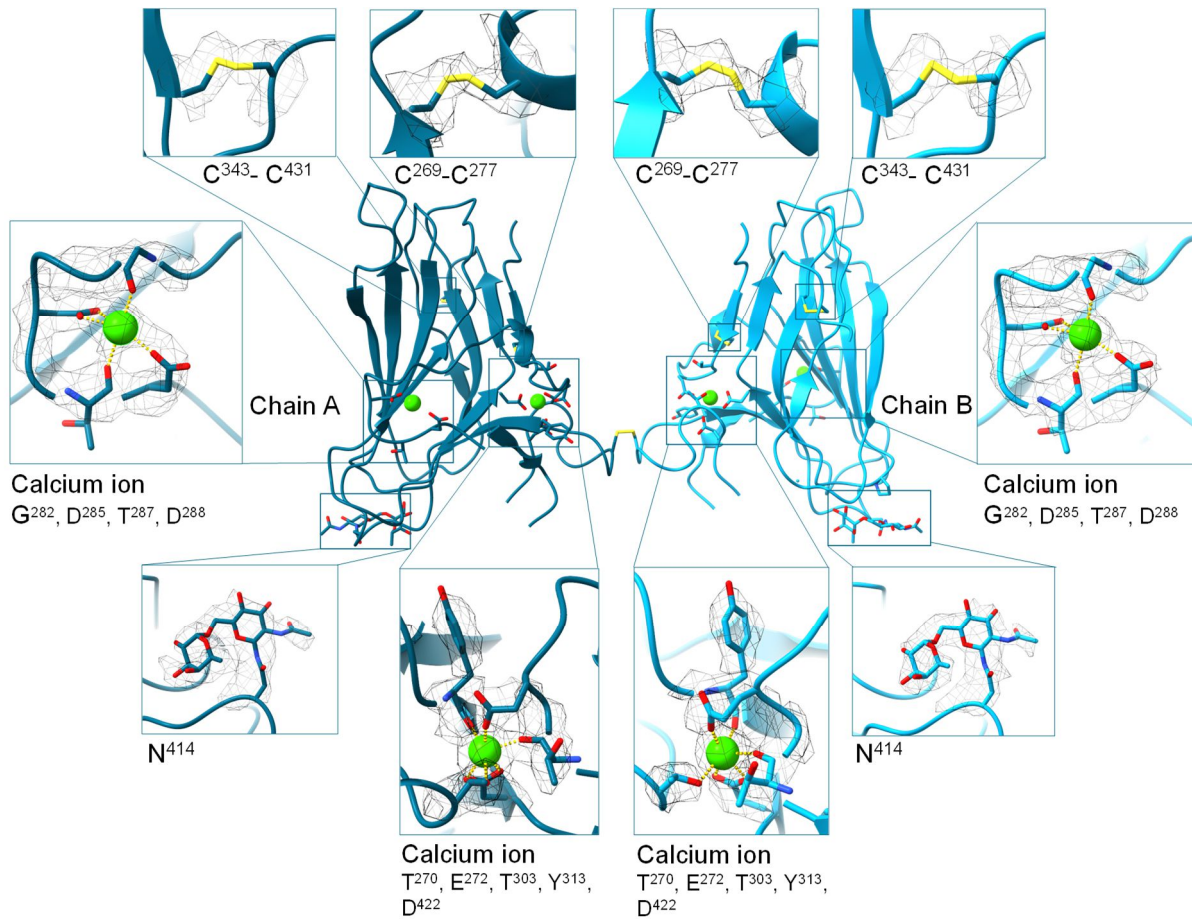
Figure 60: MAM domain of cryo-EM structure of Meprin α in complex with the specific inhibitor MWT-S-698, spanning the amino acids T^{264}-T^{434}. *Chain A and chain B linked by an intermolecular disulfide bridge. In both chains two ions are coordinated. The first calcium ion within chain A and chain B is complexed by T^{282}, D^{285}, T^{287} and a bidentate coordination to D^{288}. The second calcium ion within chain A and chain B is coordinated by T^{270}, E^{272}, T^{303}, Y^{313} as well as a bivalent interaction with D^{422}. Additionally, the MAM domains of chain A and chain B are stabilized by intramolecular disulfide bridges between C^{269}-C^{277} and C^{343}-C^{431}.*
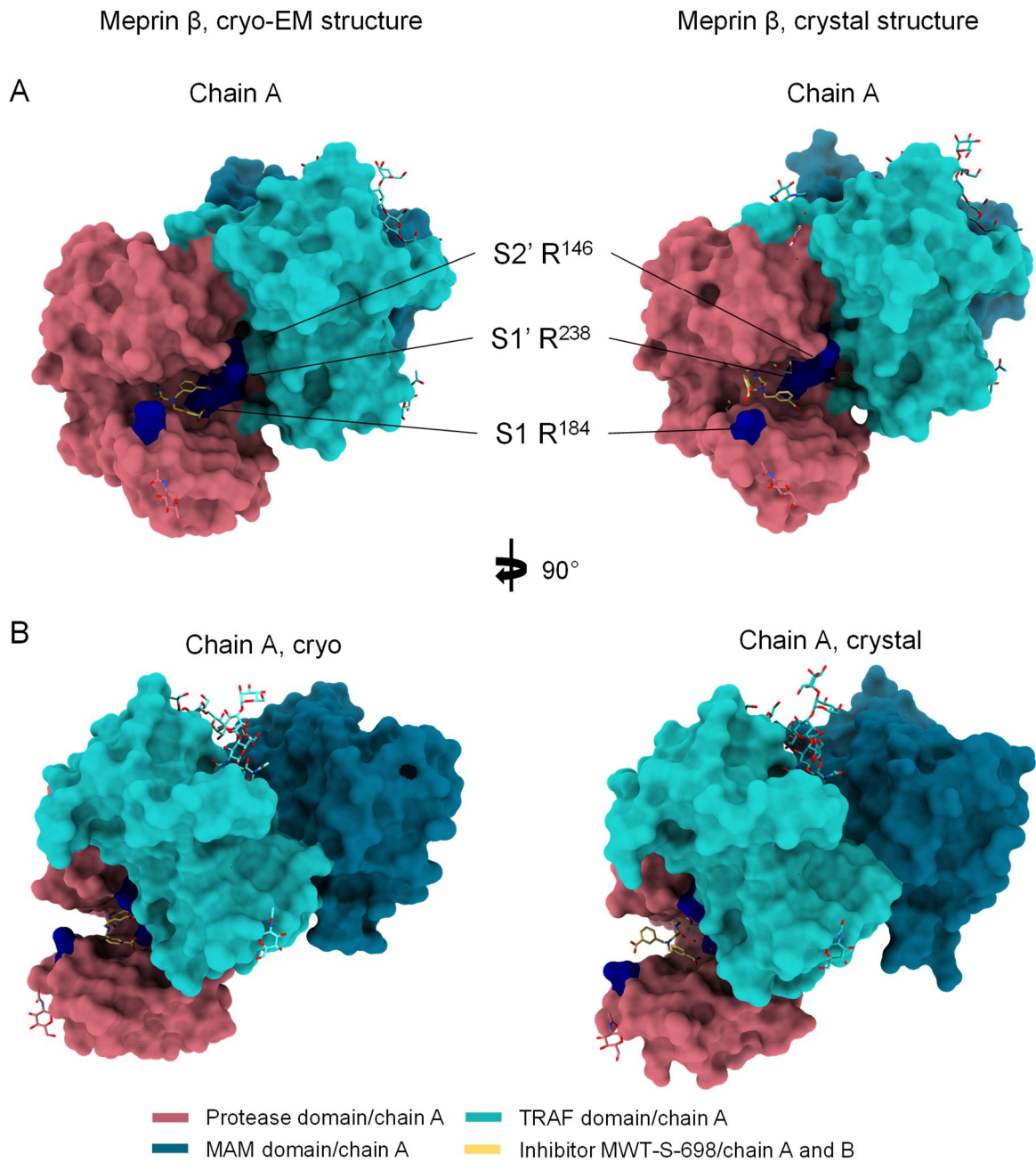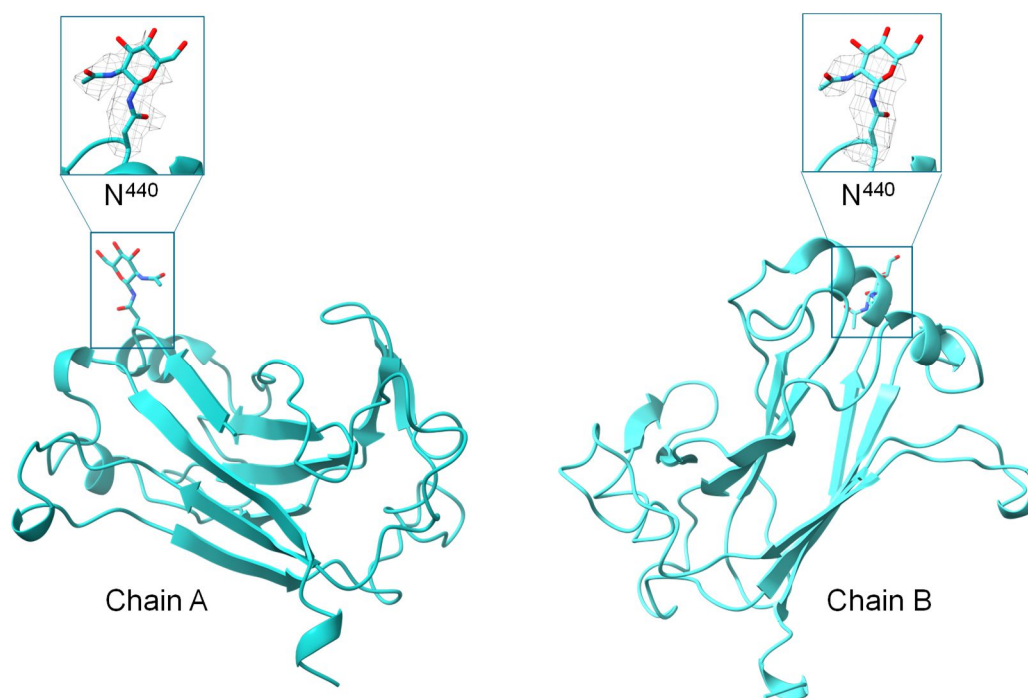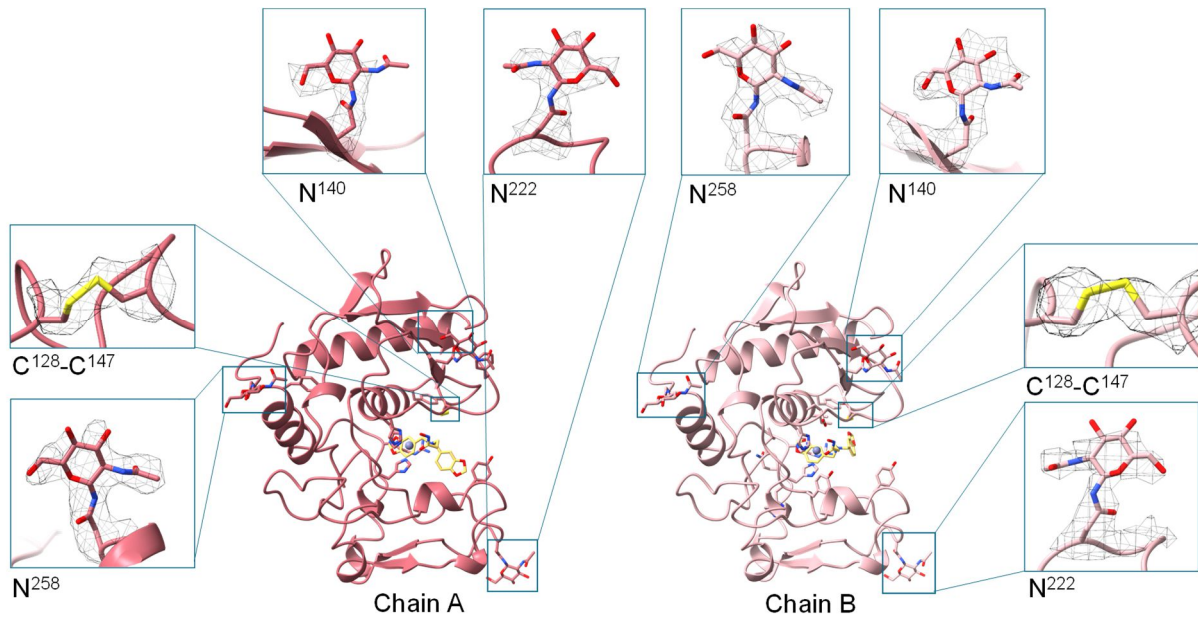
Figure 61: Protease domain of cryo-EM structure of Meprin α in complex with the specific inhibitor MWT-S-698, spanning the amino acids N^{66}-H^{263}. Both chains are stabilized by an intramolecular disulfide bridge between C^{128}-C^{147}. Three glycosylation sites were determined within chain A and chain B at N^{140}, N^{222} and N^{258}. The specific inhibitor could be docked within both chains, although ambiguous density for one of the two benzodioxolane moieties.
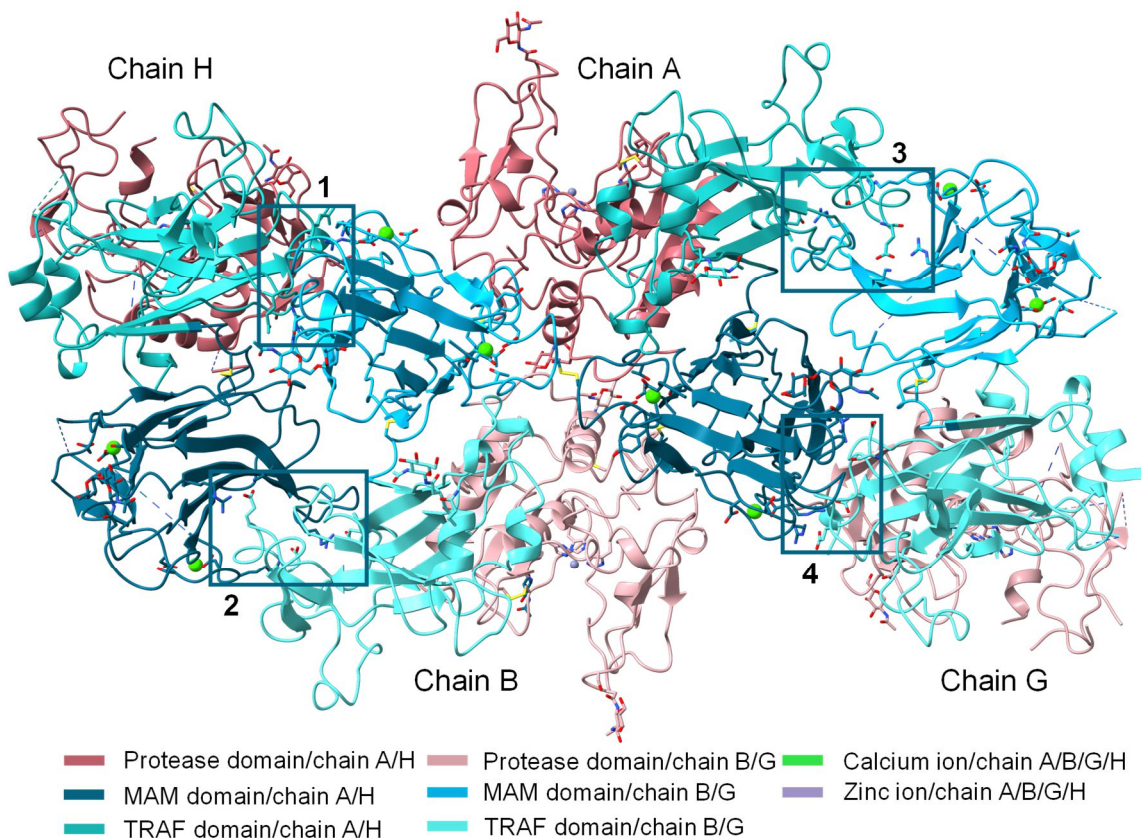
Figure 62: Dimeric Meprin α non-covalently linked to adjacent Meprin α molecules via ionic interactions within MAM and TRAF domains of chain A/B/G/H. Four interfaces (labeled 1-4) observed between dimeric Meprin α and adjacent Meprin α monomers. Within in all four interfaces the same amino acids are involved in helix formation. Colored according to domains.
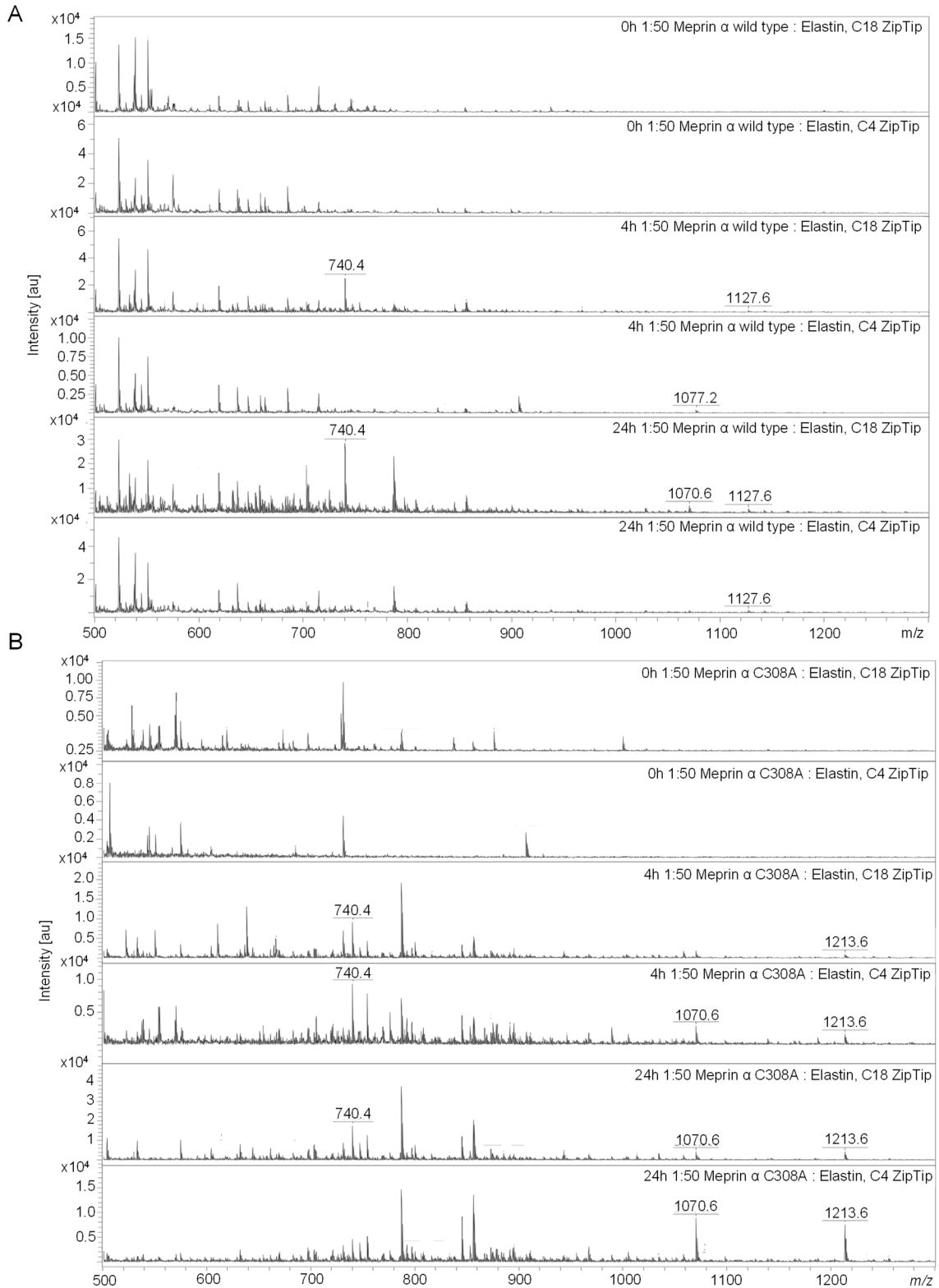
Figure 63: MALDI-TOF analysis of Elastin turnover by Meprin α wild type and Meprin α C308A, respectively. *The samples have been purified by C4 and C18 ZipTip and analyzed in reflector positive mode. Identified cleavage products are labeled.*

```
MepB:      NSIIGEKYRWPH-TIPYVLEDSLEMNAKGVILNAFERYRLKTCIDFKPWAGETNYISV-F    58
MepA:      NGLRDPNTRWTF-PIPYILADNLGLNAKGAILYAFEMFRLKSCVDFKPYEGESSYIIF-Q    58
Astacin:   AAILGDEYLWSGGVIPYTFAGVSG-ADQSAILSGMQELEEKTCIRFVPRTTESDYVEIFT    59
            .: . :  *    *** : .      :..** .::  . *:*: * *   *:..*: .

MepB:      KGSGCWSSVGNRRVGKQELSIGANCDRIATVQHEFLHALGFWHEQSRSDRDDYVRIMWDR    118
MepA:      QFDGCWSEVGDQHVGQ-NISIGQGCAYKAIIEHEILHALGFYHEQSRTDRDDYVNIWWDQ    117
Astacin:   SGSGCWSYVGRISGAQQVSLQANGCVYHGTIIHELMHAIGFYHEHTRMDRDNYVTINYQN    119
            . .**** **    .:     . .*   . : **::**:**:**::* ***:** * ::.

MepB:      ILSGREHNFNTYSDDISDSLNVPYDYTSVMHYSKTAFQN-GTEPTIVTRISDFEDVIG--    175
MepA:      ILSGYQHNFDTYDDSLITDLNTPYDYESLMHYQPFSFNKNASVPTITAKIPEFNSIIG--    175
Astacin:   VDPSMTSNFDI--DTYSRYVGEDYQYYSIMHYGKYSFSIQWGVLETIVPLQNGIDLTDPY    177
            :  .   **:   *    :.  *:* *:***   :*.         . : : .: .

MepB:      QRMDFSDSDLLKLNQLYNCSSSL       198
MepA:      QRLDFSAIDLERLNRMYNCTTTH       198
Astacin:   DKAHMLQTDANQINNLYTNECSL       200
            :: .:   *  ::*.:*.   :
```

Figure 64: Sequence alignment of protease domains of human Meprin β (MepB, UniProt: Q16820, amino acids N^{62} to L^{259}), human Meprin α (MepA, UniProt: Q16819, amino acids N^{66} to H^{263}) and crayfish Astacin protease (Asta, UniProt: P07584, amino acids A^{50} to L^{249}) by webserver Clustal Omega (McWilliam et al. 2013). Identical amino acids are marked by *, amino acids with similar feature are marked by :, amino acids with less similarity are marked by ..

Table 25: Peptides resulting upon turnover of Elastin by Meprin α C308A and Meprin α wild type, identified by nanoLC-MS/MS. The measurement was executed by Tobias Hedtke (lab of Dr. Schmelzer, Fraunhofer IWMS).

Elastin cleavage by Meprin α C308A		Elastin cleavage by Meprin α wildtype	
P1	peptide	P1	peptide
G	AAGLGGVLGAGQPFPIGGGAG	G	VGGIGGVGGLGVSTGA
G	VGGIGGVGGLGVSTGA	G	VAPGIGLGPGGVIGAG
Y	PGGVLPGAGAR	G	AGQPFPIGGG
G	AGQPFPIGGGAGGLGVGG	G	VYPGGVLPGAGAR
S	TGAVVPQLGAGVGAGV	G	QPFPIGGGAGGLGVGG
G	GLGVSTGAVVPQLG	G	GVLPGAGARFPG
G	VGGIGGVGGLGVSTG	G	AGQPFPIGGGAG
G	IGVLPGVPTGAG	G	VGVAPGVGVVP(+15.99)G
G	VAPGIGLGPGGVIGAG	G	AGQPFPIGGGAGG
G	AGQPFPIGGGAGGL	G	AGQPFPIGGGAGGLG
G	VYPGGVLPGAGAR	F	GLGPGVGVAPGVG
G	VAPGIGLGPGGVIGA	A	GQPFPIGGG
L	GAGQPFPIGGGAG	A	GQPFPIGGGAG
G	LPGVYPGGVLPGAGAR	G	YPTGTGVGPQA
G	VLPGVPTGAGV	P	FPIGGGAGGLG
G	VVPGVGVAPGIGLGPGGVIGAG	G	DLGGAGIPGGVAG
G	AGQPFPIGGGAG	V	PGVGVVPGVGVA
G	AGQPFPIGGG	A	GQPFPIGGGA
G	VGVP(+15.99)GVGVP(+15.99)GVGVP(+15.99)GVG	G	QPFPIGGGAG
G	VGGVP(+15.99)GVGIP(+15.99)AAA	G	VAPGIGLGPGGVIG
G	VAPGIGLGPGG	G	VLPGAGARFP(+15.99)G
G	QPFPIGGGAGGLGVGG	G	VLPGAGARFPG

Elastin cleavage by Meprin α C308A		Elastin cleavage by Meprin α wildtype	
P1	**peptide**	**P1**	**peptide**
G	GVLPGAGARFPG	A	GLGVGGIGGVGGL
G	VYPGGVLPGAGARFPG	A	GIPGVGPFG
L	GAGQPFPIGGG	G	VYPGGVLPGAG
G	VP(+15.99)GVGVPGVGVP(+15.99)GVGVP(+15.99)G	G	AGQPFPIGG
A	GIPGVGPFGG	G	LPGVYPGGVLPGAGAR
A	GQPFPIGGGAG	G	FPGIGDAAA
G	LGGVGGLGVGGLG		
A	GQPFPIGGGAGGLGVGG		
G	IGLGPGGVIGAGVPAAA		
G	VGVAPGIGLGPGGVIGA		
G	AVGLGGVSPAAA		
G	VGVP(+15.99)GVGVP(+15.99)GVG		
G	VGVAPGVGVVP(+15.99)G		
L	GPGVGVAPGVG		
G	GVPGVGIPAAA		
S	TGAVVPQLGAG		
F	AGIP(+15.99)GVGPFG		
G	GVLPGAGARFPGIG		
G	VLPGAGARFPG		
G	VGVP(+15.99)GVGVP(+15.99)GVGVP(+15.99)G		
A	GQPFPIGGGAGGLGVG		
G	AGQPFPIGGGAGG		
G	VPGVGVPGVGVP(+15.99)GVG		
G	VPGLGVGAGVP(+15.99)GLG		
P	FPIGGGAGGLG		
G	VP(+15.99)GVGVP(+15.99)GVGVP(+15.99)GVG		
G	YPTGTGVGPQA		
G	AGQPFPIGGGAGGLGVG		
G	LGGVLGAGQPFPIGGGAGG		
G	AGQPFPIGG		
A	GIPGVGPFG		
G	VYPGGVLPGAG		
V	GVP(+15.99)GVGVP(+15.99)GVGVP(+15.99)GVGVPGALS		
G	AVPGGVPGGVF		
G	VGPFGGQQPG		
G	GVGGLGVGGLGA		
G	VP(+15.99)GVGVPGVGVP(+15.99)GVGVP(+15.99)GVG		
L	GAGQPFPIGGGAGGL		
G	QPFPIGGGAG		
G	VPGVGVP(+15.99)GVGVP(+15.99)GVG		

Elastin cleavage by Meprin α C308A		Elastin cleavage by Meprin α wildtype	
P1	peptide	P1	peptide
G	VGGVP(+15.99)GVGIP(+15.99)AA		
G	AVGLGGVSPAA		
S	TGAVVPQLGAGVGAG		
F	GLGGVGGLGVGGLG		
G	AVVPQLGAGVGAGV		
L	GAGQPFPIGGGAGGLG		
G	VGGVPGVGIP(+15.99)AAA		
Q	FGLGPGVGVAPGVG		
G	VVPGVGVVPGVGV		
G	VGVAPGIGLGPGGVIGAG		
V	GVPGVGVP(+15.99)GVG		
G	AGQPFPIGGGAGGLG		
A	GIP(+15.99)GVGPFGGQ		
A	GVGAPDAAAAAA		
G	QPFPIGGGAGG		
R	FPGIGVLPG		
G	VLPGAGARFP(+15.99)G		
G	VGGIGGVGGLGV		
V	P(+15.99)GVGVVP(+15.99)GVGVAP(+15.99)G		
G	VGVAP(+15.99)GVGVVP(+15.99)G		
G	VLPGVPTGAG		
G	AVPGGVP(+15.99)GGVF		
G	VGGIGGVGGLGVS		
G	APGAIP(+15.99)GIGGIAGVG		
G	VGVPGVGVP(+15.99)GVG		
F	FPGAGLGGLGVG		
G	VGGVP(+15.99)GVGIPAA		
G	AVVPQLGAG		
A	GIP(+15.99)GVGPFG		
G	IGLGPGGVIGAGVPAA		
G	FPGIGDAAA		
G	GVGDLGGAGIPGGVAG		
G	AGARFPGIG		
L	GAGQPFPIG		
G	APDAAAAAAAAA		
G	IGLGPGGVIGAGVPA		
A	PGVGVVPGVG		
G	LGVGGIGGVGGLGVS		
F	GLGGVGGLGVGGL		
G	AVGLGGVSPAAAA		
L	GAGQPFPIGG		
G	ALGGVGDLGGAGIP(+15.99)G		
G	VVPGVGVVPGVG		
G	VGVAPGVGVVPG		
G	VYPGGVLPG		

Elastin cleavage by Meprin α C308A		Elastin cleavage by Meprin α wildtype	
P1	peptide	P1	peptide
V	GVPGVGVPGVG		
G	GVLPGAGARFP(+15.99)G		
F	FPGAGLGGLG		
A	GQPFPIGGGA		
G	LGGVLGAGQPFPIGGG		
S	TGAVVPQLGAGVG		
G	APGAIPGIGGIAG		
L	GAGQPFPIGGGAGG		
V	P(+15.99)GVGVP(+15.99)GVGVP(+15.99)GVG VPGALS		
A	GQPFPIGGGAGGLG		
A	GQPFPIGGG		
P	GVGVAPGVGV		
S	TGAVVPQLGA		
G	VLPGAGARFPGIG		
G	VPGLGVGAGVPGLG		
G	VP(+15.99)GVGVPGVGVP(+15.99)GVG		
G	GVPGVGIPAAAAA		
G	LPGVYPGGVLPGAG		
S	TGAVVPQLG		
A	GQPFPIGGGAGGL		
G	VPGVGVP(+15.99)GVG		
R	FPGIGVLPGVPTGAG		
F	GLGPGVGVAPGVG		
G	VPGLGVGAGVPG		
G	PGGVIGAGVPAA		
G	LGPGGVIGAGVPA		
G	APGAIP(+15.99)GIGGIA		
V	GVPGVGVPGALSPAA		
G	LGPGGVIGAGVP(+15.99)AA		
G	GVPGVGIP(+15.99)AAA		
G	APGAIPGIGGIAGVG		
G	GIAGVGAPDAAA		
G	VGVPGVGVP(+15.99)GVGVP(+15.99)G		
G	IGVLPGVPTGAGV		
G	VAPGVGVVPGVG		
G	VPGVGVPGVGVPGVG		

7. References

Aaij, C. and Borst, P. (1972). The gel electrophoresis of DNA. *Biochim. Biophys. Acta* **269**, 192–200.

Aguda, A. H., Panwar, P., Du, X., Nguyen, N. T., Brayer, G. D. and Brömme, D. (2014). Structural basis of collagen fiber degradation by cathepsin K. *Proc. Natl. Acad. Sci. U.S.A.* **111**, 17474–17479.

Ahmed, S. and Palevsky, H. I. (2014). Pulmonary arterial hypertension related to connective tissue disease: a review. *Rheum. Dis. Clin. North. Am.* **40**, 103–124.

Alegria-Schaffe, A., Lodge, A. and Vattem, K., eds. (2009). *Guide to Protein Purification, 2nd Edition. Chapter 33 Performing and Optimizing Western Blots with Emphasis on Chemiluminescent Detection*. Methods in Enzymology: Elsevier.

Armbrust, F., Colmorgen, C., Pietrzik, C. U. and Becker-Pauly, C. (2019). *The Alzheimer's disease associated bacterial protease RgpB from P. gingivalis activates the alternative β-secretase meprin β thereby increasing Aβ generation*.

Arnold, P., Otte, A. and Becker-Pauly, C. (2017). Meprin metalloproteases: Molecular regulation and function in inflammation and fibrosis. *Biochim. Biophys. Acta Mol. Cell. Res.* **1864**, 2096–2104.

Arolas, J. L., Broder, C., Jefferson, T., Guevara, T., Sterchi, E. E., Bode, W., Stöcker, W., Becker-Pauly, C. and Gomis-Rüth, F. X. (2012). Structural basis for the sheddase function of human meprin β metalloproteinase at the plasma membrane. *Proc. Natl. Acad. Sci. U.S.A.* **109**, 16131–16136.

Bai, J., Swartz, D. J., Protasevich, I. I., Brouillette, C. G., Harrell, P. M., Hildebrandt, E., Gasser, B., Mattanovich, D., Ward, A., Chang, G. et al. (2011). A gene optimization strategy that enhances production of fully functional P-glycoprotein in Pichia pastoris. *PLoS ONE* **6**, e22577.

Banerjee, S. and Bond, J. S. (2008). Prointerleukin-18 is activated by meprin beta in vitro and in vivo in intestinal inflammation. *J. Biol. Chem.* **283**, 31371–31377.

Barnes, K., Ingram, J. and Kenny, A. J. (1989). Proteins of the kidney microvillar membrane. Structural and immunochemical properties of rat endopeptidase-2 and its immunohistochemical localization in tissues of rat and mouse. *Biochem. J.* **264**, 335–346.

Barton, R., Driscoll, A., Flores, S., Mudbhari, D., Collins, T., Iovine, M. K. and Berger, B. W. (2015). Cysteines in the neuropilin-2 MAM domain modulate receptor homooligomerization and signal transduction. *Biopolymers* **104**, 371–378.

Baud, V., Liu, Z. G., Bennett, B., Suzuki, N., Xia, Y. and Karin, M. (1999). Signaling by proinflammatory cytokines: oligomerization of TRAF2 and TRAF6 is sufficient for JNK and IKK activation and target gene induction via an amino-terminal effector domain. *Genes Dev.* **13**, 1297–1308.

Becker, C., Kruse, M.-N., Slotty, K. A., Köhler, D., Harris, J. R., Rösmann, S., Sterchi, E. E. and Stöcker, W. (2003). Differences in the activation mechanism between the alpha and beta subunits of human meprin. *J. Biol. Chem.* **384**, 825–831.

Becker, D. M. and Guarente, L. (1991). [12] High-efficiency transformation of yeast by electroporation. In *Guide to Yeast Genetics and Molecular Biology* (ed. C. Guthrie and G. Fink), pp. 182–187: Elsevier.

Becker-Pauly, C., Barré, O., Schilling, O., dem Keller, U. auf, **Ohler, A., Broder, C., Schütte, A., Kappelhoff, R., Stöcker, W. and Overall, C. M.** (2011). Proteomic analyses reveal an acidic prime side specificity for the astacin metalloprotease family reflected by physiological substrates. *Mol. Cell. Proteom.* **10**, M111.009233.

Becker-Pauly, C. and Pietrzik, C. U. (2016). The Metalloprotease Meprin β Is an Alternative β-Secretase of APP. *Front. Mol. Neurosci.* **9**, 159.

Beckmann, G. and Bork, P. (1993). An adhesive domain detected in functionally diverse receptors. *Trends Biochem. Sci.* **18**, 40–41.

Bedau, T., Peters, F., Prox, J., Arnold, P., Schmidt, F., Finkernagel, M., Köllmann, S., Wichert, R., Otte, A., Ohler, A. et al. (2017). Ectodomain shedding of CD99 within highly conserved regions is mediated by the metalloprotease meprin β and promotes transendothelial cell migration. *FASEB J.* **31**, 1226–1237.

Bertenshaw, G. P., Norcum, M. T. and Bond, J. S. (2003). Structure of homo- and hetero-oligomeric meprin metalloproteases. Dimers, tetramers, and high molecular mass multimers. *J. Biol. Chem.* **278**, 2522–2532.

Bertenshaw, G. P., Turk, B. E., Hubbard, S. J., Matters, G. L., Bylander, J. E., Crisman, J. M., Cantley, L. C. and Bond, J. S. (2001). Marked differences between metalloproteases meprin A and B in substrate and peptide bond specificity. *J. Biol. Chem.* **276**, 13248–13255.

Bertenshaw, G. P., Villa, J. P., Hengst, J. A. and Bond, J. S. (2002). Probing the active sites and mechanisms of rat metalloproteases meprin A and B. *J. Biol. Chem.* **383**, 1175–1183.

Bertini, I., Calderone, V., Fragai, M., Luchinat, C., Mangani, S. and Terni, B. (2004). Crystal structure of the catalytic domain of human matrix metalloproteinase 10. *J. Mol. Biol.* **336**, 707–716.

Beynon, R. J., Oliver, S. and Robertson, D. H. (1996). Characterization of the soluble, secreted form of urinary meprin. *Biochem. J.* **315 (Pt 2)**, 461–465.

Beynon, R. J., Shannon, J. D. and Bond, J. S. (1981). Purification and characterization of a metallo-endoproteinase from mouse kidney. *Biochem. J.* **199**, 591–598.

Biasin, V., Marsh, L. M., Egemnazarov, B., Wilhelm, J., Ghanim, B., Klepetko, W., Wygrecka, M., Olschewski, H., Eferl, R., Olschewski, A. et al. (2014). Meprin β, a novel mediator of vascular remodelling underlying pulmonary hypertension. *J. Pathol.* **233**, 7–17.

Bien, J., Jefferson, T., Causević, M., Jumpertz, T., Munter, L., Multhaup, G., Weggen, S., Becker-Pauly, C. and Pietrzik, C. U. (2012). The metalloprotease meprin β generates amino terminal-truncated amyloid β peptide species. *J. Biol. Chem.* **287**, 33304–33313.

Blake, M. S., Johnston, K. H., Russell-Jones, G. J. and Gotschlich, E. C. (1984). A rapid, sensitive method for detection of alkaline phosphatase-conjugated anti-antibody on Western blots. *Anal. Biochem.* **136**, 175–179.

Bode, W., Gomis-Rüth, F. X., Huber, R., Zwilling, R. and Stöcker, W. (1992). Structure of astacin and implications for activation of astacins and zinc-ligation of collagenases. *Nature* **358**, 164–167.

Bond, J. S. (2019). Proteases: History, discovery, and roles in health and disease. *J. Biol. Chem.* **294**, 1643–1651.

Bond, J. S. and Beynon, R. J. (1995). The astacin family of metalloendopeptidases. *Protein Sci.* **4**, 1247–1261.

Bond, J. S., Matters, G. L., Banerjee, S. and Dusheck, R. E. (2005). Meprin metalloprotease expression and regulation in kidney, intestine, urinary tract infections and cancer. *FEBS Lett.* **579**, 3317–3322.

Bradford, M. M. (1976). A rapid and sensitive method for the quantitation of microgram quantities of protein utilizing the principle of protein-dye binding. *Anal. Biochem.* **72**, 248–254.

Breig, O., Yates, M., Neaud, V., Couchy, G., Grigoletto, A., Lucchesi, C., Prox, J., Zucman-Rossi, J., Becker-Pauly, C. and Rosenbaum, J. (2017). Metalloproteinase meprin α regulates migration and invasion of human hepatocarcinoma cells and is a mediator of the oncoprotein Reptin. *Oncotarget* **8**, 7839–7851.

Brito, J. A. and Archer, M. (2020). Structural biology techniques: X-ray crystallography, cryo-electron microscopy, and small-angle X-ray scattering. In *Practical Approaches to Biological Inorganic Chemistry* (ed. R. R. Crichton and R. O. Louro), pp. 375–416: Elsevier.

Broder, C., Arnold, P., Vadon-Le Goff, S., Konerding, M. A., Bahr, K., Müller, S., Overall, C. M., Bond, J. S., Koudelka, T., Tholey, A. et al. (2013). Metalloproteases meprin α and meprin β are C- and N-procollagen proteinases important for collagen assembly and tensile strength. *Proc. Natl. Acad. Sci. U.S.A.* **110**, 14219–14224.

Broder, C. and Becker-Pauly, C. (2013). The metalloproteases meprin α and meprin β: unique enzymes in inflammation, neurodegeneration, cancer and fibrosis. *Biochem. J.* **450**, 253–264.

Buchner, J. and Kiefhaber, T. (2005). *Protein folding handbook*. Weinheim: Wiley-VCH.

Burkart, A. D., Xiong, B., Baibakov, B., Jiménez-Movilla, M. and Dean, J. (2012). Ovastacin, a cortical granule protease, cleaves ZP2 in the zona pellucida to prevent polyspermy. *J. Cell Biol.* **197**, 37–44.

Carmago, S., Shah, S. V. and Walker, P. D. (2002). Meprin, a brush-border enzyme, plays an important role in hypoxic/ischemic acute renal tubular injury in rats. *Kidney Int.* **61**, 959–966.

Carrillo, P. J. P., Hervás, M., Rodríguez-Huete, A., Pérez, R. and Mateu, M. G. (2018). Systematic analysis of biological roles of charged amino acid residues located throughout the structured inner wall of a virus capsid. *Sci. Rep.* **8**, 9543.

Cereghino, G. P.L., Cereghino, J. L., Ilgen, C. and Cregg, J. M. (2002). Production of recombinant proteins in fermenter cultures of the yeast Pichia pastoris. *Curr. Opin. Biotechnol.* **13**, 329–332.

Cereghino, J. L. and Cregg, J. M. (2000). Heterologous protein expression in the methylotrophic yeast Pichia pastoris. *FEMS Microbiol. Rev.* **24**, 45–66.

Chang, C. and Werb, Z. (2001). The many faces of metalloproteases: cell growth, invasion, angiogenesis and metastasis. *Trends Cell Biol.* **11**, S37-S43.

Chang, V. T., Crispin, M., Aricescu, A. R., Harvey, D. J., Nettleship, J. E., Fennelly, J. A., Yu, C., Boles, K. S., Evans, E. J., Stuart, D. I. et al. (2007). Glycoprotein structural genomics: solving the glycosylation problem. *Structure* **15**, 267–273.

Cheng, G., Cleary, A. M., Ye, Z. S., Hong, D. I., Lederman, S. and Baltimore, D. (1995). Involvement of CRAF1, a relative of TRAF, in CD40 signaling. *Science* **267**, 1494–1498.

Cismasiu, V. B., Denes, S. A., Reiländer, H., Michel, H. and Szedlacsek, S. E. (2004). The MAM (meprin/A5-protein/PTPmu) domain is a homophilic binding site promoting the lateral dimerization of receptor-like protein-tyrosine phosphatase mu. *J. Biol. Chem.* **279**, 26922–26931.

Copeland, R. A. (2000). *Enzymes. A practical introduction to structure, mechanism, and data analysis*. New York, Toronto: Wiley-VCH.

Craig, S. S., Reckelhoff, J. F. and Bond, J. S. (1987). Distribution of meprin in kidneys from mice with high- and low-meprin activity. *Am. J. Physiol.* **253**, C535-40.

Crisman, J. M., Zhang, B., Norman, L. P. and Bond, J. S. (2004). Deletion of the mouse meprin beta metalloprotease gene diminishes the ability of leukocytes to disseminate through extracellular matrix. *J. Immunol.* **172**, 4510–4519.

Cross, J. B., Duca, J. S., Kaminski, J. J. and Madison, V. S. (2002). The active site of a zinc-dependent metalloproteinase influences the computed pK(a) of ligands coordinated to the catalytic zinc ion. *J. Am. Chem. Soc.* **124**, 11004–11007.

DeGuzman, J. B., Speiser, P. W. and Trachtman, H. (2004). Urinary meprin-alpha: a potential marker of diabetic nephropathy. *J. Pediatr. Endocrinol. Metab.* **17**, 1663–1666.

Delclaux, C., Delacourt, C., D'Ortho, M. P., Boyer, V., Lafuma, C. and Harf, A. (1996). Role of gelatinase B and elastase in human polymorphonuclear neutrophil migration across basement membrane. *Am. J. Respir. Cell Mol. Biol.* **14**, 288–295.

Dessau, M. A. and Modis, Y. (2011). Protein crystallization for X-ray crystallography. *J. Vis. Exp.*

Diane Hopkins, B., Sato, K., Nakano, A. and Graham, T. R. (2000). Introduction of Kex2 cleavage sites in fusion proteins for monitoring localization and transport in yeast secretory pathway. In *Applications of Chimeric Genes and Hybrid Proteins - Part B: Cell Biology and Physiology* (ed. J. Thorner), pp. 107–118: Elsevier.

Dubochet, J. (2012). Cryo-EM--the first thirty years. *J. Microsc.* **245**, 221–224.

Dubochet, J. and McDowall, A. W. (1981). VITRIFICATION OF PURE WATER FOR ELECTRON MICROSCOPY. *J. Microsc.* **124**, 3–4.

Duca, L., Blaise, S., Romier, B., Laffargue, M., Gayral, S., El Btaouri, H., Kawecki, C., Guillot, A., Martiny, L., Debelle, L. et al. (2016). Matrix ageing and vascular impacts: focus on elastin fragmentation. *Cardiovas. Res.* **110**, 298–308.

Ducháčková, L. and Roithová, J. (2009). The interaction of zinc(II) and hydroxamic acids and a metal-triggered Lossen rearrangement. *Chem. Eur. J.* **15**, 13399–13405.

Dumermuth, E., Sterchi, E. E., Jiang, W. P., Wolz, R. L., Bond, J. S., Flannery, A. V. and Beynon, R. J. (1991). The astacin family of metalloendopeptidases. *J. Biol. Chem.* **266**, 21381–21385.

Emsley, P., Lohkamp, B., Scott, W. G. and Cowtan, K. (2010). Features and development of Coot. *Acta Crystallogr. D. Bio.I Crystallogr.* **66**, 486–501.

Eyal, E., Gerzon, S., Potapov, V., Edelman, M. and Sobolev, V. (2005). The limit of accuracy of protein modeling: influence of crystal packing on protein structure. *J. Mol. Biol.* **351**, 431–442.

Frank, J. (1975). Averaging of low exposure electron micrographs of non-periodic objects. *Ultramicroscopy* **1**, 159–162.

Frank, J. (2016). Generalized single-particle cryo-EM--a historical perspective. *Microscopy* **65**, 3–8.

Frantz, C., Stewart, K. M. and Weaver, V. M. (2010). The extracellular matrix at a glance. *J. Cell. Sci.* **123**, 4195–4200.

Freeze, H. H. and Kranz, C. (2010). Endoglycosidase and glycoamidase release of N-linked glycans. *Curr. Protoc. Mol. Biol.* **Chapter 17**, Unit 17.13A.

Freitas-Rodríguez, S., Folgueras, A. R. and López-Otín, C. (2017). The role of matrix metalloproteinases in aging: Tissue remodeling and beyond. *Biochim. Biophys. Acta Mol. Cell. Res.* **1864**, 2015–2025.

Fritz, C., Linnert, M., Jäger, C., Schlenzig, D., Ramsbeck, D., Kleinschmidt, M., Wermann, M., Demuth, H. U. and Schilling, S. (2021). *Structure and Dynamics of Meprin β in Complex with a Hydroxamate-Based Inhibitor*. Int J Mol Sci. **5651**.

Gaboriaud, C., Gregory-Pauron, L., Teillet, F., Thielens, N. M., Bally, I. and Arlaud, G. J. (2011). Structure and properties of the Ca(2+)-binding CUB domain, a widespread ligand-recognition unit involved in major biological functions. *Biochem. J.* **439**, 185–193.

Gallagher, J. R., Kim, A. J., Gulati, N. M. and Harris, A. K. (2019). Negative-Stain Transmission Electron Microscopy of Molecular Complexes for Image Analysis by 2D Class Averaging. *Curr. Protoc. Microbiol.* **54**, e90.

Gallivan, J. P. and Dougherty, D. A. (1999). Cation-pi interactions in structural biology. *Proc. Natl. Acad. Sci. U.S.A.* **96**, 9459–9464.

Gao, X., Wang, J., Yu, D.-Q., Bian, F., Xie, B.-B., Chen, X.-L., Zhou, B.-C., Lai, L.-H., Wang, Z.-X., Wu, J.-W. et al. (2010). Structural basis for the autoprocessing of zinc metalloproteases in the thermolysin family. *Proc. Natl. Acad. Sci. U.S.A.* **107**, 17569–17574.

Gasteiger, E., Gattiker, A., Hoogland, C., Ivanyi, I., Appel, R. D. and Bairoch, A. (2003). ExPASy: The proteomics server for in-depth protein knowledge and analysis. *Nucleic Acids Res.* **31**, 3784–3788.

Geier, G. and Zwilling, R. (1998). Cloning and characterization of a cDNA coding for Astacus embryonic astacin, a member of the astacin family of metalloproteases from the crayfish Astacus astacus. *Eur. J. Biochem.* **253**, 796–803.

Goddard, T. D., Huang, C. C., Meng, E. C., Pettersen, E. F., Couch, G. S., Morris, J. H. and Ferrin, T. E. (2018). UCSF ChimeraX: Meeting modern challenges in visualization and analysis. *Protein Sci.* **27**, 14–25.

Gomis-Rüth, F. X. (2003). Structural Aspects of the Metzincin Clan of Metalloendopeptidases. *Mol. Biotechnol.* **24**, 157–202.

Gomis-Rüth, F. X. (2009). Catalytic domain architecture of metzincin metalloproteases. *J. Biol. Chem.* **284**, 15353–15357.

Gomis-Rüth, F. X., Botelho, T. O. and Bode, W. (2012). A standard orientation for metallopeptidases. *Biochim. Biophys. Acta* **1824**, 157–163.

Gu, Y., Wu, J., Faucheu, C., Lalanne, J. L., Diu, A., Livingston, D. J. and Su, M. S. (1995). Interleukin-1 beta converting enzyme requires oligomerization for activity of processed forms in vivo. *EMBO J.* **14**, 1923–1931.

Guevara, T., Yiallouros, I., Kappelhoff, R., Bissdorf, S., Stöcker, W. and Gomis-Rüth, F. X. (2010). Proenzyme structure and activation of astacin metallopeptidase. *J. Biol. Chem.* **285**, 13958–13965.

Gustafsson, C., Govindarajan, S. and Minshull, J. (2004). Codon bias and heterologous protein expression. *Trends in biotechnology* **22**, 346–353.

Hahn, D., Pischitzis, A., Roesmann, S., Hansen, M. K., Leuenberger, B., Luginbuehl, U. and Sterchi, E. E. (2003). Phorbol 12-myristate 13-acetate-induced ectodomain shedding and phosphorylation of the human meprinbeta metalloprotease. *J. Biol. Chem.* **278**, 42829–42839.

Hamilton, S. R., Bobrowicz, P., Bobrowicz, B., Davidson, R. C., Li, H., Mitchell, T., Nett, J. H., Rausch, S., Stadheim, T. A., Wischnewski, H. et al. (2003). Production of complex human glycoproteins in yeast. *Science* **301**, 1244–1246.

Harding, M. M. (2002). Metal-ligand geometry relevant to proteins and in proteins: sodium and potassium. *Acta Crystallogr. D. Bio.l Crystallogr.* **58**, 872–874.

Harding, M. M. (2006). Small revisions to predicted distances around metal sites in proteins. *Acta Crystallogr. D. Bio.l Crystallogr.* **62**, 678–682.

Hedrich, J., Lottaz, D., Meyer, K., Yiallouros, I., Jahnen-Dechent, W., Stöcker, W. and Becker-Pauly, C. (2010). Fetuin-A and cystatin C are endogenous inhibitors of human meprin metalloproteases. *Biochem.* **49**, 8599–8607.

Heinig, M. and Frishman, D. (2004). STRIDE: a web server for secondary structure assignment from known atomic coordinates of proteins. *Nucleic Acids Res.* **32**, W500-2.

Heinz, A. (2020). Elastases and elastokines: elastin degradation and its significance in health and disease. *Crit. Rev. Biochem. Mol. Biol.* **55**, 252–273.

Heinz, A., Jung, M. C., Duca, L., Sippl, W., Taddese, S., Ihling, C., Rusciani, A., Jahreis, G., Weiss, A. S., Neubert, R. H. H. et al. (2010). Degradation of tropoelastin by matrix metalloproteinases--cleavage site specificities and release of matrikines. *FEBS J.* **277**, 1939–1956.

Herzog, C., Haun, R. S., Kaushal, V., Mayeux, P. R., Shah, S. V. and Kaushal, G. P. (2009). Meprin A and meprin alpha generate biologically functional IL-1beta from pro-IL-1beta. *Biochem. Biophys. Res. Com.* **379**, 904–908.

Herzog, C., Haun, R. S., Ludwig, A., Shah, S. V. and Kaushal, G. P. (2014). ADAM10 is the major sheddase responsible for the release of membrane-associated meprin A. *J. Biol. Chem.* **289**, 13308–13322.

Herzog, C., Seth, R., Shah, S. V. and Kaushal, G. P. (2007). Role of meprin A in renal tubular epithelial cell injury. *Kidney Int.* **71**, 1009–1018.

Hopkins, D. R., Keles, S. and Greenspan, D. S. (2007). The bone morphogenetic protein 1/Tolloid-like metalloproteinases. *Matrix Biol.* **26**, 508–523.

Huang, Y., Long, Y., Li, S., Lin, T., Wu, J., Zhang, Y. and Lin, Y. (2018). Investigation on the processing and improving the cleavage efficiency of furin cleavage sites in Pichia pastoris. *Microb. Cell Factories* **17**, 172.

Ishmael, F. T., Norcum, M. T., Benkovic, S. J. and Bond, J. S. (2001). Multimeric structure of the secreted meprin A metalloproteinase and characterization of the functional protomer. *J. Biol. Chem.* **276**, 23207–23211.

Ishmael, S. S., Ishmael, F. T., Jones, A. D. and Bond, J. S. (2006). Protease domain glycans affect oligomerization, disulfide bond formation, and stability of the meprin A metalloprotease homo-oligomer. *J. Biol. Chem.* **281**, 37404–37415.

Jacobsen, J. A., Major Jourden, J. L., Miller, M. T. and Cohen, S. M. (2010). To bind zinc or not to bind zinc: an examination of innovative approaches to improved metalloproteinase inhibition. *Biochim. Biophys. Acta* **1803**, 72–94.

Jani, M., Tordai, H., Trexler, M., Bányai, L. and Patthy, L. (2005). Hydroxamate-based peptide inhibitors of matrix metalloprotease 2. *Biochimie* **87**, 385–392.

Jayaprakash, N. G. and Surolia, A. (2017). Role of glycosylation in nucleating protein folding and stability. *Biochem. J.* **474**, 2333–2347.

Jefferson, T., dem Keller, U. auf, **Bellac, C., Metz, V. V., Broder, C., Hedrich, J., Ohler, A., Maier, W., Magdolen, V., Sterchi, E. et al.** (2013). The substrate degradome of meprin metalloproteases reveals an unexpected proteolytic link between meprin β and ADAM10. *Cell. Mol. Life. Sci.* **70**, 309–333.

Johnson, R. M., Higgins, A. J. and Muench, S. P. (2019). Emerging Role of Electron Microscopy in Drug Discovery. *Trends Biochem. Sci.* **44**, 897–898.

Jones, G., Willett, P., Glen, R. C., Leach, A. R. and Taylor, R. (1997). Development and validation of a genetic algorithm for flexible docking. *J. Mol. Biol.* **267**, 727–748.

Kadowaki, T., Tsukuba, T., Bertenshaw, G. P. and Bond, J. S. (2000). N-Linked oligosaccharides on the meprin A metalloprotease are important for secretion and enzymatic activity, but not for apical targeting. *J. Biol. Chem.* **275**, 25577–25584.

Karmilin, K., Schmitz, C., Kuske, M., Körschgen, H., Olf, M., Meyer, K., Hildebrand, A., Felten, M., Fridrich, S., Yiallouros, I. et al. (2019). Mammalian plasma fetuin-B is a selective inhibitor of ovastacin and meprin metalloproteinases. *Sci. Rep.* **9**, 546.

Kaushal, G. P., Haun, R. S., Herzog, C. and Shah, S. V. (2013). Meprin A metalloproteinase and its role in acute kidney injury. *APJ-Renal Physiol* **304**, F1150-8.

Kaushal, G. P., Walker, P. D. and Shah, S. V. (1994). An old enzyme with a new function: purification and characterization of a distinct matrix-degrading metalloproteinase in rat kidney cortex and its identification as meprin. *J. Cell Biol.* **126**, 1319–1327.

Kawai, K. and Nagata, N. (2012). Metal-ligand interactions: an analysis of zinc binding groups using the Protein Data Bank. *Eur. J. Med. Chem.* **51**, 271–276.

Kimple, M. E., Brill, A. L. and Pasker, R. L. (2013). Overview of affinity tags for protein purification. *Curr. Protoc. Protein Sci.* **73**, 9.9.1-9.9.23.

Kingston, R. E., Chen, C. A. and Rose, J. K. (2003). Calcium phosphate transfection. *Curr. Protoc. Mol. Biol.* **Chapter 9**, Unit 9.1.

Kirkpatrick, R. B., Ganguly, S., Angelichio, M., Griego, S., Shatzman, A., Silverman, C. and Rosenberg, M. (1995). Heavy chain dimers as well as complete antibodies are efficiently formed and secreted from Drosophila via a BiP-mediated pathway. *J. Biol. Chem.* **270**, 19800–19805.

Kluska, K., Adamczyk, J. and Krężel, A. (2018). Metal binding properties, stability and reactivity of zinc fingers. *Coord. Chem. Rev.* **367**, 18–64.

Köhler, D., Kruse, M.-N., Stöcker, W. and Sterchi, E. E. (2000). Heterologously overexpressed, affinity-purified human meprin α is functionally active and cleaves components of the basement membrane in vitro. *FEBS Lett.* **465**, 2–7.

Kronenberg, D., Bruns, B. C., Moali, C., Vadon-Le Goff, S., Sterchi, E. E., Traupe, H., Böhm, M., Hulmes, D. J. S., Stöcker, W. and Becker-Pauly, C. (2010). Processing of procollagen III by meprins: new players in extracellular matrix assembly? *J. Invest. Dermatol.* **130**, 2727–2735.

Kruse, M.-N., Becker, C., Lottaz, D., Köhler, D., Yiallouros, I., Krell, H.-W., Sterchi, E. E. and Stöcker, W. (2004). Human meprin alpha and beta homo-oligomers: cleavage of basement membrane proteins and sensitivity to metalloprotease inhibitors. *Biochem. J.* **378**, 383–389.

Kumar, K., Woo, S. M., Siu, T., Cortopassi, W. A., Duarte, F. and Paton, R. S. (2018). Cation-π interactions in protein-ligand binding: theory and data-mining reveal different roles for lysine and arginine. *Chem. Sci. J.* **9**, 2655–2665.

Kyhse-Andersen, J. (1984). Electroblotting of multiple gels: a simple apparatus without buffer tank for rapid transfer of proteins from polycrylamide to nitrocellulose. *J. Biochem. Biophys. Methods* **10**, 203–209.

Laemmli, U. K. (1970). Cleavage of structural proteins during the assembly of the head of bacteriophage T4. *Nature* **227**, 680–685.

Law, M. J., Linde, M. E., Chambers, E. J., Oubridge, C., Katsamba, P. S., Nilsson, L., Haworth, I. S. and Laird-Offringa, I. A. (2006). The role of positively charged amino acids and electrostatic interactions in the complex of U1A protein and U1 hairpin II RNA. *Nucleic Acids Res.* **34**, 275–285.

Lee, H. S., Qi, Y. and Im, W. (2015). Effects of N-glycosylation on protein conformation and dynamics: Protein Data Bank analysis and molecular dynamics simulation study. *Sci. Rep.* **5**, 8926.

Liebschner, D., Afonine, P. V., Baker, M. L., Bunkóczi, G., Chen, V. B., Croll, T. I., Hintze, B., Hung, L. W., Jain, S., McCoy, A. J. et al. (2019). Macromolecular structure determination using X-rays, neutrons and electrons: recent developments in Phenix. *Acta Crystallogr. D. Struct. Biol.* **75**, 861–877.

Lottaz, D., Maurer, C. A., Hahn, D., Büchler, M. W. and Sterchi, E. E. (1999). Nonpolarized secretion of human meprin alpha in colorectal cancer generates an increased proteolytic potential in the stroma. *Cancer Res.* **59**, 1127–1133.

Macauley-Patrick, S., Fazenda, M. L., McNeil, B. and Harvey, L. M. (2005). Heterologous protein production using the Pichia pastoris expression system. *Yeast* **22**, 249–270.

Madoux, F., Tredup, C., Spicer, T. P., Scampavia, L., Chase, P. S., Hodder, P. S., Fields, G. B., Becker-Pauly, C. and Minond, D. (2014). Development of high throughput screening assays and pilot screen for inhibitors of metalloproteases meprin α and β. *Biopolymers* **102**, 396–406.

Mandel, M. and Higa, A. (1970). Calcium-dependent bacteriophage DNA infection. *J. Mol. Biol.* **53**, 159–162.

Manzine, P. R., Ettcheto, M., Cano, A., Busquets, O., Marcello, E., Pelucchi, S., Di Luca, M., Endres, K., Olloquequi, J., Camins, A. et al. (2019). ADAM10 in Alzheimer's disease: Pharmacological modulation by natural compounds and its role as a peripheral marker. *Biomed. Pharmacother.* **113**, 108661.

Marchand, P., Tang, J. and Bond, J. S. (1994). Membrane association and oligomeric organization of the alpha and beta subunits of mouse meprin A. *J. Biol. Chem.* **269**, 15388–15393.

Marchand, P., Tang, J., Johnson, G. D. and Bond, J. S. (1995). COOH-terminal proteolytic processing of secreted and membrane forms of the alpha subunit of the metalloprotease meprin A. Requirement of the I domain for processing in the endoplasmic reticulum. *J. Biol. Chem.* **270**, 5449–5456.

Marchand, P., Volkmann, M. and Bond, J. S. (1996). Cysteine mutations in the MAM domain result in monomeric meprin and alter stability and activity of the proteinase. *J. Biol. Chem.* **271**, 24236–24241.

McWilliam, H., Li, W., Uludag, M., Squizzato, S., Park, Y. M., Buso, N., Cowley, A. P. and Lopez, R. (2013). Analysis Tool Web Services from the EMBL-EBI. *Nucleic Acids Res.* **41**, W597-600.

Michaelis, L., Menten, M. L., Johnson, K. A. and Goody, R. S. (2011). The original Michaelis constant: translation of the 1913 Michaelis-Menten paper. *Biochem.* **50**, 8264–8269.

Micsonai, A., Wien, F., Bulyáki, É., Kun, J., Moussong, É., Lee, Y.-H., Goto, Y., Réfrégiers, M. and Kardos, J. (2018). BeStSel: a web server for accurate protein secondary structure prediction and fold recognition from the circular dichroism spectra. *Nucleic Acids Res.* **46**, W315-W322.

Micsonai, A., Wien, F., Kernya, L., Lee, Y.-H., Goto, Y., Réfrégiers, M. and Kardos, J. (2015). Accurate secondary structure prediction and fold recognition for circular dichroism spectroscopy. *Proc. Natl. Acad. Sci. U.S.A.* **112**, E3095-103.

Miekus, N., Luise, C., Sippl, W., Baczek, T., Schmelzer, C. E. H. and Heinz, A. (2019). MMP-14 degrades tropoelastin and elastin. *Biochimie* **165**, 32–39.

Minder, P., Bayha, E., Becker-Pauly, C. and Sterchi, E. E. (2012). Meprinα transactivates the epidermal growth factor receptor (EGFR) via ligand shedding, thereby enhancing colorectal cancer cell proliferation and migration. *J. Biol. Chem.* **287**, 35201–35211.

Mitra, N., Sinha, S., Ramya, T. N. C. and Surolia, A. (2006). N-linked oligosaccharides as outfitters for glycoprotein folding, form and function. *Trends Biochem. Sci.* **31**, 156–163.

Monaco, S., Sparano, V., Gioia, M., Sbardella, D., Di Pierro, D., Marini, S. and Coletta, M. (2006). Enzymatic processing of collagen IV by MMP-2 (gelatinase A) affects neutrophil migration and it is modulated by extracatalytic domains. *Protein Sci.* **15**, 2805–2815.

Moremen, K. W., Tiemeyer, M. and Nairn, A. V. (2012). Vertebrate protein glycosylation: diversity, synthesis and function. *Nat. Rev. Mol. Cell. Biol.* **13**, 448–462.

Nakamura, H., Kiyoshi, M., Anraku, M., Hashii, N., Oda-Ueda, N., Ueda, T. and Ohkuri, T. (2020). Glycosylation decreases aggregation and immunogenicity of adalimumab fab secreted from Pichia pastoris. *J. Biochem.*

Neuman, M. G. (2007). Immune dysfunction in inflammatory bowel disease. *Transl. Res.* **149**, 173–186.

Nokelainen, M., Tu, H., Vuorela, A., Notbohm, H., Kivirikko, K. I. and Myllyharju, J. (2001). High-level production of human type I collagen in the yeast Pichia pastoris. *Yeast* **18**, 797–806.

Norman, L. P., Jiang, W., Han, X., Saunders, T. L. and Bond, J. S. (2003). Targeted disruption of the meprin beta gene in mice leads to underrepresentation of knockout mice and changes in renal gene expression profiles. *Mol. Cell. Biol.* **23**, 1221–1230.

Ohler, A., Debela, M., Wagner, S., Magdolen, V. and Becker-Pauly, C. (2010). Analyzing the protease web in skin: meprin metalloproteases are activated specifically by KLK4, 5 and 8 vice versa leading to processing of proKLK7 thereby triggering its activation. *J. Biol. Chem.* **391**, 455–460.

OuYang, H.-Y., Xu, J., Luo, J., Zou, R.-H., Chen, K., Le, Y., Zhang, Y.-F., Wei, W., Guo, R.-P. and Shi, M. (2016). MEP1A contributes to tumor progression and predicts poor clinical outcome in human hepatocellular carcinoma. *Hepatology* **63**, 1227–1239.

Pakkanen, O., Pirskanen, A. and Myllyharju, J. (2006). Selective expression of nonsecreted triple-helical and secreted single-chain recombinant collagen fragments in the yeast Pichia pastoris. *J. Biotechnol.* **123**, 248–256.

Pankov, R. and Yamada, K. M. (2002). Fibronectin at a glance. *J. Cell. Sci.* **115**, 3861–3863.

Perše, M. and Večerić-Haler, Ž. (2018). Cisplatin-Induced Rodent Model of Kidney Injury: Characteristics and Challenges. *BioMed. Res. Int.* **2018**, 1462802.

Peters, F. and Becker-Pauly, C. (2019). Role of meprin metalloproteases in metastasis and tumor microenvironment. *Cancer Metastasis Rev.* **38**, 347–356.

Peters, F., Scharfenberg, F., Colmorgen, C., Armbrust, F., Wichert, R., Arnold, P., Potempa, B., Potempa, J., Pietrzik, C. U., Häsler, R. et al. (2019). Tethering soluble meprin α in an enzyme complex to the cell surface affects IBD-associated genes. *FASEB J.* **33**, 7490–7504.

Petrauskas, V., Maximowitsch, E. and Matulis, D. (2015). Thermodynamics of Ion Pair Formations Between Charged Poly(Amino Acid)s. *J. Phys. Chem. B* **119**, 12164–12171.

Pettersen, E. F., Goddard, T. D., Huang, C. C., Couch, G. S., Greenblatt, D. M., Meng, E. C. and Ferrin, T. E. (2004). UCSF Chimera--a visualization system for exploratory research and analysis. *J. Comput. Chem.* **25**, 1605–1612.

Pontén, F., Jirström, K. and Uhlen, M. (2008). The Human Protein Atlas--a tool for pathology. *J. Pathol.* **216**, 387–393.

Pretzer, D., Schulteis, B., Vander Velde, D. G., Smith, C. D., Mitchell, J. W. and Manning, M. C. (1992). Effect of zinc binding on the structure and stability of fibrolase, a fibrinolytic protein from snake venom. *Pharm. Res.* **9**, 870–877.

Prox, J., Arnold, P. and Becker-Pauly, C. (2015). Meprin α and meprin β: Procollagen proteinases in health and disease. *Matrix Biol.* **44-46**, 7–13.

Puente, X. S., Sánchez, L. M., Gutiérrez-Fernández, A., Velasco, G. and López-Otín, C. (2005). A genomic view of the complexity of mammalian proteolytic systems. *Biochem. Soc. Trans.* **33**, 331–334.

Pyati, P., Fitches, E. and Gatehouse, J. A. (2014). Optimising expression of the recombinant fusion protein biopesticide ω-hexatoxin-Hv1a/GNA in Pichia pastoris: sequence modifications and a simple method for the generation of multi-copy strains. *J. Ind. Microbiol. Biotechnol.* **41**, 1237–1247.

Querfurth, H. W. and LaFerla, F. M. (2010). Alzheimer's disease. *N. Engl. J. Med.* **362**, 329–344.

Raemaekers, R. J., Muro, L. de, **Gatehouse, J. A. and Fordham-Skelton, A. P.** (1999). Functional phytohemagglutinin (PHA) and Galanthus nivalis agglutinin (GNA) expressed in Pichia pastoris correct N-terminal processing and secretion of heterologous proteins expressed using the PHA-E signal peptide. *Eur. J. Biochem.* **265**, 394–403.

Ramachandran, R., Altier, C., Oikonomopoulou, K. and Hollenberg, M. D. (2016). Proteinases, Their Extracellular Targets, and Inflammatory Signaling. *Pharma. Rev.* **68**, 1110–1142.

Ramsbeck, D., Hamann, A., Richter, G., Schlenzig, D., Geissler, S., Nykiel, V., Cynis, H., Schilling, S. and Buchholz, M. (2018). Structure-Guided Design, Synthesis, and Characterization of Next-Generation Meprin β Inhibitors. *J. Med. Chem.* **61**, 4578–4592.

Ramsbeck, D., Hamann, A., Schlenzig, D., Schilling, S. and Buchholz, M. (2017). First insight into structure-activity relationships of selective meprin β inhibitors. *Bioorg. Med. Chem. Lett.* **27**, 2428–2431.

Ranjbar, B. and Gill, P. (2009). Circular dichroism techniques: biomolecular and nanostructural analyses- a review. *Chem. Biol. Drug. Des.* **74**, 101–120.

Rawlings, N. D., Waller, M., Barrett, A. J. and Bateman, A. (2014). MEROPS: the database of proteolytic enzymes, their substrates and inhibitors. *Nucleic Acids Res.* **42**, D503-9.

Reily, C., Stewart, T. J., Renfrow, M. B. and Novak, J. (2019). Glycosylation in health and disease. *Nat. Rev. Nephrol.* **15**, 346–366.

Renaud, J.-P., Chari, A., Ciferri, C., Liu, W.-T., Rémigy, H.-W., Stark, H. and Wiesmann, C. (2018). Cryo-EM in drug discovery: achievements, limitations and prospects. *Nat. Rev. Drug. Discov.* **17**, 471–492.

Rösmann, S., Hahn, D., Lottaz, D., Kruse, M.-N., Stöcker, W. and Sterchi, E. E. (2002). Activation of human meprin-alpha in a cell culture model of colorectal cancer is triggered by the plasminogen-activating system. *J. Biol. Chem.* **277**, 40650–40658.

Rudd, P. M. and Dwek, R. A. (1997). Glycosylation: heterogeneity and the 3D structure of proteins. *Crit. Rev. Biochem. Mol. Biol.* **32**, 1–100.

Russo Krauss, I., Merlino, A., Vergara, A. and Sica, F. (2013). An overview of biological macromolecule crystallization. *Int. J. Mol. Sci.* **14**, 11643–11691.

Sambrook, J., Fritsch, E. F. and Maniatis, T. (1989). *Molecular cloning*. Cold Spring Harbor, N.Y.: Cold Spring Harbor laboratory Press.

Sanger, F., Nicklen, S. and Coulson, A. R. (1977). DNA sequencing with chain-terminating inhibitors. *Proc. Natl. Acad. Sci. U.S.A.* **74**, 5463–5467.

Schägger, H., Cramer, W. A. and Jagow, G. von (1994). Analysis of molecular masses and oligomeric states of protein complexes by blue native electrophoresis and isolation of membrane protein complexes by two-dimensional native electrophoresis. *Anal. Biochem.* **217**, 220–230.

Schechter, I. and Berger, A. (1968). On the active site of proteases. III. Mapping the active site of papain; specific peptide inhibitors of papain. *Biochem. Biophys. Res. Com.* **32**, 898–902.

Schlenzig, D., Cynis, H., Hartlage-Rübsamen, M., Zeitschel, U., Menge, K., Fothe, A., Ramsbeck, D., Spahn, C., Wermann, M., Roßner, S. et al. (2018). Dipeptidyl-Peptidase Activity of Meprin β Links N-truncation of Aβ with Glutaminyl Cyclase-Catalyzed pGlu-Aβ Formation. *J. Alzheimer's Dis.* **66**, 359–375.

Schlenzig, D., Wermann, M., Ramsbeck, D., Moenke-Wedler, T. and Schilling, S. (2015). Expression, purification and initial characterization of human meprin β from Pichia pastoris. *Protein Expr. Purif.* **116**, 75–81.

Schlomann, U., Wildeboer, D., Webster, A., Antropova, O., Zeuschner, D., Knight, C. G., Docherty, A. J. P., Lambert, M., Skelton, L., Jockusch, H. et al. (2002). The metalloprotease disintegrin ADAM8. Processing by autocatalysis is required for proteolytic activity and cell adhesion. *J. Biol. Chem.* **277**, 48210–48219.

Schmelzer, C. E. H., Jung, M. C., Wohlrab, J., Neubert, R. H. H. and Heinz, A. (2012). Does human leukocyte elastase degrade intact skin elastin? *FEBS J.* **279**, 4191–4200.

Schneider, I. (1972). Cell lines derived from late embryonic stages of Drosophila melanogaster. *J. Embryol. Exp. Morphol.* **27**, 353–365.

Schönherr, C., Bien, J., Isbert, S., Wichert, R., Prox, J., Altmeppen, H., Kumar, S., Walter, J., Lichtenthaler, S. F., Weggen, S. et al. (2016). Generation of aggregation prone N-terminally truncated amyloid β peptides by meprin β depends on the sequence specificity at the cleavage site. *Mol. Neurodegener.* **11**, 19.

Shibata, Y., Iwamatsu, T., Oba, Y., Kobayashi, D., Tanaka, M., Nagahama, Y., Suzuki, N. and Yoshikuni, M. (2000). Identification and cDNA cloning of alveolin, an extracellular metalloproteinase, which induces chorion hardening of medaka (Oryzias latipes) eggs upon fertilization. *J. Biol. Chem.* **275**, 8349–8354.

Simons, E. R., Schneider, E. G. and Blout, E. R. (1969). Thermal effects on the circular dichroism spectra of ribonuclease A and of ribonuclease S-protein. *J. Biol. Chem.* **244**, 4023–4026.

Smith, P. K., Krohn, R. I., Hermanson, G. T., Mallia, A. K., Gartner, F. H., Provenzano, M. D., Fujimoto, E. K., Goeke, N. M., Olson, B. J. and Klenk, D. C. (1985). Measurement of protein using bicinchoninic acid. *Anal. Biochem.* **150**, 76–85.

Sterchi, E. E., Stöcker, W. and Bond, J. S. (2008). Meprins, membrane-bound and secreted astacin metalloproteinases. *Mol. Aspects Med.* **29**, 309–328.

Stöcker, W., Gomis-Rüth, F. X., Bode, W. and Zwilling, R. (1993). Implications of the three-dimensional structure of astacin for the structure and function of the astacin family of zinc-endopeptidases. *Eur. J. Biochem.* **214**, 215–231.

Stöcker, W., Grams, F., Baumann, U., Reinemer, P., Gomis-Rüth, F. X., McKay, D. B. and Bode, W. (1995). The metzincins--topological and sequential relations between the astacins, adamalysins, serralysins, and matrixins (collagenases) define a superfamily of zinc-peptidases. *Protein Sci.* **4**, 823–840.

Stöcker, W. and Zwilling, R. (1995). [19] Astacin. In *Proteolytic Enzymes: Aspartic and Metallo Peptidases* (ed. A. Barrett), pp. 305–325: Elsevier.

Sun, Q., Jin, H.-J. and Bond, J. S. (2009). Disruption of the meprin alpha and beta genes in mice alters homeostasis of monocytes and natural killer cells. *Exp. Hematol.* **37**, 346–356.

Tachioka, M., Sugimoto, N., Nakamura, A., Sunagawa, N., Ishida, T., Uchiyama, T., Igarashi, K. and Samejima, M. (2016). Development of simple random mutagenesis protocol for the protein expression system in Pichia pastoris. *Biotechnol. Biofuels* **9**, 199.

Tan, K., Jäger, C., Schlenzig, D., Schilling, S., Buchholz, M. and Ramsbeck, D. (2018). Tertiary-Amine-Based Inhibitors of the Astacin Protease Meprin α. *ChemMedChem* **13**, 1619–1624.

Tang, H., Wang, S., Wang, J., Song, M., Xu, M., Zhang, M., Shen, Y., Hou, J. and Bao, X. (2016). N-hypermannose glycosylation disruption enhances recombinant protein production by regulating secretory pathway and cell wall integrity in Saccharomyces cerevisiae. *Sci. Rep.* **6**, 25654.

Tang, J. and Bond, J. S. (1998). Maturation of secreted meprin alpha during biosynthesis: role of the furin site and identification of the COOH-terminal amino acids of the mouse kidney metalloprotease subunit. *Arch. Biochem. Biophys.* **349**, 192–200.

Tanner, W. and Lehle, L. (1987). Protein glycosylation in yeast. *Biochim. Biophys. Acta Biomembr.* **906**, 81–99.

The UniProt Consortium (2019). UniProt: a worldwide hub of protein knowledge. *Nucleic Acids Res.* **47**, D506-D515.

Thul, P. J., Åkesson, L., Wiking, M., Mahdessian, D., Geladaki, A., Ait Blal, H., Alm, T., Asplund, A., Björk, L., Breckels, L. M. et al. (2017). A subcellular map of the human proteome. *Science* **356**.

Titani, K., Torff, H. J., Hormel, S., Kumar, S., Walsh, K. A., Rödl, J., Neurath, H. and Zwilling, R. (1987). Amino acid sequence of a unique protease from the crayfish Astacus fluviatilis. *Biochem.* **26**, 222–226.

Tomkinson, B. (2000). Association and dissociation of the tripeptidyl-peptidase II complex as a way of regulating the enzyme activity. *Arch. Biochem. Biophys.* **376**, 275–280.

Tomkinson, B., Ní Laoi, B. and Wellington, K. (2002). The insert within the catalytic domain of tripeptidyl-peptidase II is important for the formation of the active complex. *Eur. J. Biochem.* **269**, 1438–1443.

Trachtman, H., Valderrama, E., Dietrich, J. M. and Bond, J. S. (1995). The role of meprin A in the pathogenesis of acute renal failure. *Biochem. Biophys. Res. Com.* **208**, 498–505.

Tschopp, J. F., Sverlow, G., Kosson, R., Craig, W. and Grinna, L. (1987). High-Level Secretion of Glycosylated Invertase in the Methylotrophic Yeast, Pichia Pastoris. *Nat. Biotechnol.* **5**, 1305–1308.

Tsukuba, T. and Bond, J. S. (1998). Role of the COOH-terminal domains of meprin A in folding, secretion, and activity of the metalloendopeptidase. *J. Biol. Chem.* **273**, 35260–35267.

Tüting, C. (2015). *Expression und Charakterisierung von humanem Meprin α*. Masterarbeit, Martin-Luther-University Halle-Wittenberg. Halle (Saale).

Vadon-Le Goff, S., Hulmes, D. J. S. and Moali, C. (2015). BMP-1/tolloid-like proteinases synchronize matrix assembly with growth factor activation to promote morphogenesis and tissue remodeling. *Matrix Biol.* **44-46**, 14–23.

van Drie, J. H. and Tong, L. (2020). Cryo-EM as a powerful tool for drug discovery. *Bioorg. Med. Chem. Lett.* **30**, 127524.

Vazeille, E., Bringer, M.-A., Gardarin, A., Chambon, C., Becker-Pauly, C., Pender, S. L. F., Jakob, C., Müller, S., Lottaz, D. and Darfeuille-Michaud, A. (2011). Role of meprins to protect ileal mucosa of Crohn's disease patients from colonization by adherent-invasive E. coli. *PLoS ONE* **6**, e21199.

Vilar, S., Cozza, G. and Moro, S. (2008). Medicinal chemistry and the molecular operating environment (MOE): application of QSAR and molecular docking to drug discovery. *Curr. Top. Med. Chem.* **8**, 1555–1572.

Villa, J. P., Bertenshaw, G. P. and Bond, J. S. (2003). Critical amino acids in the active site of meprin metalloproteinases for substrate and peptide bond specificity. *J. Biol. Chem.* **278**, 42545–42550.

Vu, T. H. and Werb, Z. (2000). Matrix metalloproteinases: effectors of development and normal physiology. *Genes Dev.* **14**, 2123–2133.

Vuorela, A., Myllyharju, J., Nissi, R., Pihlajaniemi, T. and Kivirikko, K. I. (1997). Assembly of human prolyl 4-hydroxylase and type III collagen in the yeast pichia pastoris: formation of a stable enzyme tetramer requires coexpression with collagen and assembly of a stable collagen requires coexpression with prolyl 4-hydroxylase. *EMBO J.* **16**, 6702–6712.

Walker, P. D., Kaushal, G. P. and Shah, S. V. (1998). Meprin A, the major matrix degrading enzyme in renal tubules, produces a novel nidogen fragment in vitro and in vivo. *Kidney Int.* **53**, 1673–1680.

Walsh, M. C., Lee, J. and Choi, Y. (2015). Tumor necrosis factor receptor- associated factor 6 (TRAF6) regulation of development, function, and homeostasis of the immune system. *Immunological reviews* **266**, 72–92.

Wang, H.-W. and Wang, J.-W. (2017). How cryo-electron microscopy and X-ray crystallography complement each other. *Protein Sci* **26**, 32–39.

Wang, J.-R., Li, Y.-Y., Liu, D.-N., Liu, J.-S., Li, P., Chen, L.-Z. and Xu, S.-D. (2015a). Codon Optimization Significantly Improves the Expression Level of α -Amylase Gene from Bacillus licheniformis in Pichia pastoris. *BioMed. Res. Int.* **2015**, 248680.

Wang, M., Kim, S. H., Monticone, R. E. and Lakatta, E. G. (2015b). Matrix metalloproteinases promote arterial remodeling in aging, hypertension, and atherosclerosis. *Hypertension* **65**, 698–703.

Waterhouse, A., Bertoni, M., Bienert, S., Studer, G., Tauriello, G., Gumienny, R., Heer, F. T., Beer, T. A. P. de, **Rempfer, C., Bordoli, L. et al.** (2018). SWISS-MODEL: homology modelling of protein structures and complexes. *Nucleic Acids Res.* **46**, W296-W303.

Weber, K. and Osborn, M. (1969). The reliability of molecular weight determinations by dodecyl sulfate-polyacrylamide gel electrophoresis. *J. Biol. Chem.* **244**, 4406–4412.

Wichert, R., Scharfenberg, F., Colmorgen, C., Koudelka, T., Schwarz, J., Wetzel, S., Potempa, B., Potempa, J., Bartsch, J. W., Sagi, I. et al. (2019). Meprin β induces activities of A disintegrin and metalloproteinases 9, 10, and 17 by specific prodomain cleavage. *FASEB J.* **33**, 11925–11940.

Wiedemann, C., Bellstedt, P. and Görlach, M. (2013). CAPITO--a web server-based analysis and plotting tool for circular dichroism data. *Bioinformatics* **29**, 1750–1757.

Wise, S. G., Yeo, G. C., Hiob, M. A., Rnjak-Kovacina, J., Kaplan, D. L., Ng, M. K. C. and Weiss, A. S. (2014). Tropoelastin: a versatile, bioactive assembly module. *Acta Biomater.* **10**, 1532–1541.

Wouters, M. A., Rigoutsos, I., Chu, C. K., Feng, L. L., Sparrow, D. B. and Dunwoodie, S. L. (2005). Evolution of distinct EGF domains with specific functions. *Protein Sci.* **14**, 1091–1103.

Wu, R., Lu, Z., Cao, Z. and Zhang, Y. (2011). Zinc chelation with hydroxamate in histone deacetylases modulated by water access to the linker binding channel. *J. Am. Chem. Soc.* **133**, 6110–6113.

Wyatt, P. J. (1993). Light scattering and the absolute characterization of macromolecules. *Anal. Chim. Acta* **272**, 1–40.

Yang, H., Zhai, C., Yu, X., Li, Z., Tang, W., Liu, Y., Ma, X., Zhong, X., Li, G., Di Wu et al. (2016). High-level expression of Proteinase K from Tritirachium album Limber in Pichia pastoris using multi-copy expression strains. *Protein Expr. Purif.* **122**, 38–44.

Yang, S., Kuang, Y., Li, H., Liu, Y., Hui, X., Li, P., Jiang, Z., Zhou, Y., Wang, Y., Xu, A. et al. (2013). Enhanced production of recombinant secretory proteins in Pichia pastoris by optimizing Kex2 P1' site. *PLoS ONE* **8**, e75347.

Ye, H., Arron, J. R., Lamothe, B., Cirilli, M., Kobayashi, T., Shevde, N. K., Segal, D., Dzivenu, O. K., Vologodskaia, M., Yim, M. et al. (2002). Distinct molecular mechanism for initiating TRAF6 signalling. *Nature* **418**, 443–447.

Yi, C.-W., Wang, L.-Q., Huang, J.-J., Pan, K., Chen, J. and Liang, Y. (2018). Glycosylation Significantly Inhibits the Aggregation of Human Prion Protein and Decreases Its Cytotoxicity. *Sci. Rep.* **8**, 12603.

Yiallouros, I., Kappelhoff, R., Schilling, O., Wegmann, F., Helms, M. W., Auge, A., Brachtendorf, G., Berkhoff, E. G., Beermann, B., Hinz, H.-J. et al. (2002). Activation Mechanism of Pro-astacin: Role of the Pro-peptide, Tryptic and Autoproteolytic Cleavage and Importance of Precise Amino-terminal Processing. *J. Mol. Biol.* **324**, 237–246.

Yura, R. E., Bradley, S. G., Ramesh, G., Reeves, W. B. and Bond, J. S. (2009). Meprin A metalloproteases enhance renal damage and bladder inflammation after LPS challenge. *APJ-Renal Physiol* **296**, F135-44.

Zanotti, G. (2016). Cryo-EM and X-Ray Crystallography: Complementary or Alternative Techniques? *NanoWorld J.* **2**.

Zhang, F., Skoda, M. W. A., Jacobs, R. M. J., Martin, R. A., Martin, C. M. and Schreiber, F. (2007). Protein interactions studied by SAXS: effect of ionic strength and protein concentration for BSA in aqueous solutions. *J. Phys. Chem. B* **111**, 251–259.

Zheng, H., Chruszcz, M., Lasota, P., Lebioda, L. and Minor, W. (2008). Data mining of metal ion environments present in protein structures. *J. Inorg. Biochem.* **102**, 1765–1776.

Zhou, H.-X. and Pang, X. (2018). Electrostatic Interactions in Protein Structure, Folding, Binding, and Condensation. *Chem. Rev.* **118**, 1691–1741.

Zhu, T., Guo, M., Tang, Z., Zhang, M., Zhuang, Y., Chu, J. and Zhang, S. (2009). Efficient generation of multi-copy strains for optimizing secretory expression of porcine insulin precursor in yeast Pichia pastoris. *Journal of applied microbiology* **107**, 954–963.

Danksagung

Zusätzlich geht mein herzlicher Dank an meine Kollegen des Fraunhofer IZI-MWT, die eine angenehme und entspannte Arbeitsatmosphäre ermöglichten. Für konstruktive Diskussionen und so manchen Denkanstoß möchte ich mich insbesondere bei Mathias Schenk, Dr. Nadine Taudte, Dr. Daniel Ramsbeck, Kathrin Tan und Christian Jäger bedanken.

Besonders lieben Dank gilt meinem Ehemann, meinen Eltern und meiner Schwester, durch Eure Unterstützung konnte ich dieses Ziel überhaupt in Angriff nehmen. Danke, dass Ihr mich mit motivierenden und aufmunternden Worten durch die ganze Zeit der Promotion begleitet habt!

Lebenslauf

Persönliche Daten

Name	Claudia Fritz geb. Spahn
Geburtsdatum/-ort	21.08.1991/Borna
Status	Master of Science
Nationalität	Deutsch

Akademische Ausbildung

Seit 08/2016	**Martin-Luther-Universität Halle-Wittenberg, Institut für Pharmazie** Halle (Saale), Deutschland Dissertation "*On the 3D-Structures of Meprin α and β, and the Role of Oligomerization for Stability and Activity of Meprin α*"
10/2013 – 12/2015	**Martin-Luther-Universität Halle-Wittenberg, Institut für Pharmazie** Halle (Saale), Deutschland *Pharmaceutical Biotechnology*, Master of Science
10/2010 – 09/2013	**Berufsakademie Sachsen, Staatliche Studienakademie Riesa** Riesa, Deutschland Labor- und Verfahrenstechnik: Biotechnologie, Bachelor of Science

Praktische Erfahrung

Seit 03/2020	**An-Institut für angewandte Dermatopharmazie an der Martin-Luther-Universität Halle-Wittenberg e.V.** Halle (Saale), Deutschland Wissenschaftliche Mitarbeiterin
01 – 03/2019	**Monash University, Institut für Biochemie und Molekularbiologie** Arbeitsgruppe James Whisstock, Melbourne, Australien Forschungsaufenthalt zur Strukturaufklärung von Metalloproteasen mittels cryo – Elektronenmikroskopie
08/2016 – 12/2019	**Fraunhofer Institut für Zelltherapie und Immunologie, Abteilung Molekulare Wirkstoffbiochemie und Therapieentwicklung** Halle (Saale), Deutschland Dissertation "*On the 3D-Structures of Meprin α and β, and the Role of Oligomerization for Stability and Activity of Meprin α*"

01 – 07/2016	**Fraunhofer Institut für Zelltherapie und Immunologie, Abteilung Molekulare Wirkstoffbiochemie und Therapieentwicklung** Halle (Saale), Deutschland

Wissenschaftlich-Technische Assistentin

10/2014 – 12/2015	**Fraunhofer Institut für Zelltherapie und Immunologie, Abteilung Molekulare Wirkstoffbiochemie und Therapieentwicklung** Halle (Saale), Deutschland

Masterarbeit, Projektstudie

10/2010 – 09/2013	**Serumwerk Bernburg AG**, Bernburg, Deutschland

Duales Bachelorstudium, Bachelorarbeit

Halle (Saale),   ……………………………

Claudia Fritz

Publikationsliste

Spahn C, Wermann M, Eichentopf R, Hause G, Schlenzig D, Schilling S. *Purification of recombinant Aβ(1-42) and pGlu-Aβ(3-42) using preparative SDS-PAGE*. Electrophoresis. 2017 Aug;38(16):2042-2049. doi: 10.1002/elps.201700154.

Schlenzig D, Cynis H, Hartlage-Rübsamen M, Zeitschel U, Menge K, Fothe A, Ramsbeck D, **Spahn C**, Wermann M, Roßner S, Buchholz M, Schilling S, Demuth HU. *Dipeptidyl-Peptidase Activity of Meprin β Links N-truncation of Aβ with Glutaminyl Cyclase-Catalyzed pGlu-Aβ Formation*. J Alzheimers Dis. 2018;66(1):359-375. doi: 10.3233/JAD-171183.

Fritz C, Linnert M, Jäger C, Schlenzig D., Ramsbeck R, Kleinschmidt M, Wermann M, Demuth HU, Schilling S. *Structure and Dynamics of Meprin β in complex with a Hydroxamate-Based Inhibitor*. Int J Mol Sci. 2021 May 26;22(11):5651. doi: 10.3390/ijms22115651.

Eidesstattliche Erklärung

Hiermit erkläre ich, Claudia Fritz, dass ich mich mit der vorliegenden Arbeit „*On the 3D-structures of Meprin α and β, and the Role of Oligomerization for Stability and Activity of Meprin α*" erstmals um die Erlangung des Doktorgrades bewerbe. Die vorliegende Arbeit habe ich selbstständig und ohne fremde Hilfe verfasst, außer anderweitig gekennzeichnet. Andere als die von mir verwendeten Quellen und Hilfsmittel nicht benutzt und die aus den verwendeten Werken wörtlich oder inhaltlich entnommenen Stellen als solche kenntlich gemacht.

Halle (Saale),   ………………………………

                                                                                                   Claudia Fritz